UNIVERSITY OF CALIFORNIA, SAN DIEGO

Discovery of a Higgs Boson in the H to ZZ to 4 leptons channel

A dissertation submitted in partial satisfaction of the
requirements for the degree
Doctor of Philosophy

in

Physics

by

Adish Pradeep Vartak

Committee in charge:

Professor Vivek Sharma, Chair
Professor James Branson
Professor Craig Callender
Professor Kenneth Intriligator
Professor Justin Derriter Roberts

2014

The Dissertation of Adish Pradeep Vartak is approved, and it is acceptable in quality and form for publication on microfilm and electronically:

_____

_____

_____

_____

_____

Chair

University of California, San Diego

2014

Dedication

To Pradeep and Chitra Vartak:

My parents and guiding lights

Table of Contents

List of Figures

List of Tables

Acknowledgements

The work presented in this thesis is the product of intense and exciting collaboration of thousands of scientists across the world. It is this spirit of collaboration which forms the cornerstone of the ongoing frontier research at CERN. I take this opportunity to express my gratitude to the entire community of physicists whose efforts have culminated into one of the most significant advances in our understanding of nature.

It has been my great privilege to be a small part of the momentous discovery of the Higgs boson, and I am deeply indebted to my mentor Vivek Sharma for giving me the opportunity and all the requisite guidance to participate in this great hunt of our times. I would like to specially thank my colleagues Boris Mangano, Emanuele Di Marco, Giovanni Petrucciani and Matthew LeBourgeois. Without their incessant and insightful aid, and scrupulous supervision this journey would have been a lot harder, if not altogether impossible. I also take this opportunity to thank all the teachers at San Diego who have helped me learn physics.

I convey my love and regards to Nandu Mama, Seema Mami, Swapna and Rasika for making Geneva feel a lot like home. And lastly, I express my sincere love and respect to my parents who have been two unwavering pillars of strength and support.

This thesis is a reprint of the material as it appears in "Measurement of the properties of a Higgs boson in the four-lepton final state" by CMS Collaboration, Phys. Rev. D 89 (2014) 092007, "Observation of a new boson at a mass of 125 GeV with the CMS experiment at the LHC" by CMS Collaboration, Phys. Lett. B 716 (2012) 30, and "Search for the standard model Higgs boson decaying in the H $\to ZZ \to 2\ell 2\nu$ channel in pp collisions at $\sqrt{s} = 7$ TeV" by CMS collaboration, JHEP 1203 (2012) 040. The dissertation author was the primary investigator and author of this paper.

Vita

2008 Master of Science in Physics, Indian Institute of Technology, Kanpur

2014 Doctor of Philosophy in Physics, University of California, San Diego

Publications

CMS Collaboration. Measurement of the properties of a Higgs boson in the four-lepton final state. *Phys. Rev. D*, **89**:092007, 2014. [arXiv:1312.5353 [hep-ex]]

CMS Collaboration. Observation of a new boson at a mass of 125 GeV with the CMS experiment at the LHC. *Phys. Lett. B*, **716**:30, 2012. [arXiv:1207:7235 [hep-ex]]

CMS Collaboration. Search for the standard model Higgs boson in the $H \to ZZ \to 2\ell 2\nu$ channel in pp collisions at $\sqrt{s} = 7$ TeV. *JHEP*, **1203**:040, 2012. [arXiv:1202:3478 [hep-ex]]

ABSTRACT OF THE DISSERTATION

Discovery of a Higgs Boson in the H to ZZ to 4 leptons channel

by

Adish Pradeep Vartak
Doctor of Philosophy in Physics
University of California, San Diego, 2014
Professor Vivek Sharma, Chair

A search for the standard model Higgs boson is presented using data collected in pp collisions at the LHC with the CMS detector. Two distinct Higgs boson decay channels are analyzed. The H $\to ZZ \to 2\ell 2\nu$ channel, where $\ell = e$ or μ, is analyzed with data collected in 2011 at $\sqrt{s} = 7$ TeV corresponding to an integrated luminosity of 4.6 fb^{-1}. No significant excess of events is observed above the background expectation and the presence of a standard model Higgs boson is excluded in the mass range 270–440 GeV at 95% confidence level. The H $\to ZZ \to 4\ell$ channel is analyzed with data collected in 2011 and 2012 corresponding to integrated luminosities of 5.1 and 19.7 fb^{-1} at $\sqrt{s} = 7$ and 8 TeV respectively. A new boson is observed with a local significance of 6.7 standard deviations. The mass of this particle is measured to be 125.6 ± 0.4(stat)$\pm$0.2(syst) GeV, and it has a signal strength of $1.04^{+0.29}_{-0.25}$(stat) $^{+0.14}_{-0.08}$(syst) relative to the standard model

Higgs boson expectation. The width of this particle is measured to be less than 3.6 GeV at 95% confidence level. The spin and parity of this particle is found to be consistent with the standard model Higgs boson.

Chapter 1

Introduction

The standard model (SM) of particle physics is an immensely successful theoretical framework that describes the fundamental constituents of matter and all the interactions they experience apart from gravity. One of the great triumphs of the SM has been to trace the origins of the electromagnetic, weak and strong forces to elegant symmetry principles [1–12]. However, the experimentally observed massive vector bosons mediating the weak force are indicative of a breaking of the electroweak gauge symmetry which occurs in the SM as a result of the Brout-Englert-Higgs (BEH) mechanism [13–18]. A consequence of this mechanism is a fundamental scalar boson called the Higgs boson which, in the SM, couples not only to the weak bosons but also to various quarks and leptons through Yukawa interactions, and it is through these interactions that the fundamental constituents of matter acquire mass.

Over the years, experimental investigations have provided direct evidence of all the constituents of the SM. With the discovery of the top quark at the Tevatron in 1995 [19, 20], all the particles of the SM had been directly observed with one exception. The Higgs boson was still elusive and its mass remained the only unknown parameter of the SM. Then on the 4th of July 2012, the CMS and ATLAS experiments at the Large Hadron Collider (LHC) reported the discovery of a new particle with mass of about 125 GeV whose properties were found to be consistent with the SM Higgs boson.

This introductory chapter attempts to set the stage, both from a historical as well as technical perspective, for this successful search for the Higgs boson which will remain the focus of this thesis. The chapter starts with an overview of the development of the

electroweak symmetry breaking mechanism in the 1960s, and motivates the necessity of having a particle like the Higgs boson in the SM. This is followed by a quick review of the history of the Higgs boson searches and the constraints imposed on its mass through various direct and indirect experimental measurements. The chapter ends with a discussion on the physics of Higgs boson searches in the context of hadron colliders. This leads us in to the second chapter which gives an overview of the LHC and the CMS experiment, and then describes the process of reconstructing collision events whereby the raw detector data gets translated into physics objects such as electrons and muons that are then used to perform physics analyses. The third chapter gives an account of the various statistical concepts and procedures that are employed in order to make a quantitative assessment of the collision data. The fourth chapter describes the $\mathrm{H} \to ZZ \to 2\ell 2\nu$ search which helps in excluding a heavy SM Higgs boson thereby narrowing the Higgs boson search to a mass range close to 100 GeV. In the fifth chapter we turn our attention to the $\mathrm{H} \to ZZ \to 4\ell$ channel wherein we find unambiguous evidence of the existence of a new boson that decays into four leptons. Having established the existence of a new boson, we explore the properties of this particle using four-lepton events in the sixth chapter and try to consolidate the evidence to show that the behavior of this particle is consistent with the SM Higgs boson. In order to firmly establish the SM credentials of the newly discovered particle, we need to look beyond the $\mathrm{H} \to ZZ \to 4\ell$ mode and explore the wide tapestry of interactions of the Higgs boson with other particles of the SM. Therefore, in chapter seven we broaden our purview and summarize the results of Higgs searches in several different final states across CMS and ATLAS experiments. Moreover, we see how the results obtained from these different channels together help to reinforce the predictions of the SM. Finally, the last chapter informs the reader of the contributions of the author to the Higgs search program and to the activities of the CMS experiment in general.

1.1 Theory of Electroweak Symmetry Breaking

In the 1960s, the development of the electroweak theory led to a unified description of the electromagnetic and weak forces based on the Yang-Mills theory [21] of the

gauge symmetry group $\mathrm{SU(2)_L \times U(1)_Y}$ of weak left-handed isospin and hypercharge. The electroweak theory together with the $\mathrm{SU(3)_C}$ gauge theory of strong interactions provides a a highly successful description of the three fundamental forces of nature in the context of the SM. The BEH mechanism which explains the breaking of the electroweak symmetry is a critical component of the SM. This section provides a quick overview of the BEH mechanism and explains some crucial phenomenological aspects of the resulting scalar particle. Ref. [22] provides a more detailed review on the subject.

1.1.1 Standard Model Particles and Forces

The fundamental constituents of matter are described in the SM in terms of three generations of chiral left-handed and right-handed fermionic fields. Every generation consists of two flavors of quarks which experience both strong and electroweak forces and also two flavors of leptons which experience only the electroweak interaction. The first generation consists of the up and the down quarks, the electron and the electron neutrino. The second generation consists of the charm and the strange quarks, the muon and the muon neutrino while third generation consists of the top and the bottom quarks, the tau and the tau neutrino. Each of these particles also has a corresponding anti-particle.

In the first generation, the electron carries one unit of negative electric charge $(-e)$ while the neutrino is electrically neutral. The up quark carries a $+\frac{2}{3}e$ electric charge while the down quark carries a $-\frac{1}{3}e$ electric charge. The left-handed up and down quarks, and also the left-handed electron and electron neutrino form weak isodoublets. The weak isospin quantum number of the up quark and the electron neutrino is $+\frac{1}{2}$ while that of the down quark and the electron is $-\frac{1}{2}$. While there exists no right-handed electron neutrino in the SM, the right handed up and down quarks as well as the right-handed electron are weak isosinglets. The fermionic hypercharge, can be defined as a combination of the electric charge Q in units of e and the weak isospin I^3 as $Y = 2Q - 2I^3$. These quantum numbers described for the first generation particles get replicated for the second and third generation fermions. As a result the charm and top quarks are often referred to as the 'up-type' quarks while strange and bottom quarks are referred to as the 'down-type' quarks. The particle content of the SM as described

here, is listed below.

$$
\begin{aligned}
L_1 &= \begin{pmatrix} \nu_e \\ e^- \end{pmatrix}_{\rm L}, \quad e_{\rm R_1} = e^-_{\rm R}, \quad Q_1 = \begin{pmatrix} u \\ d \end{pmatrix}_{\rm L}, \quad u_{\rm R_1} = u_{\rm R}, \quad d_{\rm R_1} = d_{\rm R} \\
L_2 &= \begin{pmatrix} \nu_\mu \\ \mu^- \end{pmatrix}_{\rm L}, \quad e_{\rm R_2} = \mu^-_{\rm R}, \quad Q_2 = \begin{pmatrix} c \\ s \end{pmatrix}_{\rm L}, \quad u_{\rm R_2} = c_{\rm R}, \quad d_{\rm R_2} = s_{\rm R} \\
L_3 &= \begin{pmatrix} \nu_\tau \\ \tau^- \end{pmatrix}_{\rm L}, \quad e_{\rm R_3} = \tau^-_{\rm R}, \quad Q_3 = \begin{pmatrix} t \\ b \end{pmatrix}_{\rm L}, \quad u_{\rm R_3} = t_{\rm R}, \quad d_{\rm R_3} = b_{\rm R}
\end{aligned}
\tag{1.1}
$$

The interactions between these fermionic fields are mediated by spin-one gauge fields. These gauge fields are associated with the generators of the gauge group in its adjoint representation. Hence, the strong force which is a manifestation of an $\mathrm{SU(3)_C}$ gauge theory has eight gluons fields $G_\mu^{1,\ldots,8}$. The electroweak sector represented by the $\mathrm{SU(2)_L \times U(1)_Y}$ gauge symmetry has two sets of fields: B_μ corresponding to the generator of the $\mathrm{U(1)_Y}$ gauge symmetry, and three fields $W_\mu^{1,2,3}$ corresponding to the three generators of the $\mathrm{SU(2)_L}$ group. In order to make the Lagrangian representing these interactions gauge invariant, the derivative terms have to be replaced by their covariant counterparts

$$
\partial_\mu \rightarrow D_\mu = \partial_\mu - ig_1 B_\mu - ig_2 T_a^3 W_\mu^a - ig_3 T_a^8 G_\mu^a \tag{1.2}
$$

where g_1, g_2 and g_3 are the couplings associated with the $\mathrm{U(1)_Y}$, $\mathrm{SU(2)_L}$ and $\mathrm{SU(3)_C}$ gauge interactions, while T_a^3 and T_a^8 are the generators of the SU(2) and SU(3) groups in the representations to which the fields on which these derivatives act, belong. The covariant derivatives play the key role of introducing interactions in the Lagrangian. This can be illustrated by considering the free field Dirac Lagrangian for a fermion which contains the term $\bar{\psi}\partial_\mu\gamma^\mu\psi$. The imposition of gauge invariance necessitates the promotion of the derivative in this term to the covariant form as shown below

$$
\bar{\psi}\partial_\mu\gamma^\mu\psi \rightarrow \bar{\psi}D_\mu\gamma^\mu\psi = \bar{\psi}(\partial_\mu - ig_1 B_\mu - ig_2 T_a^3 W_\mu^a - ig_3 T_a^8 G_\mu^a)\gamma^\mu\psi
$$

The covariant derivative introduces interaction terms in the Lagrangian between fermions and gauge bosons which take the general form $-g\bar{\psi}V_\mu\gamma^\mu\psi$. This scheme of

introducing interaction terms through the covariant derivative is known as minimal coupling. It is 'minimal' in the sense that interactions are introduced by the imposition of gauge invariance alone and no additional terms are introduced by hand. Lastly, the field strength tensors for the gauge fields are given by

$$\begin{aligned} B_{\mu\nu} &= \partial_\mu B_\nu - \partial_\nu B_\mu \\ W^a_{\mu\nu} &= \partial_\mu W^a_\nu - \partial_\nu W^a_\mu + g_2 \epsilon^{abc} W^b_\mu W^c_\nu \\ G^a_{\mu\nu} &= \partial_\mu G^a_\nu - \partial_\nu G^a_\mu + g_3 f^{abc} G^b_\mu G^c_\nu \end{aligned} \tag{1.3}$$

where ϵ^{abc} and f^{abc} are the structure constants of the SU(2) and SU(3) groups. These field strength tensors enter the Lagrangian as the kinetic energy terms of the form $-\frac{1}{4} V_{\mu\mu} V^{\mu\nu}$. In the case of the of the non-abelian gauge fields, the terms involving the structure constants are responsible for introducing self-interactions of the gauge bosons.

Putting all of this together we can write down the SM Lagrangian assuming for massless fermions and gauge bosons. Such a Lagrangian takes the following form

$$\begin{aligned} \mathcal{L}_{SM} &= -\tfrac{1}{4} B_{\mu\nu} B^{\mu\nu} - \tfrac{1}{4} W^a_{\mu\nu} W^{\mu\nu}_a - \tfrac{1}{4} G^a_{\mu\nu} G^{\mu\nu}_a \\ &\quad + i \bar{L}_i D_\mu \gamma^\mu L_i + i \bar{Q}_i D_\mu \gamma^\mu Q_i \\ &\quad + i \bar{e}_{R_i} D_\mu \gamma^\mu e_{R_i} + i \bar{u}_{R_i} D_\mu \gamma^\mu u_{R_i} + i \bar{d}_{R_i} D_\mu \gamma^\mu d_{R_i} \end{aligned} \tag{1.4}$$

The above Lagrangian, while complete and consistent in itself, does not represent reality. The reason is, of course, the assumed masslessness of all the particles. Empirically, we know that photons which are the carriers of the electromagnetic force and gluons, which transmit the strong force are indeed massless. However, we also know that the mediators of the weak force are massive (in fact, the 'weak' force is rendered weak by the rather large mass of these force carriers). Similarly, the fermions of the SM are also massive. So, this Lagrangian needs to be extended to include mass terms for these particles. And it is at this point where we encounter some trouble. Any additional terms that we might wish to incorporate into the Lagrangian need to also respect the condition of gauge invariance. The mass term for a vector field V^μ takes the form $\frac{1}{2} M^2 V^\mu V_\mu$. Assuming this to be the gauge field of the U(1) group, a gauge transformation through a local phase $\alpha(x)$ would imply the following change in the mass term: $\frac{1}{2} M^2 V^\mu V_\mu \to \frac{1}{2} M^2 (V^\mu - \frac{1}{e} \partial^\mu \alpha)(V_\mu - \frac{1}{e} \partial_\mu \alpha)$

Clearly, the mass term is not invariant under the gauge transformation and so, it cannot be added in an ad-hoc manner to the Lagrangian without breaking the gauge symmetry. The mass terms for the fermions are no less troublesome. If we have a fermion field ψ which only interacts through the strong force, we can add a mass term for it of the form $m\bar{\psi}\psi$ without breaking the $\mathrm{SU(3)_C}$ gauge symmetry. However, a problem is encountered when we attempt to incorporate the electroweak interaction. To illustrate the issue, we can rewrite the fermionic mass term as $m(\bar{\psi_{\mathrm{L}}}\psi_{\mathrm{R}} + \bar{\psi_{\mathrm{R}}}\psi_{\mathrm{L}})$. The $\mathrm{SU(2)_L}$ gauge transformation acts only on the left-handed fermions. Thus, while the left-handed component in the mass term changes under a gauge transformation, the right handed component does not vary to compensate this change. As a result the mass term does not remain gauge invariant.

1.1.2 Symmetry Breaking and Gauge Boson Mass

We are led to an impasse between the rather elegant description of fundamental forces through gauge symmetries and the empirical fact that the weak bosons and the fermions of the SM are massive. The gauge symmetries are essential to ensure the unitarity and renormalizability of the SM interactions, and hence are indispensable. To resolve this conflict let us consider a massless complex scalar field ϕ. Let us associate a scalar potential $V(\phi^*\phi)$ with this field such that the functional form of V has a global minimum at $\frac{\upsilon^2}{2}$ with $\upsilon \neq 0$. The Lagrangian for such a field can simply be written as

$$\mathcal{L}_\phi = (\partial_\mu\phi)(\partial^\mu\phi)^* - V(\phi^*\phi) \tag{1.5}$$

We see that the Lagrangian respects a global U(1) symmetry. We can introduce a U(1) gauge interaction by adding a vector field A_μ to the Lagrangian through a kinetic energy term $-\frac{1}{4}F_{\mu\nu}F^{\mu\nu}$ involving its field strength tensor $F_{\mu\nu} = \partial_\mu A_\nu - \partial_\nu A_\mu$ and by promoting the partial derivatives in the Lagrangian of the scalar field to their covariant counterparts $\partial_\mu \to \partial_\mu - igA_\mu$. The resulting Lagrangian takes the form

$$\mathcal{L}_{\phi,A} = (D_\mu\phi)(D^\mu\phi)^* - V(\phi^*\phi) - \frac{1}{4}F_{\mu\nu}F^{\mu\nu} \tag{1.6}$$

Here we have constructed a simple toy model of a complex scalar field interacting

with a U(1) gauge field A_μ which is massless. Now let us redefine the field ϕ as $\phi = \frac{1}{\sqrt{2}}(\upsilon + \theta(x))e^{i\alpha(x)}$ by introducing a new real scalar field $\theta(x)$. The phase factor $\alpha(x)$ in this redefinition of ϕ can be rotated away by exploiting the gauge freedom built into the Lagrangian. This also then requires the vector field to be gauge transformed as $A_\mu \to A_\mu + \frac{1}{g}\partial_\mu\alpha$. The Lagrangian now takes the form

$$\begin{aligned}
\mathcal{L}_{\theta,A} &= \tfrac{1}{2}D_\mu(\upsilon+\theta)(D^\mu)^*(\upsilon+\theta) - V - \tfrac{1}{4}F_{\mu\nu}F^{\mu\nu} \\
&= \tfrac{1}{2}(\partial_\mu - igA_\mu)(\upsilon+\theta)(\partial_\mu + igA^\mu)(\upsilon+\theta) - V - \tfrac{1}{4}F_{\mu\nu}F^{\mu\nu} \qquad (1.7)\\
&= \tfrac{1}{2}\partial_\mu\theta\partial^\mu\theta + \tfrac{1}{2}g^2\theta^2A_\mu A^\mu + \tfrac{1}{2}g^2\upsilon^2A_\mu A^\mu - V - \tfrac{1}{4}F_{\mu\nu}F^{\mu\nu}
\end{aligned}$$

The Lagrangian has lost its manifest gauge invariance and a mass term $\frac{1}{2}g^2\upsilon^2A_\mu A^\mu$ has appeared for the gauge field A_μ. It seems that we have successfully devised a procedure to make the vector boson A_μ massive. Since we haven't really changed the U(1) gauge invariant Lagrangian but only redefined the scalar field in it, our model is still very much a valid U(1) gauge theory. The redefinition of ϕ essentially hides away the gauge symmetry of the Lagrangian. Now, let us try to go a bit deeper into the physical meaning of υ and θ. Since υ represents the minimum of the potential function V, we expect the ground state or vacuum $|\Omega\rangle$ to satisfy $\langle\Omega|(\phi^*\phi)|\Omega\rangle = \frac{\upsilon^2}{2}$. So when we redefine ϕ as $\phi = \frac{1}{\sqrt{2}}(\upsilon + \theta(x))e^{i\alpha(x)}$ the scalar field θ represents fluctuations around the ground state. And the consequent excitation of the vacuum results in the production of a scalar particle. If $\upsilon \neq 0$, the vacuum state becomes degenerate in the U(1) phase of ϕ in $\langle\Omega|(\phi^*\phi)|\Omega\rangle = \frac{\upsilon^2}{2}$. It settles into one of the minima thus physically breaking the U(1) symmetry. What this means is that while our Lagrangian is gauge invariant, the vacuum state breaks the gauge symmetry. When looking in the vicinity of the vacuum (which is the business of perturbation theory) the gauge symmetry of the system appears to be broken and the gauge boson acquires a mass.

In acquiring mass though, the vector boson needs to pick up an additional degree of freedom corresponding to its longitudinal polarization which is absent when the vector boson is massless. Where does this additional degree of freedom come from? Looking at $\mathcal{L}_{\theta,A}$ we realize that θ represents a real scalar field with just one degree of freedom as opposed to the complex field ϕ which has two degrees of freedom. In going from ϕ to θ

one of the two degrees of freedom gets absorbed into the longitudinal polarization of the massive boson. This apparently seamless transfer of a degree of freedom is possible due to the very nature of gauge symmetries, which we exploited to rotate away the phase $\alpha(x)$.

From a historical perspective, this spontaneous symmetry breaking mechanism and the generation of vector boson mass was delivered as a finished product in the year 1964. The first to publish this mechanism were Francois Englert and Robert Brout [13], followed by Peter Higgs [14,15] and then by the trio of Tom Kibble, Gerald Guralnik and Carl Hagen [16]. However, there were several others who made important contributions along the way.

The BCS theory of superconductivity [23, 24] that emerged in the 1950s had a curious feature that it seemed to violate the electromagnetic gauge invariance. Nambu pointed out in 1960 [25] that the BCS theory actually did respect electromagnetic gauge invariance, but the symmetry was spontaneously broken in the ground state. He then extended this idea of spontaneous symmetry breaking to quantum field theories by constructing a model of chiral symmetry breaking in four fermion interactions [26, 27] which could explain the existence of pions. This prompted a rigorous examination of symmetry breaking in the context of relativistic field theories by Goldstone and others [28, 29]. Goldstone concluded that the spontaneous breaking of a continuous global symmetry in a relativistic theory necessarily produces massless scalar particles for each of the broken generators. So if a gauge symmetry were to be broken spontaneously, we would expect to see massless Goldstone bosons. But such particles were not observed in nature. This was a nagging predicament but it would be soon resolved.

In 1962 Schwinger mooted the idea that gauge invariance does not necessarily imply masslessness of the gauge bosons [30, 31]. A year later Anderson demonstrated this to be true in the context of non-relativistic plasma oscillations [32]. In this paper Anderson makes a crucial observation. Quoting from the paper itself - 'the Goldstone zero-mass difficulty is not a serious one, because we can probably cancel it off against an equal Yang-Mills zero mass problem'. In fact, Anderson's paper had all the ingredients of mass generation through spontaneous symmetry breaking but in the context of non-relativistic plasma. He did not show explicitly that the Goldstone theorem could be

evaded in the relativistic domain in which it was derived. This is precisely what Higgs and others were able to demonstrate in 1964. Quoting from the second paper of Higgs - 'This phenomenon is just the relativistic analog of the plasmon phenomenon to which Anderson has drawn attention: that the scalar zero-mass excitations of a superconducting neutral Fermi gas become longitudinal plasmon modes of finite mass when the gas is charged.' Essentially, the BEH mechanism showed that when a *gauge* symmetry is spontaneously broken the massive gauge bosons pick up an additional longitudinal degree of freedom thus absorbing the Goldstone mode. Interestingly, an independent confirmation of the BEH mechanism was proposed by two undergraduate students - Alexander Migdal and Alexander Polyakov, from the other side of the iron curtain in a paper published a year later [33].

While all the three seminal papers of 1964 successfully demonstrated the generation of vector boson mass through gauge symmetry breaking, there was one feature that was explicitly demonstrated by Higgs alone. He showed in his second paper that the scalar boson arising from the symmetry breaking process could itself be massive. Englert and Brout did not explicitly discuss the scalar boson in their paper, while the results derived in the paper of Kibble, Hagen and Guralnik correspond to a massless particle (the equation: $-\partial^2\phi_2 = 0$ in [16]). We can see how the scalar boson can be massive from the above toy study if we Taylor expand the potential V around the minimum. We get $V = V(\frac{v^2}{2}) + V''(\frac{v^2}{2})\theta^2 + ...$ If the second derivative of the potential is non-zero we end up with a mass term for the scalar field θ. In a later paper, Higgs also computed the amplitude for such a massive scalar to decay into two vector bosons [17]. The search for such a decay of a massive scalar into two gauge bosons eventually became the cornerstone of the experimental investigations of symmetry breaking phenomenon as will be demonstrated in subsequent chapters of this thesis.

1.1.3 Symmetry Breaking In The Standard Model

The mechanism that was developed in 1964 was essentially a proof of principle that gauge bosons can be massive. The next critical step was to incorporate this mechanism into the real world description of weak forces. It was Salam, Weinberg and Glashow who put together all the pieces to construct the theory of electroweak

interactions as we know it today. A Lagrangian could now be written to describe the electromagnetic and weak forces in nature. This was a remarkable achievement but it did not still complete the understanding of these forces. As Weinberg himself asked in his seminal paper on the model of electroweak interactions [2] (which would become one of the most cited papers in the field), 'Is this model renormalizable ?' In other words, it remained to be shown that the non-abelian gauge theory of electroweak interactions was perturbatively calculable in terms of its physical parameters. This was accomplished in 1971 by Veltman and 't Hooft [4, 5]. Their work was also an early exposition in the use of computer programs for performing complex particle physics calculations - a staple of modern day particle physics. The theoretical foundations for the understanding of the electroweak interactions were thus successfully and rigorously laid down. Let us now examine how the mechanism of symmetry breaking is introduced into the model of electroweak interactions.

To begin with, in the $\mathrm{SU(2)_L \times U(1)_Y}$ theory of electroweak interactions, we need to generate masses for three weak bosons while keeping the photon field massless. The three massive weak bosons need to acquire three additional longitudinal degrees of freedom. Therefore, to break the electroweak symmetry we need to introduce scalar fields with at least three degrees of freedom. The simplest possibility is a complex scalar SU(2) doublet that is covariant under the electroweak gauge group.

$$\Phi = \frac{1}{\sqrt{2}} \begin{pmatrix} \phi^1 + i\phi^2 \\ \phi^3 + i\phi^4 \end{pmatrix} = \begin{pmatrix} \phi^+ \\ \phi^0 \end{pmatrix}, Y_\Phi = 1 \tag{1.8}$$

This field Φ has four degrees of freedom. If Φ is assigned hypercharge $Y_\Phi = 1$ then its component $\phi^1 + i\phi^2$ will carry unit positive electric charge (hence represented as ϕ^+) while the component $\phi^3 + i\phi^4$ will be electrically neutral (hence represented as ϕ^0). In our toy study we let the scalar potential V be arbitrary. But the most general renormalizable potential for the scalar field Φ under consideration can be written as

$$V(\Phi) = \mu^2(\Phi^\dagger\Phi) + \lambda(\Phi^\dagger\Phi)^2 \tag{1.9}$$

In order to introduce this scalar field Φ into our massless Lagrangian of the SM from eq. 1.4, we need to add the following terms to $\mathcal{L}_{SM}$.

$$\mathcal{L}_S = (D^\mu \Phi)^\dagger (D_\mu \Phi) - \mu^2 (\Phi^\dagger \Phi) - \lambda (\Phi^\dagger \Phi)^2 \tag{1.10}$$

where $D_\mu = \partial_\mu - ig_1 B_\mu - ig_2(\frac{1}{2}\tau_a^3)W_\mu^a$, and $\frac{1}{2}\tau_a$ which are half times the Pauli matrices are the generators of the SU(2) group in the representation to which the scalar doublet Φ belongs. Looking at the potential $V(\Phi)$, we see that for the potential to have a lower bound the coefficient of the quartic term λ has to be positive. As far as the coefficient of the quadratic term is concerned, if $\mu^2 > 0$ then the potential has a minimum at $\Phi^\dagger\Phi = 0$. However, if $\mu^2 < 0$, the potential has a minimum at $\Phi^\dagger\Phi = \frac{\upsilon^2}{2}$ where $\upsilon = \sqrt{\frac{-\mu^2}{\lambda}}$. If the electroweak symmetry were to be broken in entirety any arbitrary vacuum state could be chosen such that $\Phi^\dagger\Phi = \frac{\upsilon^2}{2}$. However, the electromagnetic gauge symmetry ($\mathrm{U(1)_{EM}}$) needs to remain intact since the photon is indeed massless. This means that the vacuum expectation value of the electrically charged component of the scalar field has to be zero. In that case let us assume that the vacuum expectation value (v.e.v) of Φ is given by:

$$\langle 0 | \, \Phi \, | 0 \rangle = \begin{pmatrix} 0 \\ \frac{1}{\sqrt{2}}\upsilon \end{pmatrix} \tag{1.11}$$

We can now play the same trick as in the case of our toy model. We can express any general phi Φ in terms of a perturbation $\mathrm{H}(x)$ around υ as follows

$$\Phi(x) = \frac{1}{\sqrt{2}} \begin{pmatrix} 0 \\ \upsilon + \mathrm{H}(x) \end{pmatrix} e^{i\alpha_a(x)\tau^a/2} \tag{1.12}$$

where $\alpha_{1,2,3}(x)$ are the phases along the three generators of the SU(2) group which can be rotated away by exploiting the gauge freedom in our model. These will get absorbed into the three longitudinal degrees of freedom of the weak bosons. The remaining $\mathrm{H}(x)$ field will introduce a new scalar particle into the SM and is referred to as the Higgs field. We are now ready to see the emergence of the mass terms for the weak bosons. Recalling the toy study, we saw that the mass terms emerged from the derivative term of the scalar Lagrangian. Therefore, let us focus only on the $(D^\mu\Phi)^\dagger(D_\mu\Phi)$ term and expand it in terms of υ, H and the gauge fields W_μ^a and B_μ. This leads to

$$
\begin{aligned}
|D_\mu\Phi|^2 &= |(\partial_\mu - ig_1B_\mu - ig_2(\tfrac{1}{2}\tau_a^3)W_\mu^a)\Phi|^2 \\
&= \frac{1}{2}\left|\begin{pmatrix} \partial_\mu - \frac{i}{2}(g_2W_\mu^3 + g_1B_\mu) & -\frac{i}{2}g_2(W_\mu^1 - iW_\mu^2) \\ -\frac{i}{2}g_2(W_\mu^1 + iW_\mu^2) & \partial_\mu + \frac{i}{2}(g_2W_\mu^3 - g_1B_\mu) \end{pmatrix}\begin{pmatrix} 0 \\ \upsilon + \mathrm{H} \end{pmatrix}\right|^2 \\
&= \frac{1}{2}(\partial_\mu \mathrm{H})(\partial^\mu \mathrm{H}) + \frac{1}{8}g_2^2(\upsilon+\mathrm{H})^2(W_\mu^1 + iW_\mu^2)(W_1^\mu - iW_2^\mu) \\
&\quad + \frac{1}{8}(\upsilon+\mathrm{H})^2(g_2W_\mu^3 - g_1B_\mu)(g_2W_3^\mu - g_1B^\mu)
\end{aligned}
\tag{1.13}
$$

We see that on account of the structure of the Pauli matrices the W_μ^a and B_μ fields get rearranged. We therefore define four orthogonal fields which are linear combinations of W_μ^a and B_μ.

$$
W_\mu^\pm = W_\mu^1 \mp W_\mu^2, Z_\mu = \frac{g_2W_\mu^3 - g_1B_\mu}{\sqrt{g_1^2+g_1^2}}, A_\mu = \frac{g_1W_\mu^3 + g_2B_\mu}{\sqrt{g_1^2+g_1^2}} \tag{1.14}
$$

We can define sin $\theta_W = \frac{g_1}{\sqrt{g_1^2+g_2^2}}$. Then $Z_\mu = \cos\theta_W W_\mu^3 - \sin\theta_W B_\mu$ and $A_\mu = \sin\theta_W W_\mu^3 + \cos\theta_W B_\mu$. Thus the fields Z_μ and A_μ can be thought of as rotated or mixed forms of W_μ^3 and B_μ, and the angle θ_W represents the degree of this mixing. In fact, θ_W is known as the electroweak mixing angle. Eq. 1.13 can now be written as

$$
\begin{aligned}
(D^\mu\Phi)^\dagger(D_\mu\Phi) &= \frac{1}{2}(\partial_\mu \mathrm{H})(\partial^\mu \mathrm{H}) + \frac{1}{8}g_2^2(\upsilon+\mathrm{H})^2W_\mu^-W^{+\mu} \\
&\quad + \frac{1}{8}(g_1^2+g_2^2)(\upsilon+\mathrm{H})^2Z_\mu Z^\mu \\
&= \frac{1}{2}(\partial_\mu \mathrm{H})(\partial^\mu \mathrm{H}) + \frac{1}{8}g_2^2\upsilon^2W_\mu^-W^{+\mu} + \frac{1}{8}(g_1^2+g_2^2)\upsilon^2Z_\mu Z^\mu \\
&\quad + \frac{1}{4}g_2^2\upsilon\mathrm{H}W_\mu^-W^{+\mu} + \frac{1}{4}(g_1^2+g_2^2)\upsilon\mathrm{H}Z_\mu Z^\mu \\
&\quad + \frac{1}{8}g_2^2\mathrm{H}^2W_\mu^-W^{+\mu} + \frac{1}{8}(g_1^2+g_2^2)\mathrm{H}^2Z_\mu Z^\mu
\end{aligned}
\tag{1.15}
$$

The above equation is extremely instructive. Firstly, we see that the field A_μ does not appear at all in eq. 1.15. There is neither a mass term associated with A_μ nor is there any term involving A_μ and H. This is the electromagnetic field which is massless as it should be and it doesn't interact directly with the Higgs field at tree level. Then, the $W^\pm$ and Z fields have picked up masses $M_W = \frac{1}{2}g_2\upsilon$ and $M_Z = \frac{1}{2}(\sqrt{g_1^2+g_2^2})\upsilon$ respectively. Moreover, M_W and M_Z are related by the electroweak mixing angle since $M_W = M_Z\cos\theta_W$. There are also interaction terms involving the Higgs field and the

W, Z bosons. These include cubic terms $\frac{1}{4}g_2^2 \upsilon \mathrm{H} W_\mu^- W^{+\mu}$ and $\frac{1}{4}(g_1^2+g_2^2)\upsilon \mathrm{H} Z_\mu Z^\mu$, and quartic terms $\frac{1}{8}(\upsilon+\mathrm{H})^2(g_2 W_\mu^3 - g_1 B_\mu)(g_2 W_3^\mu - g_1 B^\mu)$ and $\frac{1}{8}(g_1^2+g_2^2)\mathrm{H}^2 Z_\mu Z^\mu$. The cubic terms which physically represent the coupling of the Higgs boson to a pair W and Z bosons give us two of the leading search channels in the discovery program of the Higgs boson which look for the decay of the Higgs boson to two Ws or two Zs.

To learn more about the Higgs boson itself, we need to look at the potential term that we have so far ignored in our discussion. On writing the potential in terms of υ and H we get

$$V = -\frac{1}{4}\lambda\upsilon^4 + \lambda\upsilon^2\mathrm{H}^2 + \lambda\upsilon\mathrm{H}^3 + \frac{1}{4}\lambda\mathrm{H}^4 \tag{1.16}$$

The term $\lambda\upsilon^2\mathrm{H}^2$ is the mass term form the Higgs field. The mass of the Higgs boson is $m_\mathrm{H} = 2\lambda\upsilon^2 = -2\mu^2$. The remaining terms (ignoring the constant term $-\frac{1}{4}\lambda\upsilon^4$) represent the self-interactions of the Higgs field. What remains now is to obtain the fermion masses. Amazingly, this can also be achieved with the scalar field Φ which till now had only been tasked with the breaking of gauge symmetry. We can introduce the gauge invariant terms into the Lagrangian which represent the renormalizable Yukawa interactions between the left and right-handed fermions and Φ. In the case of the electron and electron neutrino these Yukawa interactions can be expressed as

$$\begin{aligned}
\mathcal{L}_{e,\nu_e,\Phi} &= -\lambda_e \bar{L}\Phi e_\mathrm{R} - \lambda_\mathrm{e}\bar{e}_\mathrm{R}\Phi^\dagger L \\
&= -\tfrac{1}{\sqrt{2}}\lambda_e(\bar{\nu_e}, e_\mathrm{L}) \begin{pmatrix} 0 \\ \upsilon+\mathrm{H} \end{pmatrix} e_\mathrm{R} - \tfrac{1}{\sqrt{2}}\lambda_e \bar{e}_\mathrm{L}(0, \upsilon+\mathrm{H}) \begin{pmatrix} \bar{\nu_e} \\ e_\mathrm{L} \end{pmatrix} \\
&= -\tfrac{1}{\sqrt{2}}\lambda_e\upsilon(\bar{e}_\mathrm{L}e_\mathrm{R} + \bar{e}_\mathrm{R}e_\mathrm{L}) - \tfrac{1}{\sqrt{2}}\lambda_e\mathrm{H}(\bar{e}_\mathrm{L}e_\mathrm{R} + \bar{e}_\mathrm{R}e_\mathrm{L})
\end{aligned} \tag{1.17}$$

We see that we have generated the electron mass which can be written as $m_e = \frac{1}{\sqrt{2}}\lambda_e\upsilon$ along with an interaction term which couples the Higgs field to an electron pair. The neutrino doesn't figure in the Lagrangian and so it remains massless. We can use the same procedure to generate the mass of the down quark. However, for the up quark we have to introduce Yukawa terms involving the isodoublet $\tilde{\Phi} = i\tau^2\Phi^*$ which has hypercharge $Y_{\tilde{\Phi}} = -1$. We can write the Lagrangian part representing the masses

of the electron and the up and down quarks as

$$\mathcal{L}_F = -\lambda_e(\bar{L}\Phi e_{\mathrm{R}} + \bar{e_{\mathrm{R}}}\Phi^\dagger L) - \lambda_d(\bar{Q}\Phi d_{\mathrm{R}} + \bar{d_{\mathrm{R}}}\Phi^\dagger Q) - \lambda_u(\bar{Q}\tilde{\Phi}u_{\mathrm{R}} + \bar{u_{\mathrm{R}}}\tilde{\Phi}^\dagger Q) \tag{1.18}$$

This Lagrangian can be extended to include the second and third generation quarks and leptons as well but in doing so we need to account for an added complication of cross-generation mixing which makes the weak eigenstates different than the mass eigenstates of the quarks. This leads to the Cabibbo-Kobayashi-Maskawa (CKM) mixing matrix [34,35] which won't be discussed here. But the description of the SM with all its constituent particles is now complete. It has been established that the masses of weak bosons and fermions of the SM arise from interactions involving a scalar doublet field Φ which on breaking the electroweak symmetry gets reduced to the Higgs field H. The couplings of the interactions between the Higgs boson and the weak bosons (V) and fermions (f) in turn depend on their respective masses. So, we have

$$g_{\mathrm{H}ff} = i\frac{m_f}{\upsilon}, g_{\mathrm{H}VV} = -2i\frac{m_V^2}{\upsilon}, g_{\mathrm{HH}VV} = -2i\frac{m_V^2}{\upsilon^2} \tag{1.19}$$

We see that the strength with which the Higgs boson interacts with a fermion is directly proportional to its mass while in the case of the weak bosons it varies quadratically. Moreover, we see that the particle masses and the Higgs couplings to other particles depend on the v.e.v of the scalar potential. The v.e.v can be directly obtained from the Fermi constant ($\upsilon = (\sqrt{2}G_F)^{-1/2}$) which in turn can be obtained experimentally by measuring the average lifetime of a muon before it decays into an electron and a pair of neutrinos. The value of υ is found to be about 246 GeV [36]. We see from eq. 1.16 that in order to fully determine the scalar potential V, we need to measure λ in addition to υ. The parameter λ, however, only appears in the mass of the Higgs boson and in terms involving its self-interactions. Therefore, to measure λ we need to directly observe the Higgs boson and measure its mass. It is in this sense that the mass of the Higgs boson is the last unknown of the SM. All other parameters of the SM (the particle masses, the gauge couplings, the mixing angles) have been directly measured.

Although the mass of the Higgs boson is a free parameter, it is possible to impose

certain constraints on it from a theoretical standpoint. If the Higgs boson is too heavy, the scattering of the longitudinally polarized W and Z bosons becomes increasingly strong until it breaks the unitarity condition [37–39]. By doing some partial wave analysis it can be shown that unitarity gets violated if the mass of the Higgs boson exceeds $\sqrt{4\pi\sqrt{2}/3G_F} \sim 0.7$ TeV. One can turn around this problem to ask another question - if the Higgs boson does not exist at all but some new physics is responsible for the breaking of electroweak symmetry, what is the energy scale at which this new physics will have to emerge to cure the unitarity problem. A similar partial wave analysis yields a limit of $\sqrt{8\pi\sqrt{2}/G_F} \sim 1.7$ TeV [40]. These two upper limits, one on the mass of the Higgs boson and the other on the scale at which new physics must appear in the absence of the Higgs boson, led to the so called 'no lose theorem' which essentially said that any experiment capable of probing WW scattering at the TeV scale will necessarily find something that explains the breaking of electroweak symmetry. Such a guarantee provided impetus to the construction of the Large Hadron Collider which did end up, as we will see, finding that something.

Let us consider here, only in passing, a curiously unnatural feature of the Higgs boson in the SM. Through its interactions with itself and other particles, the Higgs boson acquires corrections to its mass that are proportional to the ultraviolet cut-off scale (the energy scale at which we assume new physics to take over the SM). Assuming this scale to be the Planck scale, for the Higgs boson to have mass in the TeV range its bare mass must be fine-tuned to a precision of 16 orders of magnitude. In other words it is extremely unnatural for the Higgs boson to be as light as we expect it to be. This uncomfortable feature is indicative of new physics beyond the standard model. It may be possible that a new, hitherto undiscovered, symmetry of nature may protect the Higgs boson mass from the extremely large quantum corrections that appear in the SM. Supersymmetry is a prominent candidate in this regard [41]. Or it may be possible that some new strong interactions emerge at the TeV scale and break the electroweak symmetry, in which case the mass of the Higgs boson (which would no longer be elementary) would be protected by the scale at the which these new interactions become strong or non-perturbative.

1.2 History of Higgs Boson Searches

1.2.1 Searches at LEP

The first comprehensive program to search for the Higgs boson was undertaken at the Large Electron Positron Collider (LEP) at CERN which started its operations in 1989 and continued running till 2000. In the first phase of operations between 1989 and 1995 (termed as LEP1) the machine was commissioned as a Z boson factory and collided electrons and positrons and center of mass energies close to the Z boson resonance. In the second phase between 1995 and 2000 (termed as LEP2) the center of mass energy was gradually increased untill it reached a maximum value of 209 GeV by the time of shutdown. A detailed review of the Higgs boson searches at LEP can be found in Ref. [42]. The final combination of the Higgs boson searches at the four LEP experiments - ALEPH, DELPHI, L3 and OPAL has been published in Ref. [43]. A brief summary is presented below.

In the LEP1 era the dominant production mechanism was the so-called Bjorken process $e^+e^- \to Z \to Z^*(f\bar{f})\mathrm{H}$ which is illustrated by the Feynman diagram shown in Fig. 1.1. The $m_\mathrm{H} < 20$ GeV region was excluded by performing searches with event topologies involving Higgs boson decays to a pair of leptons or a jet of hadrons and the off-shell Z^* decaying to a pair of neutrinos. In the case of an extremely light Higgs boson with mass less than or around twice the mass of an electron, which would be long-lived, the search topology comprised of the Z boson decays to a pair of leptons and the Higgs boson escaping undetected. For $m_\mathrm{H} > 20$ GeV, the Higgs boson which would decay predominantly two a pair of bottom quarks was searched for in association with an off-shell Z boson decaying to neutrinos, electrons or muons. At the end of LEP1, Higgs boson with mass less than 65.6 GeV was ruled out at 95% confidence level (CL).

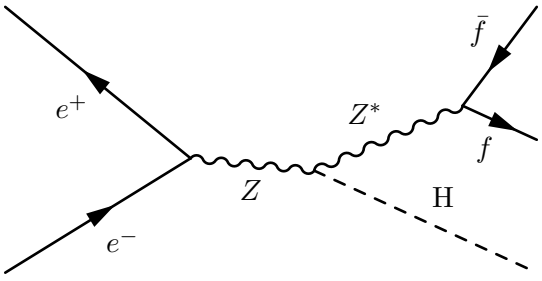

Figure 1.1 Leading order Feynman diagram for the Bjorken process

In the LEP2 era, as the center of mass energy was increased farther away from the Z pole, the dominant Higgs boson production processes were the so-called Higgs-strahlung and weak boson fusion as illustrated in Fig. 1.2(a) and 1.2(b) respectively. The search was performed looking for $H \to b\bar{b}$ events along with two fermions produced from the decay of the associated Z boson or two leptons from the weak boson fusion. By the end of 1999, using e^+e^- collisions with a center of mass energy upto 201.6 GeV the Higgs boson was excluded upto a mass of 108.6 GeV at 95% CL. Then in the year 2000, the last year of operation of the LEP machine, a final push was made to increase the center of mass energy up to 209 GeV. The exclusion was extended to 114.4 GeV at 95% CL but interestingly an excess of about two standard deviations was observed at a mass value of 115.6 GeV.

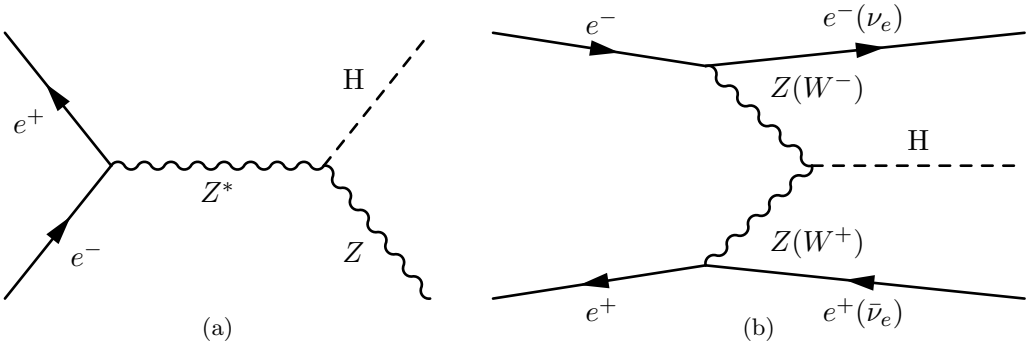

Figure 1.2 Leading order Feynman diagrams for the Higgs-strahlung and weak boson fusion processes

1.2.2 Searches at Tevatron

As LEP shutdown its operations in 2000 to start the construction of the next generation Large Hadron Collider, the only machine in the world that was capable of searching for the Higgs boson was the Tevatron collider at Fermilab. The Tevatron collider, unlike LEP, was a hadron collider which collided a beam of protons with a beam of antiprotons with a center of mass energy that ultimately reached 1.96 TeV. The Tevatron machine also ran in two phases. The first phase (termed as Run I) extended from 1986 to 1996 and saw $\mathrm{p} - \bar{\mathrm{p}}$ collisions at a center of mass energy of 1.8 TeV. The biggest achievement of this phase of the Tevatron was the discovery of the top quark, the heaviest particle in the SM. By the time LEP shutdown, Tevatron had entered its second phase (termed as Run II) which extended from 2001 to 2011 and during which

the center of mass energy of collisions was boosted to 1.96 TeV. The physics of a hadron collider is significantly different than that of a lepton collider. As we will see in the next section, the production mechanism of the Higgs boson in hadronic collisions is very different when compared to e^+e^- collisions. Also, the background from QCD induced processes is much larger in hadronic collisions. As a result, the Tevatron searches were only sensitive to $m_{\mathrm{H}} > 100$ GeV. In fact, the most sensitive spot in the Higgs boson mass spectrum for the Tevatron was around $m_{\mathrm{H}} = 2M_W \sim 160$ GeV. At this value of m_{H}, the two W bosons from the Higgs boson decay get on mass shell, and so the branching ratio of the $\mathrm{H} \to W^+W^-$ process is close to 1. In other words, for $m_{\mathrm{H}} \sim 160$, the Higgs boson almost exclusively decays to a pair of W bosons. Moreover, the event topology of the fully leptonic final state of the $\mathrm{H} \to W^+W^-$ process (wherein each of the two W bosons decays leptonically to a neutrino and either an electron or a muon) allows for effective suppression of the large backgrounds. In the year 2010, the CDF and D0 experiments combined their search results with around 6 fb^{-1} of collision data and reported the exclusion of the Higgs boson with mass between 158 to 175 GeV at 95% CL [44].

1.2.3 Constraint from Electroweak Measurements

Apart from the direct searches for the Higgs boson that were performed at LEP and Tevatron it was also possible to perform indirect measurements of the putative mass of the Higgs boson. Since the Higgs boson coupled to all the particles of the SM (apart from the photon and the gluons) it was possible to use the measured values of the SM parameters to fit for the mass of the Higgs boson. Such a fit performed in 2010 put an upper limit of 158 GeV on the Higgs boson mass at 95% CL [45]. The χ^2 distribution of the fit is shown in Fig. 1.3. This meant that the mass of the Higgs boson should be less than 158 GeV in order to be consistent with precision electroweak measurements performed by several past experiments at LEP, SLC and Tevatron.

This was the state of Higgs boson searches in 2010, the year the LHC started its operations. In one year's time the LHC overtook the Tevatron in terms of the search reach for the Higgs boson [46]. In July 2012, the LHC experiments ATLAS and CMS jointly announced the discovery of a new particles with mass of 125 GeV in their Higgs

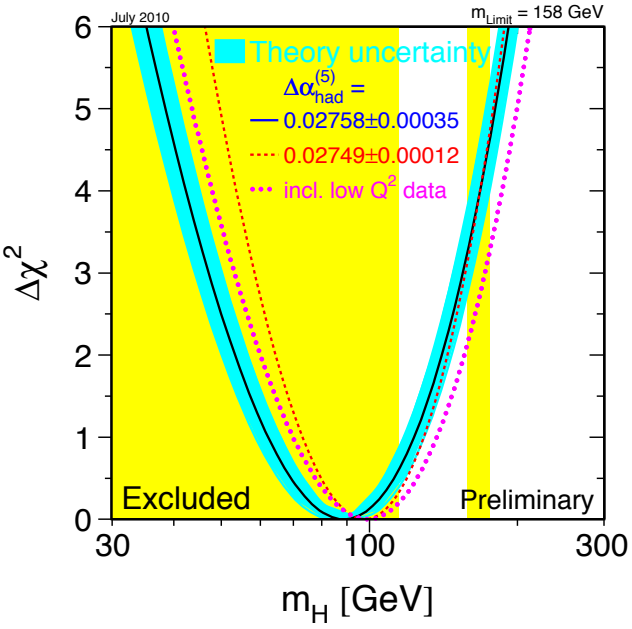

Figure 1.3 χ^2 distribution of the electroweak fit performed on the mass of the SM Higgs boson using inputs from precision electroweak measurements. The yellow region denotes the SM Higgs boson mass range directly excluded by the LEP and Tevatron experiments.

boson searches [47,48]. This discovery was simultaneously corroborated by the Tevatron experiments which observed an excess in the mass region between 120 and 135 GeV, when looking for Higgs boson decays to pair of bottom quarks in association with a W or a Z boson. This combined search which was performed by analyzing the full Run II data corresponding to an integrated luminosity of 10 fb^{-1} observed a maximum local significance of 3σ [49,50].

1.3 Higgs Hunting at Hadron Colliders

The particle colliders at the forefront of high energy physics in the past few decades have either collided two beams of leptons (electrons and positrons) as in the case of LEP or SLC, or a beam of leptons (electrons or positrons) with protons, or a beam of protons with (anti)protons as in the case of SPS, Tevatron and LHC. In the case of the e^+e^- colliders the collisions take place between two elementary particles with well-defined initial momenta. These collisions can be very effectively described using well established techniques of perturbative quantum field theory. On the other hand protons are extremely complicated physical objects that consist of three valence quarks (two up

quarks and one down quark) and a sea of quark-antiquark pairs, all bound together by gluons through non-perturbative QCD interactions. As a result, interactions involving (anti)protons are much more complex when compared to e^+e^- collisions.

1.3.1 Physics of Hadron Collisions

When proton - (anti)proton beams collide the resulting hadronic interactions can be broadly categorized as 'hard' and 'soft' depending on whether the scale of momentum transfer in the interaction lies in the perturbative or non-perturbative regime of QCD. Typically an interaction in which the momentum transfer is below the GeV scale, can be regarded as a soft interaction. The overall cross-section of hadronic interactions is dominated by the soft-interactions, which in turn can be classified into two types. The first type is known as elastic scattering where the final state also consists of two protons (electromagnetic scattering of two protons is one example). These interactions largely go unnoticed since the two protons are unlikely to fall within the detector acceptance. The second type is known as inelastic scattering in which one or both of the incoming protons disintegrate into other particles. Some of the remnants of the disintegrated protons may enter the fiducial region of the detector. Such events are termed as 'minimum bias' events, or events which can be observed by lowering the bias or the requirement on detector activity to a minimal level.

In most searches for new physics, it is typically the hard interactions that are of interest. Since the hard interactions are characterized by a high momentum transfer scale, they are capable of probing smaller distances, or in other words they are are capable of probing the very constituents of the protons. In this regime proton-(anti)proton interactions can be viewed as interactions between the constituent quarks and gluons, which are collectively termed as partons. These partons carry a variable fraction of the (anti)proton momentum and so their interactions occur over a broadband of energies even though the energy of the (anti)protons is fixed. Let us consider a generic parton-level interaction $a + b \rightarrow c + X$ where parton a from a proton interacts with a parton b from the colliding (anti)proton to produce a final state comprising of particle c and anything else (denoted by X). Let us assume the a carries a fraction x_a of the proton momentum while b carries a fraction x_b of the other colliding (anti)proton's momentum.

If the center of mass energy of the of the colliding hadrons is denoted by s, then the center of mass energy of the colliding partons is given by $\hat{s} = x_a x_b s = \tau s$. The cross-section for this process can be written as

$$d\sigma_{ab}(\hat{s}) = f_a^1(x_a) f_b^2(x_b) d\hat{\sigma}(a + b \to c + X) \tag{1.20}$$

where $d\hat{\sigma}(a+b \to c+X)$ is the cross-section of the elementary process $a+b \to c+X$ while $f_a^1(x_a)$ and $f_b^2(x_b)$ are the parton density functions (PDFs) that give the probability of finding partons a and b in the two hadrons carrying the respective momentum fractions x_a and x_b. As of now, it is not possible to derive these PDFs from first principles but they have been obtained empirically from deep inelastic scattering experiments. If we now wish to compute the cross-section for the full hadronic interaction $p+p(\bar{p}) \to c+X$ we will have to integrate over x_a and x_b and sum over all the partons. Thus we can write

$$d\sigma(s) = \sum_{a,b} \int dx_a dx_b f_a^1(x_a) f_b^2(x_b) d\hat{\sigma}(a + b \to c + X) \tag{1.21}$$

The above equation can be recast into a more informative form by defining the so-called parton-parton luminosity functions as follows [51]

$$\frac{dL_{ab}}{d\tau} = \frac{1}{1 + \delta_{ab}} \int_\tau^1 dx [f_a^1(x) f_b^2(\tau/x) + f_b^1(x) f_a^2(\tau/x)]/x \tag{1.22}$$

where δ_{ab} is the Kronecker delta function. The differential parton-parton luminosity dL_{ab} represents the number of parton-parton interactions that occur in the center of mass energy interval of $[s\tau, s(\tau + d\tau)]$. We can therefore write the differential hadronic cross-section with respect to τ as

$$\frac{d\sigma}{d\tau} = \sum_{a,b} \frac{dL_{ab}}{d\tau} \hat{\sigma}_{ab}(\hat{s}) \tag{1.23}$$

where $\hat{\sigma}_{ab}(\hat{s})$ is the partonic cross-section of the given process at center of mass energy $\hat{s}$. What we see from this equation is that the cross-section for a given hadronic interaction (e.g. $p + p \to \mathrm{H} + X$) depends not only on the elementary partonic cross-section but also on the parton-parton luminosity of a hadron collider. In Fig. 1.4 the gluon - gluon

and quark - quark (representing valence quarks of the colliding hadrons) luminosities are shown. For a particle of mass $\sim$ 100 GeV, the gluon - gluon parton luminosity is larger than the quark - quark luminosity by about an order of magnitude for a 14 TeV collider (the design energy of the LHC). In fact a TeV scale hadron collider is largely a gluon collider. This has important implications on the production of the Higgs boson but before elaborating on that let us take a small detour to establish the preferred coordinate system used in hadron collider physics studies.

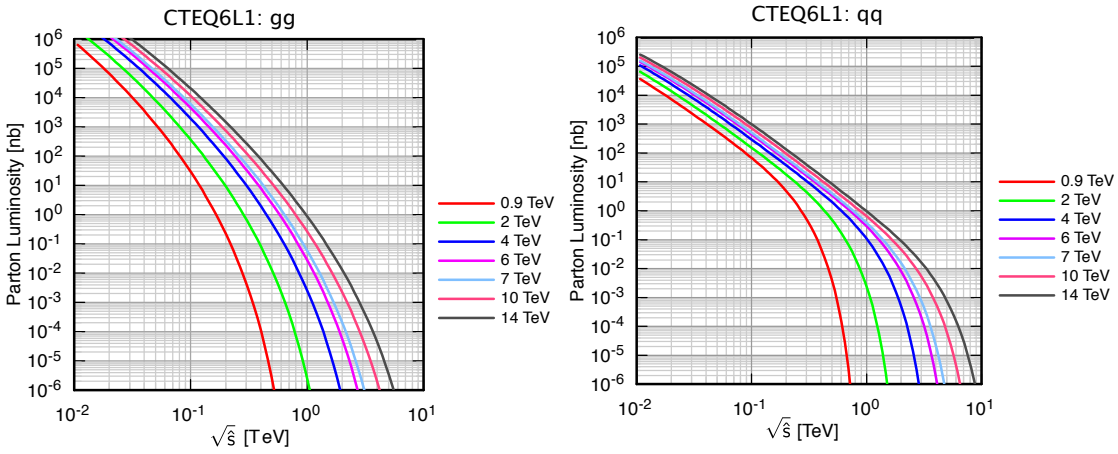

(a) (b)

Figure 1.4 Gluon - gluon luminosity shown on the left and quark - quark luminosity shown on the right [52]

1.3.2 Coordinate System for Hadron Collisions

One key distinguishing feature between hadron collisions and e^+e^- collisions is that in hadron collisions the initial momentum of the interacting partons cannot be known apriori. This feature makes hadron colliders broadband colliders and to compute a cross-section we need to integrate over all possible values of parton momenta. In our discussion above this feature manifests itself through two unknown variables x_a and x_b. We have seen that $\sqrt{x_a x_b s}$ gives the center of mass energy of the colliding partons. If x_a and x_b are not equal then colliding partons carry a longituidinal momentum $(x_a - x_b)\sqrt{s}$ with respect to the center of mass frame of the hadrons which is the laboratory frame. This is also unlike the e^+e^- collisions whose center of mass frame coincides with the laboratory frame. Since we cannot a priori know the boost of the interaction system with respect to our laboratory frame we need to define a coordinate system that is the

most convenient to use under longitudinal boosts.

Let us start with the cartesian coordinate system in which particle momentum can be expressed as (p_x, p_y, p_z), where the z-axis is aligned parallel to the direction of the incoming hadrons. A more natural system of coordinates in collider physics is the cylindrical coordinate system in which the momentum vector is denoted by (p_T, ϕ, z) such that $p_T = \sqrt{p_x^2 + p_y^2}$, $p_x = p_T \cos(\phi)$ and $p_x = p_T \sin(\phi)$. The reason for this preference is that the incoming particle momenta have no dependence on ϕ, and so the outcome of collisions has a ϕ-symmetry which can be effectively exploited in the cylindrical system. The coordinate p_T is called the transverse momentum of the particle. Now, we hope to replace the z-coordinate with a quantity which is easier to deal with under boosts along the z-axis. Let us consider the rapidity (Γ) of a particle which is defined as follows

$$\Gamma = \frac{1}{2}\ln\left(\frac{E + p_z}{E - p_z}\right) \tag{1.24}$$

where E is the particle energy. Now let us boost the system along the z-axis with a boost parameter γ such that

$$\begin{aligned} E' &= E\cosh\gamma - p_z\sinh\gamma \\ p'_z &= p_z\cosh\gamma - E\sinh\gamma \end{aligned} \tag{1.25}$$

The rapidity in the boosted frame is then given by

$$\Gamma' = \frac{1}{2}\ln\left(\frac{E' + p'_z}{E' - p'_z}\right) = \frac{1}{2}\ln\frac{(E + p_z)(\cosh\gamma - \sinh\gamma)}{(E - p_z)(\cosh\gamma + \sinh\gamma)} = \Gamma + \frac{1}{2}\ln\frac{e^{-\gamma}}{e^{\gamma}} = \Gamma - \gamma \tag{1.26}$$

Therefore, we see that rapidity changes additively under boosts which is much simpler than the transformation of p_z which is given in eq. 1.25. Moreover, differences in rapidity remain invariant under boosts i.e $\Delta\Gamma = \Gamma_2 - \Gamma_1 = \Gamma'_2 - \Gamma'_1$. In high energy collisions, the final state particles are typically detected are relativistic energies i.e. their momemta are generally much larger than their masses. In this limit we can equate the particle energy with the total momentum i.e. we can write $E \simeq \sqrt{p_T^2 + p_z^2}$. If we denote the polar angle as $\cos(\theta) = p_z/\sqrt{p_T^2 + p_z^2}$ then we can define pseudorapidity η as the

massless limit of rapidity which can be written as

$$\eta = \frac{1}{2}\ln(\frac{E + E\cos\theta}{E + E\cos\theta}) = \frac{1}{2}\ln(\frac{1 + \cos\theta}{1 + \cos\theta}) = -\ln(\tan(\theta/2)) \tag{1.27}$$

For the reasons discussed (p_T, ϕ, η) is the most commonly used coordinate system when studying hadron collisions. We will use this system exclusively in the remainder of this thesis.

1.3.3 Higgs Boson Production

Gluon Fusion

We established earlier that multi-TeV hadron colliders are essentially gluon colliders. Therefore, in such machines, the Higgs boson is is expected to be produced mainly through gluon - gluon interactions. While gluons do not directly couple to the Higgs field they can interact through a quark loop to produce a Higgs boson as shown in Fig. 1.5. For the five light quarks, all of which satisfy $4m_q^2 \ll m_{\mathrm{H}}^2$, it can be shown [51] that the gluon fusion cross-section is suppressed by m_q^2/m_{H}^2. As a result it is the top-quark loop which dominates this process. Over the years, a lot of theoretical effort has gone into improving upon the cross-section predictions for the gluon fusion process by taking into account higher order radiative QCD and electroweak corrections. The leading order (LO) cross-section process indicated by Fig. 1.5 scales as the square of the strong coupling constant α_s due to presence of the quark loop [53]. The corrections at next-to-leading order (NLO) in α_s have been computed using the exact dependence on the top and bottom quark masses [54, 55] and they result in 80 - 100% increase in the LO cross-section. The NLO computation has also been performed in the $m_t \to \infty$ limit using techniques of effective field theory and the results agree with the exact computation to within a few percent [56, 57]. This large m_t approach has then been extended to the next-to-next-to-leading order (NNLO) which shows an enhancement of around 25% to the NLO cross-section [58–64]. Further improvements have been introduced by performing the soft gluon resummation up to next-to-next-to-leading logarithm (NNLL) [65] and these contribute to less than 10% enhancement in the cross-section. Similarly, electroweak corrections up to the two loop level are known

and contribute to a few percent change in the cross-section [66–70]. Apart from providing an accurate evaluation of the cross-section, the higher order QCD corrections are also important for the correct modeling of the differential profile of the cross-section as a function of the transverse momentum of the Higgs boson, the number of additional jets in the event, etc. - variables that are exploited in several search modes to improve sensitivity.

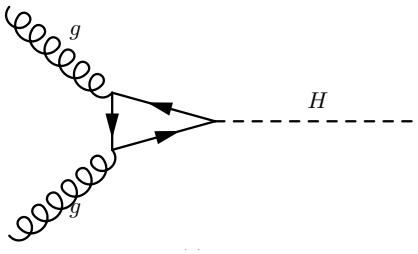

Figure 1.5 Leading order Feynman diagram for gluon fusion

Vector Boson Fusion

After gluon fusion the next two prominent modes involve 'electroweak' production of the Higgs boson i.e. these processes rely on the electroweak couplings of the quarks at leading order. The more dominant of these two processes at the LHC, which is a $p-p$ collider, is weak boson fusion or vector boson fusion (VBF). In this process, the interacting quarks from the two hadrons scatter off of each other by a t-(or u-)channel exchange of W or Z bosons which then 'fuse' into a Higgs boson. This is shown in Fig. 1.6. The final state comprises of the Higgs boson and two jets with a large pseudorapidity gap between them. Since the quark scattering is mediated by colorless weak bosons, there are no jets produced in the central region of the detector (this is similar to diffractive scattering of hadrons mediated by pomeron exchange). This striking feature of the signal (two forward jets with a large dijet invariant mass) helps in substantially reducing background in several search channels. The cross-section for VBF production is available at NLO for both QCD and electroweak corrections, [71–81] and the difference with respect to the LO calculations is only about 5 - 10% (as supposed to gluon fusion where the NLO correction was $\sim 100\%$). Further calculations at NNLO have brought down the uncertainty on the cross-section down to 1 - 2% [82].

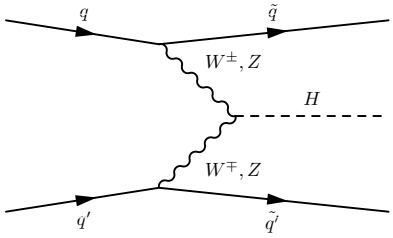

Figure 1.6 Leading order Feynman diagram for weak boson fusion

Associated Production

The other electroweak mode involves the production of the Higgs boson in association with a W or a Z boson through the s-channel as shown in Fig. 1.7(a). This mode is also known as 'Higgs-strahlung' since one can think of the Higgs boson as being radiated off of a weak boson. At the Tevatron, which is a $p-\bar{p}$ collider, this mode turns out to be more dominant than VBF. The presence of the associated W or Z boson in the event provides a very useful handle in suppressing large QCD backgrounds in several search modes. The cross-section for this process has been evaluated to NNLO in QCD corrections [83–89] by carrying over the results from the classic 'Drell-Yan' cross-section (this is possible because both processes are essentially s-channel processes involving a weak boson). For the ZH process, however, when computing the cross-section at NNLO one needs to also take into account gluon induced diagrams with a top-quark loop [90,91] as shown in Fig. 1.7(b). Electroweak corrections are also available for this process at NLO [92, 93].

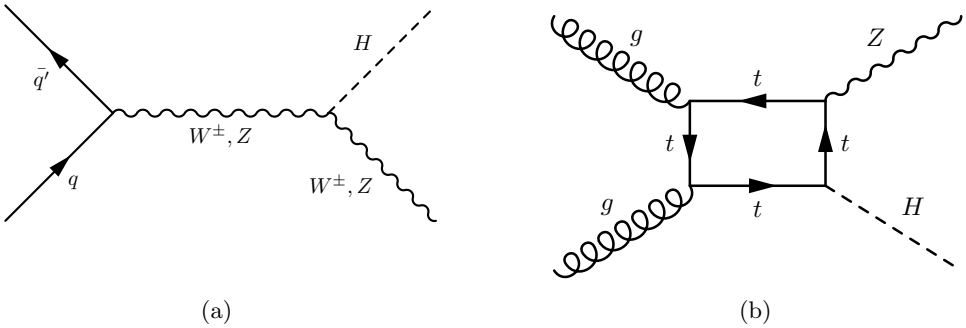

Figure 1.7 Higgs boson production in association with a W or a Z boson.

Associated Production With $t\bar{t}$ Pair

Lastly, we consider the production of the Higgs boson is association with a top-quark pair as shown in Fig. 1.8. This process has the smallest cross-section compared to all the other production modes that we have so far considered, which makes it a very difficult process to search for. However, this mode is very useful in directly determining the coupling of the Higgs boson with the top-quark. Cross-section for this process has been computed at NLO in QCD corrections [94–101] and is known with an uncertainty of around 10 - 15%.

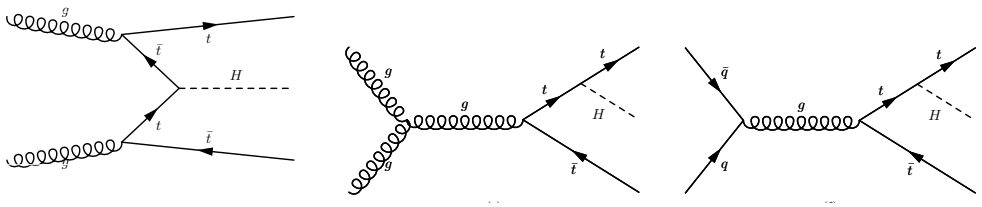

(a) (b) (c)

Figure 1.8 Higgs boson production in association with a top-quark pair.

The cross-sections for all the four production modes discussed above are plotted in Fig. 1.9 as a function of m_{H} at $\sqrt{s} = 7$ TeV for $p - p$ collisions which reflects the 2011 running of the LHC. We clearly see that gluon fusion is the predominant mode for Higgs boson production at the LHC. It is larger than at least an order of magnitude when compared to other modes at low values of m_{H}. The cross-sections decrease for increasing values of m_{H} which is expected given the evolution of the parton - parton luminosities as a function of $\hat{s}$ that we saw in Fig. 1.4. In the case of gluon fusion we see a bump in the region $m_{\mathrm{H}} \sim 2m_t$ which is expected given that it is twice the pole mass of the top quarks in the gluon fusion loop. We also notice that the cross-section for VBF decreases more slowly as compared to the other modes. This is because at high values of m_{H} the longitudinal modes of the bosons become exceedingly dominant just as in the case of WW scattering, and the coupling of the Higgs boson to the longitudinal components of the weak bosons is proportional to its mass [102]. As a result the relative contribution of the VBF process to the total cross-section increases with m_{H}.

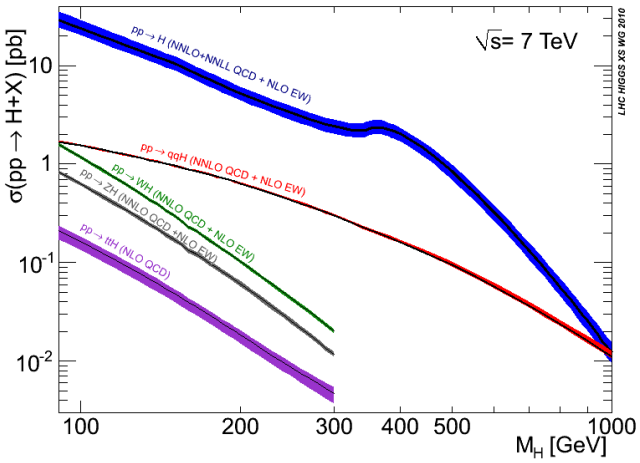

Figure 1.9 Higgs boson production cross-section by channel at $\sqrt{s} = 7$ TeV [103, 104].

Uncertainties On Production Cross-section

Before ending the discussion on the Higgs boson production let us briefly discuss the evaluation of the uncertainty on the cross-section computations since it needs to be incorporated into the analysis of all Higgs boson searches. The main source of systematic uncertainty on the cross-section values can be attributed to the fact that they are computed to a certain fixed order in perturbation theory. A remnant of this truncation is the dependance of the cross-section on certain scales. In fact, eq. 1.20 can be more accurately written as follows

$$d\sigma_{ab}(\hat{s}) = f_a^1(x_a, \mu_F) f_b^2(x_b, \mu_F) d\hat{\sigma}_{ab}(\mu_F, \alpha_s(\mu_R), \hat{s}) \tag{1.28}$$

where μ_R is the QCD renormalization scale. It is introduced in the renormalization procedure used to regularize the ultraviolet loop divergences and gets absorbed into the running coupling constant α_s. Then there are also divergences on the infrared end. These divergences are 'factorized' out or absorbed into the running parton density functions which results in the appearance of the factorization scale μ_F. Both these scales are artificial in the sense that the cross-section if computed exactly i.e. to all perturbative orders in QCD should not depend on them. This implies that as we compute higher and higher orders of radiative corrections the dependence of the cross-section on these scales should diminish. Therefore, we can assess the uncertainty on the cross-section at a fixed order by varying the scales in a reasonable range and then evaluating the

change in the cross-section. Typically μ_R and μ_F are set to the scale of the physics process under consideration. In the case of processes involving Higgs boson production this amounts to setting $\mu_R = \mu_F = m_{\mathrm{H}}$. Then in order to gauge the uncertainty on the cross-section the value of μ_R, μ_F is then varied between m_{H}/a and am_{H}, with $a = 2$ being the customary choice.

Another important source of systematic uncertainty is the choice of the PDFs themselves. As was mentioned earlier, the PDFs cannot be computed directly but have to be obtained empirically. Several groups such as CTEQ [105], MSTW [106], NNPDF [107], etc. extract PDFs from data of different experiments, using different analysis frameworks. The variation in the cross-section from the choice of these different PDFs can be considered as a measure of the uncertainty on the modeling of the PDFs themselves. Then there are several other sub-dominant sources of uncertainty which can be attributed to the choice of the top and bottom masses (pole mass v/s $\bar{\mathrm{M}}$S mass) and use of large m_t approximation at NNLO for gluon fusion implementation of the electroweak radiative corrections, etc.

1.3.4 Higgs Boson Decays

The Higgs boson, which is expected to be heavier than 100 GeV, decays almost instantaneously ($\sim 10^{-22}$ seconds) to other particles and it is through the decay products that we can attempt to reconstruct the presence of the Higgs boson in collider experiments. Fig. 1.10 shows the evolution of the branching ratios corresponding to the Higgs boson decays to several particle pairs. Branching ratio is the probability of the Higgs boson (or any other particle for that matter) to decay into a given set of particles. Fig. 1.10 shows some interesting trends in the decay pattern of the Higgs boson with increasing m_{H}. We can clearly identify a 'low-mass' region for $m_{\mathrm{H}} < 150$ GeV where the Higgs boson decays into a number of particle pairs with $b\bar{b}$ being by far the most preferred decay mode. Beyond $m_{\mathrm{H}} \sim 150$ GeV, however, the decays into weak bosons dominate almost entirely. In the region between 150 - 180 GeV, where the WW pair can be on mass-shell but the ZZ pair still hasn't crossed that threshold, the decays to WW are almost exclusive. But for $m_{\mathrm{H}} \sim 180$ GeV about two-thirds of the Higgs boson decays are into a WW pair while the remaining one-third decays go to ZZ. For

$m_{\mathrm{H}} > 350$ GeV, the direct decays of the Higgs boson to a top-quark pair also open up but remain subdominant.

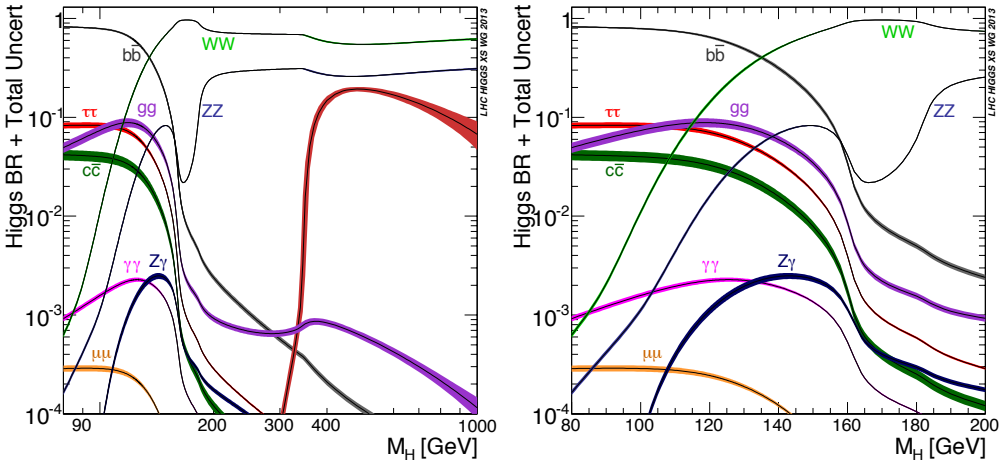

Figure 1.10 Branching ratios for Higgs boson decays to several particle pairs as a function of the m_{H} [103, 104]. The figure on the right shows a zoom into the low mass region.

The decays that we see in Fig. 1.10 also define the possible search channels that can be used to hunt for the Higgs boson. It is not feasible to search for all possible decays of the Higgs boson. The search sensitivity depends not only on the amount of expected signal events (which is given by the product of the cross-section and the branching ratio) but also on the expected background which in the case of hadron colliders can be overwhelming. Let us discuss the most sensitive channels that play an important role in the Higgs boson searches.

$\mathrm{H} \to b\bar{b}$ Channel

As we see in Fig. 1.10, a low mass Higgs boson predominantly decays to a $b\bar{b}$ pair. However, this channel suffers from an overwhelming background comprising of $b\bar{b}$ pairs produced in QCD interactions. For this channel to be at all sensitive, this large background has to be reduced by restricting the search to the associated production mode where the Higgs boson can be tagged along with a W or a Z boson decaying to leptons and/or neutrinos.

H $\to \tau^+\tau^-$ Channel

Branching ratios of the fermions are proportional to the square of their masses. Since third generation fermions are the heaviest, they have higher branching ratios compared to the fermions of the first two generations. As a result the H $\to \tau^+\tau^-$ channel plays an important role in the low mass region along with H $\to b\bar{b}$. The main background for this channel consists of τ pairs produced in the decay of the Z boson in the Drell-Yan process. By exploiting the unique topology of the jets produced in the VBF mode, or by tagging events with an additional W or a Z boson, the sensitivity of this channel gets enhanced.

H $\to \gamma\gamma$ Channel

While the Higgs boson does not couple directly to photons, it can decay into a pair photons by loop induced diagrams as shown in Fig. 1.11. This channel suffers from a large background but it is possible to obtain the signal as a sharp peak on a smoothly falling background if the photon momentum can be measured with a high resolution in the detector. As in the case of the fermionic decays, the VBF and VH event topologies are exploited to boost sensitivity.

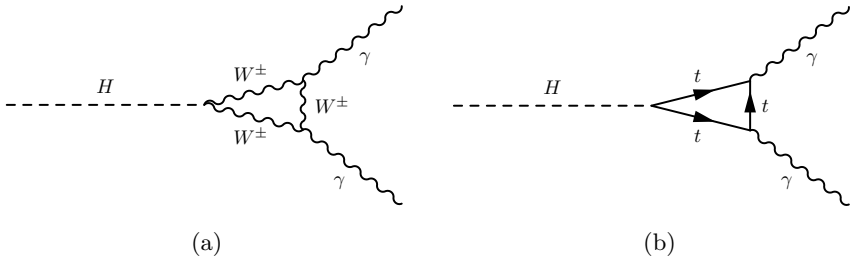

Figure 1.11 Higgs boson decay to a pair of photons

H $\to W^+W^-$ Channel

The three channels described above are exclusively low-mass channels as we can infer from Fig. 1.10. The decays of the Higgs boson into a pair of weak bosons, however, are relevant throughout the entire range of m_{H} going from 100 GeV to 1 TeV. The weak bosons are not stable particles themselves and they further decay into fermions. In the case of the H $\to W^+W^-$ channel, nearly half of the events end up in a fully hadronic

final state. These are events in which the W bosons decay to quarks. Similarly, around 10% events decay into a fully leptonic final state. The remaining 40% events are semi-leptonic in the sense that one of the two W bosons decays leptonically while the other decays hadronically. It is hopeless to search for the fully hadronic decays since the QCD background is overwhelming. Even the semi-leptonic decays are not very useful in the low mass region since they are besieged with a large W+jets background. The truly sensitive final state comprises of two leptons (that too either electron or muon) and neutrinos [108]. The main backgrounds include the electroweak WW continuum and fully leptonic $t\bar{t}$ decays.

In the high mass region, the semi-leptonic final state can be helpful in improving sensitivity. We have seen that the production cross-section of the Higgs boson falls very quickly with increasing m_{H}. Therefore at high values of m_{H} it becomes important to catch as many signal events as possible. So, while the W+jets background still remains quite large, the semi-leptonic decays of the Higgs boson provide about four times more signal events and hence, can be useful in improving sensitivity.

$\mathrm{H} \to ZZ$ Channel

In this channel as well, we need to focus on specfic decays of the Z bosons. As with the $\mathrm{H} \to W^+W^-$ channel fully hadronic decays of the ZZ pair are not useful at all. Similarly, fully invisible decays where both the Z bosons decay to neutrinos are not very sensitive. The key final state in this channel consists of both the Z bosons decaying either to a pair or muons or to a pair of electrons. This final state has very little background apart from the electroweak ZZ continuum. In fact, the signal-to-background ratio of this channel is the highest amongst all the Higgs boson search modes.

The only limitation of this channel is that it is statistically parched. Only 0.5% of the $\mathrm{H} \to ZZ$ events decay to electrons and/or muons. Consequently, in the high mass region it becomes necessary to add other final states to improve the search sensitivity. In these high mass modes, one of the two Z bosons are required to decay to an electron or muon pair to keep backgrounds under control. The second Z boson can then be allowed to decay hadronically, or to a pair of neutrinos, or to pair of tau leptons.

Other Higgs Decays

The channels considered above are the most sensitive modes for Higgs discovery. However, there are several other decays that have not been commented upon. The $H \to c\bar{c}$ channel for instance, is faced with backgrounds that are similar to the $H \to b\bar{b}$ channel. However, the $H \to c\bar{c}$ branching ratio is an order of magnitude smaller than $H \to b\bar{b}$ which diminishes its sensitivity greatly. The $H \to Z\gamma$ channel has a similar branching ratio compared to $H \to \gamma\gamma$. It also involves a loop induced decay of the Higgs boson. But for this channel to be sensitive, only the Z decays to electrons and muons have to be considered or else the QCD background becomes overwhelming. This reduces the overall branching ratio further by a factor of 0.06 making the channel much less sensitive than $H \to \gamma\gamma$. Then we can also consider the $H \to \mu^+\mu^-$ signal which sits on the tail of the $Z \to \mu^+\mu^-$ background. Owing to the small mass of the muon, the branching ratio of this decay mode is more than an order of magnitude smaller than $H \to \gamma\gamma$. Essentially, all of these channels need a lot more data to come into play when compared to the dominant modes that have been discussed above.

1.3.5 Decay Width and Line Shape

The Higgs boson being an unstable particle is typically characterized by its mass(m) and width(Γ). From an experimental perspective a narrow resonance ($\Gamma << m$) is characterized by the relativistic Breit-Wigner function which is written as follows

$$f_{\mathrm{BW}}(m, \Gamma) = \frac{k}{(p^2 - m^2)^2 + m^2\Gamma^2} \tag{1.29}$$

where k is some constant and p is the 4-momentum of the particle. To understand the origin of this function we must remember that these unstable particles typically enter as mediators between the initial state partons and final state decay particles. Such mediators are characterized by their propagators in the probability amplitudes. The propagator of a scalar particle in the momentum space according to the Feynman prescription is

$$\Delta_S = \frac{1}{p^2 - m^2 - i\epsilon} \tag{1.30}$$

The cross-section depends on the modulus squared of the amplitude and so the cross-section picks up a term of the form $\frac{1}{(p^2-m^2)^2+\epsilon^2}$ which looks similar to the Breit-Wigner function in eq. 1.29 except for the fact that the ϵ term is not a physical parameter but an infinitesimal shift that is introduced in the Feynman prescription to deal with the pole that appears in the propagator at $p^2 = m^2$. However, this propagator corresponds to a free stable particle and so it can be physically interpreted to mean that the particle has mass m and an infinitesimal width. In the case of unstable interacting particles such an imaginary term appears naturally in the propagator through the self-energy term $\Pi(p^2)$ which is a complex valued function. The propagator now takes the form

$$\Delta_S = \frac{1}{p^2 - m_0^2 + \Pi(p^2)} \tag{1.31}$$

where m_0 is the bare mass of the particle, A mass term μ can now be defined as $\mu^2 = m_0^2 + \mathrm{Re}(\Pi(p^2))$ and similarly a width term can be defined as $\mu\gamma = -\mathrm{Im}(\Pi(p^2))$. In the case of a narrow resonance which peaks at m, we can make an approximation by replacing the $\Pi(p^2)$ term in the propagator with $\Pi(m^2)$ to make it independent of p^2. With this approximation we end up with eq. 1.29 with a pole mass m and width $\Gamma = -\frac{1}{m}\Pi(m^2)$. Such an approximation works well for the W and Z bosons whose full width is just a few percent of their mass. In the case of the Higgs boson, the evolution of the width as a function of m_H is shown in Fig. 1.12. We see that for $m_\mathrm{H} < 400$ GeV the width is much smaller than the Higgs boson mass. However, as we approach 1 TeV, the width becomes comparable to m_H. What this means is that the Breit Wigner approximation breaks down for a heavy Higgs boson. In order to correctly model the line shape of such a heavy Higgs boson, one needs to switch from the pole mass m and width Γ to μ and γ which in turn depend on the computation of the self-energy term $\Pi(p^2)$. This procedure of using the complex mass $\mu^2 - i\mu\gamma$ in deriving the line shape is known as the 'Complex Pole Scheme' (CPS) [109–111].

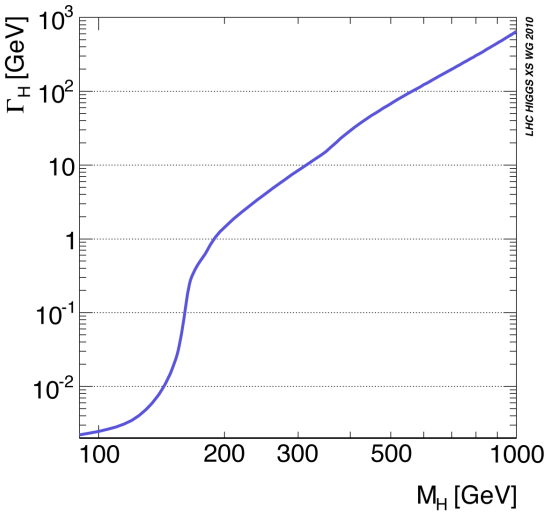

Figure 1.12 Full decay width of the Higgs boson as a function of the m_{H} [103, 104].

Chapter 2

The LHC and the CMS Experiment

2.1 The Large Hadron Collider

Talks about a future multi-TeV hadron collider to replace the LEP machine had started in the 1980s even as LEP was being constructed. The ECFA-CERN workshop organized at Lausanne in 1984 resulted in the first definitive report on the prospects of such a collider [112]. As stated in the report, 'the installation of a hadron collider in the LEP tunnel, using superconducting magnets, [had] always been foreseen by ECFA and CERN as the long term extension of the CERN facilities beyond LEP. Indeed such considerations were kept in mind when the radius and size of the LEP tunnel were decided'. In the year 1994, the CERN council approved the proposal to construct a new hadron collider inside the LEP tunnel on the Swiss-Franco border close to Geneva [113]. This tunnel, which is 26.7 km in circumference, lies at a depth of 45 m to 170 m below the earth's surface and consists of eight straight sections and eight arcs along with two transfer tunnels, 2.5 km in length each, which connect the tunnel to the CERN accelerator complex. While the initial plan was to commission the collider in two phases, starting at a center of mass energy of 10 teraelectronvolts (TeV) with a later upgrade to 14 TeV, by December 1996 the CERN council approved the construction of a 14 TeV machine in a single stage. It was decided to construct four experimental detectors on the LHC complex. Two of these experiments, namely ATLAS and CMS, were designed to be

general purpose experiments capable of probing a wide gamut of physics questions while the remaining two experiments, namely LHCb and ALICE were designed for specific studies on b quarks and heavy ion collisions respectively. While ALICE and LHCb detectors were built in pre-existing structures from LEP times at Point 2 and Point 8 respectively, new surface and underground caverns were constructed for the ATLAS and CMS experiments at Point 1 and Point 5 respectively. A graphic of the LHC complex can be seen in Fig. 2.1.

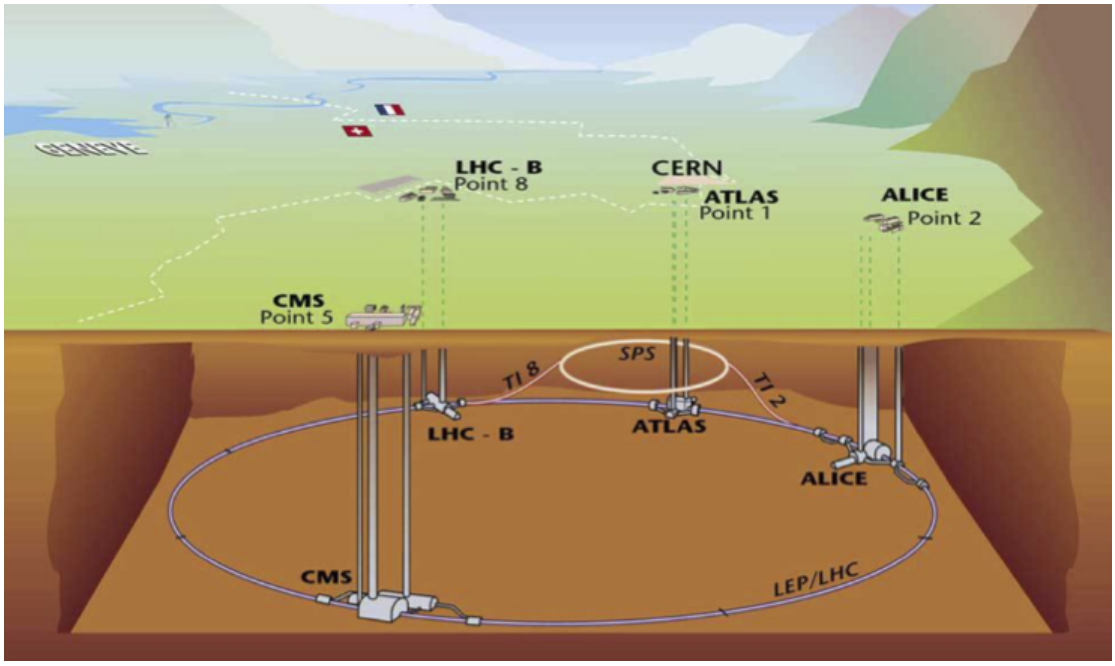

Figure 2.1 The LHC Complex

As we saw at the end of Sec. 1.3.1, a multi-TeV hadron collider can be viewed mainly as a gluon collider and in this respect proton-antiproton collisions are no different than proton-proton collisions. But in terms of machine design the aim of reaching a peak luminosity of 10^{34} cm^{-2}s^{-1} meant that the proton-antiproton configuration was ruled out and a proton-proton collider machine was planned instead. In terms of the accelerator design, this eliminated the possibility of the particle-antiparticle collider configuration of having a common vacuum and magnet system for both the circulating beams as in the case of the Tevatron accelerator, but rather necessitated two separate rings with opposite magnetic dipole fields. However, the space limitations of the pre-existing LEP tunnel whose arcs have an internal diameter of just 3.7 m, made it extremely difficult to accommodate two separate proton rings. Hence, a twin-bore mag-

net design, also known as the "two-in-one" superconducting magnet design originally proposed by John Blewett at the Brookhaven Laboratory in 1971 was adopted. The basic idea in this design, as illustrated in Fig. 2.2 is to include the two sets of magnet coils and beam channels within the same mechanical structure with a common vacuum cryostat to save space.

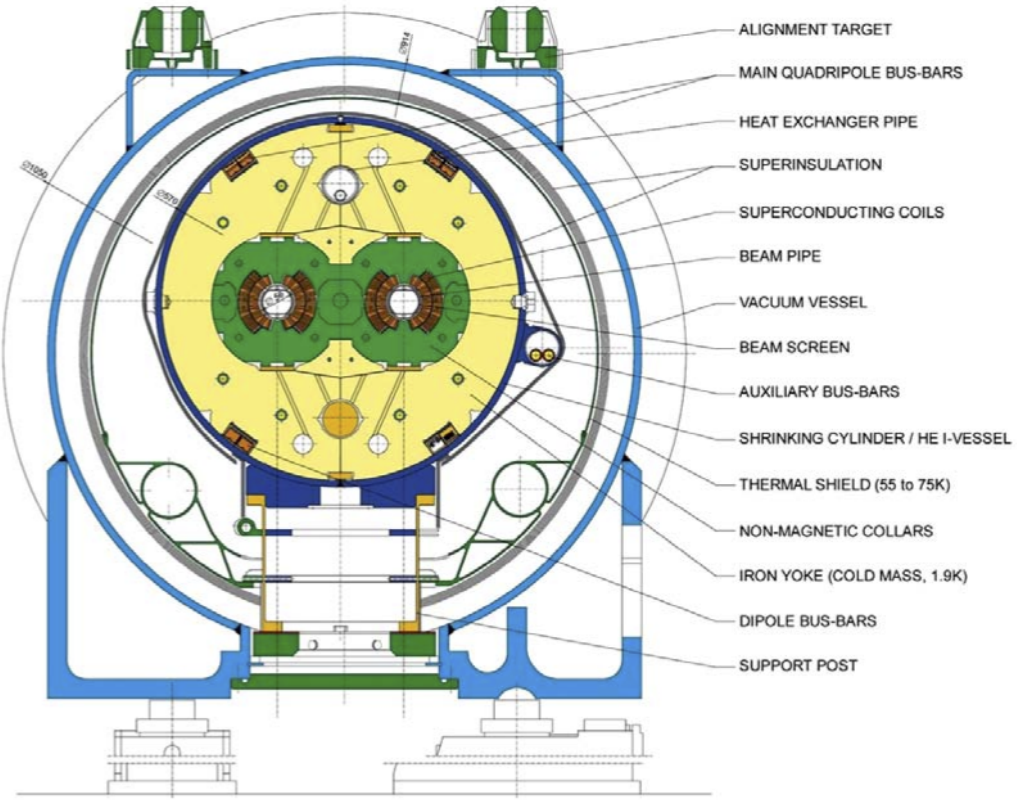

Figure 2.2 Cross-section of a cryodipole [113]

The peak beam energy that an accelerator of a given radius can reach depends on the strength of the field that its dipole magnets are capable of producing. To reach the design center of mass energy of 14 TeV, the LHC needs to accelerate each of the two proton beams up to 7 TeV which in turn necessitates a peak dipole field of 8.33 Tesla. In order to attain such a high magnetic field, the superconducting magnet coils have been constructed using the time tested NbTi technology (also used in several other accelerators such as Tevatron, HERA and RHIC) but the magnets are cooled down to 2 Kelvin as opposed to the typical temperatures of around 4-5 Kelvin in earlier experiments.

Apart from the beam energy, the other key deliverable of a particle collider is luminosity since the number of events of any physics process observed in particle collisions is directly proportional to it. The machine luminosity depends entirely on the beam parameters as given by the following relation

$$L = \frac{N_b^2 n_b f_{\mathrm{rev}} \gamma_r}{4\pi \varepsilon_n \beta^*} F \tag{2.1}$$

where N_b is the number of particles per bunch, n_b is the number of bunches per beam, f_{rev} is the revolution frequency, γ_r is the relativistic gamma factor, ε_n is the normalized transverse beam emittance, β^* is the beta function at the collision point, and F is the geometric luminosity reduction factor due to the crossing angle at the interaction point. The design luminosity of the LHC, as mentioned earlier, is 10^{34} cm^{-2}s^{-1} and nominally the machine can circulate 2808 bunches with a 25 ns spacing.

2.1.1 Overview of LHC Run 1

While the LHC was poised to start its proton-proton collisions at a center of mass energy of 14 TeV, an accident which occured on 19 September 2008 forced a revision of plans. During powering tests of the main dipole circuit, a faulty electrical bus connecting two magnets caused an electrical arc resulting in mechanical damage and release of six tonnes of helium from the magnet cold mass. The ensuing repairs forced a delay of around one year and it was decided to reduce the beam energy from the design value of 7 TeV to 3.5 TeV to ensure operational safety.

The physics impact of this downgrading of center of mass energy was quite significant. Fig. 2.3 shows the ratio of gluon - gluon and quark - antiquark luminosities between 7 and 14 TeV center of mass energies [106]. We see that the gluon - gluon luminosity for producing a 100 GeV particle decreases by a factor of 3 and this reduction factor further increases for heavier particles. Also the decrease in quark - antiquark luminosity is milder compared to the gluon - gluon luminosity reduction. If we take the case of the Higgs boson search, while the signal production cross-section is driven by the gluon - gluon luminosity, key backgrounds in several search channels are produced through quark - antiquark interactions. This means that as the center of mass energy decreases from 14 to 7 TeV both the signal yield and the signal-to-background ratio are

reduced leading to an adverse impact on the search sensitivity.

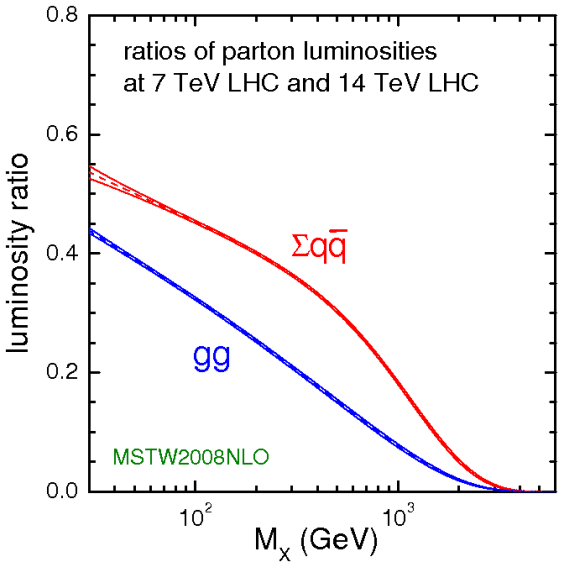

Figure 2.3 Ratio of gluon - gluon and quark - antiquark luminosities between 7 and 14 TeV center of mass energies.

The first proton-proton collisions happened in November 2009 at a center of mass energy of 900 GeV. By the end of that year, the center of mass energy was ramped up to 2.36 TeV thus making LHC the highest energy particle accelerator of all time. In 2010, the center of mass energy was further increased to 7 TeV thus marking the beginning of 'Run 1' of the LHC physics program which continued till December 2012. The beam energy was fixed at 3.5 TeV during 2010 and 2011, and was then increased to 4 TeV during 2012. In the meanwhile, the luminosity was gradually ramped up as the understanding of the machine improved. This was achieved by increasing the bunch intensity i.e. the number of protons per bunch from 1.2×10^{11} in 2010 to 1.7×10^{11} in 2012, and reducing the β^* (which is proportional to the square of the transverse beam size) from 3.5 m to 0.6 m. Moreover, the maximum number of bunches circulated per beam were increased from 368 in 2010, with a bunch spacing of 150 ns, to 1380 with a bunch spacing of 50 ns in 2011 and 2012. All of these factors led to an increase in peak luminosity from 2.1×10^{32} cm^{-2}s^{-1} in 2010, through 3.7×10^{33} cm^{-2}s^{-1} in 2011, to 7.7×10^{33} cm^{-2}s^{-1} 2012. Consequently, the LHC was able to deliver 40 pb^{-1} of proton-proton collision data in 2010, 5.6 fb^{-1} in 2011, and 23.3 fb^{-1} in 2012.

While the LHC performed remarkably well to eventually deliver nearly 80% of the design luminosity at only half the nominal rate of collisions of 40 MHz, the progressive

squeezing of the beam, and the increase in bunch intensity led to an increase in the number of simultaneous proton-proton interactions per bunch crossing, from an average of around 4 interactions towards the end of 2010 to about 37 interactions at the end of 2012. Tab. 2.1, which was reported in [114], summarizes the LHC performance from 2010-2012.

Table 2.1 Overview of performance-related parameters during LHC operations in 2010-2012.

Parameter	2010	2011	2012	Design Value
Beam Energy (TeV)	3.5	3.5	4	7
β^* (m)	2.0/3.5	1.5/1.0	0.6	0.55
Bunch spacing (ns)	150	50	50	25
n_b	368	1380	1380	2808
N_b (protons per bunch)	1.2×10^{11}	1.45×10^{11}	1.7×10^{11}	1.15×10^{11}
ε_n (mm-mrad)	~ 2.0	~ 2.4	~ 2.5	3.75
Peak luminosity ($\mathrm{cm}^{-2}\mathrm{s}^{-1}$)	2.1×10^{32}	3.7×10^{33}	7.7×10^{33}	1×10^{34}
Max. mean no. of p-p interactions	4	17	37	19
Stored beam Energy (MJ)	~ 28	~ 110	~ 140	362

2.2 The CMS Detector

The Compact Muon Solenoid (CMS) detector [115–117] has been designed and built to be capable of exploring physics processes at the TeV scale. CMS is one of two general purpose experiments at the LHC, the other being ATLAS which stands for A Toroidal LHC ApparatuS. While the CMS detector is generic in capability, its design considerations have been based upon certain benchmark searches that will be most actively pursued at the LHC. These include searches for the Higgs boson, supersymmetry, heavy vector bosons, etc. The Higgs boson searches are of particular relevance, not only for the the critical answers they are expected to provide with regards to the breaking of the eletroweak symmetry, but also for the demands that the wide variety of search modes impose on the detector performance. If we go back to our discussion in section 1.3.4 we see that in order to be able to reconstruct the presence of the Higgs boson in a collision event, the detector must be able to distinctly identfy all the three kinds of charged leptons (electrons, muons and taus), neutrinos, photons and jets emerging from bottom quarks. In addition it is important to be able to detect the presence of jets in a large pseudorapidity range to be able to tag events from vector boson fusion. Apart

from identifying particles, it is crucial that their momenta and charge-sign (in the case of electrons, muons and taus) be measured with as much precision as possible. We will see how the design of the CMS detector meets these requirements in the remainder of this section.

2.2.1 Overall design

The CMS detector can be thought of as an assembly of several concentric cylindrical components or subdetectors that measure the energy or momentum of a certain class of particles. The innermost component of the detector is the tracker whose purpose is to measure the momentum of charged particles along with the sign of their charge. This is achieved by immersing the tracker in a powerful solenoidal magnetic field so that the charged particles emerging from the $p-p$ collisions get bent in the transverse plane. It is this bend in the trajectory that is used to determine their momentum and charge-sign. The tracker is surrounded by the calorimetry which is designed to absorb and thus measure the energy of all particles except for muons and neutrinos. The calorimetry actually consists of two kinds of calorimeters. On the inside lies the electromagnetic calorimeter in which the electrons and photons lose their entire energy. This is surrounded by the hadronic calorimeter which forces the hadronic particles such as pions to dump their energy. By making the calorimetry granular it is possible to localize the particle shower thereby enabling not just the measurement of particle energy but also its direction. This is essential for measuring the momentum of neutral particles such as photons. The calorimetry is surrounded by the muon spectrometer. As was just mentioned, it is only muons and neutrinos that make it past the calorimeters. While neutrinos almost never interact with the detector, the muons being charged particles leave tracks in the muon chambers. This helps to identify muons and also provides an additional measurement of their momentum. A sketch of the CMS detector is shown in Fig. 2.4.

The performance goals of the subdetectors are as follows. The tracker must be able to measure charged particle momenta ranging from about 100 MeV to 1 TeV. The tracker should provide the ability to efficiently tag jets originating from bottom quarks, which in turn requires identification of secondary vertices and measurement of impact

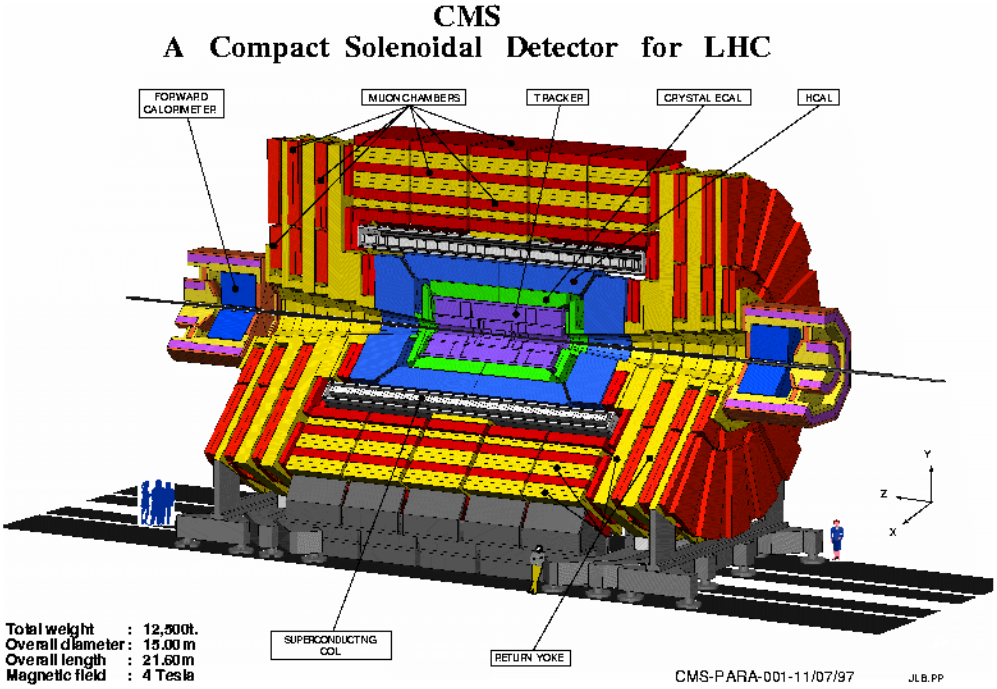

Figure 2.4 A sketch of the CMS detector [116]

parameters of charged particle tracks with a precision of ~ 100 microns. The tracker in conjunction with the muon subdetector should be able to able to provide a dimuon mass resolution of around 1% at 100 GeV (a scale relevant for the Z boson and a low mass Higgs boson). The electromagnetic calorimeter should be able to measure electron and photon momenta at a resolution scale that is comparable to the muons, and it should provide the ability to discriminate the photons from the large background of π^0's that are ubiquitously produced in QCD processes. The hadron calorimeter must enable the measurement of jet momentum with optimal resolution and must provide sufficiently large coverage ($|\eta| < 5$) to effectively measure a momentum imbalance in the transverse plane which, as we will see, provides a limited measurement of the neutrino momentum.

2.2.2 The Magnet

The CMS magnet is a solenoid of 5.9 m radius and 12.9 m length that houses the tracker and also the bulk of the calorimetry. The defining design choice of CMS was to use a single magnet for both the tracker as well as the muon system. In this configuration the return field of the solenoid magnetically saturates the iron yoke of the muon system

thereby providing the necessary bending power to measurement muon momentum. In order to achieve the design goal of measuring 1 TeV muons with ∼10% resolution with such a configuration, a strong magnetic field is required. This is achieved by pumping 19.5 kA of current through 2168 turns of the solenoid resulting in a magnetic field that is 3.8 Tesla strong.

2.2.3 The Tracker

The performance goals of CMS have imposed demanding requirements on the tracking system. The CMS tracker needs to be able to measure track momenta up to 1 TeV to be sensitive to high mass dilepton decays. On the lower end, tracks with $\sim$ 100 MeV momenta are expected to be reconstructed and measured to optimize the resolution of jets. In order to effectively reconstruct tau leptons, the tracking system must be able to resolve close-by tracks that are characteristic of hadronic tau-decays. Furthermore, the tracker must provide high spatial resolution to reconstruct the primary and secondary vertices, and measure the impact parameter of tracks with the precision necessary to achieve the desired b-jet tagging performance. In order to meet these goals the CMS tracker has been built as an entirely silicon based subdetector. It is essentially cylindrical is shape with a diameter of 2.5 m and a length of 5.8 m, and it provides fiducial reach up to $|\eta| < 2.5$. The tracker comprises of two major subsystems. The pixel detector sits at the very heart of CMS surrounding the interaction point. It provides the requisite spatial resolution for vertex reconstruction and b-jet tagging. The pixel detector is surrounded by the strip tracker which provides several additional measurement points or 'hits' along the particle trajectory and the necessary lever arm to effectively measure particle momenta up to 1 TeV. The layout of the silicon tracker is shown in Fig. 2.5.

The Pixel Tracker

The pixel detector consists of silicon modules with pixelated sensors of dimensions 100×150 μm^2. There are 768 pixel modules arranged in a 53 cm long barrel that consists of three concentric layers with mean radii of 4.4 cm, 7.3 cm and 10.7 cm from the center of the detector. There are two layers of endcap disks enclosing the barrel

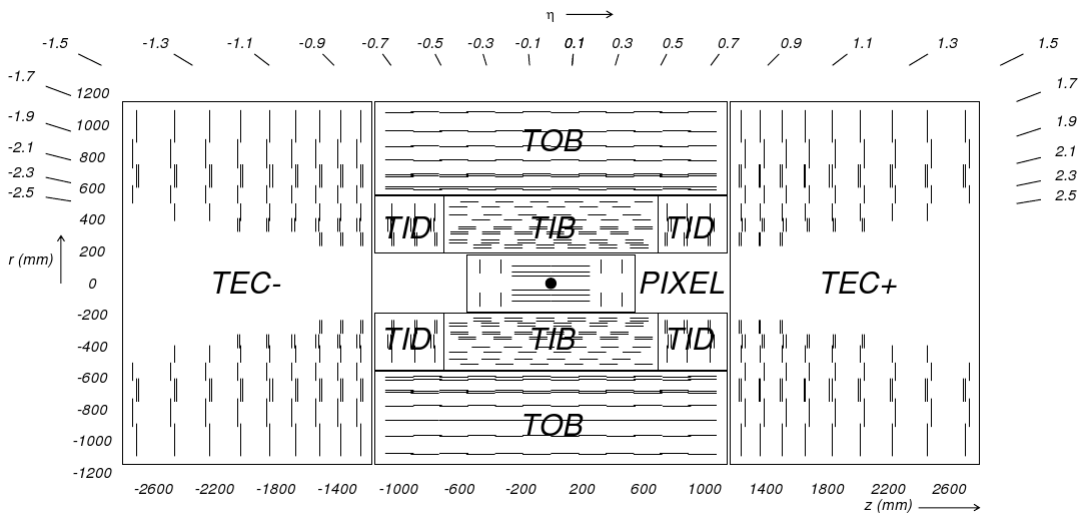

Figure 2.5 Layout of the silicon tracker [117]

on each side that are located at a longitudinal distance of 34.5 and 46.5 cm from the center of CMS. These endcap disks consist of 672 modules arranged in a turbine-like geometry that extend from a radius of 6 to 15 cm. Overall, there are about 66 million pixels covering a total area of about 1m^2. Despite being closest to the interaction point and hence being subject to the highest particle flux, the pixel detector has an average occupancy of only about 10^{-4} per pixel per LHC bunch crossing.

The Strip Tracker

The pixel detector is surrounded by the strip tracker which extends from an inner radius of 20 cm up to about 110 cm. The strip tracker can itself be divided into two parts. The inner part extends radially from 20 cm up to 55 cm and consists of silicon modules with strip cells of dimensions 10cm $\times$ (80 to 120) μm. The inner barrel (TIB) is 130 cm long and consists of four layers with the two innermost layers being 'stereo' i.e. comprising of two layers of strip sensors placed at an angle of 100 mrad with respect to one another. This stereo geometry improves the longitudinal resolution to about 230 μm. The TIB is enclosed on both sides by three layers of inner disks (TID). Each disk is in turn made up of three rings, the inner two of which are stereo. The inner TIB and TID are surrounded by a six-layer, 220 cm long outer barrel (TOB). Since the particle flux drops sufficiently in the outer region of the tracker, the strip dimensions are increased to 25cm $\times$ (120 to 180) μm. As in the case of the inner barrel, the first two

layers of TOB are stereo and provide a longitudinal resolution of 530 μm. The TOB is enclosed by nine layers of endcaps on either side (TEC), extending longitudinally from 120 cm to 280 cm with respect to the center of CMS. The first two and fifth rings of the endcaps are stereo. The strip tracker on the whole covers an area of 200 m^2 and has 9.6 million strips. The average occupancy, though higher than the pixels, is still at the level of a few percent per strip per LHC bunch crossing.

Tracker Material

A challenge in the design of the tracking system is to control the amount of material in the path of particles as they traverse through the tracker. Apart from the active elements, the tracker modules need to have a lot of front-end electronics and need to be supplied with considerable amount of power. The power carrying copper wires as well as the detector modules generate considerable amount of heat which needs to be removed to ensure optimal running conditions. This necessitates additional material to be introduced into the tracker volume to provide the requisite cooling. The material budget of the tracker is defined as the amount of matter that a particle needs to traverse through while passing through the tracker volume. It is measured in units of the radiation length or the nuclear interaction length. The radiation length is the average amount of distance that an electron traverses through a material before its energy is reduced by a factor $1/e$ due to bremsstrahlung. In the case of photons, radiation length is (7/9) times the mean free path of a photon through a material before it converts to an e^+e^- pair. The nuclear interaction length on the other hand gives the mean free path of a hadron before it undergoes an inelastic nuclear interaction. Fig. 2.6 shows the material budget distribution of the tracker as a function of pseudorapidity.

In order to understand the impact of the tracker material on physics performance let us consider the case of electrons. Fig. 2.7(a) shows several categories of electrons depending on their interaction with the tracker. The light green distribution shows the fraction of 'golden' electrons which are characterized by low bremsstrahlung radiation. Similarly, the purple distribution shows the fraction of 'showering' electrons which are characterized by bremsstrahlung emission all along their trajectory inside the tracker. We can see that the proportion of golden and showering electrons changes in accordance

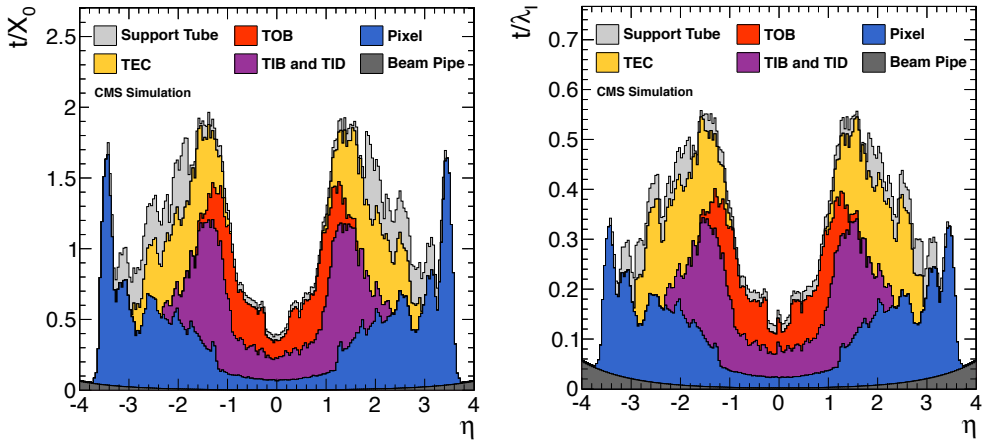

Figure 2.6 Material budget of the tracker expressed as a function of pseudorapidity (η) in units of radiation length(left) and nuclear interaction length(right) [118].

with the increasing material budget as we move away from the central region of the tracker. Moreover, Fig. 2.7(b) shows the ratio of the measured energy of the electrons to their actual energy. We clearly see that the energy measurement of the showering electrons is considerably degraded with respect to the golden electrons, thus illustrating the adverse impact of the material budget on physics performance.

2.2.4 The Electromagnetic Calorimeter

The CMS electromagnetic calorimeter (ECAL), which surrounds the silicon tracker, is a granular and homogeneous calorimeter made up of lead tungstate crystals and is housed entirely within the solenoid of the magnet. The material of choice for the ECAL, lead tungstate, has a short radiation length of 0.89 cm and a small Moliere radius of 2.2 cm. While the short raditiation length helps in containing the shower of electrons and photons longitudinally, thereby enabling the ECAL to be compact, a small Moliere radius helps in containing the lateral spread of the shower allowing the calorimeter to be granular. Moreover, the ECAL is radiation hard and fast enough to handle the high rate of LHC bunch crossings. The main challenge, however, is that the light yield of about 30 photons per MeV is relatively low. This has necessitated the use of avalanche photodiodes in the barrel region and vacuum phototriodes in the endcaps. These photodetectors provide the necessary signal amplification and can also operate in the strong 3.8 T magnetic field of CMS.

The layout of the ECAL is shown in Fig. 2.8. The ECAL consists of a central

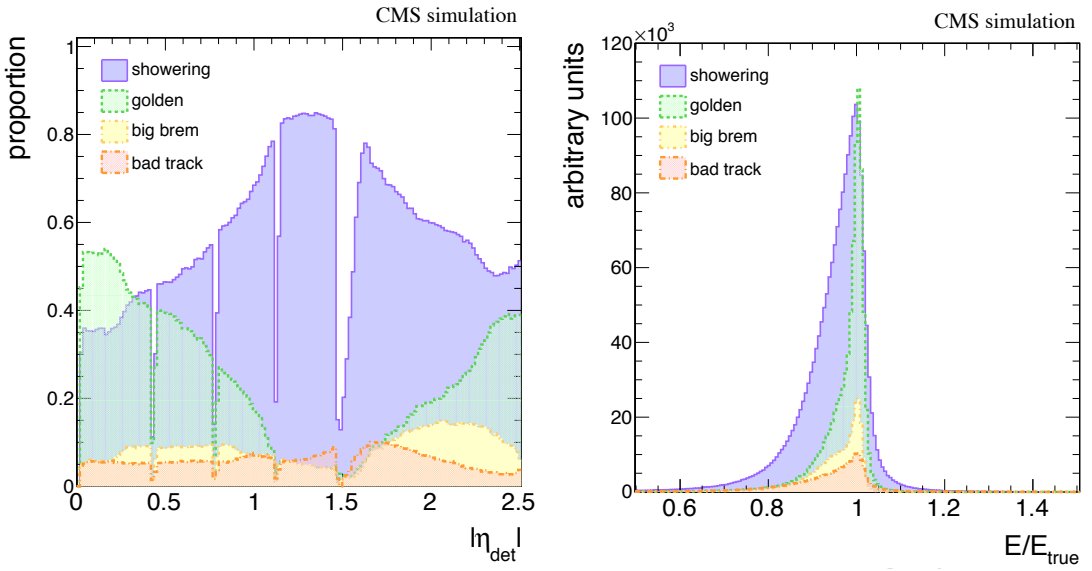

(a) (b)

Figure 2.7 Fig.(a) shows the proportion of the different categories of electrons as a function of pseudorapidity. The golden electrons radiate very little energy while moving through the tracker, the showering electrons typically radiate energy all along their trajectory in the tracker, while the big brem electrons tend to lose a lot of energy in a single interaction. The sharp fissures in the plot are indicative of the cracks in the electromagnetic calorimeter. Fig.(b) shows the ratio of the measured of electrons in the different categories to their actual energy. [119]

barrel (EB) that has an inner radius of 129 cm and extends up to $|\eta| < 1.479$. The EB consists of 61200 leab tungstate crystals each with lateral dimensions of 0.0174×0.0174 in $\eta - \phi$ and a length of about 230 mm which corresponds to 25.8 radiation lengths. The crystals in EB are arranged in 36 supermodules, 18 on either side of $\eta = 0$, such that each supermodule covers 20 degrees in ϕ.

The ECAL endcaps (EE) are mounted at a longitudinal distance of 314 cm from the center of CMS and cover a pseudorapidity range of $1.479 < |\eta| < 2.5$. Each endcap consists of two D-shaped units in which lead tungstate crystals are arranged in 5×5 units called supercystals. The endcap crystals have an $x - y$ geometry with a cross-section of 28×28 mm^2 and a length of 220 mm which corresponds to 24.7 radiation lengths.

There is a preshower placed in front the EE which consists of two active layers of silicon placed at depths of 2,3 radiation lengths between lead absorber material. The preshower is intended to help improve discrimination between photons and π^0s in the

forward region of the ECAL which is less granular compared to the barrel. Also, a longitudinal sampling of the photon trajectory in the preshower helps in the determination of their point of origin which in turn contributes to improving the mass resolution of diphoton decays such as $H \rightarrow \gamma\gamma$.

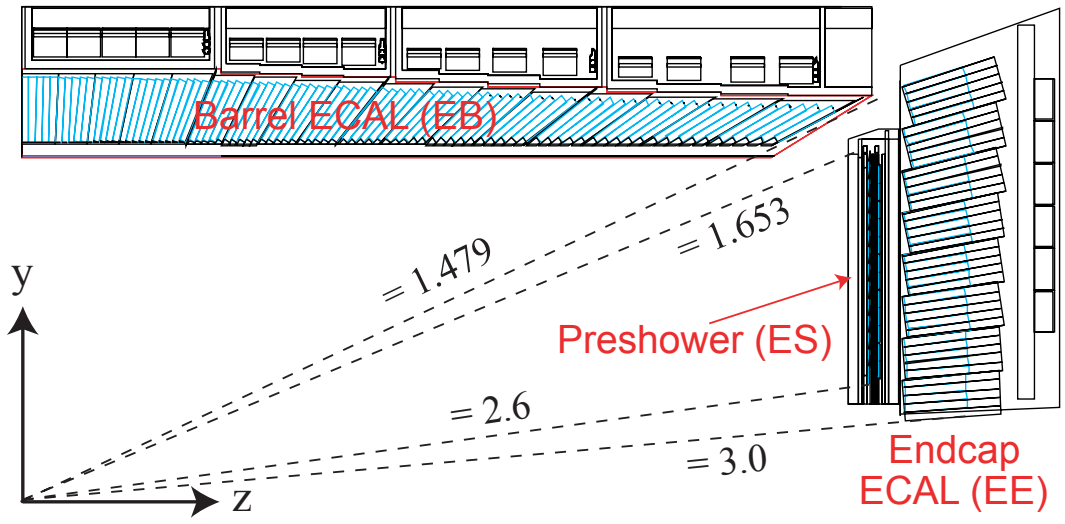

Figure 2.8 Layout of the electromagnetic calorimeter [115]

2.2.5 The Hadronic Calorimeter

The design choice of CMS to include the calorimetry within the magnet coil has critical implications on the hadronic calorimeter (HCAL). The HCAL, which surrounds the ECAL, is required to contain the hadronic energy emerging from $p-p$ collisions within the volume of the solenoid. This has necessitated the maximization of the absorber material with respect to the active sampling material that makes up the HCAL. Brass has been the material of choice as an absorber since it has a short nuclear interaction length and is also non-magnetic. The absorber material is interleaved with plastic scintillator tiles that are used to sample the energy of the hadronic shower. This sampled energy is readout through wavelength shifting fibres that connect to multi-channel hybrid photodiodes.

The layout of the HCAL is shown in Fig. 2.9. The central barrel region of the HCAL (HB) extends up to $|\eta| < 1.4$ and consists of 2304 towers that provide a granularity of 0.087×0.087 in $\eta - \phi$. The hadron endcaps (HE) provide a pseudorapidity coverge of $1.3 < |\eta| < 3.0$. Each endcap consists towers with a variable ϕ-segmentation

ranging from 5 to 10 degrees and η-segmentation ranging from 0.087 to 0.35. In order to catch the tails of the hadronic shower which may leak through beyond the magnet coil, an outer hadron detector (HO) has been constructed in the pseudorapidity range $|\eta| < 1.26$. This tail-catcher effectively increases the HCAL material to over 10 interaction lengths thereby improving the jet momentum resolution. Finally, the coverage of the HCAL is extended upto $|\eta| = 5.0$ with the help of the hadron forward calorimiter (HF) which is a steel/quartz fibre sampling calorimeter located at a longitudinal distance of 11.2 m from the center of CMS.

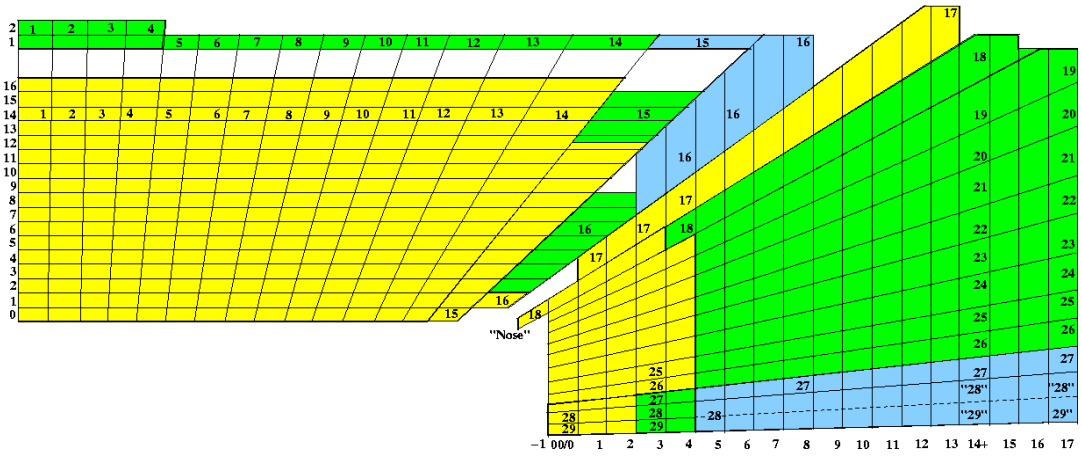

Figure 2.9 Layout of the hadronic calorimeter calorimeter [115]

2.2.6 The Muon System

The muon system is the outermost and, in terms of size, the largest subsystem of CMS. It consists of the iron yoke which when saturated by the 3.8T magnetic field provides the requisite bending power to measure muon momentum. The muon measurement itself takes place in three different types of detectors - the drift tubes (DTs) which are used in the barrel region, the cathode strip chambers (CSCs) which are located in the muon endcaps, and the resistive plate chambers (RPCs) which are used both in the barrel as well as the endcaps. The layout of the muon system is shown in Fig. 2.10.

The barrel of the muon system extends up to $|\eta| < 1.2$ and consists of 250 DT chambers organized into four concentric layers within the iron yoke at radii of 4.0, 4.9, 5.9 and 7.0 m from the beam axis. Longitudinally, the barrel is divided into five wheels each of which has 12 sectors covering an azimuthal angle of 30 degrees. Of the four

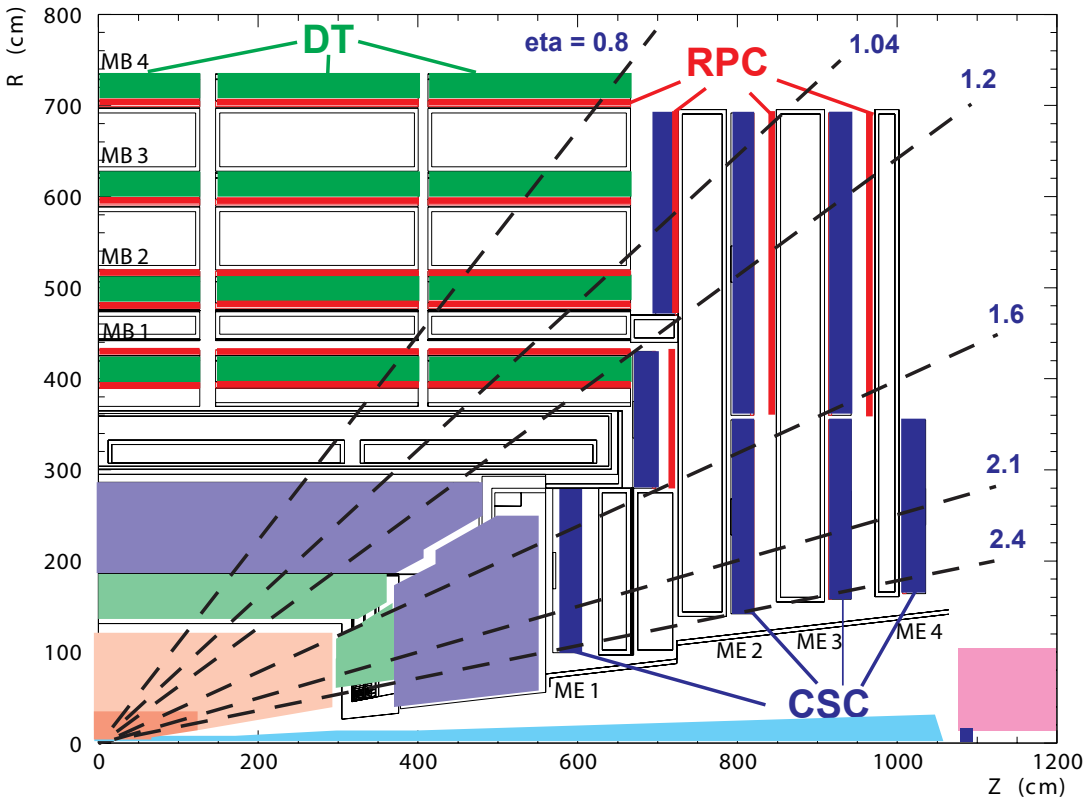

Figure 2.10 Layout of the muon system [115]

concentric layers, the two innermost layers have DTs sandwiched between two RPCs, while the two outermost layers have a single RPC placed on the inner side of the DTs. These chambers in the four layers are staggered in such a way as to ensure that a muon passes through at least three of them even at the sector boundaries. Each DT chamber provides two $r-\phi$ and one z measurement, and is able to pin-point the muon position to within 100 microns in ϕ and in direction to within 1 mrad.

The endcaps extend the muon coverage to $|\eta| < 2.4$. Each endcap consists of four stations that are located at an increasing distance from the collision point. Each endcap station consists of a circular arrangement of the trapezoid shaped CSCs in two rings (except for the innermost station which has three rings). The CSCs in the outer ring which extend up to $|\eta| < 1.6$ are also complemented with RPCs. Each trapezoidal CSC has six gas-gaps or six distinct layers each consisting of cathode strips in the radial direction and anode wires along the azimuthal direction, thus providing six distinct position measurements. Each CSC chamber provides a spatial resolution of 200 microns and is able to measure the muon direction to within 1 mrad.

2.2.7 Trigger and Data Acquisition System

The $p-p$ collisions at the LHC are designed to occur at a frequency of 40 MHz. However, it is impossible to readout the detector at such a high rate or to store the readout information for every collision event (each event produces $\sim$ 1 MB of raw data, so storing every collision event would generate 40 TB of data per second!). To make data acquisition manageable, the event rate needs to be reduced to around $\sim$100 Hz which means reduction by a factor of around 10^6. Moreover, this reduction in event rate must not affect the physics interests of the experiment i.e. the CMS detector should be able to store all interesting event signatures that could indicate the presence of the Higgs boson, supersymmetry, or any new physics. This task is achieved by a dedicated two-tier trigger system.

The Level-1 Trigger

The first of these two tiers is known as the Level-1 or L1 trigger. The L1 trigger is expected to bring down the event rate to about 100 kHz. They key challenge is to make quick decisions about whether an event is interesting enough to be retained for further analysis or it can be thrown away. The L1 system uses dedicated, fast and largely programable hardware to make these decisions in about 3.2 μs. A part of this time is spent in moving data from the detector to the service cavern which houses a part of the L1 electronics, and also communicating the decision back to the detector. The data fragments or trigger primitives that are used for the L1 decision come from either the muon system or the calorimetry. An event may be retained if it contains, for instance, a high p_T muon track stub, or an electromagnetic energy deposit above a certain threshold, or an indication of a global transverse momentum imbalance. It is also possible to correlate the primitives, e.g. require a muon and an electromagnetic cluster and so on. During the latency period of L1 processing, the data from all the subdetectors is pipelined so that it can be readout in the case of a positive decision.

Detector Readout: Strip Tracker Example

On the receipt of a L1 trigger accept decision, the entire detector is readout in a two-step process. Every subdetector has a readout system which buffers data and sends

it to the front-end drivers (FEDs) that are housed in the service cavern. The data from the FEDs is then read into the central data acquisition (DAQ) system which collates the information from all subdetectors and sends it further downstream for processing. The readout system of every subdetector is unique to it. Here, the example of the strip tracker is presented.

The basic readout unit of the strip tracker is a custom-made integrated circuit called APV25. An APV25 chip amplifies and shapes the signals from 128 strip sensors and buffers them in a 192 element deep pipeline sampled at 40 MHz to allow for the 4 μs latency of the L1 trigger. Every strip tracker module has either 4 or 6 APV25 readout chips depending on its geometry. The APV25 chips are read out through optical links which carry the data from the detector up to the service cavern. Each optical fibre carries multiplexed data from two APV25 chips, which corresponds to 256 channels. The fibres are grouped in 96-way ribbon cables and every such group feeds into a FED module which then digitizes the signal and applies pedestal corrections, common-mode noise subtraction and zero suppression. The data from the strip tracker, sitting in 440 FEDs is now ready to be transferred to the central DAQ system.

The Data Acquisition System

The DAQ system is charged with the duty of integrating the event data from the FEDs and transmit it to the Event Filter complex for processing. The FEDs from various subdetectors have a common interface to the DAQ system provided by the SLink64 card. Upto two SLink64 inputs (and hence two FEDs) can be merged by the Front-end Readout Link (FRL) which then transmits the data to the Event Builder. The Event Builder system consists of the FED builder which assembles the information from $\sim$512 FRLs into 72 super-fragments, each with a size of about 16 kBytes. These super-fragments are buffered in Readout Units (RU) and then assigned to 8 RU-builder units for further intergration. Each RU-builder belongs to one DAQ 'slice' which is a nearly autonomous system in itself and can handle event rates up to 12.5 kHz. The entire event is then transferred to the Event Filter.

A crucial component of this DAQ chain is the Trigger Throttling System (TTS). Delays in downstream processing, or fluctuations in event rates may lead to a backpres-

sure on the FEDs. This may cause an overflow of their buffers and hence, loss of data. The TTS provides a fast feedback from the FEDs to throttle the global trigger so as to prevent the FEDs from overflowing.

The High Level Trigger

The Event Filter needs to reduce the L1 event rate by almost three orders of magnitude to bring it at the level of ∼300 Hz. This is achieved by filtering the incoming events through the High Level Trigger (HLT) system. The HLT has access to the fully granular data from the detector (as opposed to the coarse primitives that are provided to the L1 system) and it can employ sophisticated algorithms for event rate reduction. Events can be partially/regionally reconstructed to assess possibly interesting signatures. The HLT system is entirely software based and is run on a farm of around thousand commercial processors. Being software driven, the HLT is completely flexible and adaptable to the needs of the experiment. Once an event is selected by the HLT, it is transferred to the CERN data center for storage and becomes available for analysis.

Trigger Performance During Run I

The CMS trigger system was subjected to considerable stress during the first run of the LHC. As we saw in Tab. 2.1 LHC was able to deliver a peak luminosity of 3.7×10^{33} cm^{-2} s^{-1} in 2011. This was ramped up to 7.7×10^{33} cm^{-2} s^{-1} towards the end of 2012, thus attaining almost 80% of the design specification of 10^{34} cm^{-2} s^{-1}. At the same time the average number of proton-proton interactions in a bunch crossing were almost twice the design specification. This meant that the trigger system had to deal with a high amount of detector activity for a given event. In terms of the overall bandwidth, the most demanding trigger paths were those involving leptons. Given the nature of the final states in several crucial physics analyses (Higgs boson searches, supersymmetry searches, standard model measurements, etc.) the trigger system was required to support single and two-leg trigger paths for muons, electrons and photons with reasonably low p_T thresholds. Tab. 2.2 [120] shows the snapshot of the most important L1 trigger paths that were used when the LHC was delivering a peak luminosity of 6.6×10^{33} cm^{-2} s^{-1} in mid-2012. At the HLT level, the trigger rate was kept under control by progressively

tightening the selection on the lepton candidates with the increase in luminosity. The basic idea was to keep the trigger rate in check while requiring the p_T thresholds on the leptons to be low. This ensured that the phase space of the signal was not encroached upon. Tab. 2.3 [121] shows a snapshot of the prominent HLT paths for the 6.6×10^{33} cm^{-2} s^{-1} running conditions.

Table 2.2 Most important L1 trigger paths for the 6.6×10^{33} cm^{-2} s^{-1} instantaneous luminosity scenario.

Trigger	Threshold (GeV)	Rate (kHz)
Single electron/photon	20	13
Double electron/photon	13,7	8
Single muon	14 ($\|\eta\| < 2.1$)	7
Double muon	10, 0	6
Electron/photon and muon	12, 3.5	3
Muon and electron/photon	12, 7	1.5
Single jet	128	1.5
Four jets	36	3.5
Hadronic transverse energy sum (H_T)	150	5
Transverse momentum imbalance (E_T^{miss})	36	8

Table 2.3 Most important HLT paths for the 6.6×10^{33} cm^{-2} s^{-1} instantaneous luminosity scenario.

Trigger	Threshold (GeV)	Rate (Hz)
Single electron	80	8
Single isolated electron	27	59
Single photon	150	5
Double electron	17,8	8
Double photon	36,22	7
Single muon	40	21
Single isolated muon	24	43
Double muon	17,8	20
Muon and electron cross-triggers	(17,8), (5,5,8), (8,8,8)	3
Single jet	320	9
Four jets	80	8
Six jets	$(6 \times 45), (4 \times 60, 2 \times 20)$	3
Hadronic transverse energy sum (H_T)	750	6
Transverse momentum imbalance (E_T^{miss})	120	4

2.3 Event Reconstruction

Events that pass the trigger selections have their data shipped to the offline storage system where it becomes available for a full-blown reconstruction. Event re-

construction is essentially the process of translating the detector data into physically relevant objects such as electrons, muons, jets, etc. and measuring their properties such as momentum and charge. The reconstruction of certain physics objects like electrons or muons requires combination of inputs from several subdetectors. These objects may themselves then feed into the reconstruction of more complicated physics entities like jets. This section provides a quick overview of this process.

2.3.1 Track Reconstruction

Charged particles are measured by the tracks that they leave in the silicon tracker. The reconstruction of particle trajectories in the tracker, which is called tracking, is the most computationally intensive process in the entire reconstruction chain. Tracking is essentially the mechanism of joining the dots or hits that charged particles leave behind in the various layers of the tracker. What complicates matters is that a collision event may produce a large number of charged particles resulting in ~ 1000 tracker hits. If we divide them over 10 tracker layers we end up with about 100 hits per layer. If we naively consider all possible hit combinations we end up with a huge combinatoric factor of 100^{10}. This is a clear indication that track reconstruction demands a rather sophisticated treatment.

The track reconstruction sequence in CMS [118] is iterative in nature i.e. the algorithm starts with tracks that are easiest to reconstruct (typically prompt, high p_T tracks), then removes the hits belonging to these tracks to reduce the combinatorics and runs again to find tracks that were missed earlier. Six such iterations have been implemented in the tracking sequence.

In every iteration, the process of building tracks begins with 'seeds' or track-stubs that can be extended to form complete tracks. A charged particle moving in a solenoidal magnetic field follows a helical trajectory. To determine this helix completely, five parameters are required. These are the transverse momentum of the particle (p_T), its orientation in the transverse plane (ϕ), the transverse and longitudinal impact parameters (d_0 and d_z), and $\cot(\theta)$ where θ is the polar angle that the momentum vector makes with the z-axis. The seeds must provide an initial estimate of these track parameters, which requires information from at least three hits. A pair of hits can also

be used, but in that case constraint from the 'beam-spot' or the luminous center of the $p-p$ collisions is needed. The seeds are typically generated in the pixel detector. This is because the average occupancy of the pixel detector, inspite of it being closer to the interaction point, is about two orders of magnitude smaller than the strip tracker on account of its finer granularity. What this means is that in a given layer, the separation between hits relative to their spatial resolution is larger in the case of the pixel detector as compared to the strip tracker. This leads to a smaller combinatorial ambiguity while constructing the seed triplets/pairs.

The seeds are passed on to the track finding algorithm. The track finder takes the track parameters of a seed and the corresponding uncertainties to determine a geometric window in which to search for an additional hit in the successive tracker layer. If a suitable hit is found, it is added to the track and the track parameters are updated. This process continues till all possible hits are accounted for. Finally, a fit is performed using the information from all the hits to get the best estimate of the track parameters.

Two key performance parameters of tracking are efficiency and momentum resolution. Fig. 2.11 shows the efficiency and the momentum resolution as a function of p_T, for tracks that are reconstructed in simulated $t\bar{t}$ decays at $\sqrt{s} = 8$ TeV. We see that the efficiency for tracks with p_T in the range of 1 - 100 GeV is greater than 90% while the momentum resolution for tracks in this range is less than 2%. The momentum resolution begins to degrade as p_T exceeds 100 GeV. This is where the size of tracker's lever-arm begins to affect its resolution. On the lower end of p_T as well, we see a worsening of resolution. This is on account of multiple scattering which dominates the measurement of low-p_T tracks.

The tracks in an event are further used to reconstruct primary vertices which help ascertain the coordinates of the interaction point. Given the high luminosities at which LHC operates, a hard interaction is typically accompanied by a number of simultaneous minimum bias interactions. These are known as 'pileup' interactions. The primary vertex reconstruction algorithm tries to ascertain the position of as many pileup interactions as possible. The process starts with the selection of tracks that are produced promptly i.e. tracks whose impact parameter is consistent with the beam spot. These tracks are then clustered using a dedicated 'deterministic annealing' algorithm into

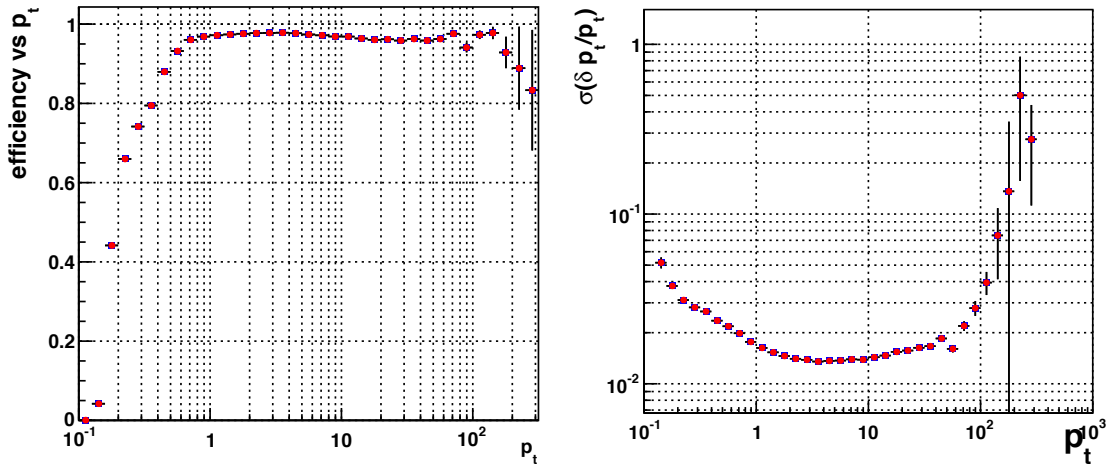

(a) (b)

Figure 2.11 Figure on the lefts show tracking efficiency as a function of p_T (GeV) in $t\bar{t}$ events at $\sqrt{s} = 8$ TeV. Only tracks that leave at least three hits in the tracker are considered in the efficiency computation. The figure on the right shows the momentum resolution of tracks in the same set of events as a function of p_T.

groups of tracks that can be associated with a single vertex. Finally tracks in each cluster are used to fit for the position of the primary vertex. Given the multiplicity of primary vertices, a procedure needs to be adopted to determine the primary vertex corresponding to the hard interaction. In the case of hard interactions which produce high p_T charged particles in the final state (e.g. $Z \to \mu^+\mu^-$) an effective approach is to rank the vertices in decreasing order of the sum of p_T^2 of their constituent tracks and to associate the vertex with the highest rank (largest $\sum p_T^2$) with the hard interaction.

2.3.2 Muon Reconstruction

Muons are detected by the tracks that they leave behind in the inner silicon tracker as well as the outer muon system. Muon tracks that are independently reconstructed in the muon system are called 'standalone muon' tracks. A standalone muon track can be extrapolated 'outside-in' to find a matching tracker track. A combined fit can then be performed using hits from the tracker track and the standalone muon track to form a 'global muon' track. We saw that as p_T exceeds ~ 100 GeV the momentum resolution provided by the tracker begins to degrade due to the size of its lever-arm. In this momentum regime, the muon system with its larger size helps in improving the momentum resolution as shown in Fig. 2.12.

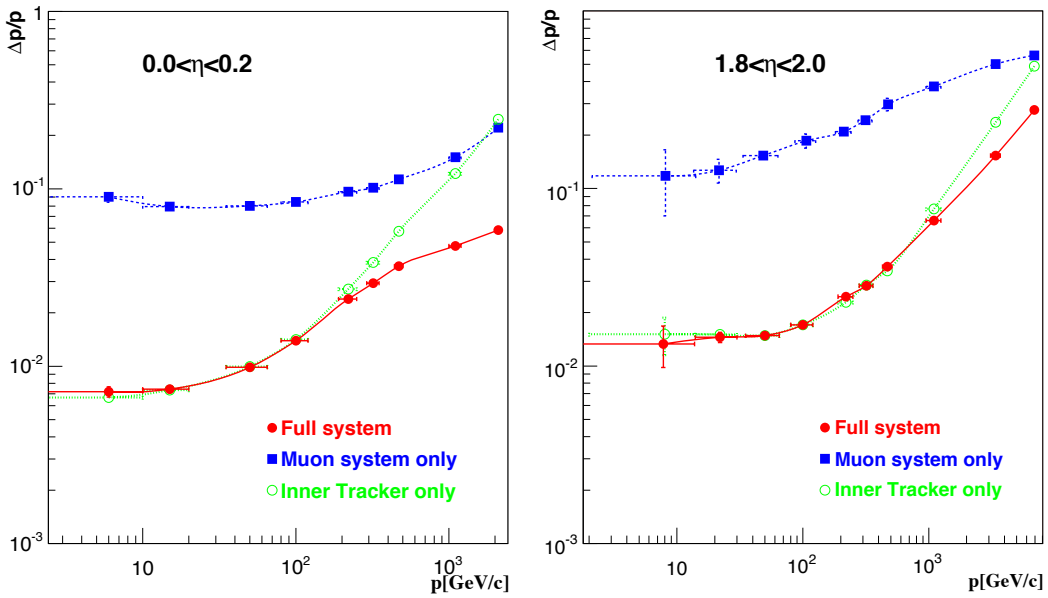

Figure 2.12 Muon momentum resolution for standalone muons tracks, tracker tracks and global muon tracks in the central (left) and forward (right) regions of the detector [115].

However, if the muon momentum is low, with $p_T \sim 5$ GeV or smaller, the muon may not have sufficient energy to penetrate through the muon system and may only leave behind partial track segments. In order to reconstruct such muon candidates tracker tracks are extrapolated 'inside-out' to match with the muon segments. These are known as 'tracker muons'. Global and tracker muon candidates taken together provide a very high reconstruction efficiency ($\sim 99\%$) for muons that are typically produced in $p-p$ collisions.

2.3.3 Electron and Photon Reconstruction

The ECAL is designed to ensure that electrons and photons deposit their entire energy into it. Electrons, being electrically charged also leave a track in the tracking system. Thus, electron candidates are reconstructed by associating tracks in the tracker with clustered energy deposits in the ECAL [122]. Photons on the other hand are electrically neutral, and so photon reconstruction relies almost exclusively on the ECAL [123].

The reconstruction of both electrons and photons depends on finding energy 'superclusters' in the ECAL. Superclusters are groups of energy deposits that can be geometrically associated with each other. A supercluster may have a wider spread in

the ϕ-dimension compared to its η-width. This is explained by the fact that electrons tend to radiate photons as they interact with the tracker material. But the electrons also bend in ϕ as they move through the tracker resulting in a spray of photons along ϕ as they pass through successive tracker layers. The supercluster profile of photons is similar to that of the electrons. A photon on interacting with the tracker material may convert to an e^+e^- pair which further produces an electron-like energy profile in the ECAL. Algorithms searching for superclusters do account for this characteristic feauture of the geometric spread of the energy of electrons and photons in the ECAL. Furthermore, it is important to differentiate the superclusters of electrons and photons from the energy residue that jets may leave behind in the ECAL. An important factor which discriminates electrons and photons from jets is that they cannot typically reach the HCAL. Therefore, a requirement of low HCAL activity behind the supercluster is imposed to reduce the jet induced background.

The superclusters provide an estimate of the energy of electrons and photons. The supercluster energy is obtained by the following relation [124]:

$$E_{e,\gamma} = F_{e,\gamma}[G.\sum_i S_i(t).C_i.A_i + E_{ES}] \tag{2.2}$$

where A_i is the readout signal amplitude of each crystal, G is a conversion factor that translates the ADC signal from the crystals to a corresponding measure of energy (this factor is different for the barrel and endcap crystals), C_i is the crystal-specific calibration constant called the intercalibration constant which needs to be obtained from data, $S_i(t)$ is a time-dependent calibration factor that reflects the change in crystal response as it is exposed to more and more radiation (this also needs to be obtained from data), E_{ES} is the energy correction due to the preshower and $F_{e,\gamma}$ is a correction factor that accounts for material effects and differences in the shower profiles between electrons and photons. An elaborate calibration program is required to obtain the values of these parameters so that the best possible estimate of supercluster energy can be derived.

The weighted center of energy of the supercluster provides a position measurement that can be used to ascertain the particle direction. This is particularly relevant for photons which do not leave any tracks. The center of the supercluster can be matched to the primary vertex of the hard interaction, if it can be unambiguously identified, to

obtain the photon direction. However, in certain type of events, such as H $\rightarrow \gamma\gamma$ decays, locating the interaction vertex may not be a trivial task. In such cases, some other inputs such as identifying photon conversion and locating its point of origin, may be utilized.

In the case of electrons, the momentum direction is determined from the tracker track. The reconstruction of this track, however, poses a challenge. Given that electrons tend to lose energy as they traverse through the tracker, their trajectory is not exactly helical. As a result, the standard track reconstruction technique discussed in the previous section is not perfectly suited for electron tracks. A dedicated algorithm called the Gaussian Sum Filter (GSF) is used for reconstructing electron tracks. This algorithm takes into account energy losses due to bremsstrahlung. The GSF track reconstruction is initiated by geometrically matching the ECAL superclusters with tracker seeds. The momentum of the reconstructed GSF tracks is then optimally combined with the supercluster energy estimate to obtain the electron momentum. The GSF track gives the direction of the electron as well its impact parameter.

This process of electron reconstruction which starts with the ECAL superclusters and then proceeds inwards to find matching tracks, is said to be 'ECAL-driven'. For electrons with $p_T \sim 20$ GeV or higher, which are typical of the $W \rightarrow e\nu$ and $Z \rightarrow ee$ decays, the ECAL-driven approach proves to be highly efficient. However, for lower p_T electrons or electrons inside jets, a complimentary 'tracker-driven' approach has been developed which starts with tracker tracks and matches them to energy clusters in the ECAL.

In terms of performance, the momentum resolution of electrons and photons is mainly determined by the resolution of the supercluster energy which is given by the following relation

$$\frac{\sigma_E}{E} = \frac{S}{\sqrt{E}} \oplus \frac{N}{E} \oplus C \tag{2.3}$$

where S is the stochastic term arising from shower fluctuations, N is the noise term and C is a constant. Unlike the momentum obtained from tracks, we see that supercluster energy resolution actually improves with energy. As a result, tracks do not play an important role in the determining the energy of high p_T electrons. However, at low p_T

the track momentum does help in improving the resolution as shown in Fig. 2.13. In the case of photons, the energy measurement has to necessarily rely on the supercluster alone. Moreover, the uncertainty in the determination of photon direction can have some adverse impact on the mass resolution of diphoton decays.

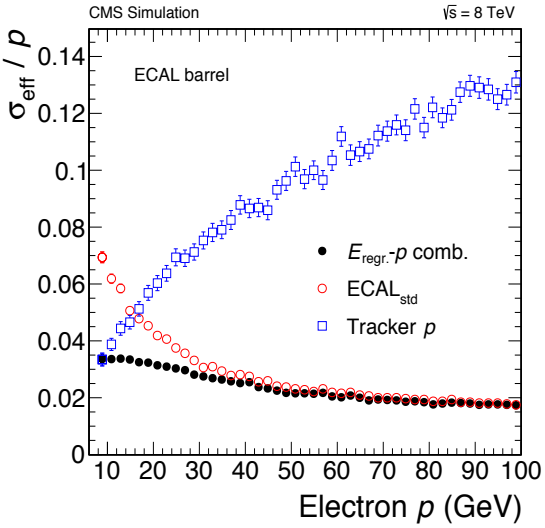

Figure 2.13 Electron momentum resolution using only the supercluster information (red open circles), only the tracker information (blue squares), and using a combination of the supercluster and electron track (black circles) [125].

2.3.4 Jet Reconstruction

Quarks and gluons produced in $p-p$ interactions cannot be detected in isolation. Instead, they hadronize to form jets of particles like pions and kaons. Therefore, the study of any process which involves these strongly interacting particles (e.g. VBF Higgs boson production) needs to look for jets in the detector. There exist several algorithms that can clusterize the energy deposits in the detector into jets [126–130]. A complete paradigm of event description called particle-flow [131–134] has been developed which provides the best possible inputs to these clustering algorithms. The particle flow algorithm combines information from all the sub-detectors to form a list of particles that are produced in the event. Particles are categorized as muons, electrons, photons, neutral hadrons and charged hadrons. The goal here is to find the best possible description of the detector activity in terms of the passage or flow of certain types of particles. These particle are then clusterized into jets.

The energy measured in the reconstructed jets may differ from the partonic

energy on account of several factors such as detector calibration, pileup etc. Therefore, the jets need to be calibrated to ensure that their energy matches on average with that of the partons. These corrections are applied in a factorized manner [135]. The 'L1' corrections account for pileup effects by computing the average p_T density of soft interactions in an event and then subtracting this pileup contribution from the jet energy [136–138]. The 'L2' corrections try to make the jet response uniform over the entire η range. These are derived from dijet events in data. Given that the p_T of the two jets in these events should match, one of the jets at a certain value of η can be calibrated against another jet at a different η. This still leaves the possibility of an absolute shift in the measurement jet p_T. This is accounted for by the 'L3' corrections which are derived from simulation by computing the ratio of the reconstructed jet p_T and the p_T of the generator level jets. Lastly, residual corrections are applied to correct for differences between data and simulation. The momentum resolution of particle-flow jets reconstructed with the anti-k_{T} algorithm with a size parameter of 0.5 is shown in Fig. 2.14.

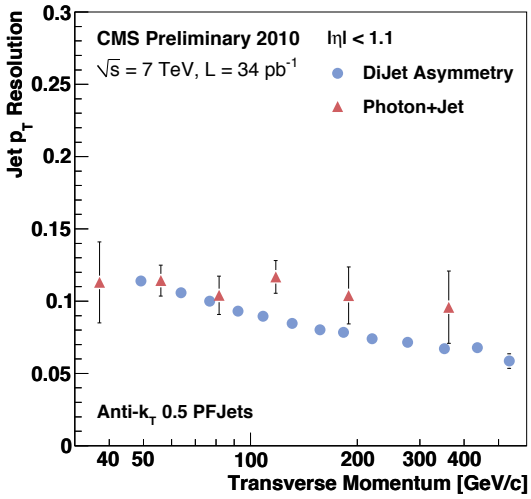

Figure 2.14 Jet p_T resolution of anti-k_{T} particle flow jets with a size parameter of 0.5 [139].

2.3.5 Tau Reconstruction

Tau leptons are the heaviest of all leptons in the SM. With a mass of 1.776 GeV, these are the only leptons that are capable of hadronic decays. The taus, however, are short-lived with a mean lifetime of 2.9×10^{-13} seconds which corresponds to a path

length of 87 μm. As a result, most tau leptons decay even before leaving the beam-pipe and have to be reconstructed from their decay products. About 35% of taus decay leptonically producing either an electron or a muon and a couple of neutrinos. In the remaining cases, the taus decay hadronically, producing one or three charged hadrons, a neutrino and upto two neutral pions which promptly decay into photons.

Hadronic decays of taus can be identified with either one or three hadronic tracks along with clustered deposits of photons in the ECAL. Such decays can be reconstructed as jets, and in fact particle-flow based anti-k_{T} jets serve as the starting point for identifying taus in an event. The principle algorithm for tau reconstruction is called the Hadron Plus Strip (HPS) algorithm [140]. This algorithm considers several possibilities depending on the presence of one or three particle flow charged hadrons in the jet. Neutral pion decays are identified in the form of strips of particle flow photons in the ϕ dimension. Several decay topologies are considered. These include a single charged hadron with zero, one or two strips as well as three charged hadrons all emerging from a common secondary vertex. In order to reconstruct the four momentum of the tau lepton, the charged hadrons are assumed to be pions, and depending on the decay mode, they are required to be consistent with the masses of the intermediate meson resonances such as ρ and a_1. To improve the purity of the tau candidates, certain isolation requirements are imposed on the presence of additional charged hadrons and photons above a certain p_T threshold in a cone of radius $\Delta R = 0.5$ around the τ-direction in the $\eta - \phi$ plane. The tau efficiency expected from simulation for three working points is shown in Fig. 2.15.

2.3.6 B Jet Tagging

Jets originating from bottom quarks are identified by exploiting the fact that B hadrons have a relatively long lifetime, with $c\tau$ typically in the range of 400 microns, when compared to the impact parameter resolution offered by the CMS tracker. The impact parameter is the distance from the primary vertex to a given track at its point of closest approach to the vertex. A useful quantity in tagging b jets is the impact parameter significance which is the value of the measured impact parameter relative to its uncertainty. Moreover, a sign can be assigned to the impact parameter which is taken from the sign of the dot product between the jet axis and the vector from the

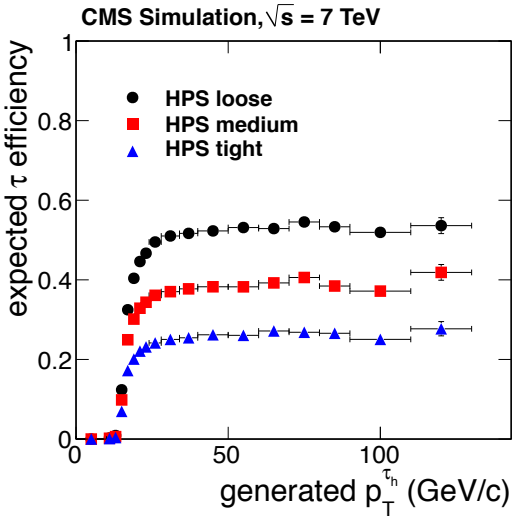

Figure 2.15 Tau reconstruction efficiency for 'loose', 'medium' and 'tight' working points which are tuned to have a fake rate of 1%, 0.5% and 0.25% respectively from the QCD background [140].

primary vertex to the point of closest approach. When a long-lived particle such as a B hadron decays, the resulting tracks typically have a large, positive impact parameter significance.

Several algorithms are employed in CMS to tag jets originating from b quarks [141]. In the simplest case, the impact parameter of tracks associated with a jet is used as a discriminator to identify b jets. The 'Track Counting High Efficiency' (TCHE) algorithm uses the impact parameter significance of the track with the second highest impact parameter significance to tag b jets. To have a higher purity of b jets, the track with the third highest impact parameter significance is used instead, resulting in the 'Track Counting High Purity' (TCHP) tagger. Another approach is to construct the overall probability of tracks associated to a given jet to originate from the primary vertex and to use this probability as a discriminator. This is the idea behind the 'Jet Probability' (JP) algorithm. A variation of this approach is to consider the the probability of the four most displaced tracks in a jet to originate from the primary vertex. This is motivated by the fact that the decay of a b hadron typically produces five tracks. This is known as the 'Jet B Probability' (JBP) algorithm.

The decay of a long-lived particle is also characterized by the presence of a secondary vertex. Such a secondary vertex may be reconstructed from tracks associated with a jet. The signed decay length significance of the secondary vertex with respect to

the primary vertex can serve as a discriminator to identify b jets. This is known as the 'Simple Secondary Vertex' (SSV) tagger. Depending on whether a minimum of two or three tracks are required in the construction of the secondary vertex, the SSV tagger can be used to yield high efficiency (SSVHE) or high purity (SSVHP). Typically, a mass constraint is imposed on the secondary vertex to remove vertices from K, Λ decays or photon conversions.

Finally, to achieve the most optimal discrimination between b jets and other light jets, a 'Combined Secondary Vertex' (CSV) tagger has been constructed which combines the information from secondary vertices as well displaced tracks into a single discriminant. The b-tagging performance of all the different algorithms is summarized in Fig. 2.16.

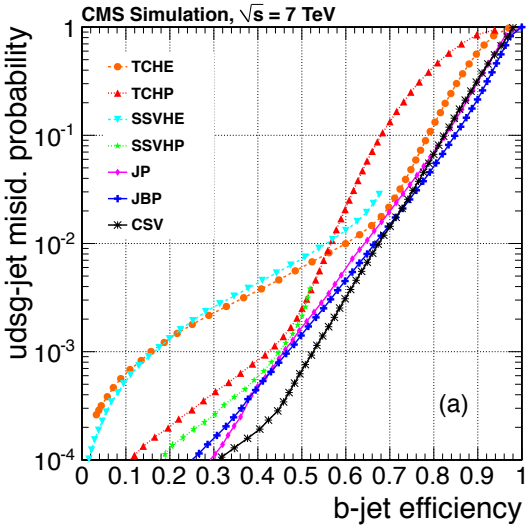

Figure 2.16 Performance curves showing b-jet identification efficiency v/s the rate of mistagging jets from light quarks and gluons as b jets [141].

2.3.7 Reconstruction of Missing Transverse Energy

Neutrinos cannot be reconstructed in a detector like CMS since they rarely ever interact with any matter. So while direct detection of neutrinos, or similar other weakly interacting particles that may possibly exist in nature, is not possible their presence can be inferred from the momentum imbalance that they create in an event by flying away undetected. In hadron colliders, we have seen that the total longitudinal momentum of the interacting partons is not known a priori. However, given that the initial momentum

of the partons is along the beam direction the total momentum in the plane transverse to the beam axis must be zero before and after the collision. As a result, if neutrinos are produced in an event, the fact that they remain undetected implies that the transverse vector sum of the momenta of all the detected particles will not add up to zero. In fact, the negative of a such a vector sum gives the total transverse momentum of the escaping neutrinos. This is known as missing transverse energy or E_T^{miss}. We have seen that the particle flow algorithm captures the flow of energy through the detector. E_T^{miss} is therefore computed simply as the negative vector sum of all the particle flow candidates in a given event [131].

Unlike other physics objects that we have discussed, E_T^{miss} is truly a global variable i.e. its resolution depends on how well all the physics objects are reconstructed in the detector. Fluctuations in the p_T measurements of all the particle-flow candidates add up to degrade the measurement of E_T^{miss}. Hence, E_T^{miss} resolution decreases with an increase in detector activity as shown in shown in Fig. 2.17.

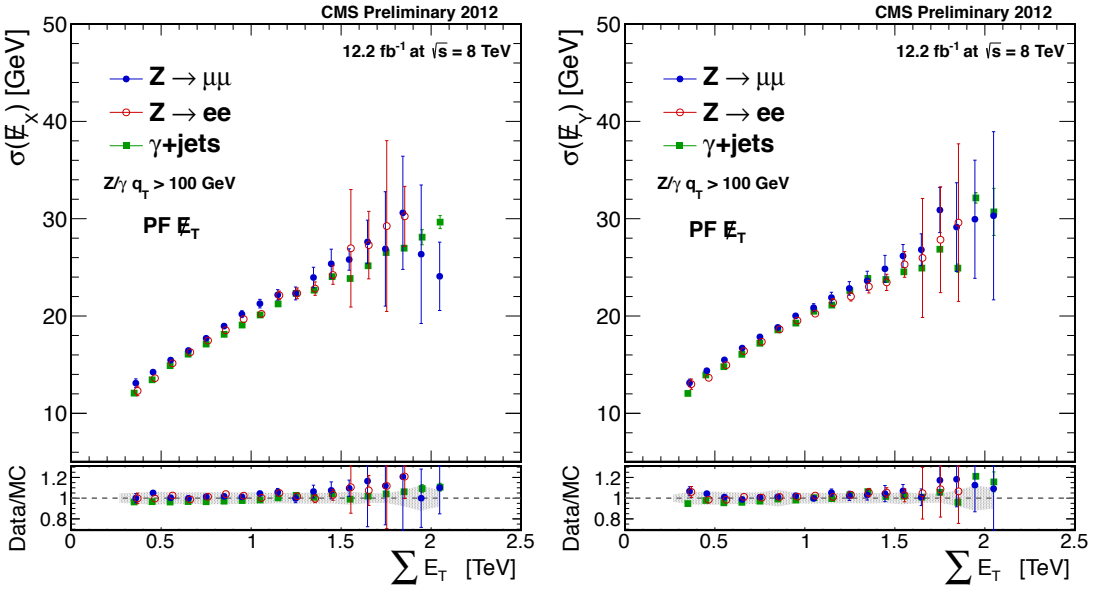

Figure 2.17 Absolute resolution of the x (left) and y (right) components of E_T^{miss} as a function of the total transverse energy reconstructed in the detector [142].

2.3.8 Impact of Pileup

In the high luminosity environment of the LHC several proton-proton interactions occur simultaneously during a bunch crossing. In 2011, an average of 10 such

interactions occurred per LHC bunch crossing. The number increased to 21 in 2012. Fig. 2.18 shows the luminosity recorded in 2012 as a function of the average number of pileup interactions per bunch crossing. We can see that the distribution extends beyond 40 pileup interactions. Fig. 2.19 shows the display of a recorded event with as many as 78 reconstructed primary vertices. These overlapping interactions are also known as 'in-time' pileup interactions since they occur concurrently with a given hard interaction. But there is also another kind of pileup. Some of the sub-detectors allow data to be read in an extended time window. This causes some energy from the preceding and succeeding events to penetrate into the measurement of a given event. Such an overhang of energy from neighboring events is termed as 'out-of-time' pileup. The impact of out-of-time pileup in the first run of the LHC has been considerably smaller than the in-time pileup.

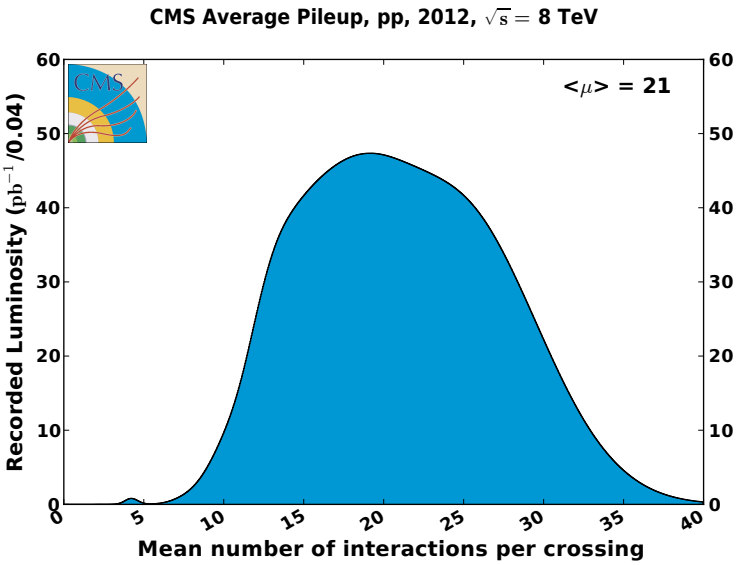

Figure 2.18 Distribution of the luminosity recorded in 2012 as a function of the average number of pileup interactions per bunch crossing.

We saw in Fig. 2.17 how the E_T^{miss} resolution gets degraded with increase in detector activity. Pileup also affects the momentum determination of physics objects which rely on calorimteric information. The p_T of jets, for instance, needs to be corrected to account for additional energy from pileup which gets reconstructed as a part of the jet. We discussed this as the L1 correction in the section on jet reconstruction. Fig. 2.20 shows the p_T correction that needs to be applied to jets as a function of the number of

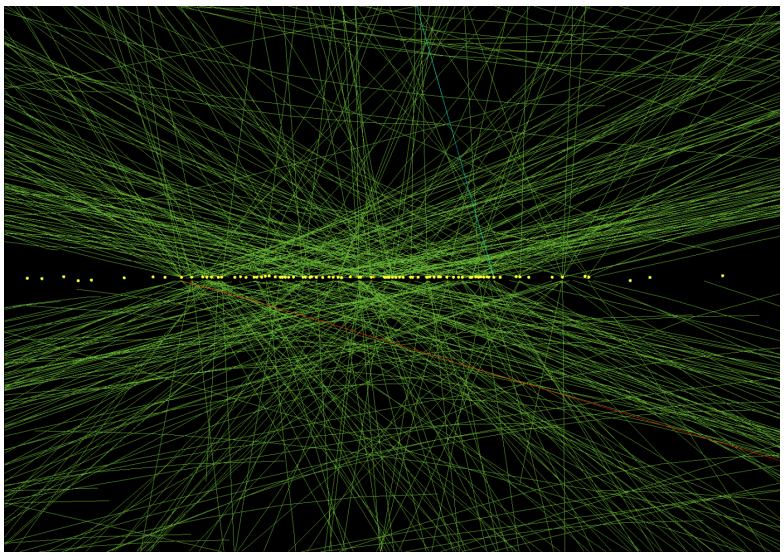

Figure 2.19 Display of an event with 78 reconstructed primary vertices.

reconstructed primary vertices. The energy of electrons and photons also needs to be corrected for the pileup energy that gets captured in the ECAL superclusters.

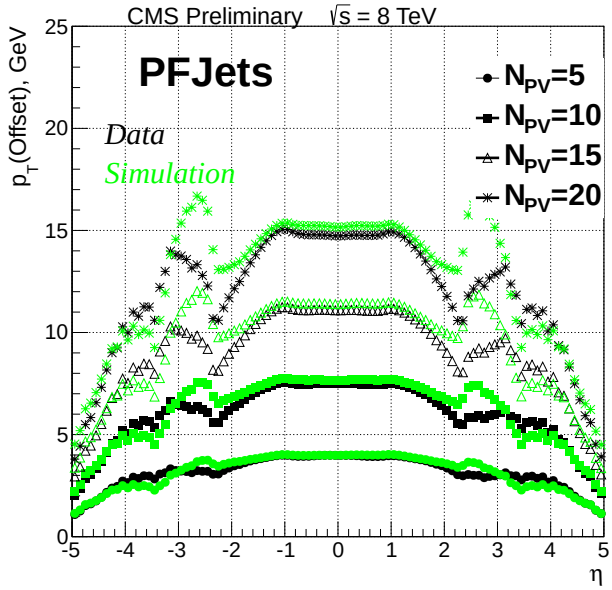

Figure 2.20 The L1 pileup correction for anti-k_{T} particle flow jets with a distance parameter of 0.5, plotted as a function of jet pseudorapidity in data (black) and simulation (green).

Apart from affecting the p_T measurement of jets, pileup can also throw up additional jets in the event. It is quite possible that the energy spewed by multiple pileup interactions overlaps to mimic a hard jet. It can be shown that the probability for such an overlap is proportional to the square of the number of pileup interaction. Therefore,

at high pileup we have to devise a strategy to separate the 'pileup jets' from the jets that are produced in the hard interaction under consideration. The pileup jets are identified with a multivariate discriminant that takes into several variables that distinguish the pileup jets from a 'real' jet [143]. These variables can be categorized into two types - track based variables which look at the compatibility of the charged candidates in a jet with the primary vertex associated with the primary interaction (see the end of Sec. 2.3.1 to understand how this primary vertex is chosen), and shape based variables that look at how the energy is geometrically distributed in the jet. Fig. 2.21 shows the distribution of the multivariate discriminant for jets in the central region of the detector.

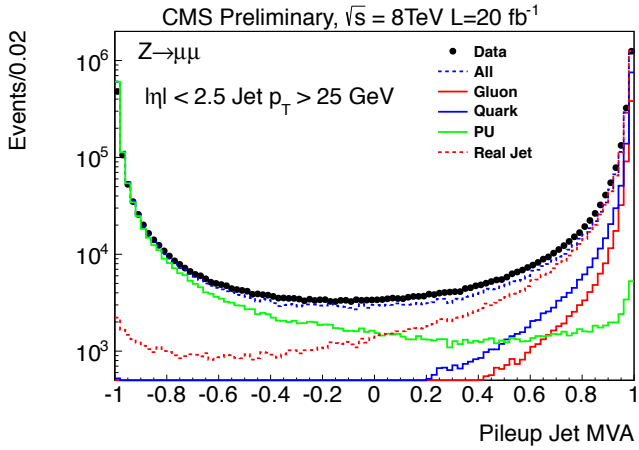

Figure 2.21 Distribution of the multivariate discriminant used to identify pileup jets, shown for anti-k_{T} particle flow jets with a distance parameter of 0.5 produced in the central region of the detector ($|\eta| < 2.5$) and having $p_T > 25$ GeV.

Certain key physics processes result in the production of leptons and photons that are isolated. An isolated particle has very little activity in its immediate vicinity. Isolation is the measure of energy in a small neighborhood of a particle. A lepton produced in the decay of a W or a Z boson is typically isolated, while a particle inside a QCD jet is typically surrounded by a considerable amount of energy, and hence is not isolated. Isolation serves as an extremely important discriminant against QCD background. The presence of pileup however, degrades this discrimination. Pileup events spew energy uniformly across the detector. As a result, particles which would be isolated in the absence of pileup, pick up this additional energy in their neighborhood. Corrections have to be made to account for pileup in the measure of isolation of a given particle. In the case of charged particles which enter the isolation sum, the tracks are

required to be consistent with the interaction vertex that is associated with the hard interaction (see the end of Sec. 2.3.1 to understand how this primary vertex is chosen). In the case of isolation computed from calorimetric energy, the overall ambient energy is computed on an event-by-event basis from the transverse energy density (ρ) of soft jets and an appropriate correction is applied. This is conceptually similar to the L1 correction that is applied to jets and is often referred to as the 'ρ-correction'. Fig. 2.22 shows how ρ and the isolation sum increases as a function of the number of reconstructed vertices in the 8 TeV collision data. We can also see how the isolation sum flattens out, thus becoming independent of pileup, when the ρ-correction is applied. An alternate approach to correct the isolation sum for pileup contamination is referred to as the '$\Delta\beta$-correction'. The basic idea behind this approach is the fact there are twice as many charged hadrons produced on average in QCD interactions as there as neutral hadrons. Therefore, one can compute the energy sum of all the charged particles falling in the isolation region that are not consistent with the interaction vertex, and assume half of this sum to be the ambient neutral energy due to pileup.

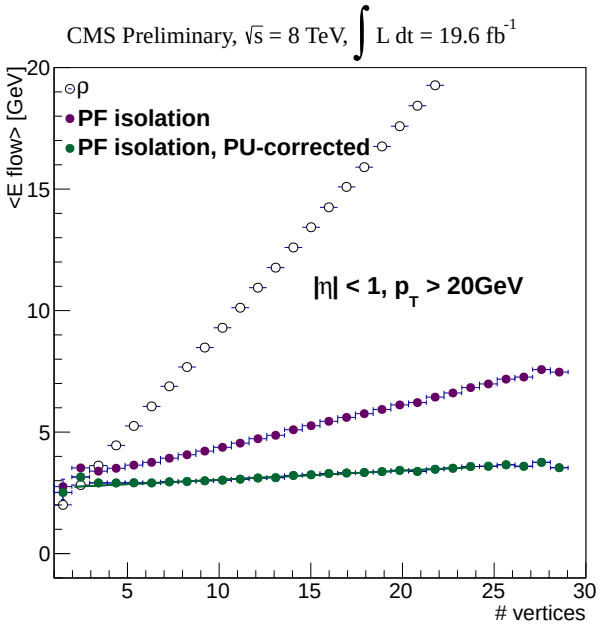

Figure 2.22 The transverse energy density ρ (hollow marker) is shown as a function of the number of reconstructed primary vertices in the 8 TeV collision data. The figure also shows the isolation energy around electrons in $Z \to e^+e^-$ decays both with (green marker) and without (purple marker) the ρ correction.

2.4 Event Simulation

Simulations play an extremely important role in the design and execution of every physics analysis. They help in constructing a realistic model of the experiment thereby enabling a detailed investigation of the signal and background processes that are expected to be encountered in a given analysis. There are dedicated software programs called event generators that can simulate a wide range of physics interactions which occur in particle collisions. The key steps in this process of event generation are summarized below.

2.4.1 Hard Interaction

Event simulation starts with the hard interaction that occurs between partons when the hadrons collide. Event generators can typically evaluate the differential cross-section of a partonic interaction at LO (e.g. MadGraph [144]) or NLO (e.g. POWHEG [145]) in perturbation theory. This parton level differential cross-section when convolved with the PDFs (see eq. 1.20) and integrated over the phase space of the final state particles, gives the total cross-section of the hard scattering process. Event generators employ the Monte Carlo technique [146] to perform the convolution and the phase space integration. The idea is to randomly sample discrete points in the momentum space of the final state particles in accordance with the distribution of the integrand. Each of these discrete points then represents an event in which the outgoing particles are assigned certain specific momenta.

2.4.2 Parton Showering

If the final state particles of a hard interaction carry color charge, they can radiate gluons just as electrically charged particles radiate photons. Since the gluons themselves carry color charge, they can further radiate gluons or split into a quark - antiquark pair. This process of parton splitting ($q \rightarrow q + g$, $g \rightarrow g + g$, $g \rightarrow q + \bar{q}$) produces a shower of particles in the event. Certain generators such as PYTHIA [147], SHERPA [148], HERWIG [149] have the capability of simulating these showers from the products of the hard interaction.

2.4.3 Underlying Event

When a hard scattering occurs, the structure of the interacting hadrons gets completely destroyed. The hadronic remnants that are left after we separate the hard process are termed as the 'Underlying Event' (UE). We need to add the UE to the simulation of a hard interaction in order to complete the description of an event. The UE model is derived empirically from the data collected at hadron colliders. The simulations that are used in this thesis employ the 'Z2 tune' of PYTHIA [150] which is based on the results of early data collected by CMS.

2.4.4 Hadronization

As the parton shower evolves, the momentum transfer scale in parton splitting goes on decreasing. A point is reached, where the QCD interactions become non-perturbative. The event generators terminate the shower at this stage and the partons are hadronized to form color singlet final states which we can observe experimentally. The resulting hadrons may themselves be unstable and are suitably decayed into other particles.

2.4.5 Detector Simulation

The event generators essentially produce a list of outgoing particles for a given physics process, and each particle is assigned a four-momentum. These particles are then propagated through a detailed simulation of the detector which tries to model, as accurately as possible, the interactions of these particles with all the detector elements. A dedicated software package called GEANT [151] is used for this purpose. A full blown detector simulation enables us to transform the four-momenta of generated particles into the digital signals that we expect to readout during data-taking. These can then be processed through the event reconstruction chain that was discussed in Sec. 2.3 to obtain a realistic experimental description of a given physics interaction.

Chapter 3

Concepts of Statistical Analysis

The previous chapters provided the essential theoretical and experimental inputs to search for the Higgs boson. What is still needed is a statistical toolkit that can be used to interpret the data collected in the experiment in a rigorous and quantitative manner. While a thorough exposition of these statistical techniques is beyond the scope of this thesis, an attempt is made to expose the key underlying principles in this chapter. Various statistical concepts and techniques that will be used for the Higgs analyses in the subsequent chapters are developed and presented here so that this chapter can serve as an explanatory reference for them when they are employed to quantify the analysis results.

3.1 Likelihood and Parameter Estimation

A particle collider is essentially a machine that keeps on repeatedly performing one single experiment - that of colliding two particles at a certain fixed energy. The measured outcome of this repeated experiment, however, varies unpredictably from one collision to another. One fundamental source of this randomness is quantum mechanics, which by its very nature is non-deterministic. Another source is the experimental apparatus itself, which may be prone to errors that could induce random variations in measurements. This means that we have to construct a probabilistic model to interpret the observed data. The mathematical representation of this model is called the 'likelihood function' or simply the 'likelihood'. Loosely speaking, the likelihood function

yields a value that is proportional to the probability of observing a certain set of data, given the parameters of the underlying model.

As an illustration let us consider a simple counting analysis. As the name suggests such an analysis basically counts the number of events of a certain type in data. Some of these events come from a signal process that is of interest to us. The remaining events belong to the background that has infiltrated our selection. Let us assume that we expect an average of b events in our dataset. We are interested in estimating the average rate of signal events using our data. Let us say that the signal rate is predicted to be s from certain a priori estimates. We define a 'signal-strength modifier' μ such that we can write the total expected event rate as $\mu s + b$. Our goal is then to get an estimate of μ from data which would help us measure the average signal rate in relation to our initial prediction. If we observe N events in our dataset then the likelihood function can be written in terms of the Poisson distribution as follows

$$\mathcal{L}(\text{data}|\mu) = \frac{(\mu s + b)^N e^{-(\mu s+b)}}{N!} \tag{3.1}$$

$\mathcal{L}(\text{data}|\mu s + b)$ gives the probability of observing N events in data assuming an average rate of $\mu s + b$. Given this probabilistic interpretation of $\mathcal{L}$, we can say that the best estimate of μ is that value of μ (denoted by $\hat{\mu}$) which maximizes the likelihood. In practice, it is more convenient to write the likelihood in terms of a χ^2 function which is defined as $\mathcal{L} = e^{-\chi^2/2}$. Then $\hat{\mu}$ becomes the value of μ which minimizes the χ^2 function.

We can also use the χ^2 distribution of μ to determine the uncertainty on the estimate $\hat{\mu}$. The uncertainty associated with a parameter estimate is indicative of a 'confidence interval' with a certain 'confidence level' (CL) or 'coverage'. This confidence interval is itself estimated from the data that we observe. The meaning of a confidence interval for parameter μ at some $X\%$ confidence level can be understood as follows. If the given measurement were to be repeated a large number of times, and if we were to derive the confidence interval for each of these measurements, then the true value of parameter μ, let's call it $\tilde{\mu}$, would be contained in this interval in $X\%$ of the measurements.

When the sample size is sufficiently large ($N \gg 1$) the central limit theorem [152] implies that the χ^2 distribution becomes parabolic (or alternatively the likelihood becomes Gaussian). In the Gaussian limit, the central confidence interval with a coverage

of M standard deviations ($\sigma_{\hat{\mu}}$) around $\hat{\mu}$ is given by the following relation [153]

$$\chi^2(\hat{\mu} \pm M\sigma_{\hat{\mu}}) - \chi_0^2 = M^2 \tag{3.2}$$

In particular the case $M = 1$, corresponds to the 68.3% confidence interval which we can estimate graphically by obtaining the μ values where the value of $\chi^2 - \chi_0^2$ becomes equal to 1. Similarly we can obtain the 95.4% confidence interval from the μ values at which $\chi^2 - \chi_0^2$ becomes equal to 4. However, instead of 95.4% it is customary to quote the 95% confidence interval which is obtained by setting $\chi^2 - \chi_0^2$ equal to 3.84. We must always be mindful of the fact that the confidence intervals obtained with this approach match the classical confidence intervals only in the Gaussian limit. Nevertheless, it can be shown that these intervals do approximate the classical confidence intervals even if the likelihood is non-Gaussian [154, 155]. As an illustration Fig. 3.1 shows a χ^2 distribution as a function of μ. We see that the minimum of the distribution lies at $\mu = 1$ while it crosses the value of 1 at $\mu = 0.86$ and $\mu = 1.14$. Therefore, we can write the measured value of μ as $\hat{\mu} = 1.0 \pm 0.14$ at 68% CL.

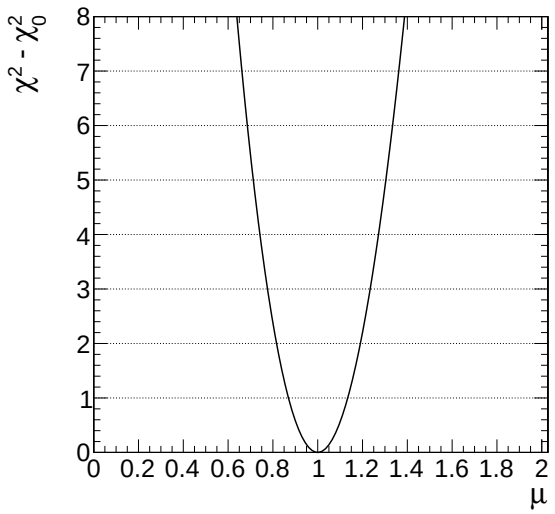

Figure 3.1 An example of a χ^2 distribution.

3.2 Analysis Types

The counting analysis that we have considered may not be the most optimal approach to measure μ. We haven't made use of any discriminating features between

the signal and the background. Typically we can find some kinematic variable whose shape is different between signal and background. If we bin our data in this variable, we would find certain bins to have a much higher fraction of expected signal events as compared to the counting analysis. The enrichment of the signal content helps in improving the measurement. In general, if we divide our dataset into n bins such that the expected signal and background rates in the i^{th} bin are s_i and b_i respectively, then the likelihood of this binned analysis is given by

$$\mathcal{L}(\text{data}|\mu) = \prod_i \frac{(\mu s_i + b_i)^{N_i} e^{-(\mu s_i + b_i)}}{N_i!} \tag{3.3}$$

We can think of a binned analysis as a statistical combination of n independent measurements. In fact the notion of bins can be quite generic. The bins need not necessarily correspond to a distribution of a discriminating variable. We can treat the different channels of a signal process, e.g. the various decay modes of the Higgs boson, as individual bins. Combining the results from all these bins then amounts to performing a statistical combination of all the different channels.

When we bin the distribution of a certain variable, we smear out the discrimination between signal and background within every bin. Therefore, we still lose out on some discriminating power when it comes to events within a single bin. We can make the binning irrelevant and perform an unbinned analysis if we know the underlying analytical shapes of the signal and background distributions. Let us assume that the signal and background distributions of a certain discriminating variable m are described by probability distribution functions (p.d.f.s) $f_s(m)$ and $f_b(m)$ respectively. We start by constructing binned distributions of these p.d.f.s with bins of extremely small size Δm. Let us assume these bins to be so small that each of them can contain either zero or one event. If s and b are the total signal and background rates then the expected signal in the i^{th} bin is given by $sf_s(m_i)\Delta m$ while the expected background is given by $bf_b(m_i)\Delta m$ (we can take m_i to be the center of he i^{th} bin). We can now rewrite eq. 3.3 as

$$\mathcal{L}(\text{data}|\mu) = \prod_i \frac{(\mu s f_s(m_i)\Delta m + b f_b(m_i)\Delta m)^{N_i} e^{-(\mu s f_s(m_i)\Delta m + b f_b(m_i)\Delta m)}}{N_i!} \tag{3.4}$$

Using the fact that $N_i = 0$ or 1, the above equation reduces to the following

$$\mathcal{L}(\text{data}|\mu) = (\Delta m)^P (\prod_j \mu s f_s(m_j) + b f_b(m_j)) e^{-(\mu s + b)} \tag{3.5}$$

where P is the total number of small bins in which we have divided the distribution, and the product is taken over every event of the dataset. Given that $(\Delta m)^P$ is a constant multiplicative factor it will not play a role in any inference that we make using the likelihood. Therefore, we can drop it from the likelihood definition. The unbinned likelihood can now be written as follows

$$\mathcal{L}(\text{data}|\mu) = (\prod_j \mu s f_s(m_j) + b f_b(m_j)) e^{-(\mu s + b)} \tag{3.6}$$

In general, one can say that an unbinned analysis gives the most optimal results. However, it is possible to perform such an analysis only when the shape of the discriminating variable is known analytically (in other words we need to know the signal and background p.d.f.s). This may not always be possible. However, we saw in the derivation of the likelihood function that an unbinned analysis can be thought of as a binned analysis in the limit of a large number of bins. Therefore, if an unbinned analysis is not possible, we can perform a binned analysis with an optimal choice of binning such that further increase in the number of bins does not substantially improve performance.

3.3 Multiple Parameters of Interest

So far, we have restricted ourselves to the measurement of a single parameter, namely μ. But an analysis may have more than one parameter of interest. Let us consider an additional parameter m_0 that we are interested in measuring. This could be, for instance, the mass of the signal particle. To get the best fit values of both μ and m_0 we need to find the point $(\hat{\mu}, \hat{m_0})$ in the $\mu - m_0$ plane at which the χ^2 function of the likelihood $\mathcal{L}(\text{data}|\mu, m_0)$ is at a minimum.

Next, we need to measure the uncertainties on these parameters. Let us take the case of parameter m_0. In order to determine the uncertainty on $\hat{m_0}$ we construct a 'profile likelihood' denoted by $\mathcal{L}(\text{data}|\hat{\hat{\mu}}, m_0)$. This likelihood is constructed such that

for a given value of m_0 we use that value of μ, denoted by $\hat{\hat{\mu}}$, which maximizes the likelihood at m_0. Let us define the χ^2 function of the profile likelihood as follows

$$\chi^2_p = -2\log(\frac{\mathcal{L}(\text{data}|\hat{\hat{\mu}}, m_0)}{\mathcal{L}(\text{data}|\hat{\mu}, \hat{m_0})}) \tag{3.7}$$

The χ^2_p function by construction goes to zero at its minimum. We can determine the 68% confidence interval by scanning χ^2_p and finding the values of m_0 at which $\chi^2_p = 1$. In this construction, the signal strength is said to be 'profiled'. However, instead of profiling μ, we may be interested in finding all the values of μ and m_0 that fall within a certain confidence region. Such a confidence region will define a certain area in $\mu - m_0$ space. While the confidence interval for a single parameter is defined by two boundary points, the confidence region for two parameters is defined by a boundary contour. Fig. 3.2 shows an illustrative 2-dimensional scan of a χ^2 function in the $\mu - m_0$ space. In the large sample limit, the χ^2 distribution for two parameters becomes a paraboloid. The conditions which give the the contours of the 68% and 95% confidence regions in this paraboloid are $\chi^2(\mu, m_0) - \chi^2_0 = 2.30$ and $\chi^2(\mu, m_0) - \chi^2_0 = 5.99$ respectively [153]. These are indicated by the solid and dashed contours in Fig. 3.2.

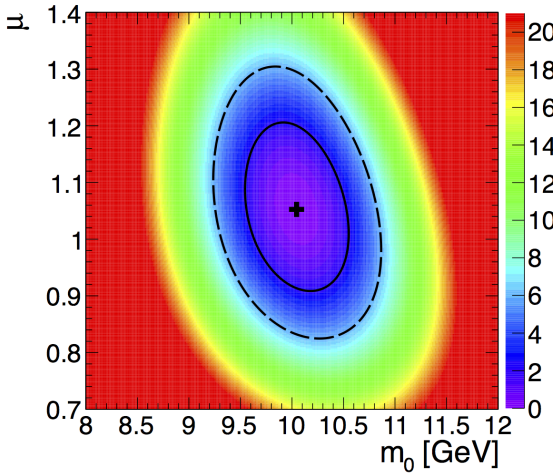

Figure 3.2 An example χ^2 distribution plotted as a function of μ and m_0. The solid and dashed contours in this figure indicate the 68% and 95% confidence regions in the $\mu - m_0$ space.

3.4 Systematic Uncertainties

In all our discussion up to this point we have assumed that inputs to the model used to construct the likelihood are known without any uncertainty. For example, we have assumed that the average event rates for signal and background are known precisely. We have also assumed that the signal and background p.d.f.s in the case of an unbinned analysis are known exactly. As a result, the only source of uncertainty in the measured parameters is statistical. In other words, we could arbitrarily reduce the uncertainty on these parameters by increasing the size of our dataset. However, in real life experiments the signal and background models are not known with such exactitude. In fact, there is no single physical quantity that we know with infinite precision. Every input that goes into the construction of our likelihood has some uncertainty associated with it. Some inputs may be known with much greater precision than others. The uncertainties on such inputs may not have a noticeable impact on the analysis result, and so they may be ignored. One key challenge in experimental analysis is to determine all the relevant sources of systematic uncertainties associated with the inputs that go into the construction of the statistical model. How these uncertainties are determined depends on the details of each analysis. Here, let us discuss how systematic uncertainties get included in the likelihood and how they impact the analysis result.

3.4.1 Normalization Uncertainties

One important class of systematic uncertainties are those which are associated with the event rates. These are often termed as normalization uncertainties. In our example, it may be the case that the expected number of background events b are known with a relative uncertainty given by σ_b. This could be attributed to the uncertainty involved in the theoretical computation of the background cross-section as we discussed at the end of section 1.3.3. Similarly, let us also assume a relative uncertainty σ_s on the expected number of signal events s. There are three possible ways of relating systematic uncertainties with one another. If the sources of these uncertainties on the signal and background rates are unrelated, the two uncertainties should be independent of each other. On the other hand it is conceivable that some uncertainties are fully correlated

between the signal and the background. For example, let us assume a relative uncertainty σ_c on the estimated luminosity corresponding to the data that we have analyzed. Since the expected event rates are proportional to the luminosity, any error in the luminosity measurement will have a simultaneous impact on both the signal and background rates (unless, the background is estimated from the observed data itself - but let us ignore this nuance in our case). A third possibility is that of a given systematic uncertainty being completely anti-correlated. For example, if we decide to split our analysis into two bins, there exists the possibility of bin migration wherein we are not certain whether we are mis-placing a certain fraction of events in one bin instead of the other. In such a case, the corresponding systematic uncertainty would be completely anti-correlated between the two bins since over counting of one bin implies underestimation of the other.

Let us now consider how to incorporate these uncertainties in our likelihood. The expected signal and background yields (s and b) are treated as fixed parameters of our statistical model. In order to allow a variation of these yields, we need to introduce additional floating parameters. So, to introduce the uncertainty σ_b on the background yield, we redefine b as $b(\theta_b) = b(1 + \sigma_b\theta_b)$. When we say that the background yield has a relative uncertainty σ_b we imply a certain constraint on the allowed variation of b. This constraint, in the frequentist context, translates into an auxiliary measurement of parameter θ_b. Such an auxiliary measurement may be real - it may correspond to a measurement of the background in a control region - or it may be purely symbolic. For instance, we can construct an auxiliary measurement of a certain variable $\tilde{\theta}_b$ such that $\tilde{\theta}_b$ obeys a Gaussian p.d.f. $p(\tilde{\theta}_b|\theta_b)$ that is centered at θ_b and has unit width. By introducing $p(\tilde{\theta}_b|\theta_b)$ multiplicatively into the likelihood we essentially impose a Gaussian constraint on θ_b. Similarly, for the signal we have the uncorrelated uncertainty σ_s which can be introduced as $s(\theta_s) = s(1 + \sigma_s\theta_s)$. The associated parameter θ_s can then be constrained by another Gaussian function $p(\tilde{\theta}_s|\theta_s)$. The uncertainty σ_c that we have assumed to be correlated between the the signal and background enters as a multiplicative factor for both the signal as well as the background yields. The signal yield now becomes $s(\theta_s, \theta_c) = s(1 + \sigma_s\theta_s)(1 + \sigma_c\theta_c)$ and the background yield becomes $b(\theta_b, \theta_c) = b(1 + \sigma_b\theta_b)(1 + \sigma_c\theta_c)$. The likelihood function takes the following form

$$\mathcal{L}(\text{data}|\mu, \theta_s, \theta_b, \theta_c) = \text{Poiss}(\text{data}|\mu s(\theta_s, \theta_c) + b(\theta_b, \theta_c))L(\theta s, \theta_b, \theta_c) \tag{3.8}$$

where $\text{Poiss}(\text{data}|\mu s(\theta_b, \theta_c) + b(\theta_b, \theta_c))$ represents the 'Poissonian' or the statistical part of the likelihood that we elaborated in the earlier sections while $L(\theta s, \theta_b, \theta_c) = p(\tilde{\theta}_b|\theta_b) \times p(\tilde{\theta}_s|\theta_s) \times p(\tilde{\theta}_c|\theta_c)$ is the component of the likelihood which represents the auxiliary measurements that help to constrain $\theta_s, \theta_b, \theta_c$. The θ parameters are known as 'nuisance parameters' as opposed to μ which is a 'parameter of interest' or the parameter that we are aiming to measure in our analysis.

At this point, it should be mentioned that we may not know the exact nature of the auxiliary p.d.f.s. The shapes that we assign to these p.d.f.s are typically some educated assumptions. The Gaussian p.d.f. that we used to model the auxiliary measurements actually has an unpleasant feature that it is non-zero even for values of θ that make the yield negative. Therefore, it needs to be truncated at some point to zero. To avoid such pathologies one can rewrite the signal and background yields as $s(\theta_s, \theta_c) = s(1 + \sigma_s)^{\theta_s}(1 + \sigma_c)^{\theta_c}$ and $b(\theta_b, \theta_c) = b(1 + \sigma_b)^{\theta_b}(1 + \sigma_s)^{\theta_s}$. The θ parameters are still associated with the same Gaussian auxiliary measurements and may take on negative values, but the yield always remains positive. It can be shown that this redefinition is equivalent to changing the auxiliary measurement from a Gaussian to a log-normal p.d.f. In the discussion that follows in the subsequent chapters, we will always use the log-normal model for normalization uncertainties unless specified otherwise.

We have seen that in order to incorporate systematic uncertainties into the likelihood we need to introduce additional nuisance parameters which make the likelihood multi-parametric. Therefore, to measure the signal strength μ we make use of the profile likelihood that was discussed in section 3.3 whose χ^2 function can be written as follows

$$\chi^2_p = -2\text{log}(\frac{\mathcal{L}(\text{data}|\mu, \hat{\hat{\theta}})}{\mathcal{L}(\text{data}|\hat{\mu}, \hat{\theta})}) \tag{3.9}$$

where θ represents all the nuisance parameters of the model. The $\hat{\mu}$, $\hat{\theta}$ in the denominator of χ^2_p represent the best-fit values of the signal strength and the nuisance parameters, while $\hat{\hat{\theta}}$ represents the profiled value of the nuisance parameters with the signal strength

fixed at μ.

3.4.2 Shape Uncertainties

In the case of an unbinned analysis we can also assign uncertainties to the parameters of the signal and background p.d.f.s. Let us imagine that our signal line shape can be parametrized by the Gaussian distribution. We need two parameters to define the Gaussian p.d.f. The width of the Gaussian (σ) is indicative of the detector resolution (assuming the natural width of the resonance to be very small). Depending on how well we understand the detector response, we should assign a resolution uncertainty on σ. The other parameter of the Gaussian is the location of the peak (m_0). It may be possible that our measurement introduces a bias or a shift in the peak position with respect to its true value. We should then assign an uncertainty to m_0 in order to model our understanding of this bias. This is referred to as the scale uncertainty δ_m. We can implement this uncertainty by redefining the signal p.d.f. as $e^{-(m-m_0(1+\delta_m\theta_m))^2/2\sigma^2}$ where θ_m is a nuisance parameter that we constrain with a Gaussian auxiliary measurement. Fig. 3.3 shows an illustrative χ^2 distribution of m_0 both with and without the scale uncertainty. We see that the χ^2 distribution broadens on introducing the scale uncertainty. This is a general effect of introducing systematic uncertainties. The broadening of the χ^2 distribution results in an increase in the total uncertainty (σ_{tot}) on the measured parameter. We can divide this total uncertainty into a statistical (σ_{stat}) and a systematic (σ_{syst}) component. The σ_{tot} and σ_{stat} values can be obtained from χ^2 distributions obtained with and without introducing systematics. Then assuming that σ_{tot} is given by the quadrature sum of σ_{stat} and σ_{syst}, i.e. $\sigma_{tot}^2 = \sigma_{stat}^2 + \sigma_{syst}^2$ we can obtain the systematic uncertainty as $\sigma_{syst} = \sqrt{\sigma_{tot}^2 - \sigma_{stat}^2}$.

In the case of a binned analysis, we do not have signal and background shapes in analytical form. But we can think of the bins as constituting a histogram. We may have a source of uncertainty which may cause a coherent variation in the contents of all the bins (e.g. jet energy scale when dealing with quantities depending on jet p_T). This will appear as a distortion in the shape of the histogram. In order to incorporate the systematic uncertainty due to this shape distortion we start with the best estimate of the binned shape, which can be termed as the central shape. Let η_i^0 be the content

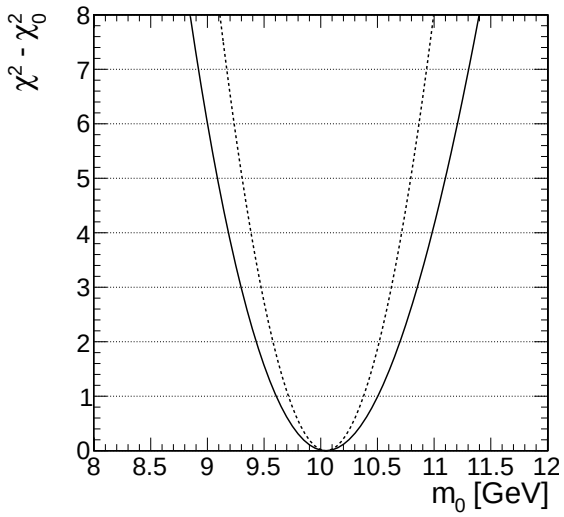

Figure 3.3 The dotted line shows the χ^2 distribution of m_0 without any systematic uncertainty. The solid line shows the χ^2 distribution after adding the scale uncertainty.

of the i^{th} bin of this histogram. We then construct two bounding histograms which correspond to $\pm 1\sigma$ variations in the binned shape. As an example Fig. 3.4 shows the central and bounding histograms for some variable x that may be used in a binned analysis. Let η_i^+, η_i^- be the contents of the i^{th} bins of these bounding histograms. We define a single nuisance parameter θ which can continuously morph the shape of the central histogram to the '+' and '-' histograms. The content of the i^{th} bin then becomes a function of θ which needs to satisfy three equations : $\eta_i(\theta = 0) = \eta_i^0$, $\eta_i(\theta = 1) = \eta_i^+$ and $\eta_i(\theta = -1) = \eta_i^-$. In order to satisfy three independent equations, we need the $\eta_i(\theta)$ function to be at least a quadratic for θ between -1 and 1.

3.5 Hypothesis Tests

The discussion up to this point has focused on using data to measure certain parameters of our physics model. But we may be interested in testing the validity of the model itself when compared to an alternative hypothesis. Generally speaking, this translates to the question - 'given two hypotheses, which is more compatible with data, and is there a way to quantify this compatibility?'. As an example we can consider two possible ways of parameterizing our signal p.d.f. One possibility is to assume a Gaussian shape $e^{-(m-m_0)^2/2\sigma^2}$. Lets call this hypothesis G. An alternate possibility is to define the signal shape using the non-relativistic Breit-Wigner function $1/[(m-m_0)^2+\frac{1}{4}\sigma^2]$. Let us

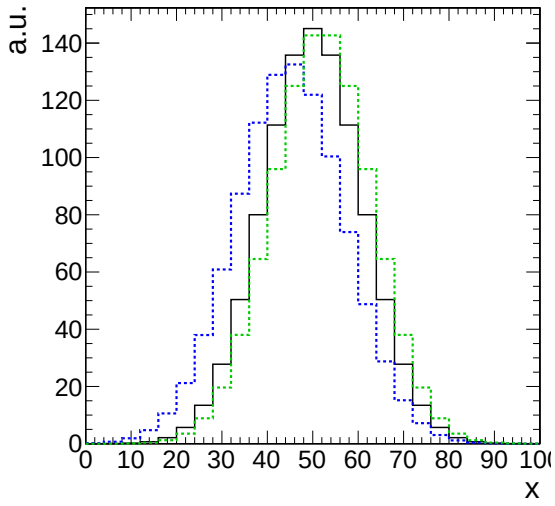

Figure 3.4 The solid black line shows the central shape of a variable x used in a binned analysis, while the dotted green and blue lines show histograms corresponding to $\pm 1\sigma$ variation in the binned shape.

call this hypothesis B. Let us assume that hypothesis G is our default or baseline choice. We then call G as the 'null hypothesis' and hypothesis B as the alternate hypothesis.

The process of hypothesis testing starts by the construction of a 'test statistic' q which is a function of the observed data. Then we determine the p.d.f. of the test statistic given hypothesis G. This is indicated as $f(q|\mathrm{G})$. Let q_{obs} be the observed value of the test statistic in data. Then the compatibility of data with hypothesis G can be expressed in terms of the p-value (p_{G}) where $p_{\mathrm{G}} = \int_{q_{obs}}^{\infty} f(q|\mathrm{G})dq$. The p-value indicates the probability of getting a value of the test statistic which is equal to or larger than q_{obs}. Therefore, a smaller p-value indicates weaker compatibility between data and the hypothesis. One can decide before-hand on a significance level denoted by α such that if $p_{\mathrm{G}} < \alpha$, the hypothesis G stands rejected. The same procedure also applies to hypothesis B.

According to the Neyman-Pearson lemma [156] the test statistic given by the likelihood ratio $\mathcal{L}_{\mathrm{G}}/\mathcal{L}_{\mathrm{B}}$ provides the maximum discrimination between hypotheses G and B. Here $\mathcal{L}_{\mathrm{G}}$ is the likelihood function obtained assuming hypothesis G while $\mathcal{L}_{\mathrm{B}}$ is the likelihood function obtained assuming hypothesis B. It is more convenient to use the log of the likelihood ratio and so we use the test statistic defined as $q = -2\ln(\mathcal{L}_{\mathrm{B}}/\mathcal{L}_{\mathrm{G}})$.

Having defined our test statistic we need to determine the p.d.f.s $f(q|\mathrm{G})$ and $f(q|\mathrm{B})$. Generally speaking, it is not possible to describe these p.d.f.s analytically. How-

ever, we can estimate their distribution by using 'toy Monte Carlo'. The idea is to generate a large number of pseudoexperiments in accordance with a certain hypothesis. So for hypothesis G we generate a large number of datasets sampled from the background-plus-Gaussian physics model. We then evaluate the test statistic $q = -2\ln(\mathcal{L}_{\mathrm{B}}/\mathcal{L}_{\mathrm{G}})$ for every one of those datasets and create a distribution of these values to get the shape of $f(q|\mathrm{G})$. We can evaluate the p-value for hypothesis G by taking the ratio of toys having $q > q_{obs}$ with the total number of toys. The same procedure then applies for $p(q|\mathrm{B})$ as well. As an illustration Fig. 3.5 shows the distributions of $f(q|\mathrm{G})$ and $f(q|\mathrm{B})$, and the value of q_{obs}. We see that hypothesis B which assumes a Breit-Wigner signal shape is disfavored compared to hypothesis G which assumes a Gaussian signal. It is customary to quote the p-values in terms of the significance Z expressed in 'sigmas' which can be obtained by the following relation

$$p = \int_{Z}^{\infty} \frac{1}{\sqrt{2\pi}} e^{-x^2/2} \tag{3.10}$$

A lower p-value translates to a higher significance. The p-value for hypothesis G in Fig. 3.5 is 0.7σ while the p-value for hypothesis B is $\sim 4\sigma$.

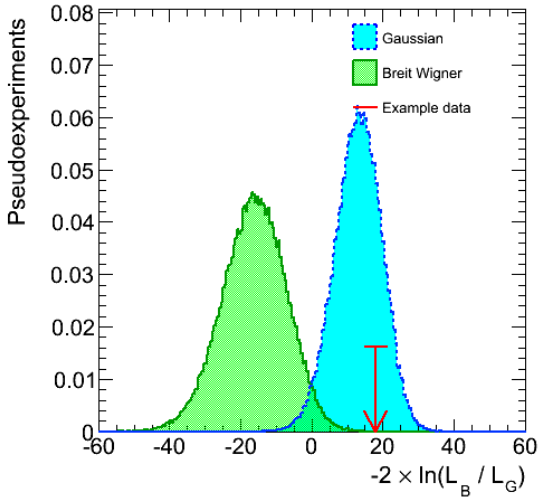

Figure 3.5 The p.d.f. of the test statistic q given hypothesis G is shown by the green distribution while the p.d.f. of q given hypothesis B is shown by the blue distribution. The arrow indicates the value of q_{obs}

In certain situations, the likelihoods $\mathcal{L}_{\mathrm{G}}$ and $\mathcal{L}_{\mathrm{B}}$ may contain floating parameters of interest which need to be fit from data. For example, we may not know the signal

strength μ before hand and we may want to estimate it from data. In that case, μ is estimated independently for each of the two hypothesis and the best fit values of μ, lets call them $\hat{\mu}_{\mathrm{G}}$ and $\hat{\mu}_{\mathrm{B}}$, are used in the likelihoods $\mathcal{L}_{\mathrm{G}}$ and $\mathcal{L}_{\mathrm{B}}$.

3.6 Quantifying Searches

So far we have assumed that the existence of the signal is not in question. What we have done is to probe and measure the properties of some known physics process which we treat as our signal. But there is an entire class of analyses whose aim is to search for new, hitherto unknown phenomena. The search for the Higgs boson is certainly a prominent case in point. In such analyses it is the very existence of the signal that is sought to be established. If an analysis claims to discover a new signal, it should be able to quantify the degree of confidence in that claim. Similarly, if an analysis does not observe any signal it needs to outline the reach of its search. In this section we discuss how the results of searches are quantified.

3.6.1 Excesses

When searching for new physics, we are essentially interested in observing a deviation from the background expectation in terms of an excess of events. In the statistical model that we have developed, this excess shows up as the signal contribution μs. Setting $\mu = 0$ corresponds to the background-only scenario. If we treat $\mu = 0$ as our null hypothesis then the presence of signal in data will reduce the p-value that we obtain from testing this hypothesis. If the p-value is sufficiently small, we can lay claim to a discovery. To perform this test we define a test statistic using the profile likelihood ratio [157]

$$q = -2\ln\frac{\mathcal{L}(\mathrm{data}|0,\hat{\hat{\theta}})}{\mathcal{L}(\mathrm{data}|\hat{\mu},\hat{\theta})} \quad \text{and } \hat{\mu} \geq 0 \tag{3.11}$$

where $\hat{\hat{\theta}}$ are the values of nuisance parameters obtained by maximizing the likelihood with $\mu = 0$. The condition $\mu \geq 0$ ensures that downward fluctuations are treated as being consistent with the background-only hypothesis. We now seek to construct the p.d.f. of the test statistic for the background-only hypothesis which is written as

$f(q|0,\hat{\hat{\theta}}_{obs})$. where $\hat{\hat{\theta}}_{obs}$ represents the values of the nuisance parameters which maximize the likelihood of the observed data for $\mu = 0$. We can construct this p.d.f. using the same toy Monte Carlo approach that was discussed in section 3.5. The p-value can then be computed using $p = \int_{q_{obs}}^{\infty} f(q|0,\hat{\hat{\theta}}_{obs})dq$. However, in the large sample limit it can be shown that the significance is given by the simple relation $Z = \sqrt{q_{obs}}$ [158] (the relation between p and Z is shown in eq. 3.10). To claim a discovery it is customary to require the significance to be larger than 5σ.

3.6.2 Upper Limits

In the absence of a significant deviation from the background expectation we need to give a quantitative answer to the following question - 'how feeble does the signal have to be to escape detection in the analysis?' We can translate this question into a hypothesis test of the signal-plus-background model. Given a certain fixed value of μ we test the compatibility of the $\mu s + b$ model with data. If the p-value is smaller than a certain significance level α (the most typical choice is 0.05) then we can reject the signal-plus-background hypothesis for that value μ. If we now keep on lowering μ we will reach a point μ_α such that the p-value for the $\mu_\alpha s + b$ hypothesis becomes equal α. Reducing the signal strength below this point will make the signal too weak to be rejected by the hypothesis test. The value μ_α is termed as the upper limit on μ at a confidence level of $1 - \alpha$. We can think of $(0,\ \mu_\alpha)$ as a one-sided confidence interval of μ at a confidence level of $1 - \alpha$. All values of μ greater than μ_α are said to excluded at $(1 - \alpha)$ CL. To perform the hypothesis test for a given μ we use the following test statistic [157]

$$q_\mu = -2\ln\frac{\mathcal{L}(\text{data}|\mu,\hat{\hat{\theta}})}{\mathcal{L}(\text{data}|\hat{\mu},\hat{\theta})} \quad \text{and } 0 \leq \hat{\mu} < \mu \tag{3.12}$$

In this case the nuisance parameters $\hat{\hat{\theta}}$ are obtained by maximizing the likelihood assuming signal strength μ. The condition $\hat{\mu} < \mu$ enforces the fact that we are measuring upper limits while the requirement $\hat{\mu} > 0$ comes from our assumption that signal can only add to the background yield. To obtain the p-value from the test statistic we need the p.d.f. $f(q_\mu|\mu,\hat{\hat{\theta}}_{obs})$. While one can obtain this distribution from toy MC, approximate

results are available in analytical form in the large sample limit [158]. In fact, the upper limit μ_α can be obtained directly from the following relation [153, 158]

$$\mu_\alpha = \hat{\mu} + \sigma\Phi^{-1}(1-\alpha) \tag{3.13}$$

where σ is the variance of $\hat{\mu}$ and Φ is the cumulative distribution function of a Gaussian with zero mean and unit width. In the case of the Higgs boson, the expected signal rate is well-defined in the SM for a given value of m_{H}, and so we expect $\mu = 1$. Therefore, if we observe $\mu_\alpha < 1$ for a certain value of m_{H} then a SM Higgs boson of that mass is said to be excluded.

3.6.3 $\mathrm{CL_s}$ Upper Limits

In a given experiment, a downward fluctuation of the background may lead to a stronger upper limit than the actual strength of the signal itself. This is quite consistent with the statistical interpretation of an upper limit. If an experiment were to be performed repeatedly, we do expect the actual value of the signal strength to be greater than the 95% upper limit in 5% of the experiments. But given that we may not necessarily get a chance to repeat an experiment, we would prefer to disfavor the exclusion of signal driven by a downward fluctuation of the background. For this purpose we construct a quantity called $\mathrm{CL_s}$ [159, 160] as follows

$$\begin{aligned} \mathrm{CL_{s+b}} &= \int_{q_{\mu,obs}}^{\infty} f(q_\mu|\mu, \hat{\hat{\theta}}_{obs})dq \\ \mathrm{CL_b} &= \int_{q_{\mu,obs}}^{\infty} f(q_\mu|0, \hat{\hat{\theta}}_{obs})dq \\ \mathrm{CLs} &= \frac{\mathrm{CL_{s+b}}}{\mathrm{CL_b}} \end{aligned} \tag{3.14}$$

If $\mathrm{CL_s} < \alpha$ for a given μ, then that μ is said to be excluded in the $\mathrm{CL_s}$ scheme at $(1-\alpha)$ CL. In the case of the Higgs boson, if we get $\mathrm{CLs} < \alpha$ for $\mu = 1$ at a given value of m_{H}, the SM Higgs boson is said to be excluded at that mass. Since $\mathrm{CL_b}$ is always smaller than or equal to unity, the value of $\mathrm{CL_s}$ is always greater than the usual p-value indicated by $\mathrm{CL_{s+b}}$. As a result the $\mathrm{CL_s}$ approach always yields a more conservative upper limit compared to the classical case. Moreover, when the background underfluctuates, the value of $\mathrm{CL_b}$ decreases thereby increasing the value of $\mathrm{CL_s}$ which in turn makes exclusion harder.

3.6.4 Expected Upper Limits and Significance

While designing and performing a search one is often interested in evaluating the significance that would be expected for a certain amount of data if a signal does exist, or the value of the expected upper limit in the absence of one. These values give an indication of the sensitivity of the analysis. The expected values could also be used for optimization i.e. one could use the expected significance or the expected upper limit as a benchmark to tune the selection requirements that are imposed in the analysis.

To evaluate the expected significance of an analysis, one needs to determine the p.d.f. of the significance assuming the signal strength $\mu = 1$. In other words, we want to know how the significance (Z) of our analysis would be distributed assuming the signal to exist as predicted, if we were to repeat our experiment a large number of times. Here we need to decide on the values of the nuisance parameters to be used for determining this distribution. There are two possibilities. When optimizing an analysis, we want to stay as blind as possible to the actual data. Therefore, it is best to use the values of nuisance parameters that we expect a priori (θ_0). However, if we want to present the expected result as a comparison to what we observe in data, we may want to use the best estimates of the nuisance parameters obtained by maximizing the likelihood under the assumption $\mu = 1$. Let us call these $\theta^{obs}_{\mu=1}$. Then the p.d.f. we are trying to determine can be represented either as $g(Z|\mu = 1, \theta_0)$ (for optimization) or $g(Z|\mu = 1, \theta^{obs}_{\mu=1})$ (for comparison with observation). We can obtain this distribution by generating a large number of toy Monte Carlo datasets and evaluating the significance for each of these toys. We can then take the median of this distribution as the expected significance.

The same rationale applies also to the expected upper limit. In this case we want to know how the upper limit on the signal strength (μ_α) is distributed assuming there is no signal i.e. $\mu = 0$. We can denote this p.d.f. as $h(\mu_\alpha|\mu = 0, \theta_0)$ or $h(\mu_\alpha|\mu = 0, \theta^{obs}_{\mu=0})$ depending on how we want to treat the nuisance parameters. We can then take the median value of the p.d.f. as our expected upper limit. We can also use the p.d.f. to obtain 68% or 95% confidence intervals for the expected upper limit. Ref. [158] provides details on how to evaluate the expectations for upper limits and significance in the asymptotic or large sample approximation.

Lastly, let us consider Fig. 3.6 which is a useful illustration taken from Ref. [161]

that helps to explain how to make sense of the exclusion curves for the SM Higgs boson. We will encounter such plots in the next two chapters. An exclusion curve is essentially a translation of the upper limits into a statement about the (non)-existence of a certain physics phenomenenon - in this case the SM Higgs boson of a certain mass. The dotted black line shown in the figure is the median expected upper limit at 95% CL on the signal strength of the SM Higgs boson. What we learn from this curve is the following. If the SM Higgs boson does not exist, and if we conduct repeated measurements of its signal strength, then the median value of the measured 95% CL upper limit on the signal strength for a given value of m_{H} will be given by the point on the dotted line at that value of m_{H}. The green band tells us that 68% of these repeated measurements will result in an upper limit that falls inside this band. Similarly, the yellow band tells us that 95% of these measurements will result in an upper limit that falls within the yellow bounds. The solid black line shows the observed upper limit on the signal strength for a given experiment. It goes above the median expectation when the data is in excess of the background prediction. Similarly, it falls below the median expectation when there is a deficit of events in data compared to the expected background. In general, we do expect the observed upper limit to fluctuate around the median expectation, and the yellow/green bands give us an indication of how statistically significant this fluctuation is. Wherever the observed upper limit falls below unity we can claim that the signal, if it at all exists, is weaker than the SM prediction at 95% CL. In other words the Higgs boson as predicted by the SM stands excluded in this region. In Fig. 3.6 we see that the SM Higgs boson is excluded in the mass range of 135–225 GeV and 290–490 GeV. We should keep in mind that this observed exclusion is specific to the given measurement. In other words, the excluded mass range may change if we were to repeat the experiment.

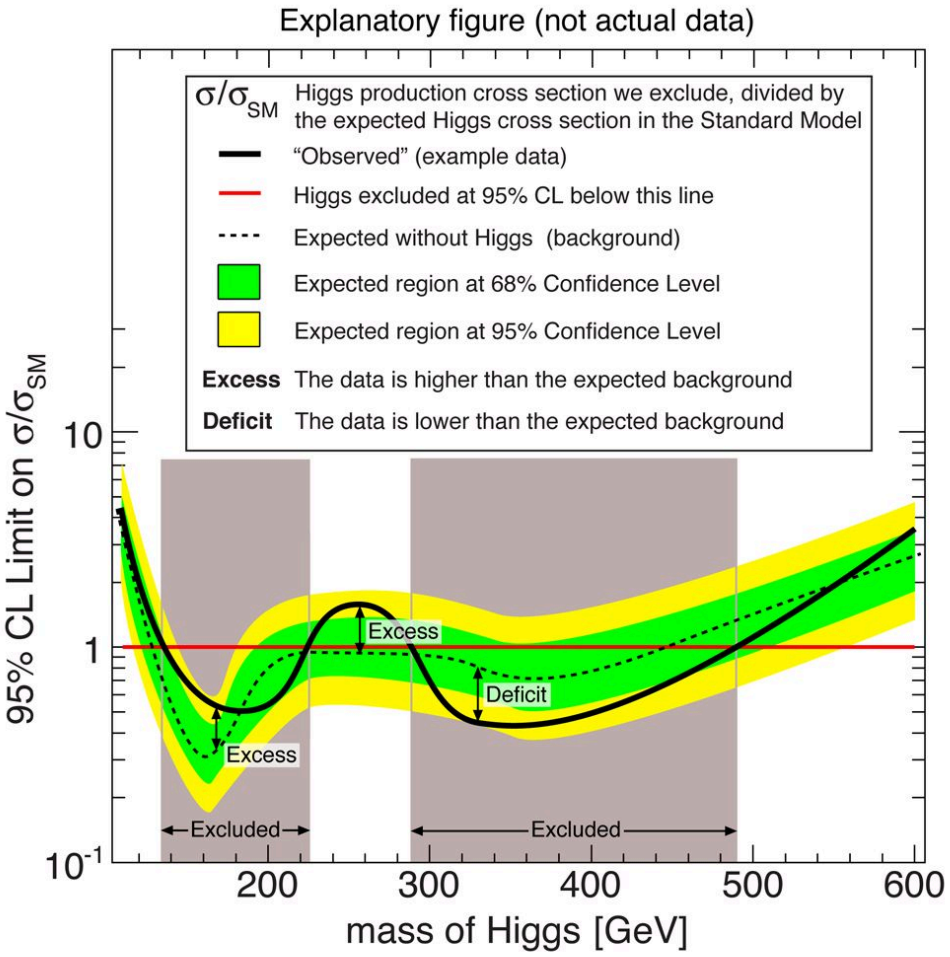

Figure 3.6 An illustration of the exclusion curve for the SM Higgs boson.

Chapter 4

Higgs Boson Search in the $\mathrm{H} \to ZZ \to 2\ell 2\nu$ Channel

4.1 Motivation

To motivate the SM Higgs boson search in the $\mathrm{H} \to ZZ \to 2\ell 2\nu$ channel, let us look back at the status of the CMS Higgs program at the beginning of 2010 when the LHC started its physics run at $\sqrt{s} = 7$ TeV. While the SM Higgs boson was expected to be lighter than 200 GeV (Sec. 1.2.3), there was a lack of any direct experimental evidence to indicate where the Higgs boson mass would be between 114 GeV (the lower limit set by LEP) to about 700 GeV (the upper limit set by the unitarity requirement). Tevatron had excluded a sliver of $m_{\mathrm{H}} \in [158, 175]$ GeV in this region but otherwise the entire mass range was open to investigation.

We saw in Sec. 1.3.4 that several decay modes are accessible for $m_{\mathrm{H}} < 150$ GeV but at higher masses the Higgs boson decays almost entirely to a pair of weak bosons. At the time, the Higgs boson searches in the high mass region were based exclusively on the $\mathrm{H} \to W^+W^- \to \ell^+\bar{\nu}\ell^-\nu$ and $\mathrm{H} \to ZZ \to 4\ell$ final states (where $\ell = e, \mu$). These canonical channels do provide high performance but as the Higgs boson becomes heavier, their signal yield starts drying up and the search sensitivity degrades.

If we consider the $\mathrm{H} \to ZZ \to 4\ell$ channel, we see that only 0.5% of all $\mathrm{H} \to ZZ$ events end up in the 4ℓ final state. Thus if we were to depend on the 4ℓ channel alone, we would be blind to more than 99% of the $\mathrm{H} \to ZZ$ decays. In order to explore the

possibility of exploiting some of this untapped reserve of Higgs signal let us look at the various possible final states that a pair of Z bosons may decay into. These are listed in increasing order of their branching ratios in Tab. 4.1. We see that the $ZZ \to 4q$ final state constitutes nearly half of all the ZZ decays. This final state produces four jets in the event. The QCD background in this case is too large to even contemplate triggering on these events. If triggered upon, the enormous background would render the final state almost useless in terms of sensitivity. The same reasoning also eliminates the $\mathrm{H} \to ZZ \to 2\nu 2q$ channel from contention thus taking away a further 28% of the ZZ decays. In fact we could argue that the only final states which could potentially be useful are those in which one of the two Z bosons decays to a pair of electrons or muons ($Z \to 2\ell$). Owing to the presence of two high p_T, isolated leptons these events would have negligible QCD background. In fact the largest background here would comprise of $Z + X$ events in which the Z boson decays leptonically. We could then attempt to curtail this background by imposing strict selection requirements on X.

Table 4.1 Table of various possible ZZ final states along with their branching ratios (BR). Here $\ell = e, \mu$ and $q = u, d, c, s, b$

$ZZ \to 4f$ final state	$ZZ \to 4f$ BR (%)
$ZZ \to 4\ell$	0.5
$ZZ \to 2\ell 2\tau$	0.5
$ZZ \to 2\nu 2\tau$	1.4
$ZZ \to 2\ell 2\nu$	2.8
$ZZ \to 4\nu$	4.0
$ZZ \to 2\tau 2q$	4.6
$ZZ \to 2\ell 2q$	9.2
$ZZ \to 2\nu 2q$	28
$ZZ \to 4q$	49

With this hope, feasibility studies were conducted in 2010 on the $\mathrm{H} \to ZZ \to 2\ell 2\nu$, $\mathrm{H} \to ZZ \to 2\ell 2q$ and $\mathrm{H} \to ZZ \to 2\ell 2\tau$ channels. The results of these studies are summarized in Fig. 4.1 which shows the projections of the expected upper limits at 95% CL on the SM Higgs boson signal strength for 5 fb^{-1} of integrated luminosity at $\sqrt{s} = 7$ TeV. For $m_{\mathrm{H}} > 200$ GeV, the expected upper limits from the $\mathrm{H} \to ZZ \to 2\ell 2\nu$ and $\mathrm{H} \to ZZ \to 2\ell 2b$ channels have also been included. We see that $\mathrm{H} \to ZZ \to 2\ell 2\nu$ is actually the most sensitive decay mode for Higgs boson masses larger than 300 GeV.

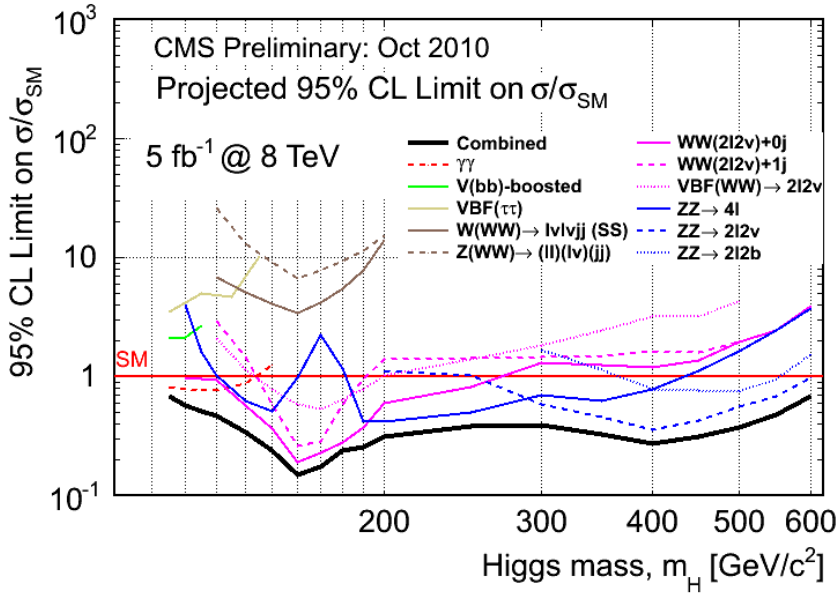

Figure 4.1 Projections for the expected upper limits at 95% CL on the SM Higgs boson signal strength for various search channels. An integrated luminosity of 5 fb^{-1} is assumed at $\sqrt{s} = 7$ TeV. The H $\to ZZ \to 2\ell 2\nu$ channel is shown by the blue curve while the combination of all the channels.

4.2 Signal and Background Description

When a heavy Higgs boson ($m_{\mathrm{H}} \sim 250$ GeV or higher) decays to a pair of Zs, they are typically produced with a large transverse momentum. In the H $\to ZZ \to 2\ell 2\nu$ channel, one of the Z bosons decays to a pair of neutrinos which cause a large E_T^{miss} in the event. The other Z boson decays into a pair of high p_T, isolated, opposite-charged leptons (e^+e^- or $\mu^+\mu^-$). Since the Z bosons are produced on mass shell, the invariant mass of the lepton pair is expected to be consistent with the Z peak. Fig. 4.2 shows a schematic display of one such event. Given this event topology there are several physics processes that can pose as background to the Higgs signal. The largest background comprises of Z+jets events in which the Z boson decays leptonically and a fake E_T^{miss} is generated in the event due to the mismeasurement of jets. Another source of background consists of fully leptonic $t\bar{t}$ and tW decays ($t\bar{t} \to 2\ell 2\nu 2b$ and $tW \to 2\ell 2\nu b$) which also produce high p_T, isolated leptons, and neutrinos in the final state. The electroweak diboson processes ($WW \to 2\ell 2\nu$, $WZ \to 3\ell\nu$, and $ZZ \to 2\ell 2\nu$) further contribute to the background. Some other processes such W+jets events in which the W boson decays leptonically and one of the jets is misidentified as a lepton, may also contribute but their

impact is quite negligible. Table 4.2 lists the cross-section times branching ratio of the signal and background processes that are relevant to this analysis.

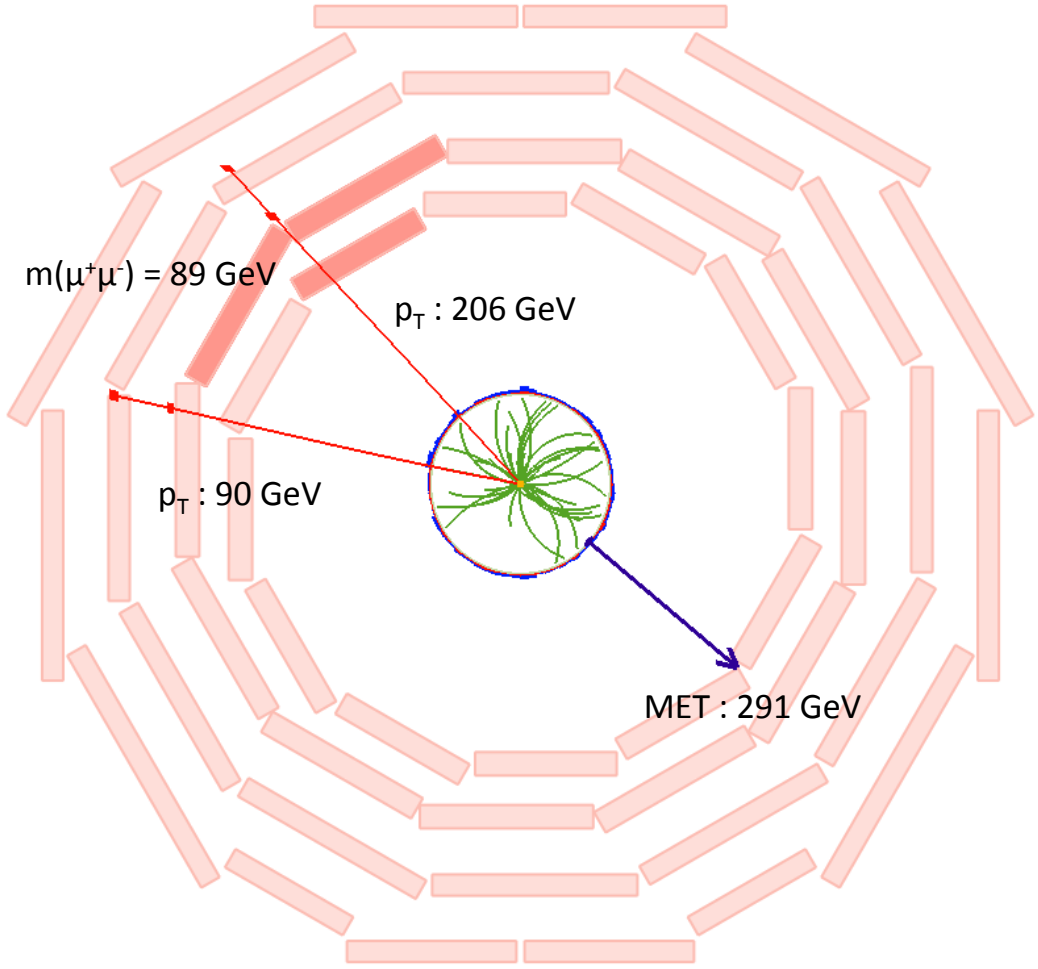

Figure 4.2 Display of an event with H $\rightarrow ZZ \rightarrow 2\ell 2\nu$ characteristics.

Table 4.2 The values of cross-section times branching ratio listed for all the relevant physics processes in the H $\rightarrow ZZ \rightarrow 2\ell 2\nu$ analysis at $\sqrt{s} = 7$ TeV.

Process	$\sigma\times$ BR (pb)	Pert. Order
$gg \rightarrow$ H(250 – 600 GeV) $\rightarrow ZZ \rightarrow 2\ell 2\nu$	2.4×10^{-3} – 2.7×10^{-2}	NNLO + NNLL
$qq \rightarrow$ H(250 – 600 GeV) $\rightarrow ZZ \rightarrow 2\ell 2\nu$	5.3×10^{-4} – 4.4×10^{-3}	NLO
$Z + X \rightarrow 2\ell + X$	2032	NNLO
$t\bar{t} \rightarrow 2\ell 2\nu 2b$	11.5	NLO + NNLL
$tW \rightarrow 2\ell 2\nu b$	1.08	NLO
$WW \rightarrow 2\ell 2\nu$	3.19	NLO
$WZ \rightarrow 3\ell\nu$	0.579	NLO
$qq \rightarrow ZZ \rightarrow 2\ell 2\nu$	0.119	LO

4.3 Event Simulation and Reweighting

Several Monte Carlo event generators are used to simulate the signal and background processes that are relevant to this analysis. The signal events and the top-quark background (both $t\bar{t}$ and tW) are generated using the POWHEG 2.0 event generator while the Z+jets background and the diboson processes (WW, WZ and ZZ) are generated with the MadGraph 5.1.3 generator. These events are then propagated through the PYTHIA 6.4.22 generator to simulate parton showering and hadronization. Some alternate samples are produced using PYTHIA for the diboson processes in order to evaluate certain systematic uncertainties.

While the gluon fusion production cross-section of the signal is available at NNLO+NNLL, the POWHEG generator is able to simulate the Higgs boson kinematics only up to NLO. Higher order corrections modify the Higgs boson p_T distribution which in turn affects the Z boson p_T and the E_T^{miss} distributions. Hence signal events are reweighted to correct for the Higgs boson p_T shape at NNLO+NNLL.

As we will see later, the electroweak $ZZ \to 2\ell 2\nu$ process is left as one of the main backgrounds after the analysis selection. The estimate for this background is obtained from simulation, and so it is essential to model the process as accurately as possible. A differential NLO k-factor has been derived for the $qq \to ZZ$ cross-section as a function of the p_T of the Z boson using the MCFM program [162]. This k-factor can be expressed by the following relation

$$k_{\text{NLO}} = 1.11 + 2.42 \times 10^{-3} \times p_{T_Z} + 1.66 \times 10^{-3} \times p_{T_Z}^2 \tag{4.1}$$

This k-factor is applied as an event-by-event weight to the $qq \to ZZ$ simulation to account for the NLO corrections (the p_T of the dilepton candidate is taken as p_{T_Z}). A small contribution to the ZZ background comes from the $gg \to ZZ$ background which is not simulated by MadGraph. This process has $\sim 12\%$ of the LO $qq \to ZZ$ cross-section [163]. A corresponding correction is applied to the ZZ background yield.

To emulate the impact of pileup, minimum bias interactions are added to every event in the simulated samples. In order to match the simulation to the observed pileup conditions, the Monte Carlo samples are reweighted so that the distribution of the

expected pileup matches with data. To illustrate the effect of this reweighting Fig. 4.3 shows a comparson between the primary vertex multiplicity distributions of $Z \to \mu^+\mu^-$ events in simulation and data, before and after reweighting.

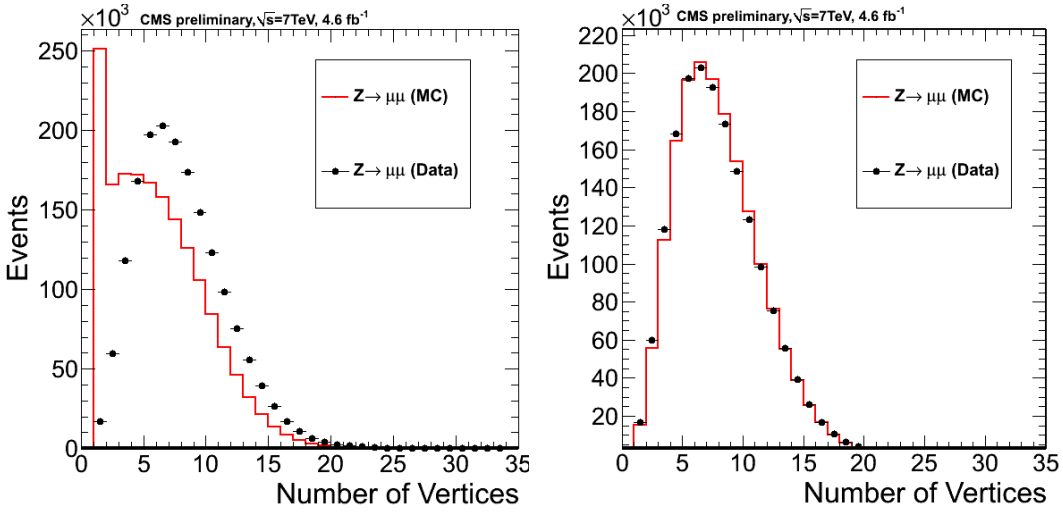

Figure 4.3 Primary vertex multiplicity distributions of $Z \to \mu^+\mu^-$ events from data and simulation before (left) and after (right) pileup reweighting.

4.4 Selection of Dilepton Events

This analysis is geared towards identifying events in which a dilepton candidate consistent with a Z boson is found along with a large E_T^{miss}. The essential highlights of the event selection are mentioned below to give a sense of how the Higgs boson signal is sought to be isolated from the background. The remainder of this section describes this event selection in greater detail.

- Events are required to contain two well-identified, isolated, high p_T leptons of the same flavor but with opposite charge.
- The invariant mass of the dilepton candidate should be consistent with the Z boson.
- Events containing a b-tagged jet are vetoed to suppress the top-quark background.
- Events with a third well-identified, isolated lepton are vetoed to suppress the WZ background

- A large amount of E_T^{miss} is required in the event to reduce the Z+jets background to manageable levels.

- Finally, a transverse mass variable is used to isolate the signal from the remaining background

4.4.1 Triggers

Since we seek a pair of high p_T electrons or muons in the final state, events that fire the dielectron or dimuon triggers suit our needs perfectly. The dielectron triggers have a threshold of 17 and 8 GeV on the p_T of the leading and subleading electrons respectively. Certain isolation and identification requirements are imposed on the electron candidates to keep the trigger rate under control. In the case of the dimuon triggers, the p_T thresholds on the muon legs have been increased progressively from 7 GeV per muon candidate to 17 and 8 GeV on the leading and subleading muon candidates to combat the increasing instantaneous luminosity delivered by the LHC during the 2011 data-taking period. Single muon triggers with p_T thresholds varying between 17 and 24 GeV are also used in the analysis to complement the dimuon triggers. These manage to recover $\sim 5\%$ signal events that are missed by the dimuon triggers.

4.4.2 Lepton Selection

The lepton candidates in the analysis are required to pass certain identification and isolation requirements to suppress jet induced backgrounds. The muons are required to be reconstructed by both the global and tracker muons algorithms (see Sec. 2.3.2). They are required to pass certain identification requirements based on the number of hits in the tracker and the muon chamber, and the quality of the reconstructed muon track. Since the Z boson decays promptly the longitudinal and transverse impact parameters of the tracks are required to be consistent with the highest weighted primary vertex (see the end of Sec. 2.3.1). Finally, the isolation sum in a cone of $\Delta R = \sqrt{\Delta\eta^2 + \Delta\phi^2} = 0.3$ around the muon direction is required to be smaller 15% of the muon p_T. The isolation sum is computed by taking the $\sum p_T$ of the tracks in the isolation cone (excluding the muon track) and adding it to the $\sum E_T$ of the energy deposits in the ECAL and HCAL. A ρ-correction (see Sec. 2.3.8) is applied to the isolation sum to account for the pileup

contamination. The exact details of all the selection requirements are listed in Tab. 4.3.

Table 4.3 Muon Selection Requirements

Cut Variable	Cut Value
$\|\eta\|$	< 2.4
Hits in Muon Chamber	$>= 1$
Matching muon stations	$>= 2$
Tracker Hits	> 10
Pixel Hits	$>= 1$
χ^2 of the global track fit	< 10
$\sigma(p_T)/p_T$	< 0.1
Combined Relative Isolation ($\Delta R = 0.3$)	< 0.15
Transverse Impact Parameter	< 0.02 cm
Longitudinal Impact Parameter	< 0.1 cm

The electron candidates are subjected to similar isolation and impact parameter requirements as muons. In addition certain identification requirements are imposed based on the lateral shape of the ECAL supercluster (denoted by the $\sigma_{i\eta i\eta}$ variable) and the $\Delta\eta, \Delta\phi$ matching between the direction of the electron track and position of the ECAL supercluster. Furthermore, the hadronic energy behind the supercluster is required to be small compared to the supercluster energy (this is denoted by the H/E ratio). Electrons that end up in the transition region between the ECAL barrel and endcap ($1.4442 < |\eta| < 1.566$) have a significant likelihood of being mismeasured, and hence are vetoed. In order to reject electrons produced from photon conversions the electron tracks are required to have no missing hits in the inner tracker layers. Also, electron candidates are vetoed if a collinear partner track is found. The details of electron selection are listed in Tab. 4.4.

Table 4.4 Electron Selection Requirements

Cut Variable	Cut Value (Barrel)	Cut Value (Endcap)
$\|\eta\|$ of supercluster	< 1.4442	$1.566 < \|\eta\| < 2.5$
$\sigma_{i\eta i\eta}$	< 0.01	< 0.03
$\Delta\phi$	< 0.06	< 0.03
$\Delta\eta$	< 0.004	< 0.007
H/E	< 0.04	< 0.1
Combined Relative Isolation ($\Delta R = 0.3$)	< 0.1	< 0.1
Transverse Impact Parameter	< 0.02 cm	< 0.02 cm
Longitudinal Impact Parameter	< 0.1 cm	< 0.1 cm
Transverse distance to partner track	> 0.02	> 0.02
$\Delta\cot\theta$ of partner track	> 0.02	> 0.02
number of missing hits	0	0

4.4.3 Z Candidate Selection and Extra Lepton Veto

Z boson candidates are reconstructed in events with a pair of oppositely charged leptons of the same flavor, which pass the identification and isolation criteria listed above. The leptons are required to have $p_T > 20$ GeV to be able to efficiently pass the trigger requirements. The invariant mass of the Z candidates is required to lie in a 15 GeV window around the nominal Z peak at 91.186 GeV. In order to suppress the WZ background, events are required to have no additional electron or muon, with $p_T > 10$ GeV that passes the selection requirements. Figure 4.4 shows the Z mass peak observed in data in the electron and muon channels. A slight disagreement is visible in the Z boson line-shape between data and simulation particularly in the electron channel. It can be attributed to a systematic difference in the electron momentum scale and resolution. Since this analysis is not very sensitive to the Higgs boson mass, we do not attempt to correct this difference.

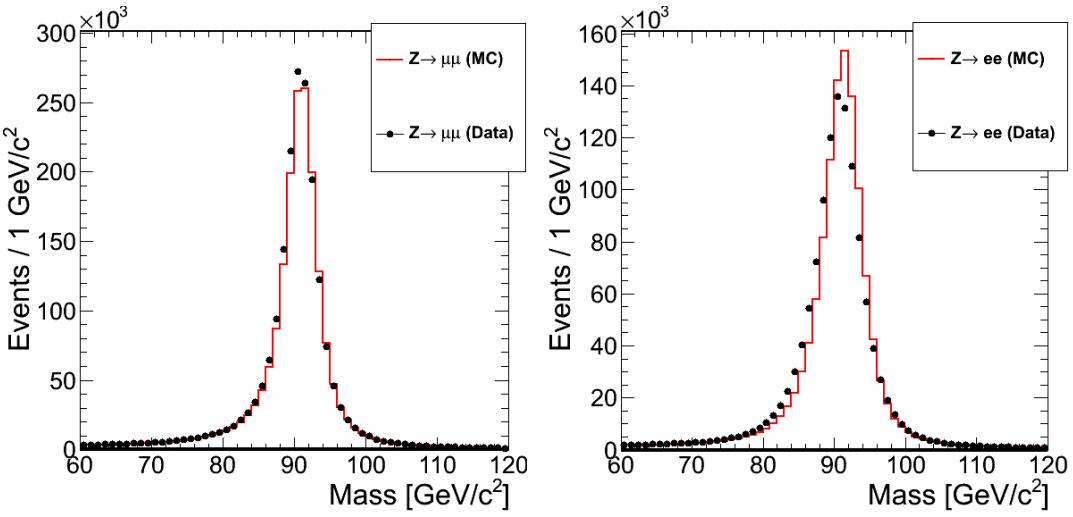

Figure 4.4 Z mass peak in the muon (left) and electron (right) channels with 4.6 fb^{-1} of data compared to the Z+jets simulation.

4.4.4 B Jet and Soft Muon Veto

At this stage of the analysis we are almost entirely dominated by the Z+jets background. The relative contribution from other sources is negligible. However, as we start requiring a large E_T^{miss} in the event, the Z+jets background falls off quite quickly and other backgrounds start becoming visible. The largest background after Z+jets

comes from top quark decays. A key distinguishing feature of these events is that they contain of a b quark. Therefore to suppress this background we veto events in which a b-tagged jet is identified. The Track Counting High Efficiency algorithm (see Sec. 2.3.6) is used for tagging b jets, and if the algorithm returns a value greater than 2.0 for any jet with $p_T > 30$ GeV the event is discarded.

In order to identify b quarks which decay leptonically, we look for the presence 'soft muons' in the event which satisfy the following criteria

- $p_T > 3$ GeV
- Reconstructed as a tracker muon,
- Number of hits in the tracker > 10,
- Certain geometric matching requirements are met between the outermost muon segments and the extrapolated tracker track
- Transverse impact parameter < 0.2 cm,
- Longtudinal impact parameter < 0.2 cm,
- If $p_T > 20$ GeV, isolation sum $< 0.1 \times p_T$.

Any event containing a soft muon is vetoed.

4.5 Scale Factors For Simulated Dilepton Events

Dilepton events in simulation need to be rescaled to account for differences in lepton selection efficiencies when compared to data. Also, no trigger requirements are imposed on the simulated events. Therefore, an additional rescaling has to be done to account for possible trigger inefficiency.

Efficiency measurements, in general, are performed using the 'tag-and-probe' technique. Let us look at this procedure in the context of measuring the lepton selection efficiency. We start with a tag lepton in a given event that passes all our selection requirements. It is then paired with a probe in that event which corresponds to the denominator of our efficiency measurement. We can group the tag-and-probe pairs into

two categories. The 'pass' category consists of probes that pass the lepton selection while the 'fail' category corresponds to the probes that fail the selection. We can fit the tag-and-probe mass distribution in each category to a model of a Z boson peak sitting on top of a background with polynomial shape. The yield of Z events can be extracted from the fit in both the categories. The efficiency is then obtained by taking the ratio $N_Z(\text{pass})/[N_Z(\text{pass}) + N_Z(\text{fail})]$. We can measure the efficiency in different η and p_T bins by restricting the probe leptons accordingly. The efficiency measurement is performed in both data and simulation and the ratio of these efficiencies is applied as a scale factor per lepton to every event in simulation. The scale factor for muons is found to be consistent with unity within 1%. Hence the dimuon events in simulation are not rescaled. The data-to-simulation scale factors for electrons are shown in table 4.5.

Table 4.5 Data-to-simulation scale factors for the electron selection. Uncertainties are purely statistcal.

p_T (GeV)	Barrel	Endcap
20–30	0.969 ± 0.003	0.988 ± 0.005
30–40	0.988 ± 0.001	0.989 ± 0.005
40–50	0.985 ± 0.001	0.999 ± 0.001
> 50	0.982 ± 0.002	0.997 ± 0.002

We also need to rescale the simulation with the trigger efficiency that is measured in data. In measuring the trigger efficiency we want to determine the fraction of dilepton events with both leptons passing the analysis selection, that also fire the trigger. The trigger efficiency for the dielectron trigger is found to be consistent with unity. In the muon channel, we use both single and dimuon triggers. Their combined efficiency is computed using the following relation

$$\begin{aligned} \varepsilon(p_{T1},\, \eta_1,\, p_{T2},\, \eta_2) &= \varepsilon_D(p_{T1},\, \eta_1)\varepsilon_D(p_{T2},\, \eta_2) \\ &= +\, \varepsilon_S(p_{T2},\, \eta_2)(1 - \varepsilon_D(p_{T1},\, \eta_1)) \\ &= +\, \varepsilon_S(p_{T1},\, \eta_1)(1 - \varepsilon_D(p_{T2},\, \eta_2)) \end{aligned} \tag{4.2}$$

where $\varepsilon_D(p_T,\, \eta)$ is the per leg efficiency of the dimuon triggers while $\varepsilon_S(p_T,\, \eta)$ is the single lepton trigger efficiency, both computed as a function of p_T and η. They are listed in tables 4.6 and 4.7 respectively.

Table 4.6 Dimuon trigger efficiency.

p_T (GeV)	$\|\eta\| < 0.8$	$0.8 \leq \|\eta\| < 1.2$	$1.2 \leq \|\eta\| < 2.1$	$2.1 \leq \|\eta\| < 2.4$
20 - 30	0.977 ± 0.002	0.962 ± 0.005	0.954 ± 0.004	0.872 ± 0.001
30 - 40	0.977 ± 0.002	0.958 ± 0.005	0.956 ± 0.003	0.880 ± 0.001
40 - 50	0.976 ± 0.003	0.958 ± 0.005	0.954 ± 0.004	0.889 ± 0.001
> 50	0.976 ± 0.002	0.959 ± 0.004	0.949 ± 0.003	0.869 ± 0.001

Table 4.7 Single muon trigger efficiency.

p_T (GeV)	$0 < \|\eta\| < 0.8$	$0.8 < \|\eta\| < 1.2$	$1.2 < \|\eta\| < 2.1$	$2.1 < \|\eta\| < 2.4$
20 - 30	0.6951 ± 0.0039	0.5887 ± 0.0060	0.5763 ± 0.0041	0.1533 ± 0.0070
30 - 40	0.8840 ± 0.0015	0.7962 ± 0.0030	0.7877 ± 0.0023	0.2210 ± 0.0055
40 - 50	0.8860 ± 0.0014	0.8060 ± 0.0025	0.8023 ± 0.0020	0.2295 ± 0.0061
> 50	0.8795 ± 0.0025	0.8061 ± 0.0046	0.8004 ± 0.0037	0.2269 ± 0.0115

4.6 Event Selection Based On E_T^{miss}

In order to suppress the overwhelming Z+jets background in this analysis, a requirement of large E_T^{miss} in the event is essential. Fig. 4.5 shows the distribution of E_T^{miss} in dilepton events passing the event selection that has been described so far. We see that the Z+jets background drops sharply with increasing E_T^{miss}. This is to be expected since the Z+jets events do not contain any genuine E_T^{miss} from escaping neutrinos.

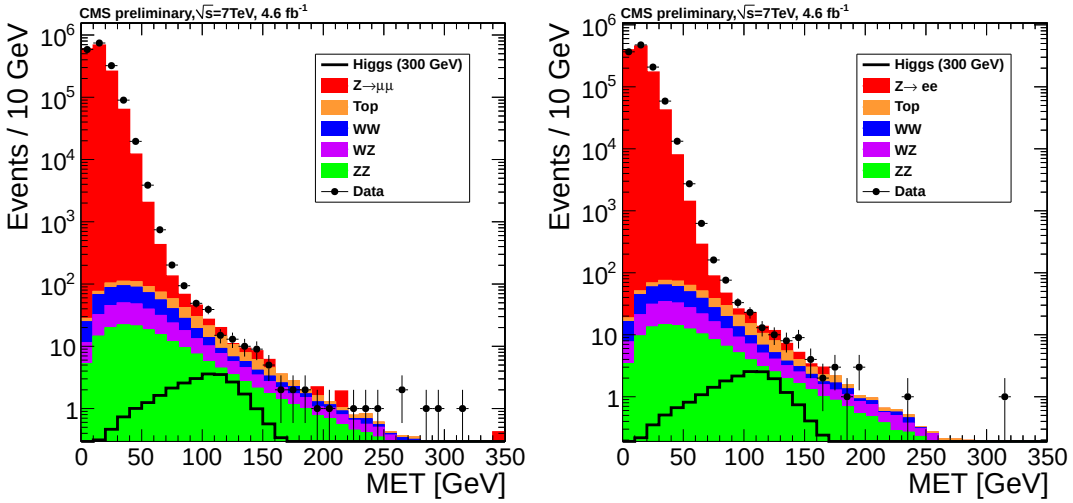

Figure 4.5 E_T^{miss} distribution in dimuon (left) and dielectron (right) events.

4.6.1 Dilepton p_T Threshold

We see a considerable discrepancy between data and Z+jets simulation in figure 4.5. The E_T^{miss} distribution in data is broader compared to the Z+jets simulation. This can be attributed to inaccurate modeling of pileup which can have a significant impact on E_T^{miss} resolution. Therefore, the Z+jets simulation is found to be unsuitable for use in the analysis. Instead, the Z+jets background is estimated from γ+jets events in data using a technique that is detailed in Sec. 4.7. One key aspect of this procedure is that it depends on matching the p_T spectrum of the photons with that of the Z bosons. The single photon triggers used in data have a minimum threshold of 50 GeV. For the γ+jets approach to work, a similar threshold needs to be imposed on the p_T of the dilepton candidates. Hence, a requirement of $p_T > 55$ GeV is imposed on all dilepton candidates used in the analysis. The Z bosons produced in the decay of a high mass Higgs boson typically have a large p_T as shown in Fig. 4.6. Therefore, this requirement has negligible impact on overall performance.

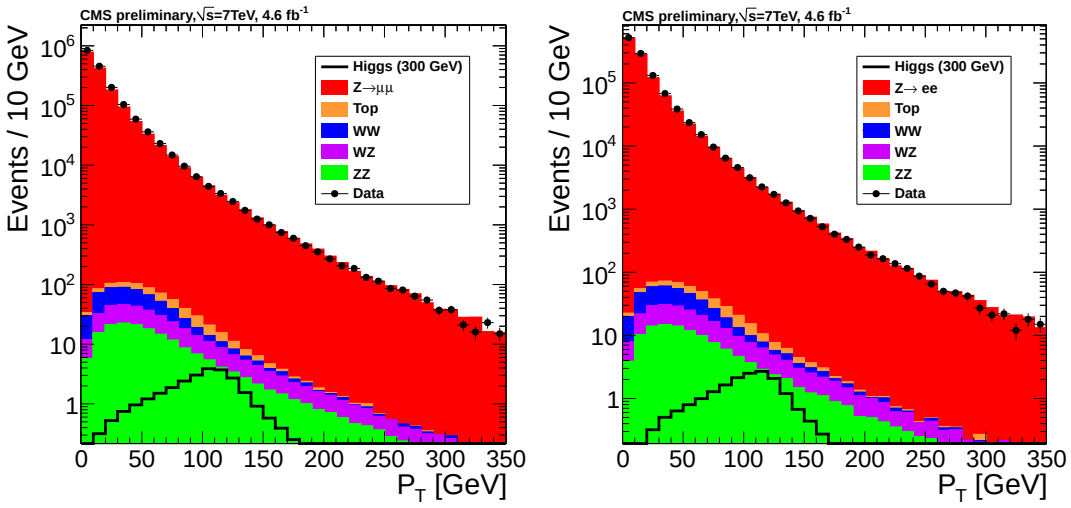

Figure 4.6 p_T distribution of dimuon(left) and dielectron(right) candidates.

Fig. 4.7 shows the E_T^{miss} distribution in dilepton events from data in comparison to the background expectation which now uses the γ+jets model. We find a much improved agreement between data and the background prediction. Therefore from here on, we use the γ+jets sample in developing the analysis.

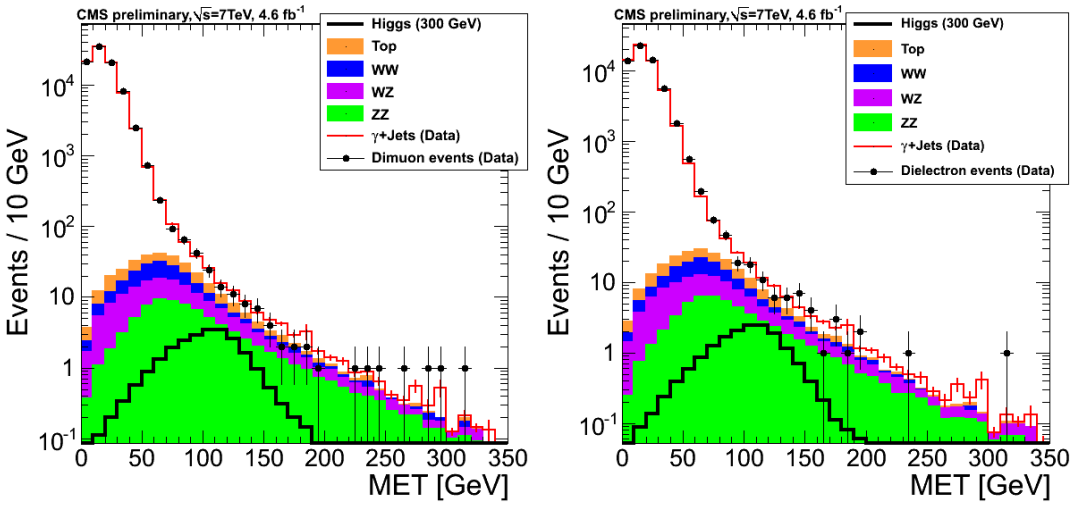

Figure 4.7 E_T^{miss} distribution in dimuon (left) and dielectron (right) events. The Z+jets background is modeled using γ+jets events.

4.6.2 Minimum Requirements On E_T^{miss} and $\Delta\phi(E_T^{\text{miss}}$, jet)

The bulk of the Z+jets background is removed by requiring a minimum of 70 GeV of E_T^{miss} in the event. The Z+jets background that survives this requirement consists of events in which the jets have been significantly mismeasured leading to a large momentum imbalance. In such events the E_T^{miss} is often aligned along the jet direction in ϕ. Fig. 4.8 shows the azimuthal angular separation between E_T^{miss} and the nearest jet with $p_T > 30$ GeV. If no jet with $p_T > 30$ GeV is found, the requirement is lowered to 15 GeV.

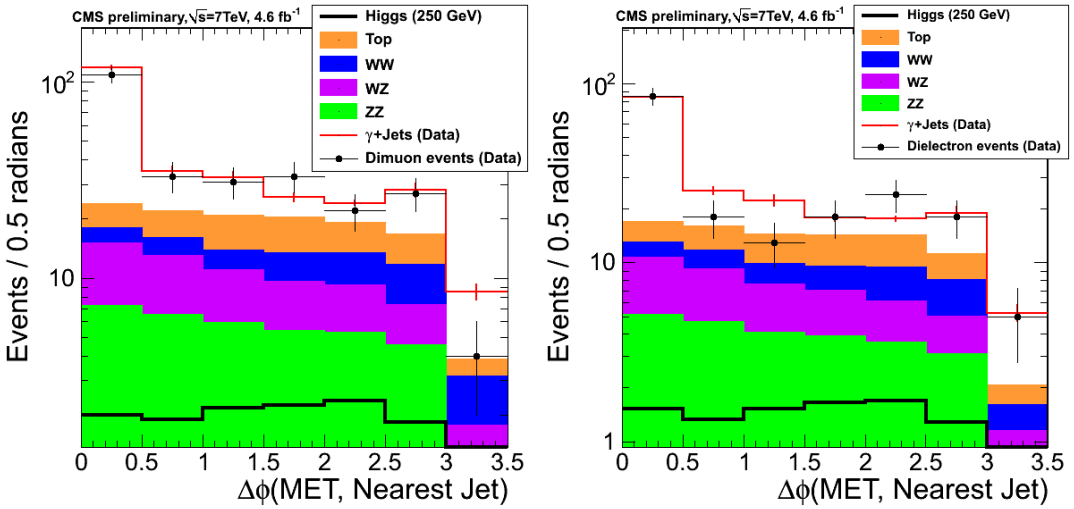

Figure 4.8 Distribution of $\Delta\phi$ between E_T^{miss} and the nearest jet observed in dimuon (left) and dielectron (right) channels. The E_T^{miss} is required to be greater than 70 GeV in these events.

We see that events with a small $\Delta\phi(E_T^{\rm miss}$, jet) are largely dominated by the Z+jets background. Hence, a requirement of $\Delta\phi(E_T^{\rm miss}$, jet) > 0.5 is imposed to further reduce this background.

4.6.3 The Transverse Mass M_T

In order to discriminate the signal from the background events passing the selection that we have discussed so far, a transverse mass is defined for the (dilepton + $E_T^{\rm miss}$) system as follows

$$M_T{}^2 = (\sqrt{p_{T,\ell\ell}{}^2 + m_{\ell\ell}{}^2} + \sqrt{E_T^{\rm miss}{}^2 + m_{\ell\ell}{}^2})^2 - (\vec{p}_{T,\ell\ell} + \vec{E}_T^{\rm miss})^2 \tag{4.3}$$

Two possible approaches of using the M_T variable to extract signal from the observed events are considered. In one approach, the selection criteria for M_T and $E_T^{\rm miss}$ variables are optimized for different values of $m_{\rm H}$ and a counting analysis is performed. In the other approach the shape of the M_T variable is used to perform a binned analysis. Table 4.8 lists the $m_{\rm H}$-dependent requirements imposed on M_T and $E_T^{\rm miss}$ for the counting and binned shape analyses.

Table 4.8 Higgs boson mass-dependent selection for $E_T^{\rm miss}$ and M_T variables in the counting and binned shape analyses.

m_H (GeV)	250	300	350	400	500	600
Cut-based analysis selection						
$E_T^{\rm miss}$ (GeV)	> 70	> 79	> 95	> 115	> 150	> 161
M_T (GeV)	[222, 272]	[264, 331]	[298, 393]	[327, 460]	[382, 605]	[452, 767]
Shape-based analysis selection						
$E_T^{\rm miss}$ (GeV)	> 70	> 80	> 80	> 80	> 80	> 80
M_T (GeV)	[180, 300]	[250, 350]	[250, 400]	[250, 450]	[250, 600]	[250, 750]

4.7 Background Estimation

The backgrounds in this analysis can be grouped into three types. In the first category we have the Z+jets background in which there is no genuine $E_T^{\rm miss}$ due to escaping neutrinos. In the second category, we have processes such as $t\bar{t}, tW, WW, W$+jets in which there is no Z boson peak. These processes are collectively referred to as the non-resonant backgrounds. The last category comprises of the WZ and ZZ backgrounds.

The Z+jets and non-resonant backgrounds are estimated using data-driven techniques that are described below, while the WZ and ZZ backgrounds are estimated from simulation.

4.7.1 Z+jets Background

The Z+jets background is modeled using γ+jets events from data. In both of these processes, there are no neutrinos in the final state and so the E_T^{miss} is an artifact of the detector response. Moreover, in both processes we expect the leptons and photons to be well-measured and so the E_T^{miss} can be attributed to the mismeasurement of the associated jets and pileup. The γ+jets events are collected from several single photon triggers with varying prescales. The lowest p_T threshold in these triggers is 50 GeV. Hence, the p_T of the reconstructed photons is required to be larger than 55 GeV. To ensure that the photons are well-measured the following selection requirements are imposed on the photon candidates.

Table 4.9 Photon Selection

Variable	Selection
p_T	> 55 GeV
$\lvert\eta\rvert$ of supercluster	< 1.4442
Matching Pixel Track Seed	None
$\sigma_{i\eta i\eta}$	$0.001 < \sigma_{i\eta i\eta} < 0.013$
$\sigma_{i\phi i\phi}$	> 0.001
H/E	< 0.05
Tracker Isolation Sum ($\Delta R = 0.4$)	$< 2.0 + 0.001 \times p_T$
ECAL Isolation Sum ($\Delta R = 0.4$)	$< 4.2 + 0.006 \times p_T$
HCAL Isolation Sum ($\Delta R = 0.4$)	$< 2.2 + 0.0025 \times p_T$

The strategy to estimate the Z+jets background is as follows. Dilepton events are selected based on requirements detailed in Sec. 4.4. In addition the p_T of the dilepton candidates is required to be greater than 55 GeV. These events are dominated by the Z+jets background. A similar selection (b-jet veto, soft muon veto) is applied on the γ+jets events. The two samples are made kinematically similar by reweighting the γ+jets events such that the shapes of their p_T and jet multiplicity distributions match with those of the dilepton candidates. Since the prescales on the single photon triggers have changed through the period of data taking to cope with the increasing instantaneous luminosity, the γ+jets sample does not accurately represent the pileup

conditions corresponding to the dilepton sample which is collected from unprescaled triggers. In order to account for this difference the γ+jets events are further reweighted such that their vertex multiplicity distribution matches with that of dilepton events. Finally, the yield of the γ+jets events is renormalized to match the number of dilepton events.

The reweighted p_T, jet multiplicity and vertex multiplicity distributions of γ+jets events are shown in comparison to the dilepton events in Fig. 4.9, 4.10 and 4.11 respectively. This reweighted γ+jets sample can now be used instead of simulation in order to estimate the Z+jets background. As we saw in Fig. 4.7, the E_T^{miss} distribution of the reweighted γ+jets events agrees extremely well with that of the dilepton events.

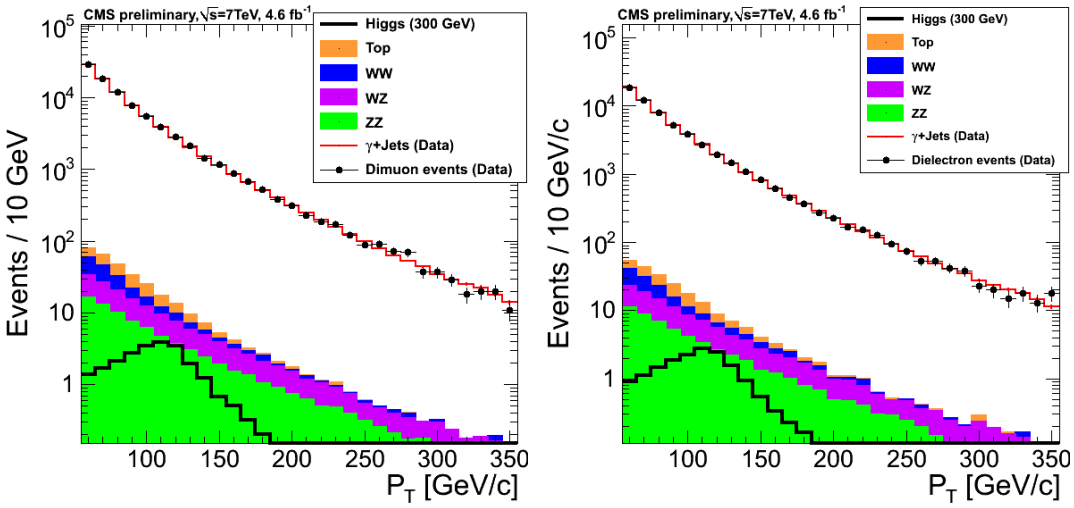

Figure 4.9 p_T distribution of dilepton events and reweighted single photon events. Dimuon channel is shown on the left and and the dielectron channel is shown on the right.

The M_T variable that we use in the analysis depends on the invariant mass of the dilepton candidate. Therefore, an artificial mass is assigned to the photon in each event by sampling from a probability distribution obtained from fitting to the observed $Z \to \ell\ell$ line shape.

At high values of E_T^{miss}, the γ+jets control sample is contaminated by processes in which a photon is produced in association with neutrinos. These processes include $Z(\nu\bar{\nu}) + \gamma$, $W(\ell\nu) + \gamma$ and $W(\ell\nu)$+ jets in which a jet is mismeasured as a photon. In order suppress this contamination, we require at least one jet in every γ+jets event with $p_T > 15$ GeV. This requirement largely removes events in which there is no hadronic

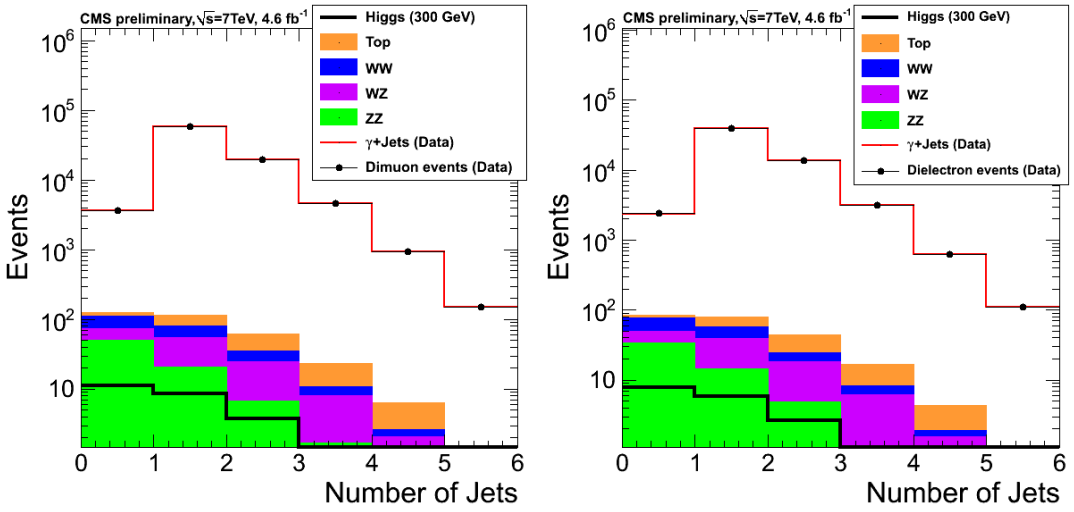

Figure 4.10 Jet Multiplicity in dilepton events and reweighted single photon events. Dimuon channel is shown on the left and the dielectron channel is shown on the right.

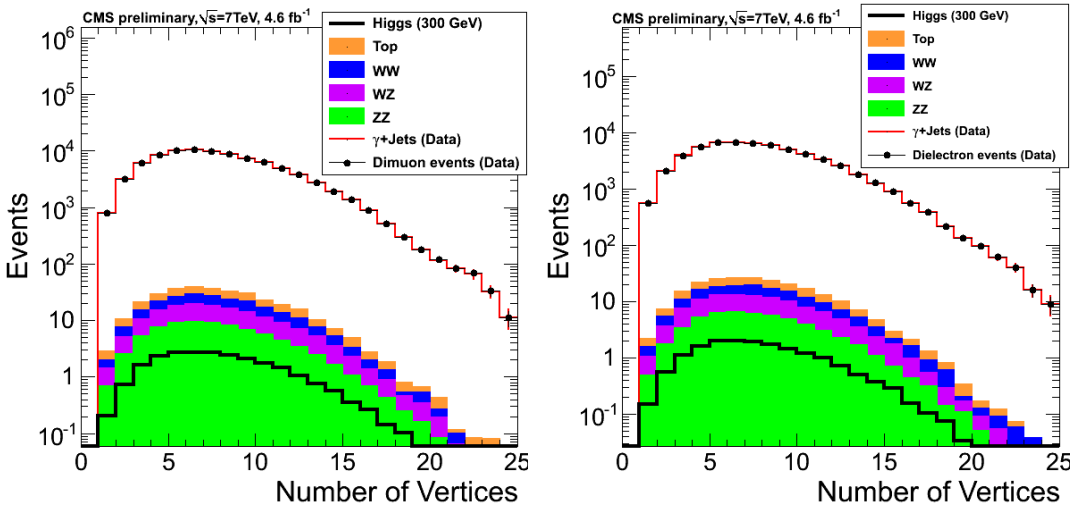

Figure 4.11 Distribution of number of vertices in dilepton events and reweighted single photon events. Dimuon channel is shown on the left and the dielectron channel is shown on the right.

recoil against the photon, which is typical of events with genuine E_T^{miss}. However, this contamination cannot be completely eliminated, and so the estimate from the γ+jets control sample is considered only as an upper bound on the Z+jets background. To take this into account, we take half of the γ+jets estimate as the nominal prediction for the Z+jets background and assign 100% uncertainty to this estimate thereby allowing the background to vary between 0 and the γ+jets estimate in the fit.

4.7.2 Non-resonant Background

The non-resonant background contribution can be attributed to processes such as $t\bar{t}, tW, WW, W$+jets. A characteristic feature of these processes is that they produce the $e^{\pm}\mu^{\mp}$ and the $e^{+}e^{-}, \mu^{+}\mu^{-}$ final states in equal measure. Hence, we use events with $e^{\pm}\mu^{\mp}$ pairs as a control sample to estimate this background. The events in the control sample are subjected to the same selection criteria as those imposed in the analysis. The $e^{\pm}\mu^{\mp}$ events that survive the analysis requirements are then scaled using the following relation to evaluate the background estimate

$$\begin{aligned} N_{ee} &= \alpha_e \times N_{e\mu} \\ N_{\mu\mu} &= \alpha_\mu \times N_{e\mu} \end{aligned} \tag{4.4}$$

The scale factors α_e and α_μ are computed by taking the ratio of the number of $e^{+}e^{-}$ or $\mu^{+}\mu^{-}$ events to the number of $e^{\pm}\mu^{\mp}$ events in the sidebands (SB) of the Z mass peak in the region [40, 70] GeV and [110, 200] GeV.

$$\begin{aligned} \alpha_e &= N_{ee}^{SB}/N_{e\mu}^{SB} \\ \alpha_\mu &= N_{\mu\mu}^{SB}/N_{e\mu}^{SB} \end{aligned} \tag{4.5}$$

The events in the sidebands are selected by requiring a b-tagged jet and $E_T^{\text{miss}} > 70$ GeV in order to suppress the $Z \to \ell\ell$ contribution.

This technique is tested on the non-resonant backgrounds in simulation and its predictions are found to be in good agreement with the actual yields, as can be seen in table 4.10. The procedure is then exercised in data and the α parameters are found to be $\alpha_\mu = 0.58 \pm 0.02$ and $\alpha_e = 0.42 \pm 0.02$. Table 4.11 lists the non-resonant background yields evaluated in data for several m_{H}-dependent selections. In the binned shape analysis, the M_T shape of the $e\mu$ events is used to model the non-resonant background. A smoothing procedure [164] is employed in order to smear out the statistical bumps in the M_T distribution due to the limited size of the $e\mu$ control sample.

At this point a subtle aspect of our signal needs to be elucidated. While we expect the bulk of our signal events to come from $\text{H} \to ZZ \to 2\ell 2\nu$ decays, there is some 'non-resonant' signal contribution which comes from $\text{H} \to WW \to 2\ell 2\nu$ events in

which the dilepton invariant mass is consistent with the Z mass window of the analysis. If the Higgs boson signal were to exist, this non-resonant signal contribution would also contribute to the $e\mu$ control sample and hence will be evaluated as a part of the background. Therefore, the $\mathrm{H} \to WW \to 2\ell 2\nu$ events are not considered as a part of our signal and the analysis is restricted exclusively to the $\mathrm{H} \to ZZ \to 2\ell 2\nu$ decays.

Table 4.10 Comparison in simulation between the true yields of non-resonant backgrounds and the predictions from the $e\mu$ control sample. Each row corresponds to the event selection used in the counting analysis for a given value of m_{H}. An integrated luminosity of 4.6 fb^{-1} is assumed in normalizing the yields. The quoted uncertainties are purely statistical.

m_H (GeV)	Predicted Yields ($\mu\mu$)	Actual Yields ($\mu\mu$)	Predicted Yields (ee)	Actual Yields (ee)
250	35.4 ± 0.7	36.3 ± 0.9	25.0 ± 0.5	26.7 ± 0.8
300	9.19 ± 0.34	9.77 ± 0.47	6.44 ± 0.24	6.66 ± 0.39
350	2.15 ± 0.16	2.14 ± 0.22	1.5 ± 0.1	1.65 ± 0.19
400	0.58 ± 0.08	0.58 ± 0.13	0.41 ± 0.06	0.62 ± 0.12

Table 4.11 Non-resonant background yield measured in data. Each row corresponds to the event selection used in the counting analysis for a given value of m_{H}. Statistical uncertainties are quoted.

m_H (GeV)	Yields ($\mu\mu$)	Yields (ee)
250	37.7 ± 4.7	27.3 ± 3.4
300	10.4 ± 2.5	7.56 ± 1.78
350	1.16 ± 0.82	0.84 ± 0.59
400	0	0
500	0	0
600	0	0

4.8 Systematic Uncertainties

4.8.1 Normalization Uncertainties

The signal and background yields have several sources of systematic uncertainty. In the case of the signal, the uncertainties on the production cross-section evaluated by varying the QCD scales and the PDF sets are documented in [103, 104]. A similar procedure is also employed on the simulation-driven WZ and ZZ backgrounds revealing $\sim 10\%$ uncertainties on their cross-sections.

The signal events used in the analysis are generated using an approximation in

which a Breit-Wigner line-shape is assigned to the Higgs boson decay such that the peak of the Breit-Wigner sits at the putative value of the Higgs boson mass (m_{H}) and the width of the Breit-Wigner is set equal to the total decay width of the Higgs boson at m_{H}. However, we discussed in Sec. 1.3.5 that this Breit-Wigner approximation is only valid when the width is much smaller than m_{H}, and a more accurate description is provided by the Complex Pole Scheme. To account for this mismodeling of the Higgs boson line-shape in simulation an uncertainty of 10–30% is assigned for $m_{\mathrm{H}} \geq 400$ GeV.

As discussed in Sec. 4.5 events in simulation have to be rescaled to account for differences in trigger and lepton selection efficiencies with respect to data. The uncertainty on account of these scale factors is estimated to be less than 2%. We saw in Fig. 4.4 that there is a discrepancy in the Z boson line-shape between data and simulation which can be attributed to the differences in modeling of the lepton momentum scale and resolution. To account for this difference, uncertainties of 2% and 5% are assigned to the events yields derived from simulation in the muon and electron channels respectively. While we do not use jets explicitly in the analysis, the b-jet veto and $\Delta\phi(E_T^{\mathrm{miss}}, \text{jet})$ selection are dependent on jets. The corresponding uncertainties due to jet energy scale and b-jet veto efficiency mismatch between data and simulation are found to be $\sim 1\%$. The signal and WZ/ZZ yields are normalized according to the measured value of the integrated luminosity of data. The uncertainty on this luminosity measurement is found be 4.5% [165].

The estimate of the Z+jets background has a large uncertainty of 100% due to the fact that the γ+jets control sample is contaminated with events with genuine E_T^{miss}, as described in Sec. 4.7.1. In the case of the non-resonant backgrounds, the estimated event yield has a significant statistical uncertainty owing to the limited number of events in the $e\mu$ control sample, as shown in table 4.11. In fact, the control sample runs out of events for selections at higher values of m_{H} (400 GeV and beyond). In order to model the statistical uncertainty on backgrounds estimated using sparse control samples, the gamma function is found to be more suitable in comparison to the log-normal function that was discussed in Sec. 3.4.1. The form of the gamma function is given below

$$\rho(n) = \frac{1}{\alpha} \frac{n/\alpha^N}{N!} e^{-n/\alpha} \tag{4.6}$$

Here, n is the background yield, α corresponds to the α_e and α_μ parameters and N stands for the number of $e\mu$ events in the control sample that pass the analysis selection.

All the normalization uncertainties used in the analysis are summarized in table 4.12.

Table 4.12 Summary of all the systematic uncertainties on event yields.

Source	Uncertainty [%]
Luminosity	4.5
PDF for Higgs production (gluon fusion)	8.2–10.4
PDF for Higgs production (VBF)	3.8–7.6
PDF for $qq \to ZZ$	4.8
PDF for $qq \to WZ$	5.5
QCD scale for Higgs production (gluon fusion)	7.6–11.1
QCD scale for Higgs production (VBF)	0.4–2
QCD scale for $gg \to ZZ$	20
QCD scale for $qq \to ZZ$	6.2
QCD scale for $qq \to WZ$	8.5
Higgs boson line shape	10–30
Trigger	1 (for ee), 2 (for $\mu\mu$)
Lepton identification and isolation	2
Lepton momentum scale	5 (for ee), 2 (for $\mu\mu$)
Jet energy scale	1–1.5
b jet Veto	1–1.2
Pile-up	1–3
Non-resonant background	15–100
Z+jets	100

4.8.2 Shape Uncertainties

In the shape-based analysis certain shape uncertainties are assigned to various processes in addition to the normalization uncertainties. These shape uncertainties are propagated using two alternate shapes with respect to the nominal M_T shape for a given process (see the end of Sec. 3.4.2).

The uncertainty on the M_T distributions arising from the limited number of events in the bins is taken into account by scaling all the bins up and down by their respective statistical uncertainties. In the case of the ZZ and WZ backgrounds, alternate shapes are derived from PYTHIA-generated samples to account for possible mismodeling in the MadGraph generator from which the nominal shape is obtained. The uncertainty on the M_T shape of the non-resonant backgrounds is taken into account by using alternate shapes from simulation. In the case of signal, alternate shapes are obtained by varying the renormalization and factorization scales by a factor two.

As an example, the shape uncertainties on the WZ and ZZ backgrounds are shown in Fig. 4.12.

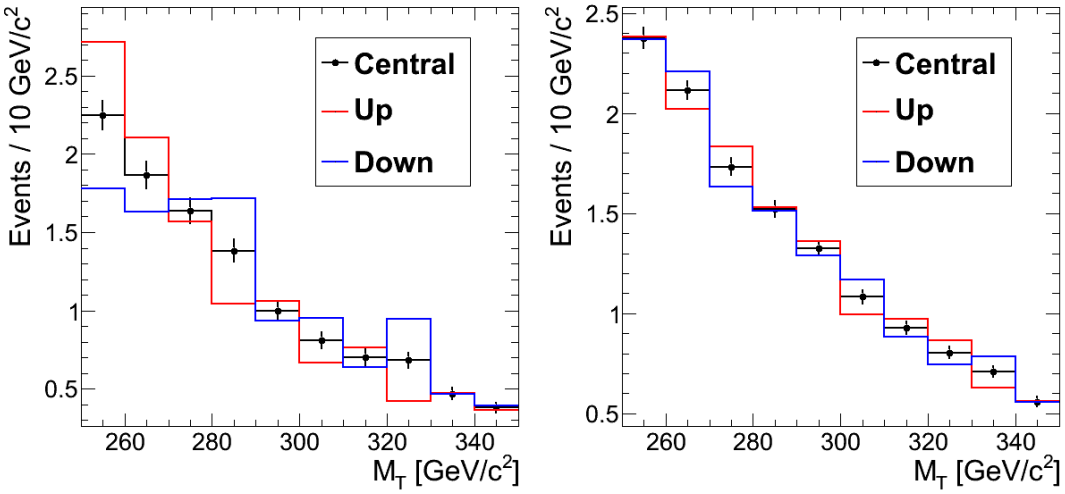

Figure 4.12 Nominal and alternate shapes are shown for the WZ background in the dimuon channel (left) and the ZZ background in the dielectron channel(right). The nominal shape is derived from the MadGraph generator. The 1σ 'up' shapes are derived from the PYTHIA generator while the 1σ 'up' shapes are obtained by mirroring the difference between the nominal and up shapes.

4.9 Results

The analysis has been performed using the entire 2011 dataset which corresponds to an integrated luminosity of 4.6 fb^{-1} at $\sqrt{s} = 7$ TeV. The event yields for the cut-based analysis are listed in Tab. 4.13 for several values of m_{H}. The M_T distributions for the shape-based analysis based on the selections described in table 4.8 for $m_{\mathrm{H}} = 300$ and 400 GeV hypotheses are shown in Fig. 4.13.

Table 4.13 Background estimates,signal predictions, and observed number of events for an integrated luminosity of 4.6 fb^{-1} after the cut-based selection. The uncertainties include the statistical and systematic components (in that order). The results for signal contain only the systematic uncertainties as the statistical uncertainties are negligible. For the non-resonant background, the 68% upper limit is quoted in the case where the background prediction is zero.

m_H (GeV)	ZZ	WZ	Top/WW/ W+jets/Z$\to \tau\tau$	Z+Jets	Total Background	Expected Signal	Data
250	$36.0 \pm 0.2 \pm 2.6$	$24.0 \pm 0.3 \pm 2.0$	$65.0 \pm 3.8 \pm 5.8$	15.0 ± 15.0	$140.0 \pm 3.8 \pm 16.0$	22.0 ± 2.2	142
300	$23.0 \pm 0.2 \pm 1.7$	$13.0 \pm 0.2 \pm 1.1$	$18.0 \pm 1.1 \pm 3.0$	6.3 ± 6.3	$60.0 \pm 1.1 \pm 7.3$	21.0 ± 2.1	64
350	$16.0 \pm 0.1 \pm 1.1$	$7.0 \pm 0.2 \pm 0.6$	$2.0 \pm 0.1 \pm 1.0$	4.1 ± 4.1	$29.0 \pm 0.3 \pm 4.4$	21.0 ± 2.5	26
400	$12.0 \pm 0.1 \pm 0.9$	$4.6 \pm 0.1 \pm 0.4$	< 1.1	2.7 ± 2.7	$19.0 \pm 0.2 \pm 2.9$	17.0 ± 2.0	18
500	$7.5 \pm 0.1 \pm 0.5$	$2.0 \pm 0.1 \pm 0.2$	< 1.1	1.4 ± 1.4	$11.0 \pm 0.1 \pm 1.5$	7.4 ± 1.3	14
600	$3.9 \pm 0.1 \pm 0.3$	$0.8 \pm 0.1 \pm 0.1$	< 1.1	0.6 ± 0.6	$5.3 \pm 0.1 \pm 0.7$	2.9 ± 0.7	5

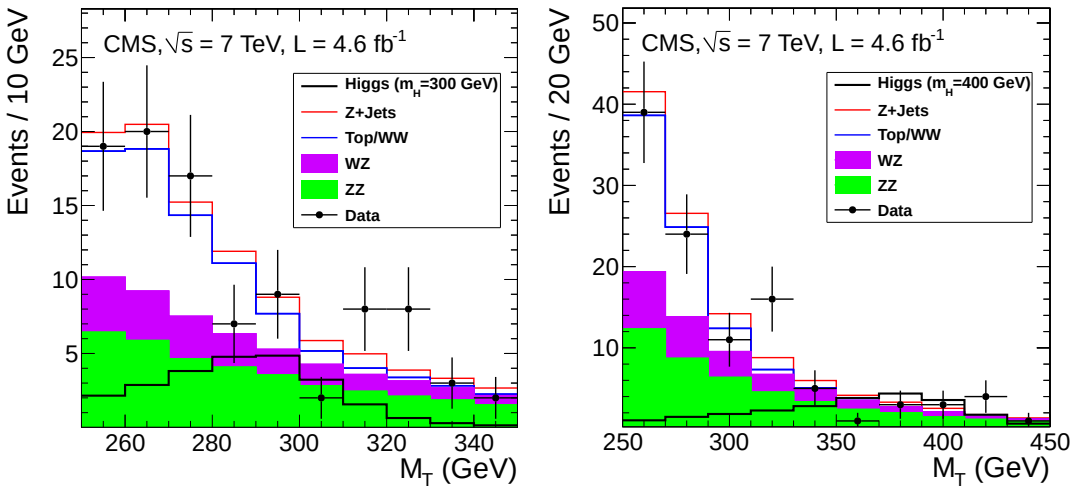

Figure 4.13 The M_T distribution for events passing m_H selections for 300 GeV (left) and 400 GeV (right). The dielectron and dimuon channels are combined.

No significant excess of events is observed over the background expectation, and so limits are set on the signal strength of the SM Higgs boson as a function of m_{H}. Fig. 4.14 shows the median expected and observed 95% CL upper limits on $\mu = \sigma/\sigma_{\mathrm{SM}}$ obtained using the $\mathrm{CL_s}$ approach. For the cut-based analysis the SM Higgs boson is excluded in the mass range 310–465 GeV at 95% CL, while the expected exclusion limit in the background-only hypothesis is 305–470 GeV. For the shape-based analysis the SM Higgs boson is excluded in the mass range 270–440 GeV at 95% CL while the expected exclusion limit for the background-only hypothesis is 290–490 GeV.

4.10 Concluding Remarks

We have seen in this chapter how the $\mathrm{H} \to ZZ \to 2\ell 2\nu$ contributed to the search of the SM Higgs boson in the high mass range of 250–600 GeV during the 2011 data-taking period. The $\mathrm{H} \to ZZ \to 2\ell 2\nu$ channel was able to exclude on its own the SM Higgs boson in the mass range of 270–440 GeV at 95% CL. These results led to a CMS publication [166], one of the first Higgs boson search papers published with the 7 TeV data collected in 2011.

When all the Higgs boson decay modes were statistically combined [157], the exclusion region was enlarged to 127–600 GeV at 95% CL as shown in Fig. 4.15. Therefore, the Higgs boson was ruled out from almost the entire landscape of m_{H} except for

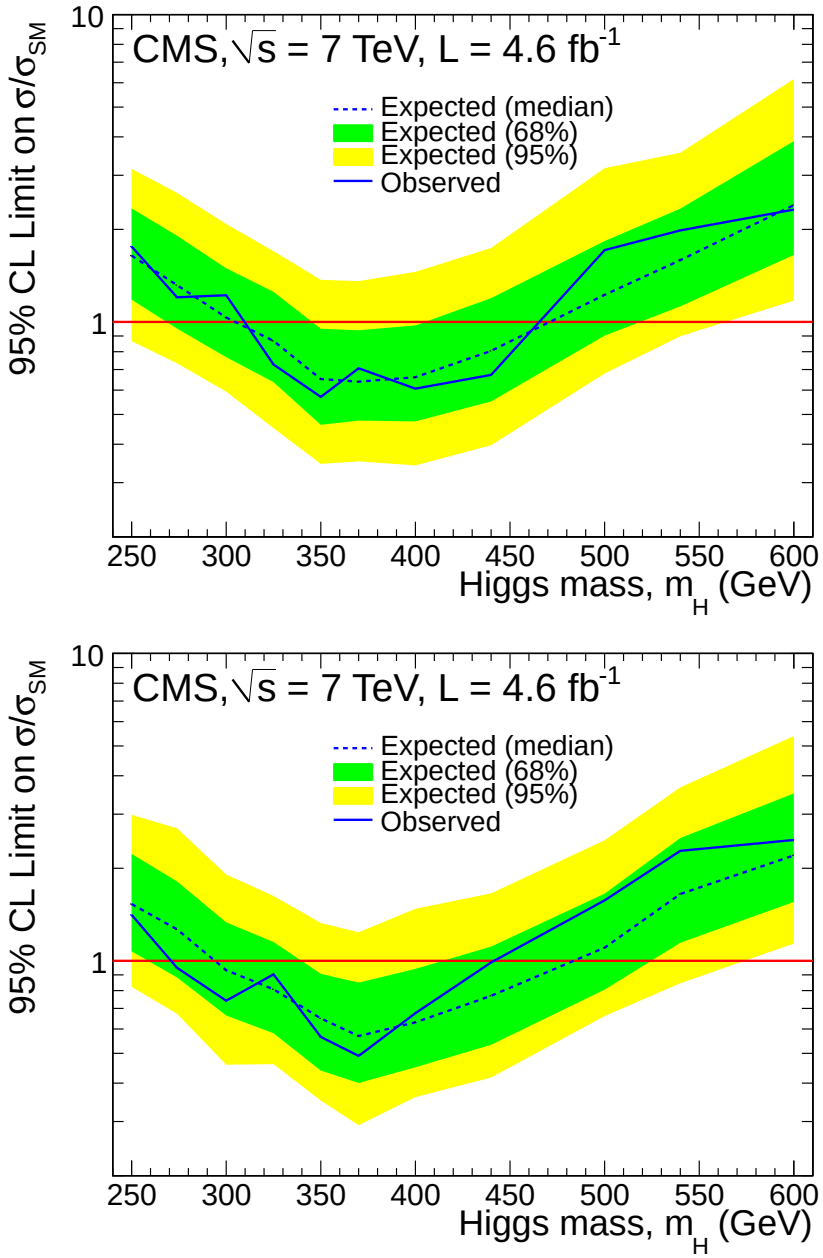

Figure 4.14 The 95% CL upper limit on the signal strength μ as a function of the Higgs boson mass m_{H} for the cut-based (top) and shape-based (bottom) analyses.

a curious excess that was seen around 125 GeV. We will see in the next chapter that it is this excess which eventually turned into the Higgs boson discovery.

Chapter 4, in full, is the reprint of the material as it appears in "Search for the standard model Higgs boson decaying in the $\mathrm{H} \to ZZ \to 2\ell 2\nu$ channel in pp collisions at $\sqrt{s} = 7$ TeV" by CMS Collaboration, JHEP 1203 (2012) 040. The dissertation author was the primary investigator and author of this paper.

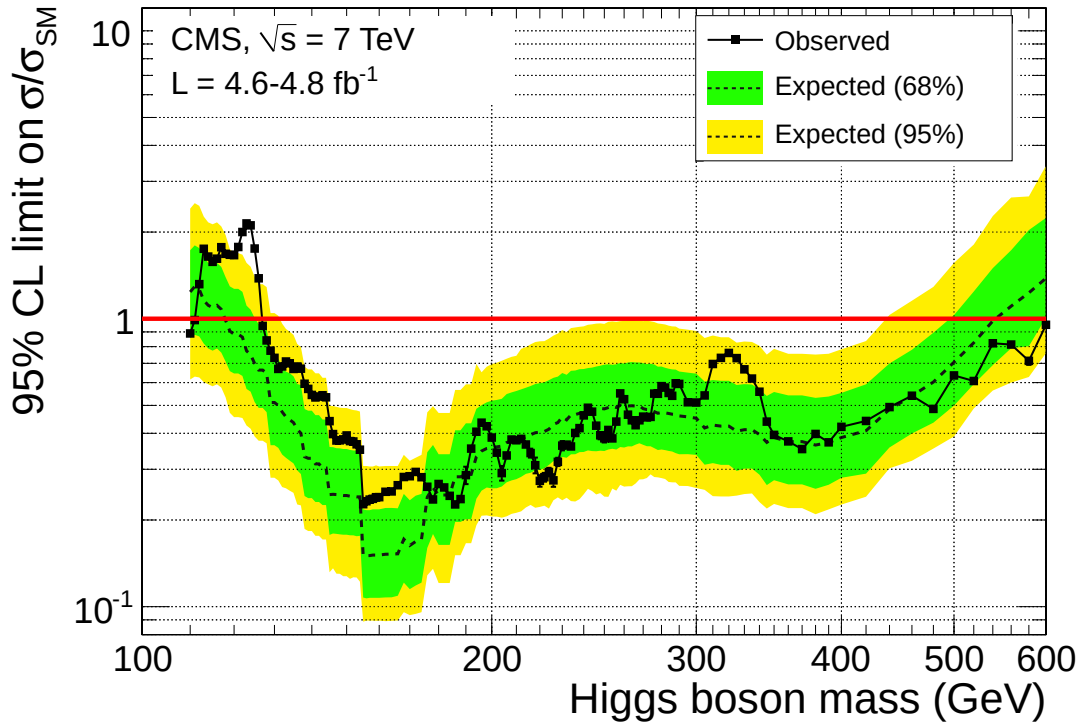

Figure 4.15 The combined 95% CL upper limit on the signal strength, as a function of the SM Higgs boson mass in the range 110–600 GeV

Chapter 5

Higgs Boson Discovery in the $\mathrm{H} \to ZZ \to 4\ell$ Channel

The $\mathrm{H} \to ZZ \to 4\ell$ channel has played a central role in the discovery of the Higgs boson and the measurement of its properties. This channel is often referred to as the gold-plated channel for the study of the Higgs boson. This can be attributed to the fact that it is the cleanest of all the Higgs boson decay modes i.e. it has the largest signal-to-background ratio of all the Higgs channels. The 4ℓ final state is fully reconstructible unlike say the $\mathrm{H} \to ZZ \to 2\ell 2\nu$ channel is which we only have partial information about the neutrino momenta. Since we can measure the electron and muon momentum very precisely in the detector, the $\mathrm{H} \to ZZ \to 4\ell$ channel has an extremely high mass resolution. Furthermore, the four-lepton final state provides an extremely fertile ground for exploring the spin/parity character of the Higgs boson.

In this chapter we will focus on the search analysis which establishes the existence of a new resonance in the 4ℓ final state. As we saw in chapter 4, the SM Higgs boson had been excluded between 127–600 GeV by the end of 2011 by combining all the Higgs searches performed using 7 TeV data. But some excess was seen building up close to $m_{\mathrm{H}} = 126$ GeV. We will see how this hint of an excess transforms into a conclusive discovery with the addition of ~ 20 fb^{-1} of data at $\sqrt{s} = 8$ TeV. While the main focus is on the low mass region, the analysis is performed in the range $m_{\mathrm{H}} \in [110, 1000]$ GeV in order to test the consistency of data with the standard model prediction right up to 1 TeV.

5.1 Signal and Background Description

The H $\rightarrow ZZ \rightarrow 4\ell$ search can be broadly categorized into two Higgs boson mass ranges. For $m_{\mathrm{H}} > 180$ GeV, the Higgs boson decays into two Z bosons that are produced on mass shell. The subsequent decays of the Z bosons result in four high p_T, isolated leptons in the event. However, if m_{H} is less than 180 GeV, one or both of the Z bosons get produced off mass shell. As m_H decreases, the p_T distribution of the lowest p_T lepton becomes softer. Fig. 5.1 shows the p_T distribution of the four leptons produced in the decay of a 126 GeV Higgs boson. We can see that in a large fraction of events the lowest p_T lepton has transverse momentum less than 10 GeV. This means that the lepton selection that we employ in this analysis, must be loose enough to pick up these soft leptons as efficiently as possible . This is a very important concern for the 4ℓ channel because the branching ratio of $ZZ \rightarrow 4\ell$ is quite small to begin with.

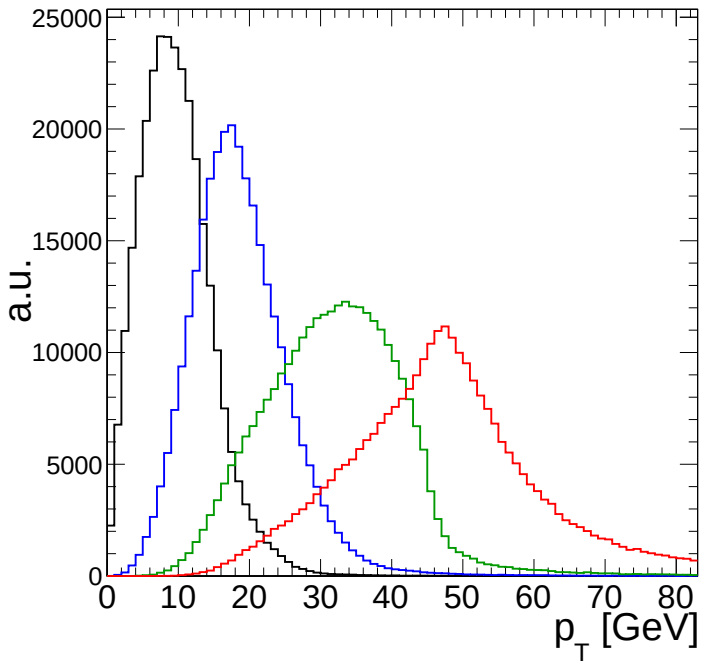

Figure 5.1 Transverse momentum distributions of the four leptons produced in the decay of a 126 GeV Higgs boson. The leptons are sorted by p_T.

A great asset of the H $\rightarrow ZZ \rightarrow 4\ell$ channel is that its background is quite small. The most dominant background in this final state is the electroweak production of ZZ or $Z\gamma^*$ bosons which further decay to four leptons. For brevity, the combination of the ZZ and $Z\gamma^*$ processes will be from here onwards referred to as simply the ZZ background.

Given the presence of one or two low p_T leptons in a 4ℓ event particularly for a Higgs boson with small m_{H}, there is also some contribution from 'reducible background' sources. These include Z+jets events in which two jets are mismeasured as leptons, or $t\bar{t} \to 2\ell 2\nu 2b$ decays in which the two b quarks decay leptonically, or $WZ \to 3\ell\nu$ events in which an additional jet gets mismeasured as the fourth lepton. But overall, the requirement of four prompt and isolated leptons reduces these reducible background contributions to levels that are subdominant to the 'irreducible' ZZ process. Table 5.1 lists the cross-section times branching ratio of the signal and background processes that are relevant to this analysis.

Table 5.1 The values of cross-section times branching ratio listed for all the relevant physics processes in the $\mathrm{H} \to ZZ \to 4\ell$ analysis at $\sqrt{s} = 7$ and 8 TeV.

Process	$\sigma\times$ BR (pb) 7 TeV	$\sigma\times$ BR (pb) 8 TeV	Pert. Order
$gg \to \mathrm{H}(110\text{-}1000\ \mathrm{GeV}) \to ZZ \to 4\ell$	$[0.03 - 6] \times 10^{-3}$	$[0.05 - 8] \times 10^{-3}$	NNLO + NNLL
$qq \to \mathrm{H}(110\text{-}1000\ \mathrm{GeV}) \to ZZ \to 4\ell$	$[0.02 - 0.7] \times 10^{-3}$	$[0.04 - 1] \times 10^{-3}$	NLO
$qq \to ZZ \to 4e(4\mu)$	66×10^{-3}	77×10^{-3}	NLO
$qq \to ZZ \to 2e2\mu$	152×10^{-3}	177×10^{-3}	NLO
$gg \to ZZ \to 4e(4\mu)$	1.7×10^{-3}	4.8×10^{-3}	NLO
$gg \to ZZ \to 2e2\mu$	3.5×10^{-3}	12×10^{-3}	NLO
$Z + X \to 2\ell + X$ ($m_{\ell\ell} > 50$ GeV)	2032	2336	NNLO
$t\bar{t} \to 2\ell 2\nu 2b$	11.5	15.76	NLO + NNLL
$WZ \to 3\ell\nu$	0.579	0.705	NLO

5.2 Event Simulation and Reweighting

The signal simulation used in the analysis has been produced by using a combination of the POWHEG and JHUGEN [167, 168] generators. The POWHEG generator is used to simulate the production of the Higgs boson at NLO while the decay of the Higgs boson to four leptons is handled by JHUGEN which correctly takes into account interference effects in the $4e$ and 4μ final states associated with the exchange of identical leptons. The signal line-shape for $m_{\mathrm{H}} \geq 400$ GeV has been modeled using the complex pole scheme (see Sec. 1.3.5).

The $qq \to ZZ$ background has been simulated using the POWHEG generator while the $gg \to ZZ$ background has been simulated with the GG2ZZ generator [163]. The Z+jets and WZ processes have been produced using the MadGraph generator while the $t\bar{t}$ background has been produced with the POWHEG generator.

The LO generators use the CTEQ6L set of PDFs while the NLO simulations are produced using the CT10 PDF set. The simulated events for all the signal and background processes are fed into PYTHIA for parton-showering. The underlying event is simulated in PYTHIA using the Z2 and Z2star tunes for 7 and 8 TeV samples respectively. Minimum bias interactions are added to every simulated event to emulate the effect of pileup as discussed in Sec. 4.3. The simulation is then reweighted to match the pileup profile observed in data.

5.3 Event Selection

The H $\rightarrow ZZ \rightarrow 4\ell$ analysis is performed in three final state configurations, namely – 4μ, $4e$ and $2e2\mu$. The essential highlights of the procedure to select 4ℓ candidate events are as follows.

- Events are required to have four muons ($\mu^+\mu^-\mu^+\mu^-$), or four electrons ($e^+e^-e^+e^-$), or a pair of muons and a pair of electrons $\mu^+\mu^-e^+e^-$, that pass certain selection requirements.

- The lepton candidates are required to be prompt, isolated and well-identified. Muons are required to have $p_T > 5$ GeV while the electrons have a p_T threshold of 7 GeV.

- Z boson candidates are constructed from dilepton combinations. Combinatoric ambiguity is resolved by first selecting the dilepton candidate with mass closest to the Z peak.

- If a photon is found in the event that is indicative of final state radiation, its momentum is added to the nearest lepton when computing the Z candidate mass, or the 4ℓ mass, of the decay angles of the leptons.

Figs. 5.2, 5.3 and 5.4 show schematic displays of a 4μ, a $4e$ and a $2e2\mu$ event respectively observed in data passing the analysis selection.

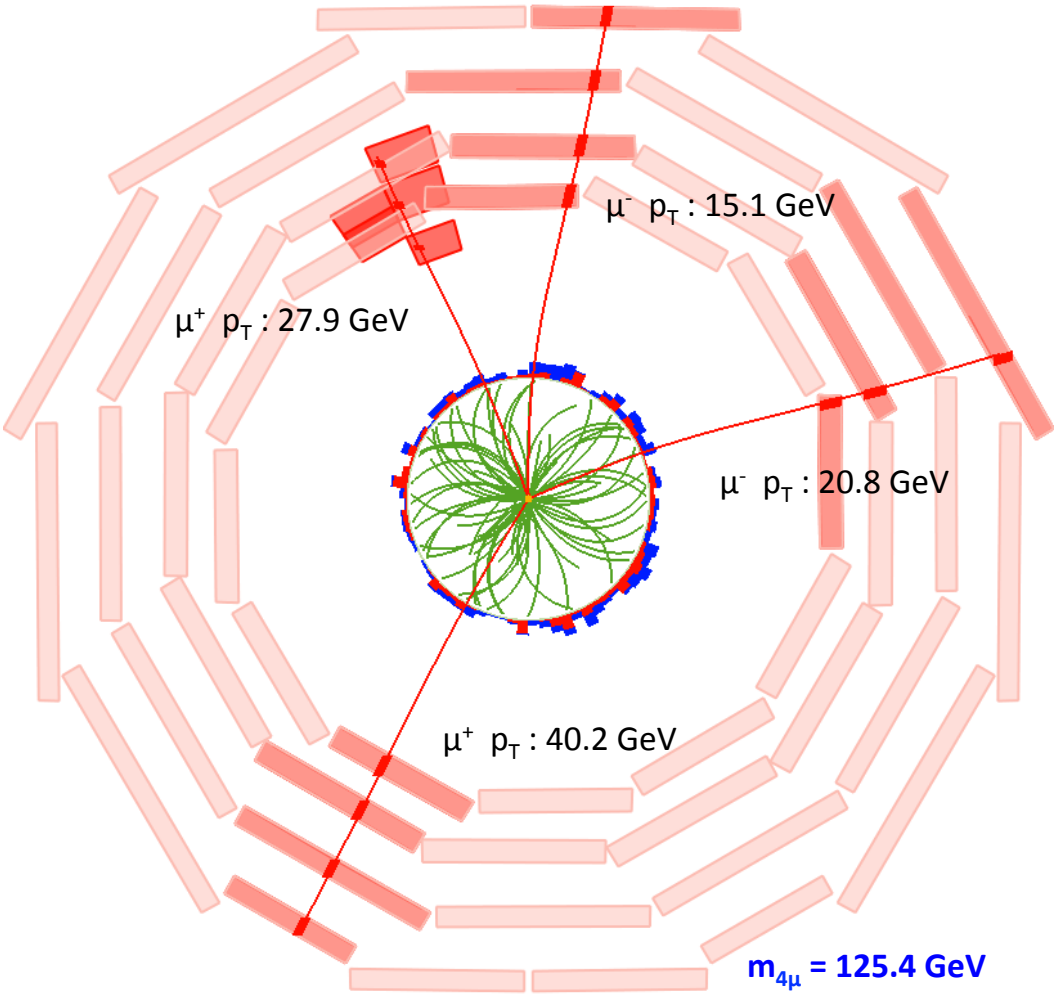

Figure 5.2 Display of a 4μ event in data passing the analysis selection. The red curves depict the trajectories of the muon candidates. The green curves depict all the reconstructed tracks in the event with $p_T > 1$ GeV. The calorimetric activity is depicted by the red (ECAL) and blue (HCAL) towers. The pair of muons with $p_T = 20.8$ and 40.2 GeV have an invariant mass of 58.2 GeV which is the closest to the nominal Z peak of all the possible $\mu^+\mu^-$ combinations. The remaining pair of muons have an invariant mass of 45.8 GeV. The invariant mass of the 4μ system is 125.4 GeV.

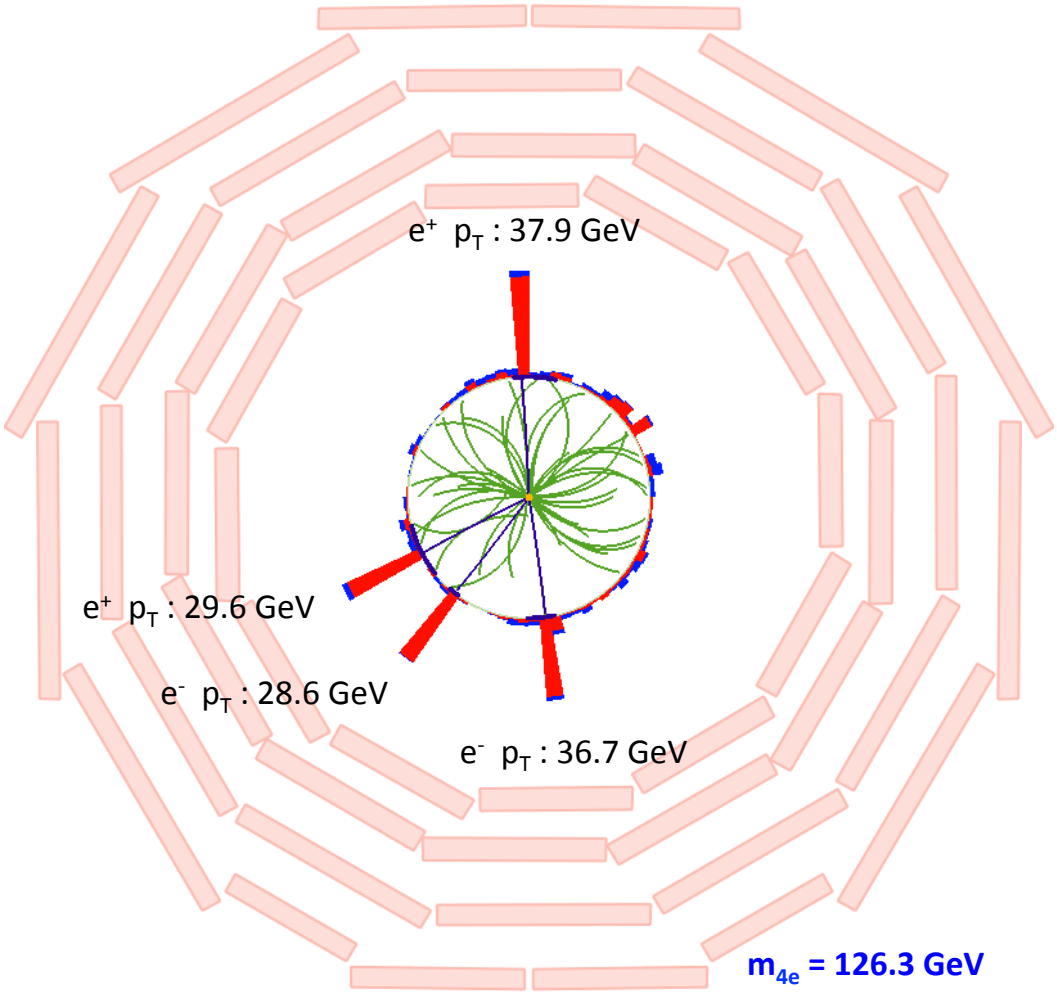

Figure 5.3 Display of a $4e$ event in data passing the analysis selection. The dark blue curves indicate the tracks of electrons. The green curves depict all the reconstructed tracks in the event with $p_T > 1$ GeV. The calorimetric activity is depicted by the red (ECAL) and blue (HCAL) towers. The pair of electrons with $p_T = 36.7$ and 37.9 GeV have an invariant mass of 74.6 GeV which is the closest to the nominal Z peak of all the possible e^+e^- combinations. The remaining pair of electrons have an invariant mass of 14.2 GeV. The invariant mass of the $4e$ system is 126.3 GeV.

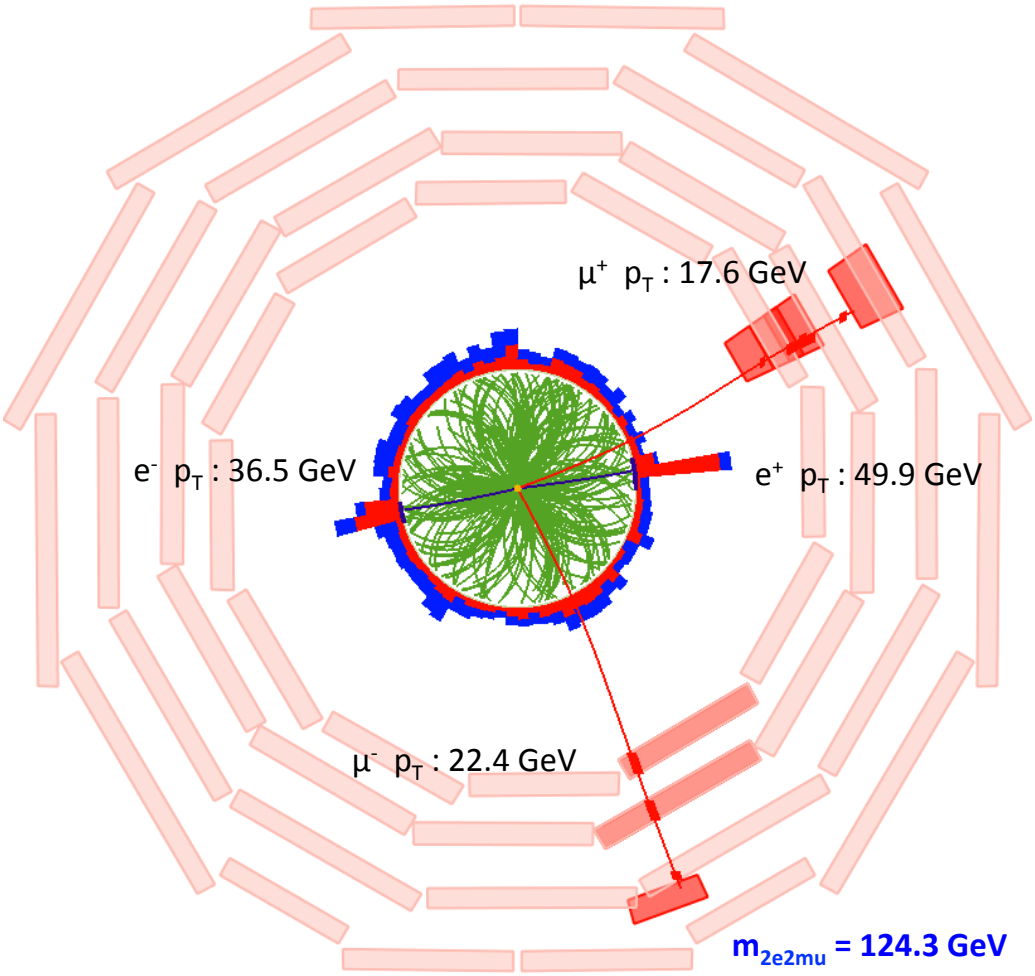

Figure 5.4 Display of a $2e2\mu$ event in data passing the analysis selection. The red curves depict the trajectories of the muon candidates while the dark blue curves indicate the tracks of electrons. The green curves depict all the reconstructed tracks in the event with $p_T > 1$ GeV. The calorimetric activity is depicted by the red (ECAL) and blue (HCAL) towers. The pair of electron candidates observed in the event form an invariant mass of 90.1 GeV which is consistent with the nominal peak of the Z boson. The muon candidates form an invariant mass of 26.9 GeV while the invariant mass of the $2e2\mu$ system is found to be 124.2 GeV.

5.3.1 Triggers

The majority of the four-lepton events used in the analysis are selected with dilepton triggers that have p_T thresholds of 17 and 8 GeV on the leading and subleading leptons respectively. The dilepton triggers have double muon, double electron, as well as electron-muon configurations. In the case of the $4e$ final state, a tri-electron trigger with thresholds of 15, 8 and 5 GeV on the electron legs is added to catch events with low p_T electrons which may fail the selection requirements of the dielectron trigger. The presence of four leptons provides a certain redundancy due to which the trigger efficiency is fairly high ($\sim 98\%$). Similar triggers are also applied in simulation and the data-to-simulation scale factors are found to be consistent with unity.

5.3.2 Electron Selection

Electron candidates used in the analysis are required to have p_T larger than 7 GeV and $|\eta| < 2.5$. A multivariate discriminant is constructed using the 'Boosted Decision Tree' (BDT) technique which helps provide optimal discrimination between genuine electrons and fake candidates. Several variables are used as inputs while building the BDT discriminant. These variables can be grouped into three categories – variables based on the momentum and geometric matching of the ECAL supercluster and the electron track, variables based on the shape of the supercluster, and variables based on the quality of the electron track. Fig. 5.5 shows the distribution of the discriminant in the case of genuine electrons from $Z \to ee$ simulation, and fake electron candidates observed in $Z + 1$ electron events in data. Electron candidates are selected based on certain requirements imposed on the BDT discriminant value that are listed in Tab. 5.2.

Table 5.2 Electron identification requirements based on the output of the BDT discriminant.

p_T (GeV)	Cut Value for $\lvert\eta\rvert < 0.8$	Cut Value for $0.8 < \lvert\eta\rvert < 1.479$	Cut Value for $1.479 < \lvert\eta\rvert < 2.5$
< 10	> 0.47	> 0.004	> 0.295
> 10	> -0.34	> -0.65	> 0.60

The electrons that pass the identification criteria are also required to be isolated. The isolation sum is computed by summing up the transverse momenta of particle-flow candidates in a $\Delta R = 0.4$ cone around the electron, and is required to be less than 40%

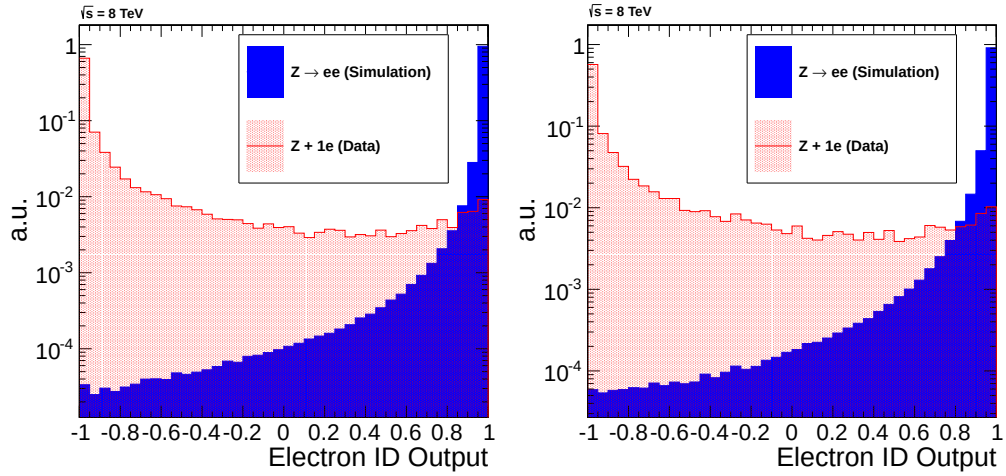

Figure 5.5 The distribution of the BDT discriminant in the case of genuine electrons from $Z \to ee$ simulation, and fake electron candidates observed in data using $Z + 1$ electron events. Plot on the left shows the distribution for electrons candidates in the barrel region ($|\eta| < 1.4442$), while the plot on the right shows the distribution for the endcaps.

of the electron p_T. A ρ-correction (see Sec. 2.3.8) is applied to the isolation sum to account for the pileup contamination.

In order to suppress the $t\bar{t}$ and $Z + b\bar{b}$ backgrounds in which two electrons are produced from the decays of b quarks, the three-dimensional impact parameter significance of the electron with respect to the primary vertex is required to be less than 4. This ensures that the electrons used in the analysis are produced promptly, as would be expected in Z boson decays. The background due to converted photons is suppressed by requiring that the electrons have no more than one missing hit in the inner layers of the tracker.

5.3.3 Electron Momentum Assignment

In the case of electrons with p_T larger than ~ 15 GeV, the momentum estimate is essentially driven by the measurement of the ECAL supercluster energy. The raw energy of the supercluster needs to be corrected to account several effects such as the lateral and longitudinal leakage of the electron shower, loss of electron energy due to interactions with the upstream tracker material, energy leakage in the gaps between ECAL crystals or between ECAL modules (physical groupings of ECAL crystals), and energy contamination due to pileup. This correction factor is derived from a multivariate

regression procedure which is trained on the response of electrons in simulation. There are about 60 variables that are used as inputs for the regression. These include variables such as the energy of the supercluster, it geometrical coordinates, variables describing the shower shape of the supercluster, variables describing the energy and position of the seed cluster and its distance from nearby cracks or gaps, the ratio of the hadronic energy behind the seed cluster to the energy of the seed cluster, the total number of energy clusters in the supercluster, energies of several subleading clusters, etc.

The corrected energy of the supercluster is then combined with the track momentum to get the best estimate of the electron momentum. The track information is particularly helpful in improving the momentum resolution of low-p_T electrons and electrons which fall into ECAL gaps. The combination of the supercluster energy and the track momentum is performed using a second regression that takes as input several variables such as the supercluster energy and its relative uncertainty, the track momentum and its relative uncertainty, the ratio of supercluster energy and track momentum and the uncertainty of this ratio, the type of electron depending on the degree of energy loss due to bremsstrahlung, whether the electron has been reconstructed using the ECAL driven or tracker-driven algorithm, etc.

The electron momentum measurement in data can have two sources of systematic difference with respect to the simulation. There may be a relative shift in the measured momentum between data and simulation, and there may be a difference in the resolution or the smearing of momentum between data and simulation. A systematic shift in momentum would lead to a difference in the predicted and observed position of the signal mass peak, while a difference in momentum resolution would cause a variation between the predicted and observed width/spread of the signal resonance. Given the high resolution that 4ℓ channel affords, it is extremely important to correct for these biases.

The momentum scale difference between data and simulation can be attributed to several factors. There could be imperfections in the corrections applied for recovering the transparency loss in the ECAL crystals. The pileup conditions and their effect on the ECAL clusters may not be correctly reproduced in simulation. Moreover, there could discrepancies in the modeling of the electron shower in the ECAL crystals, and also

imperfections in the estimation of the tracker material which could lead to differences in shower profile between data and simulation. In order to correct for these differences, the supercluster energy is corrected or scaled in data to match the prediction from simulation. A scale factor of $(1 + \Delta p)$ is applied where Δp is computed as the difference between the fitted value of the Z peak in simulation and in data, relative to the nominal Z boson mass. Several key sources of scale difference such as transparency effects, pileup conditions evolve with the period of data-taking. As a result the Δp correction is derived separately for different sets of runs. But even in a given run range the transparency loss varies as a function of pseudorapidity since the radiation dose received by the ECAL is not uniform with respect to η. Therefore, the corrections are further split into four η-bins for every run range. To remove any residual differences, a second iteration of corrections is derived separately for showering and non-showering electrons. The resulting scale-calibrated supercluster energy is then combined with the track momentum.Since the calibration procedure relies on $Z \to ee$ events in data and simulation, the bulk of its input consists of electrons in the p_T range of 20–50 GeV. However, the 4ℓ analysis accepts electrons with p_T down to 7 GeV. To correct for possible deficiencies in the calibration of low p_T electrons, a further p_T dependent correction is applied to the electron momentum. This correction is obtained by comparing the Z mass peak in data and simulation for different electron p_T bins.

The validity of the momentum scale calibration procedure can be tested by comparing the corrected dielectron resonances (Z, J/Ψ, Υ) in data with simulation. This comparison is shown in Fig. 5.6(a). We can see that for low p_T electrons ($p_T < 20$ GeV) the agreement between data and simulation is within 0.2% in the ECAL barrel region while it worsens to about 0.3% in the endcaps.

Apart from the scale calibration, the difference in momentum resolution between data and simulation also needs to be corrected. The electron momentum resolution observed in data is worse than the prediction from simulation. This can again be attributed to some inaccuracies in the modeling of the interaction of electrons with the detector. To correct for this difference, the supercluster energy of electrons in the simulation is smeared by a random factor sampled from a Gaussian distribution. The width of this Gaussian is derived for different ranges of η, and different types of electrons (showering

and non-showering), by maximizing the likelihood between data and smeared simulation. Fig. 5.6(b) shows the relative difference in resolution between data and simulation for the different categories of electrons after applying the smearing.

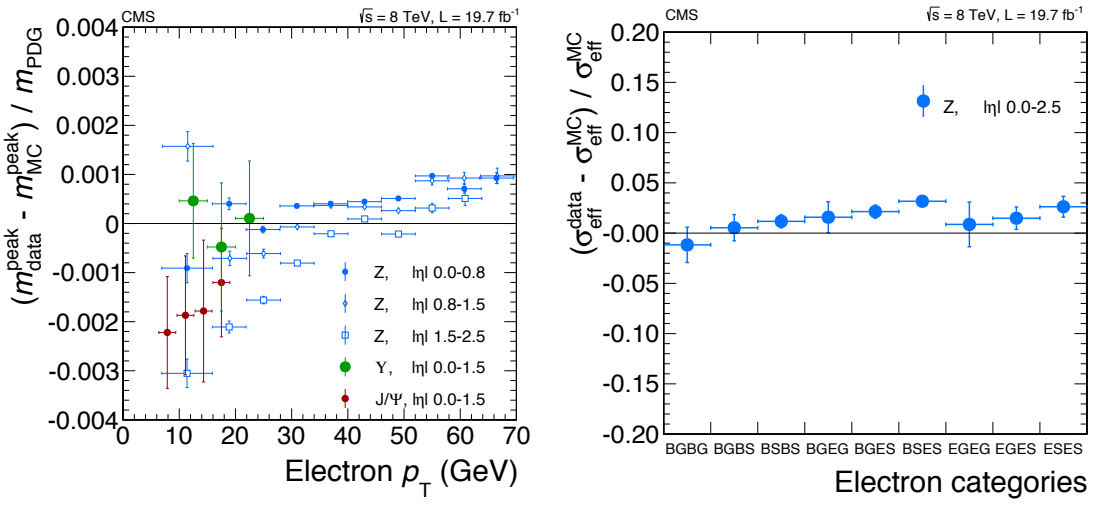

(a) (b)

Figure 5.6 Fig.(a) shows the relative difference in the Z, J/Ψ, Υ masses measured with dielectron events in data and simulation for different ranges of electron p_T and η. Fig.(b) shows the relative difference in the resolution of the $Z \to e^+e^-$ resonance between data and simulation for various electron categories. The categories are labeled as "B" for barrel electrons, "E" for endcap electrons, "S" for showering electrons, and "G" for golden or non-showering electrons.

5.3.4 Muon Selection

Muon candidates in the 4ℓ analysis are required to have $p_T > 5$ GeV and $|\eta| < 2.4$. Muons may be reconstructed by either the global muon reconstruction algorithm which performs an 'outside-in' matching between the muon track and a tracker track, or the tracker muon reconstruction algorithm which performs an 'inside-out' matching between a tracker track and muon track stubs (see Sec. 2.3.2). The tracker muon algorithm which requires a minimum of one muon segment matched to the tracker track, helps in improving the reconstruction efficiency for low-p_T (~ 5 GeV) muons that may not be able to push through the entire muon system.

The muon candidates are subjected to the identification criteria of the particle-flow algorithm. These include some fairly minimal requirements on the muon track quality in addition to ensuring that the calorimetric deposits associated with the muon

are low, as expected for a minimum ionizing particle. A further 'ghost' cleaning procedure is implemented to remove duplicate candidates that may be reconstructed by matching the muon track with two split tracks of the same particle in the tracker, or by matching a muon track to two near-by tracker tracks.

As in the case of electrons, the three-dimensional impact parameter significance of muons with respect to the primary vertex is required to be less than 4 to ensure that they are produced promptly. Furthermore, the isolation sum of the p_T of particle flow candidates in a $\Delta R = 0.4$ cone around the muon direction is required to be less than 40% of the p_T of the muon. The pileup contamination to the muon isolation sum is corrected using the $\Delta\beta$-correction (see Sec. 2.3.8).

5.3.5 Muon Momentum Assignment

Muons are the most well-measured physics objects in the CMS detector. Therefore, the 4ℓ final states with muons dominate the mass measurement of the Higgs boson signal. The muon momentum is measured by performing a combined fit of the muon tracks in the tracking system and the muon chambers. As in the case of electrons, the muon momentum needs to be calibrated in order to ensure that the momentum scale and resolution agree between data and simulation. Systematic differences may arise due to mismodeling of the detector alignement, inaccurate description of the magnetic field, incorrect modeling of multiple-scattering effects, etc.

Scale correction to be applied to the muon momentum in data is derived using the MuScleFit technique [169]. In this approach, the scale correction is modeled as a function of the track variables. The parameters of this function are then derived by performing a likelihood fit on the difference in the Z peak between data and simulation. The same approach is also used to obtain smearing factors with which to vary the momentum in simulation in order to match with the observed resolution in data. Fig. 5.7 shows the relative difference in the peak positions and resolutions of the Z, J/Ψ, Υ resonances in data and in simulation after applying the corrections.

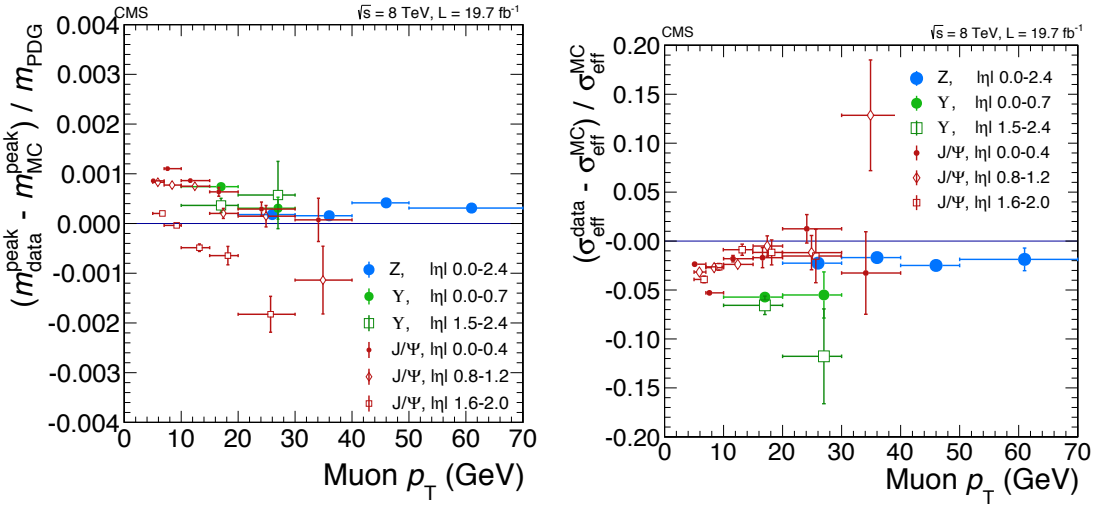

(a) (b)

Figure 5.7 Fig.(a) shows the relative difference in the peak positions of the Z, J/Ψ, Υ resonances measured using dimuon events in data and simulation. Fig.(b) shows the relative difference in the measured resolution of these resonances.

5.3.6 Reconstruction of Z and ZZ Candidates

Having selected a set of leptons in a given event, the next step is to look for a pair of Z boson candidates that can be associated with a Higgs boson decay. To understand the logic behind the procedure for reconstructing ZZ candidates, we need to consider the kinematics of the Higgs boson decay. If the Higgs boson mass is greater than $\sim$ 180 GeV, the two Z bosons are produced on mass shell. But if $m_{\mathrm{H}} < 180$ GeV, typically one of the two Z bosons is produced with an invariant mass close to the nominal Z peak, while the other Z boson accommodates the remainder of the Higgs boson mass and is produced off mass shell.

With this in mind, we start by first identifying the Z candidate whose mass is closest to the nominal Z peak of 91.188 GeV. This candidate is referred to as Z_1. From the remaining set of dilepton combinations, the pair with the highest scalar p_T sum of the leptons is chosen as the Z_2 candidate. The Z_1 candidate is required to have invariant mass between 40 and 120 GeV. This mass window helps to capture not just the signal events in which the Z_1 candidates are produced on shell but also the $\mathrm{H} \to Z^*Z^*$ decays in which the mass of the Z_1 candidate may not be close to the Z pole. In the case of the Z_2 candidate, the minimum requirement on the mass is lowered further down to 12

GeV. This requirement of $m_{Z_2} > 12$ GeV helps to suppress background events in which the Z_2 candidate originates from the dilepton decays of quarkonium resonances such as J/ψ and Υ. Additionally, all the same flavor, opposite charge dilepton combinations are required to have an invariant mass larger than 4 GeV in order to further suppress the J/$\Psi \to \ell^+\ell^-$ background. Lastly, it is required that there be atleast two leptons in the 4ℓ set with $p_T > 20$ and 10 GeV in order to meet the trigger thresholds.

5.3.7 Final State Readiation Recovery

The leptons produced in the decay of Z bosons may radiate photons and lose momentum. If we fail to account for the momentum lost to final state radiation (FSR), the measured 4ℓ mass becomes different than the mass of the ZZ system. This is detrimental to our search which looks for a bump in ZZ mass distribution. In order to have the best determination of the ZZ mass, we need to look for FSR photons and if found, associate them with the appropriate photon. The procedure for FSR recovery is as follows. We start by looking for photon candidates with $p_T > 4$ GeV in a $\Delta R = 0.5$ cone around the leptons. In the case of photons that are found to be closely aligned to the leptons ($\Delta R < 0.07$), this threshold is lowered to 2 GeV. The isolation sum of particle flow candidates around a candidate FSR photon is required to be less than the p_T of the photon. No pileup correction is made to the isolation sum to disfavor photons that may themselves be produced from pileup interactions.

Of all the photons that pass the above selection, only those are retained which help push the mass of the Z candidates (either Z_1 or Z_2) closer to 91.188 GeV while requiring $m_{\ell\ell\gamma}$ to be less than 100 GeV. If there are more than one photons that remain associated with a Z candidate, the photons are sorted in p_T, and the photon with the largest p_T is selected provided its $p_T > 4$ GeV. If there are no photons with $p_T > 4$ GeV i.e. all photon candidates are within a $\Delta R = 0.07$ cone around the leptons, then the lepton with the smallest ΔR separation is chosen. An event may therefore, have either zero, one or two FSR photons that can be associated with the leptons of the Z candidates.

When computing the mass of the ZZ system, the momentum of the FSR photons is vectorially added to the momentum of the associated leptons. The requirements of the

mass of the Z_1 and Z_2 candidates are imposed after taking into account the corrected mass of the dilepton system. Furthermore, the isolation requirements on the leptons are also imposed on the corrected isolation value which is obtained by subtracting the photon p_T from the isolation.

The FSR correction affects about 6% of signal events for $m_{\mathrm{H}} = 126$ GeV. Fig. 5.8 shows the mass distribution of H(126GeV) $\rightarrow ZZ \rightarrow 4\ell$ events in which one or two FSR photons have been identified. The improvement in mass reconstruction of the signal is clearly visible. Furthermore, the FSR recovery procedure leads to an overall improvement of about 3% in the selection efficiency, which is mainly due to the correction applied to the isolation sum. The purity of the FSR selection, that is the fraction of cases in which a genuine FSR photon is identified is about 80% for $m_{\mathrm{H}} = 126$ GeV. The impact of FSR recovery is more pronounced in the case of muons as compared to electrons. This is due to the fact FSR photons typically get absorbed in the electron superclusters and are therefore largely corrected for in the elecron reconstruction procedure itself.

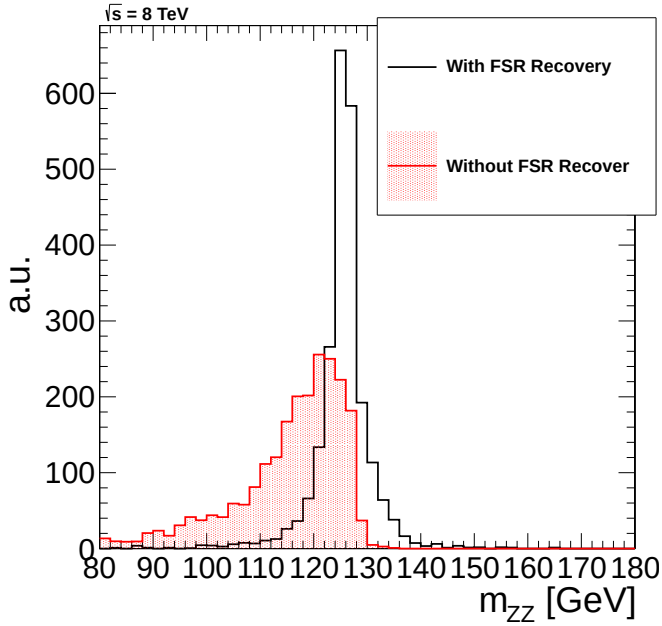

Figure 5.8 Mass distributions of H(126GeV) $\rightarrow ZZ \rightarrow 4\ell$ events with one or two FSR photons are shown both with and without the FSR correction.

5.4 Search Using $m_{4\ell}$

Having selected a set of four lepton events, let us now turn our attention to the search strategy for finding the Higgs boson signal amidst the background. The invariant mass of the four-lepton system is the most important discriminating variable between the Higgs boson signal and the background. In this section we will consider the simplest possible approach of performing a 'bump hunt' in the four-lepton mass distribution to search for the Higgs boson. The idea is to parametrize the signal and background mass distributions by analytical p.d.f.s and then search for a signal peak by performing an unbinned fit. In the next section we will extend this approach to include additional kinematic information derived from the four-lepton system to help improve the discrimination between the signal and background.

5.4.1 Signal Model

The theoretical line-shape of a low mass Higgs boson can be described with the relativistic Breit-Wigner function (see Sec. 1.3.5):

$$f_{\mathrm{BW}}^{rel}(m) = \frac{\tilde{k}}{(m^2 - m_{\mathrm{H}}^2)^2 + m_{\mathrm{H}}^2\Gamma^2} \tag{5.1}$$

where Γ is the total decay width of the Higgs boson and $\tilde{k}$ is a normalization factor. For a narrow resonance we can assume $|m - m_{\mathrm{H}}| << m_{\mathrm{H}}$ in which case the above equation reduces to:

$$f_{\mathrm{BW}}(m) = \frac{k}{(m - m_{\mathrm{H}})^2 + \frac{\Gamma^2}{4}} \tag{5.2}$$

While the Breit-Wigner function (BW) defined in eq. 5.2 effectively describes the theoretical line-shape of the Higgs boson, the resonance that we expect to observe in data gets smeared due to the finite momentum resolution of the detector. Hence, the reconstructed signal line-shape is modeled as a convolution of the BW function and a double sided Crystal Ball (dCB) function which captures the momentum scale and resolution effects. The dCB function is defined as follows

$$f_{\mathrm{dCB}}(m) = \begin{cases} e^{-(m-m_0)^2/2\sigma^2} & \text{if } -\alpha_L < (m-m_0)/\sigma < \alpha_R \\ A_L(B_L - (m-m_0)/\sigma)^{-n_L} & \text{if } (m-m_0)/\sigma < \alpha_L \\ A_R(B_R + (m-m_0)/\sigma)^{-n_R} & \text{if } (m-m_0)/\sigma > \alpha_R \end{cases} \tag{5.3}$$

where $A_L = \left(\frac{n_L}{\alpha_L}\right)^{n_L} \times e^{-\alpha_L^2/2}$, $B_L = \left(\frac{n_L}{\alpha_L} - \alpha_L\right)$, $A_R = \left(\frac{n_R}{\alpha_R}\right)^{n_R} \times e^{-\alpha_R^2/2}$, $B_R = \left(\frac{n_R}{\alpha_R} - \alpha_R\right)$. The parameter m_0 represents the overall shift in the reconstructed signal peak compared to m_{H} while the parameter σ represents the detector resolution. The parameters α_L, α_R, n_L and n_R represent the non-Gaussian tails of the detector response. The parameters of the dCB function are obtained by fitting the dCB $\otimes$ BW p.d.f. to the reconstructed signal mass distribution in simulation.

The dCB $\otimes$ BW function describes the signal mass distribution very well for Higgs boson masses up to 400 GeV. For $m_{\mathrm{H}} < 180$ GeV, the natural width of the Higgs boson is much smaller than the detector resolution, and so a dCB function can by itself describe the signal shape very effectively. Fig. 5.9 shows the mass distribution of the SM Higgs boson with $m_{\mathrm{H}} = 126$ GeV in the $4\mu, 2e2\mu$ and $4e$ channels fitted with the dCB function.

In the case of a high mass Higgs boson ($m_{\mathrm{H}} = 400$ GeV or higher), the Breit-Wigner approximation breaks down and the complex pole scheme (see Sec. 1.3.5) needs to be used. Moreover, in this mass region the interference between the Higgs boson signal and the $gg \to ZZ$ background becomes non-negligible. While the interference does not have a significant impact on the signal cross-section, it does change the line-shape of the signal mass distribution. Taking all these factors into account the signal model for m_{H} larger than 400 GeV is modeled using a convolution of a dCB function with a relativistic-Breit-Wigner-like function $f_{\mathrm{HM}}(m)$ defined as follows

$$f_{\mathrm{HM}}(m) = \frac{\kappa.m}{(m^2 - m_{\mathrm{H}}^2)^2 + m^2\Gamma_{\mathrm{HM}}^2} \tag{5.4}$$

where κ is a normalization factor. The dCB function in this case does not physically represent the detector response as such, but is simply a part of the description of the signal model. The parameters of the dCB function and the Γ_{HM} parameter of f_{HM} are

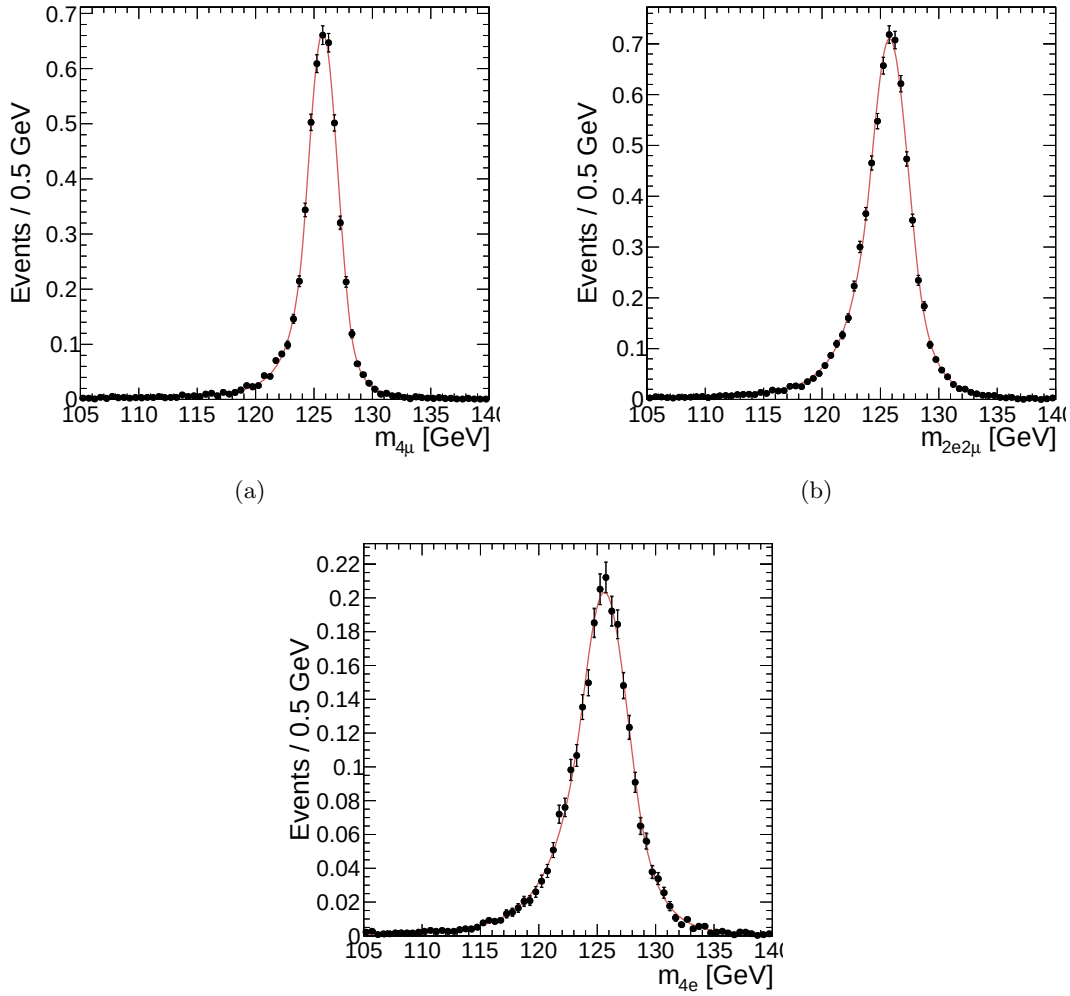

Figure 5.9 Four-lepton invariant mass distribution of the SM Higgs boson with $m_{\mathrm{H}} = 126$ GeV is shown for the 4μ, $2e2\mu$ and $4e$ channels. A dCB function is fitted to the reconstructed mass distribution in each channel.

fitted to the reconstructed mass distribution. Fig. 5.10 shows the mass distribution of the SM Higgs boson with $m_{\mathrm{H}} = 500$ GeV in the $4\mu, 2e2\mu$ and $4e$ channels fitted with the dCB $\otimes$ f_{HM} function.

5.4.2 ZZ Background Model

The electroweak ZZ and $Z\gamma^*$ production forms the main background in the 4ℓ analysis. The ZZ background gets contributions from two production mechanisms. A part of the ZZ background can be attributed to the $gg \to ZZ$ process which is shown in Fig. 5.11(a). But the major chunk of the ZZ background comes from the

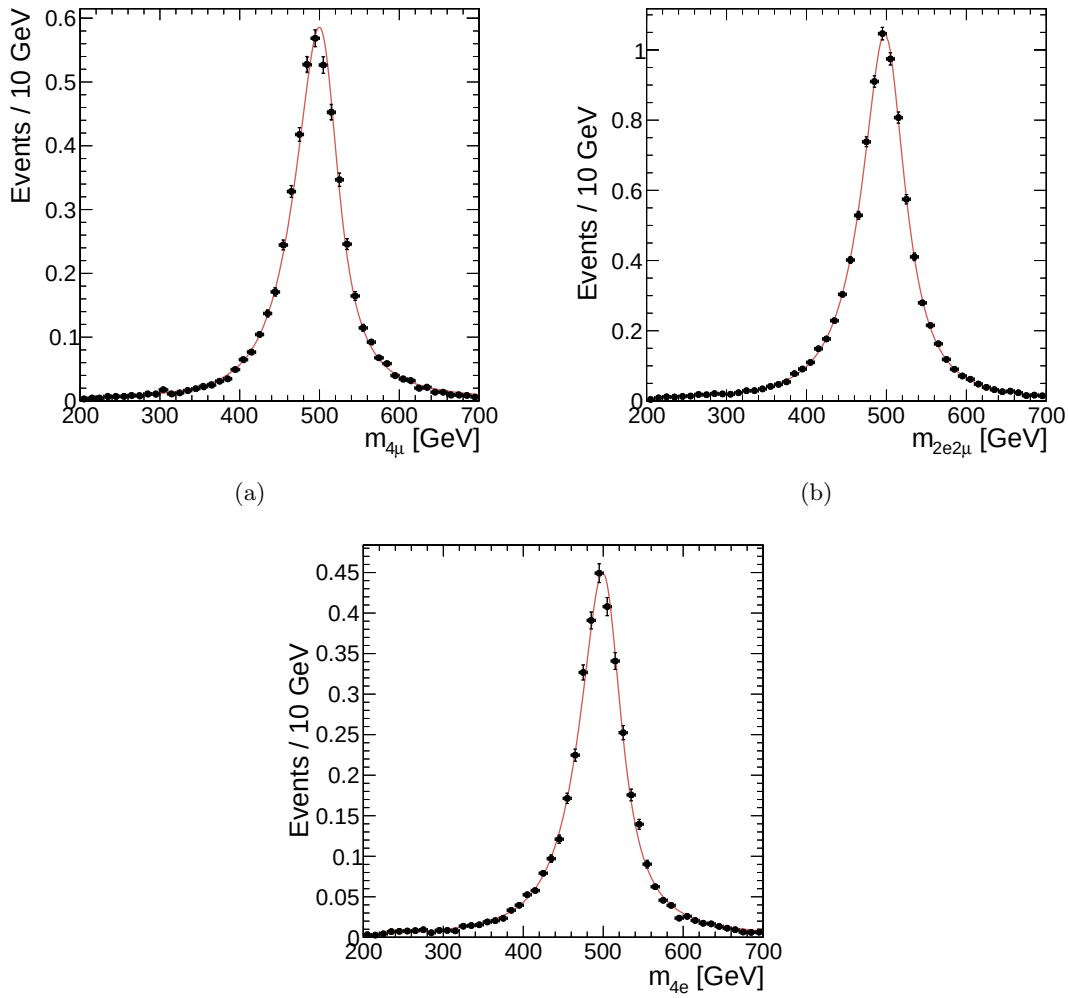

Figure 5.10 Four-lepton invariant mass distribution of the SM Higgs boson with $m_{\mathrm{H}} = 500$ GeV is shown for the 4μ, $2e2\mu$ and $4e$ channels. A dCB $\otimes$ f_{HM} function is fitted to the reconstructed mass distribution in each channel.

$qq \to ZZ$ process shown in Fig. 5.11(b). The $qq \to ZZ$ background also has an s-channel contribution as shown in Fig. 5.11(c) which essentially produces a $Z \to 4\ell$ resonance. While the irreducible background for the 4ℓ analysis is referred to as the 'ZZ' background in this thesis, the contributions from the $Z\gamma^*$ process are also taken into account.

The estimate of the ZZ background is derived from simulation. The invariant mass distributions of the $gg \to ZZ$ and $qq \to ZZ$ processes are shown in Fig. 5.12(a) and 5.12(b) respectively. The shapes of these distributions are modeled using empirical functions $f_{qq\to ZZ}$ and $f_{gg\to ZZ}$ which are defined as follows

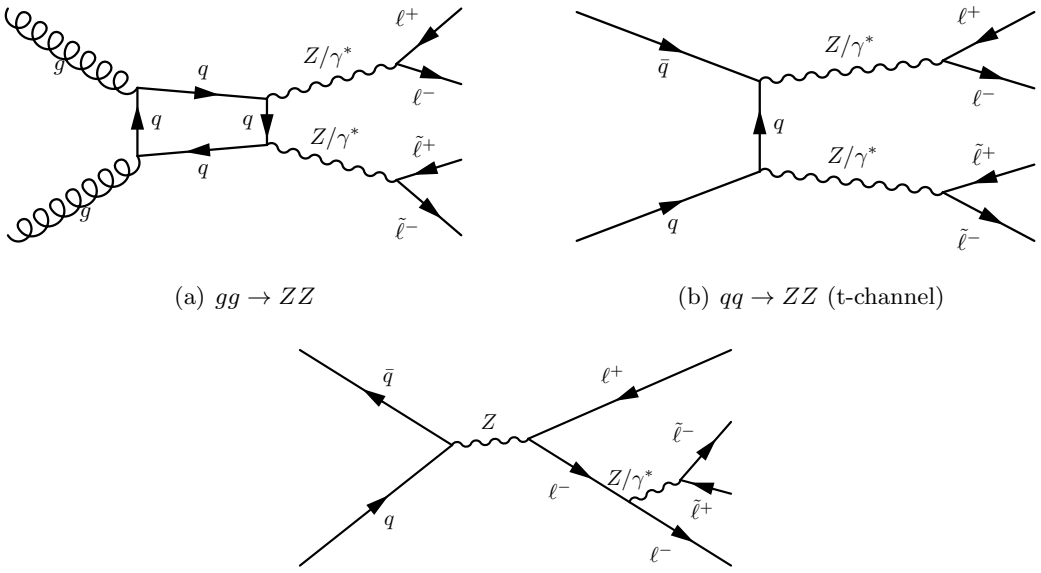

(a) $gg \to ZZ$

(b) $qq \to ZZ$ (t-channel)

(c) $qq \to ZZ$ (s-channel)

Figure 5.11 Feynman diagrams for the ZZ background.

$$
\begin{aligned}
f_{qq\to ZZ}(m) \;=\; & \left(\tfrac{1}{2}+\tfrac{1}{2}\times \mathrm{Erf}(\tfrac{m-a_0}{a_1})\right)\left(\tfrac{a_3}{1+e^{(m-a_0)/a_2}}\right)+ \\
& \left(\tfrac{1}{2}+\tfrac{1}{2}\times \mathrm{Erf}(\tfrac{m-a_4}{a_5})\right)\left(\tfrac{a_7}{1+e^{(m-a_4)/a_6}}+\tfrac{a_9}{1+e^{(m-a_4)/a_8}}\right)+ \\
& \left(\tfrac{1}{2}+\tfrac{1}{2}\times \mathrm{Erf}(\tfrac{m-a_{10}}{a_{11}})\right)\left(\tfrac{a_{13}}{1+e^{(m-a_{10})/a_{12}}}\right)
\end{aligned}
\tag{5.5}
$$

$$
\begin{aligned}
f_{gg\to ZZ}(m) \;=\; & \left(\tfrac{1}{2}+\tfrac{1}{2}\times \mathrm{Erf}(\tfrac{m-b_0}{b_1})\right)\left(\tfrac{b_3}{1+e^{(m-b_0)/b_2}}\right)+ \\
& \left(\tfrac{1}{2}+\tfrac{1}{2}\times \mathrm{Erf}(\tfrac{m-b_4}{b_5})\right)\left(\tfrac{b_7}{1+e^{(m-b_4)/b_6}}+\tfrac{b_9}{1+e^{(m-b_4)/b_8}}\right)
\end{aligned}
\tag{5.6}
$$

where 'Erf' stands for the error function given by $\mathrm{Erf}(x) = 2/\sqrt{\pi}\int_0^x e^{-t^2}dt$. The parameters a_0–a_{13} and b_0–b_9 are obtained by fitting the $f_{qq\to ZZ}$ and $f_{gg\to ZZ}$ functions to the $qq \to ZZ$ and $gg \to ZZ$ mass distributions respectively in the various 4ℓ channels.

5.4.3 Reducible Background Model

The 4ℓ analysis searches for events with four leptons that pass certain selection criteria - they are required to be prompt, isolated and well-identified. Since the expected yield of signal events is quite low, the lepton selection criteria are designed to be as loose and inclusive as possible. While a large chunk of the background events that pass the

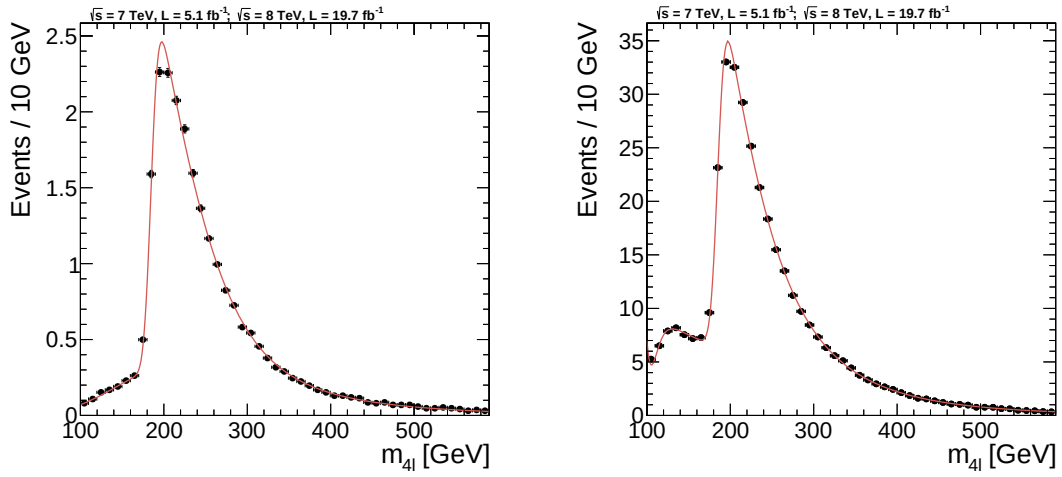

(a) $gg \to ZZ$ (b) $qq \to ZZ$

Figure 5.12 Four-lepton invariant mass distributions for the $gg \to ZZ$ (left) and $qq \to ZZ$ (right) backgrounds are shown. The $4\mu, 2e2\mu$ and $4e$ channels are combined. The shapes of the mass distributions are parameterized using empirical functions $f_{qq\to ZZ}$ and $f_{gg\to ZZ}$.

event selection consist of four genuine leptons produced in the decays of Z bosons, a part of the background originates from processes in which one or two jets get mismeasured as leptons, or processes in which leptons are produced from decays of b-quarks. As discussed in Sec. 5.1 this reducible background can be attributed to processes such as Z+jets, fully leptonic $t\bar{t}$ decays, fully leptonic WZ decays, etc.

The reducible background is estimated in this analysis using a data-driven approach. The underlying technique is the same as that used in the estimation of the reducible W+jets background in the $\mathrm{H} \to WW \to 2\ell 2\nu$ analysis [170]. The first step is to identify events that have a dilepton candidate that passes the Z_1 selection requirements of the analysis. These dilepton candidates have very little contamination from fake leptons and consist overwhelmingly of Z boson decays. We then consider a subset of these events in which there are a pair of leptons in addition to the Z_1 candidate that pass certain loose selection criteria. The 'loose' leptons are required to have the same flavor and opposite charge. Moreover, they are required to pass p_T, η and impact parameter requirements imposed in the analysis. The electrons are required to have fewer than two missing hits in the inner pixel layers while the muons are subjected to the duplicate cleaning procedure. The $Z_1 + 2$ loose lepton candidates are subjected to the same kinematic and combinatorial selections that are imposed on the ZZ candidates in

the analysis. The FSR recovery procedure is also extended to these candidates.

The next step is to device a strategy to estimate the reducible background, which from hereon is termed as the $Z + X$ background, from the $Z_1 + 2$ loose lepton control sample. In order to explain this strategy, let us start by establishing certain lepton categories. A lepton can be categorized as a fake/bad lepton (labeled by letter 'B') or a genuine lepton (labeled by letter 'G') depending on whether or not it originates from a reducible source (jets, b decays, etc.) Similarly, a lepton can be categorized as a passing (lepton labeled by letter 'P') or a failing lepton (labeled by letter 'F') depending on whether or not is passes the lepton selection imposed in the analysis.

Let f denote the fake rate or the probability of a fake lepton to pass the lepton selection of the analysis. Let p denote the prompt rate or the probability of a genuine lepton to pass the lepton selection requirements. The prompt rate is essentially the efficiency of lepton selection that is measured in data using the tag-and-probe method. In order to compute the fake rate the following procedure is adopted. First, a clean sample of Z events is selected by imposing the Z_1 selection on dilepton candidates. A subset of these events is selected such that there is exactly one loose lepton in the event in addition to the Z_1 daughters. The Z_1 mass requirement is tightened to $m_{\ell\ell} \in [81.188, 101.188]$ GeV. This substantially removes events in which a fake lepton gets associated with the Z_1 candidate while the genuine lepton from Z decay is counted as the additional loose lepton. The $E_T^{\rm miss}$ in the event is required to be less than 25 GeV to suppress WZ events in which there are three genuine leptons. Furthermore, the invariant mass of the same flavor, opposite sign lepton pairs is required to be greater than 4 GeV in order to be consistent with a similar requirement imposed in the selection of 4ℓ candidates in the analysis. The collection of Z_1+1 loose lepton events that pass these requirements is then binned in p_T and η. The loose leptons in these events are almost entirely fake leptons. Therefore the fraction of loose leptons that pass the lepton selection requirements in each p_T, η bin gives the fake rate for leptons in that p_T, η range. Fig. 5.13 shows that fake rates for muons and electrons computed in bins of p_T for the central and forward regions of the detector.

Now let us imagine that we have a set of N loose leptons. Let N_G be the number of genuine leptons and N_B be the numbers of fake leptons in this set. Similarly let N_P

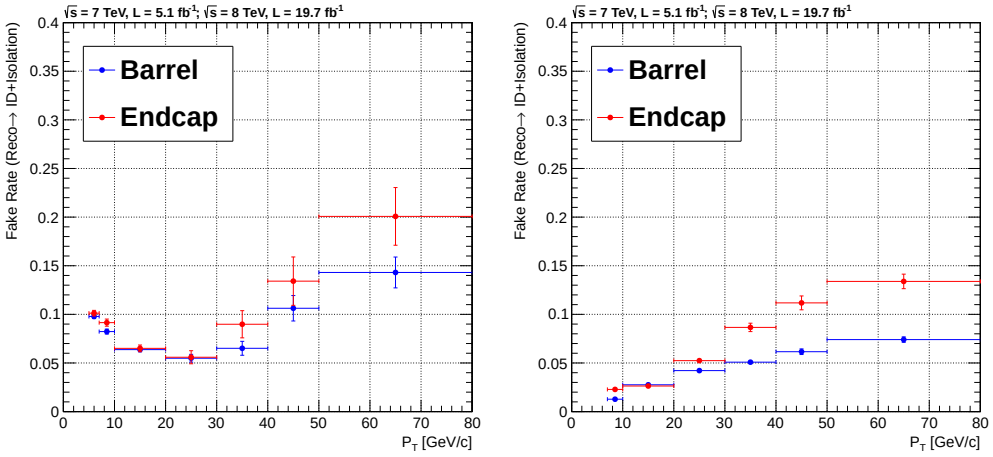

Figure 5.13 Fake rate of muons(left) and electrons(right) as a function of p_T. The fakes rates are computed separately for the barrel ($|\eta| < 1.479$) and endcap($|\eta| > 1.479$) regions.

be the number of passing leptons and N_F be the number of failing leptons. We do not have a priori information about N_G and N_B. In data, all we can know is N_P and N_F i.e. the number of lepton candidates that pass or fail our selection. From this information we want to determine the number of fake leptons N_B. We can determine N_B with the help of the following set of relations

$$\begin{aligned} N &= N_G + N_B \\ &= N_P + N_F \\ N_P &= pN_G + fN_B \\ N_F &= (1-p)N_G + (1-f)N_B \end{aligned} \tag{5.7}$$

Here we have a system of linear equations which we can solve for N_B. This gives us $N_B = \frac{1}{p-f}[pN_P - (1-p)N_F]$. What we really want to know is not the actual number of fake leptons (N_B) in the set of N leptons but rather the number of fake leptons that pass our selection requirements. Therefore, what we are looking for is $N_B^{pass} = fN_B = \frac{f}{p-f}[pN_P - (1-p)N_F]$. In the limit where the prompt rate is close to unity (or the lepton selection efficiency is high) this relation takes the form $fN_B = \frac{f}{1-f}N_P$.

Now, in our Z+2 loose lepton control sample we are dealing with a pair of leptons. This means that in a set of $Z+2$ loose lepton events we would have N_{GG}, N_{GB}, N_{BG}, N_{BB} events with zero one or two fake leptons and similarly we would have N_{PP}, N_{PF}, N_{FP}, N_{FF} events with zero, one or two leptons failing the lepton selection. A linear

system of equations can be constructed in order to relate (N_{GG}, N_{GB}, N_{BG}, N_{BB}) with (N_{PP}, N_{PF}, N_{FP}, N_{FF}). Our goal is to find the fraction of $N_{GB} + N_{BG} + N_{BB}$ events that pass the lepton selection requirements. This is given by the following relation

$$N_{BG}^{pass} + N_{GB}^{pass} + N_{BB}^{pass} = \frac{-\epsilon_1\epsilon_2 N_{FF} + \epsilon_2 N_{PF} + \epsilon_1 N_{FP} + (\epsilon_1\epsilon_2\eta_1\eta_2 - \epsilon_1\eta_1 - \epsilon_2\eta_2)N_{PP}}{(1-\epsilon_1\eta_1)(1-\epsilon_2\eta_2)} \tag{5.8}$$

where $\epsilon = \frac{1-p}{p}$, $\eta = \frac{f}{1-f}$, and the subscripts 1,2 refer to the two loose leptons. Essentially, we can obtain the reducible background yield by assigning the following weights to the $Z + 2$ loose leptons control sample on an event-by-event basis depending on whether or not either of the two loose leptons passes or fails the lepton selection.

$$\begin{aligned} w_{FF} &= -\epsilon_1\epsilon_2[(1-\epsilon_1\eta_1)(1-\epsilon_2\eta_2)]^{-1} \\ w_{PF} &= \epsilon_2[(1-\epsilon_1\eta_1)(1-\epsilon_2\eta_2)]^{-1} \\ w_{FP} &= \epsilon_1[(1-\epsilon_1\eta_1)(1-\epsilon_2\eta_2)]^{-1} \\ w_{PP} &= (\epsilon_1\epsilon_2\eta_1\eta_2 - \epsilon_1\eta_1 - \epsilon_2\eta_2)[(1-\epsilon_1\eta_1)(1-\epsilon_2\eta_2)]^{-1} \end{aligned} \tag{5.9}$$

Fig. 5.14 shows the mass ditribution of $Z + 2$ loose lepton events in which both the loose leptons fail the lepton selection (which corresponds to N_{FF} events). Similarly, Fig. 5.15 shows the mass distribution of events in the control sample where one of the two leptons passes the lepton selection (which corresponds to $N_{PF} + N_{FP}$ events). We see that the Z+jets simulation significantly understimates the yield of $Z_1 + 2$ loose muons. Fig. 5.16 shows the mass distribution of the $Z + X$ background in the 4μ, $2e2\mu$ and $4e$ channels derived using reweighted $Z + 2$ loose lepton events. The background shape is parametrized as either a single Landau function or a sum of two Landau functions for the different channels.

5.4.4 Systematic Uncertainties

Normalization Uncertainties

There are several sources that contribute to systematic errors in the evaluation of signal and background yields. The signal and the ZZ background is estimated from simulation. The uncertainty on the theoretical cross-sections of these processes is evaluated

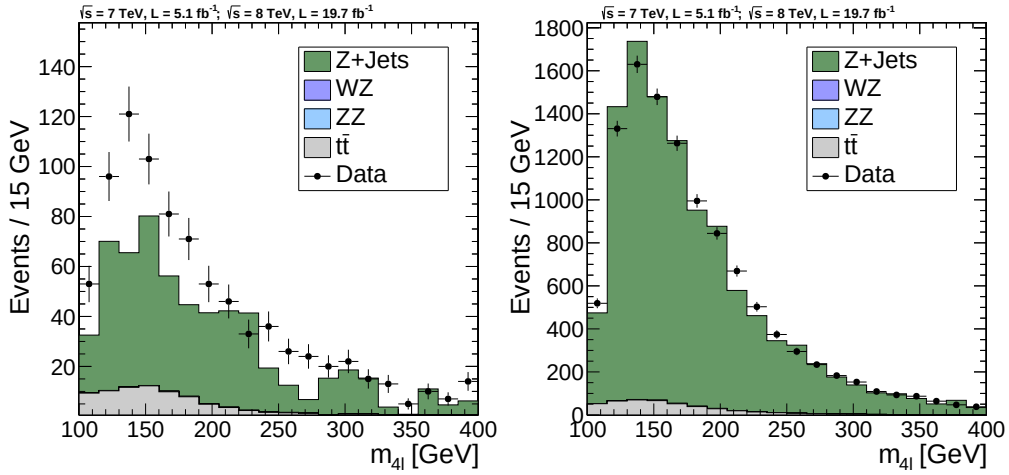

Figure 5.14 Four-lepton mass distribution of $Z_1 + \mu^+\mu^-$ events (left) and $Z_1 + e^+e^-$ events (right) in which both the loose leptons fail the analysis selection.

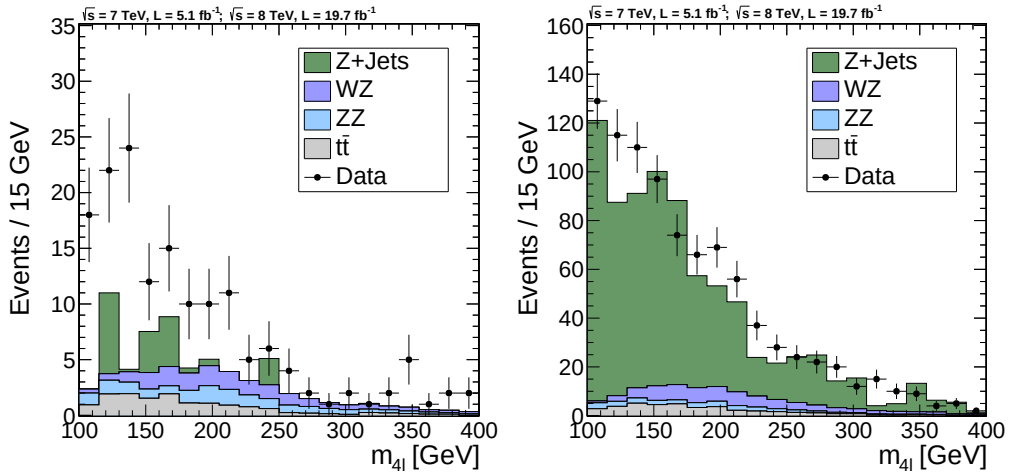

Figure 5.15 Four-lepton mass distribution of $Z_1 + \mu^+\mu^-$ events (left) and $Z_1 + e^+e^-$ events (right) in which one of the two loose leptons fails the analysis selection.

by varying the QCD renormalization and factorization scales and by varying the PDF sets used for Monte Carlo generation. The uncertainties on the signal cross-sections are reported as a function of m_{H} for all the Higgs boson production modes in [103,104]. For $m_{\mathrm{H}} > 400$ GeV the uncertainty on the complex pole scheme and interference corrections to the signal line-shape is covered by assigning a 5% systematic on the Γ_{HM} parameter of the $f_{\mathrm{HM}}(m)$ function defined in eq. 5.4. The uncertainties on the ZZ background processes have been evaluated as a function of $m_{4\ell}$ and are found to vary between 3–10% for the $qq \to ZZ$ background and between 25–50% for the $gg \to ZZ$ background.

The uncertainty on the measured luminosity of estimated to be 2.2% for the 7 TeV data and 2.6% for the 8 TeV. The uncertainty on the data-to-simulation scale

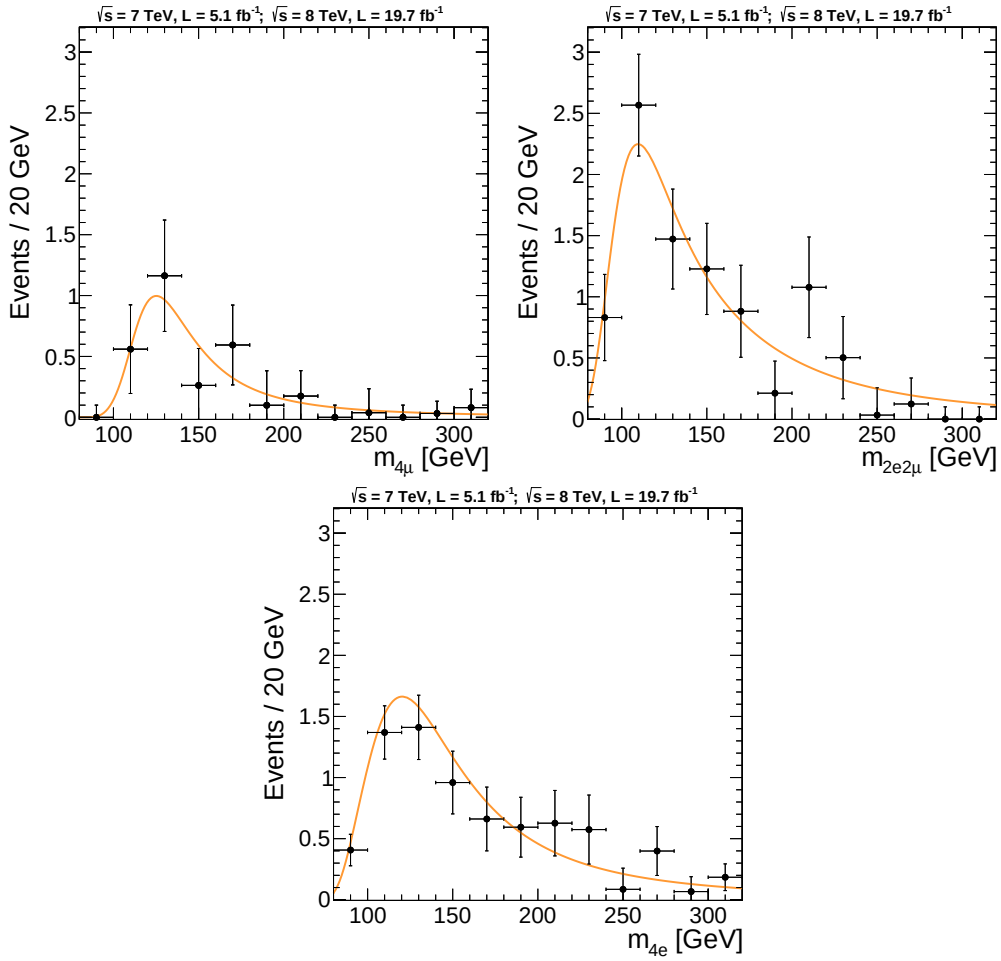

Figure 5.16 Four-lepton mass distribution of the $Z + X$ background in the 4μ (left), $2e2\mu$ (center) and $4e$ (right) channels.

factors for the lepton selection efficiency, when propagated to the signal yield varies between 3–11% depending on the 4ℓ channel and value of m_{H}. The uncertainty on the reducible background is estimated by looking at the variation in the fake rates of leptons in the simulation of different types of processes such as $Zb\bar{b}$ and $t\bar{t}$ which have leptons produced in b decays, Z+light jets in which leptons are essentially mismeasured jets, and $Z\gamma$ events in which electrons are produced in photon coversions. The statistical uncertainty due to the limited number of events in the Z+ two loose leptons control sample is also taken into account. Moreover, a closure test is performed in data by testing the $Z + X$ estimation procedure on $Z + e^{\pm}\mu^{\mp}$ events. This leads to uncertainty estimates of 40%,25% and 20% for the $Z+X$ background in the 4μ, $2e2\mu$ and $4e$ channels respectively.

Shape Uncertainties

Apart from the normalization uncertainties on the signal and background yields, there are shape uncertainties associated with the scale and resolution of the signal peak. These uncertainties are evaluated by propagating the per-lepton data-to-simulation differences in scale and resolution observed using the Z, J/Ψ and Υ resonances to the Higgs boson mass shape. The scale uncertainty is estimated to be 0.1%, 0.1% and 0.3% for the 4μ, $2e2\mu$ and $4e$ channels respectively and is assigned to the peak of the dCB function used in the modeling of the signal shape. Similarly, the resolution uncertainty is estimated to be 20% for all the channels and is assigned to the width of the dCB function.

Table 5.3 summarizes all the systematic uncertainties that are included in the analysis.

Table 5.3 Summary of all the systematic uncertainties affecting the H $\rightarrow ZZ \rightarrow 4\ell$ analysis.

Source	Uncertainty [%]
Luminosity	2.2 (7 TeV), 2.6 (8 TeV)
Uncertainty on gg partonic luminosity	7–10
Uncertainty on qq partonic luminosity	2–5
QCD scale for $gg \rightarrow$ H production	8–10
QCD scale for $qq \rightarrow$ H production	4–8
QCD scale for $gg \rightarrow ZZ$ production	3–7
QCD scale for $qq \rightarrow ZZ$ production	25–50
H $\rightarrow 4\ell$ branching ratio	2
Lepton identification and isolation	1–2 (4μ), 2–4 ($2e2\mu$), 5–11 ($4e$)
Lepton momentum scale	0.1 (4μ, $2e2\mu$), 0.3 ($4e$)
Lepton momentum resolution	20
Reducible background yield	40 (4μ), 25 ($2e2\mu$), 20 ($4e$)
High mass signal line-shape	5% (on Γ_{HM})

5.4.5 Results

We have seen at the end of the last chapter that the SM Higgs boson had been excluded in the high mass region with the data collected in 2011 at $\sqrt{s} = 7$ TeV. Therefore, lets start by looking at events with $m_{4\ell} > 150$ GeV to test the agreement between data and the background prediction assuming there to be no signal in this region. Tab. 5.4 summarizes this comparison and we see that our estimate of the ZZ background, which is based entirely on simulation, is consistent with observation.

Table 5.4 Yield of four-lepton events with $m_{4\ell} > 150$ GeV observed in data and the predictions for the ZZ and $Z + X$ backgrounds. Results from 7 and 8 TeV datasets have been combined.

	Event yield in 4μ channel	Event yield in $2e2\mu$ channel	Event yield in $4e$ channel	Total event yield
ZZ background	106 ± 13	177 ± 23	72 ± 9	355 ± 28
$Z + X$ background	1.5 ± 0.6	5.5 ± 1.4	4.0 ± 0.8	11 ± 1.8
Total background	108 ± 13	182 ± 23	76 ± 10	366 ± 28
Data	109	216	77	402

We now extend our examination to the entire mass spectrum. The mass distribution of 4ℓ events is shown in Fig. 5.17. We can see a peak in the ZZ background around the Z pole. This peak comes from the s-channel contribution to the $qq \to ZZ$ process whose Feynman diagram is shown on Fig. 5.11(c). We also see events building up in excess of the background prediction around $m_{4\ell} \sim 126$ GeV. This excess is consistent with the prediction of a 126 GeV SM Higgs boson. Fig. 5.18 shows the distributions of the Z_1 and Z_2 candidates in a 9 GeV window between 121.5–130.5 GeV which contains the bulk of this excess. Here again, we find good agreement between data and the prediction for a 126 GeV Higgs boson. Table 5.5 shows the expected and observed event yields in this 9 GeV window. We expect about 9 events from the background and about 19 events from a 126 GeV Higgs boson, and we observe 25 events in data. We can evaluate the p-value corresponding to the deviation caused by the excess compared to the background prediction. Fig. 5.19 shows the p-value scan as a function of m_{H}. A maximum of 4.9σ significance is observed for a Higgs boson hypothesis of $m_{\mathrm{H}} = 125.7$ GeV. The expected significance at this mass point is 5.5σ. Therefore, we have clear evidence of a new particle in our search for the SM Higgs boson. Furthermore, no excess is observed in the remainder of the Higgs mass range.

Table 5.5 Yield of four-lepton events in a 9 GeV window of 121.5–130.5 GeV around $m_{\mathrm{H}} = 126$ GeV. Results from 7 and 8 TeV datasets have been combined

	Event yield in 4μ channel	Event yield in $2e2\mu$ channel	Event yield in $4e$ channel	Total event yield
ZZ background	2.7 ± 0.1	3.4 ± 0.2	1.2 ± 0.2	7.3 ± 0.3
$Z + X$ background	0.5 ± 0.2	0.8 ± 0.2	0.7 ± 0.1	2.0 ± 0.3
Total background	3.2 ± 0.2	4.2 ± 0.3	1.9 ± 0.2	9.3 ± 0.4
H(126 GeV)	7.2 ± 0.8	8.5 ± 1.0	3.4 ± 0.5	19.1 ± 1.5
Data	8	13	4	25

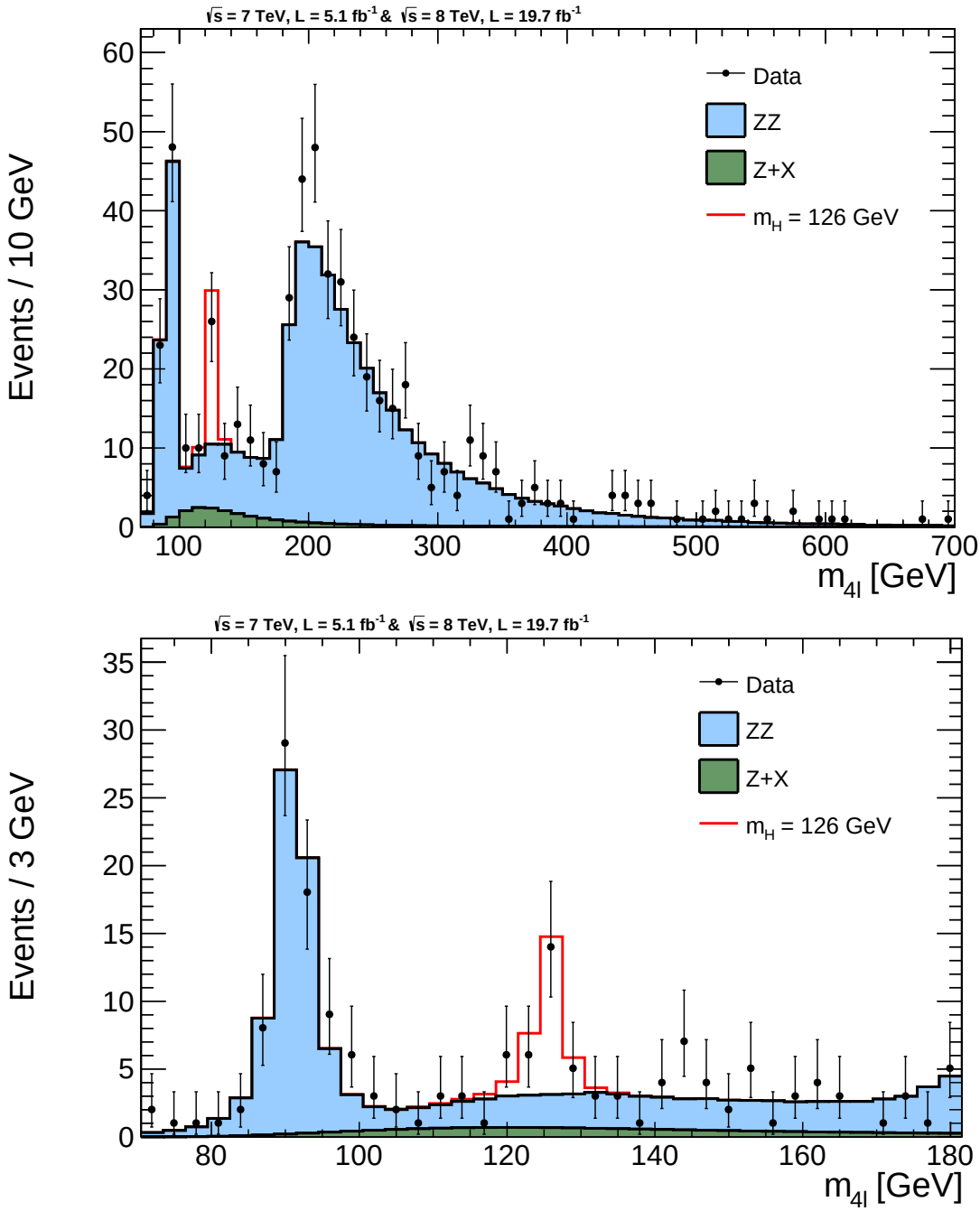

Figure 5.17 Figure on the top shows the four-lepton mass distribution in the range 70–700 GeV. Figure at the right provides a zoom into the mass range 70–180 GeV. We can clearly identify a peak in the mass distribution at the Z pole. This peak corresponds to the s-channel $qq \to ZZ$ background process. Then, we also see a build up of events around the four-lepton mass of about 126 GeV. This peak is in excess of the background expectation and is found to be consistent with the prediction of a 126 GeV SM Higgs boson. In the 9 GeV window between 121.5–130.5 GeV which basically comprises of three bins in the bottom figure around 126 GeV, we observe 25 events in data. In the mass window there are 9 events expected from the background and 19 events expected from a 126 GeV Higgs boson.

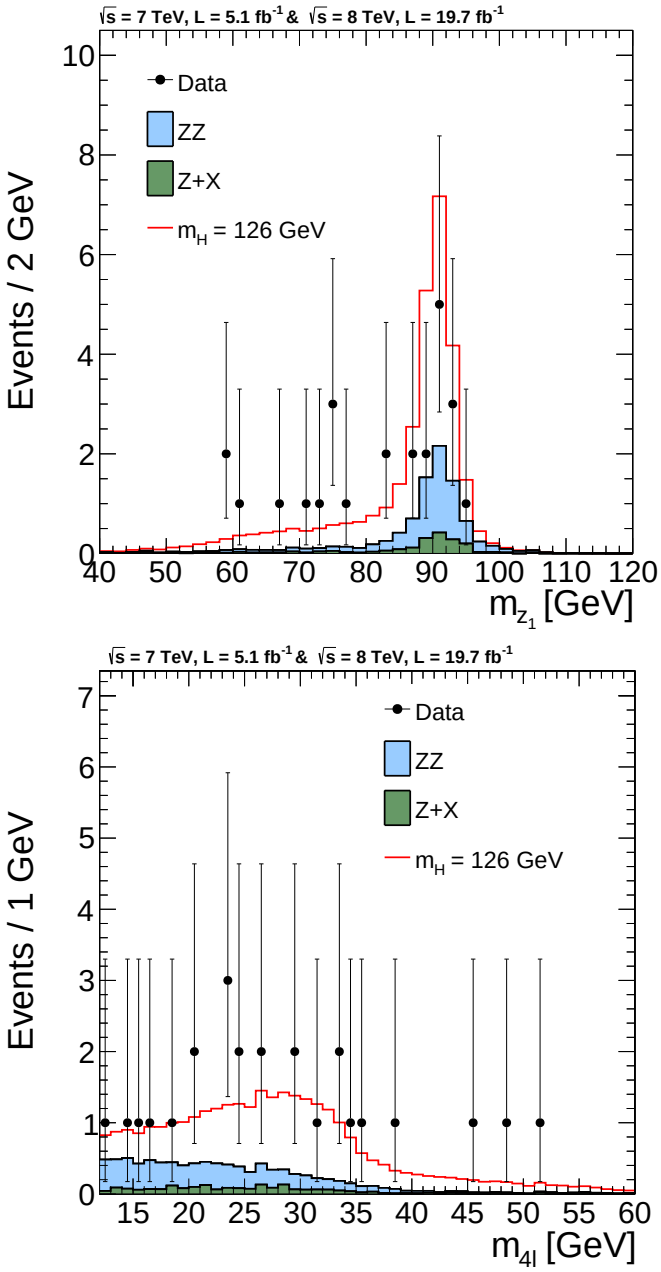

Figure 5.18 Figure on the left shows the mass distribution of the Z_1 candidates in four-lepton events where the mass of the four-lepton candidate is between 121.5–130.5 GeV. Figure on the right shows the corresponding mass distribution of the Z_2 candidates. We can see that data is consistent with a 126 GeV SM Higgs boson on top of the background.

5.5 Search Using $m_{4\ell}$ and Kinematic Discriminant

So far we have only used the mass of the four-lepton system to isolate the signal. Indeed, $m_{4\ell}$ is the most powerful discriminating variable in the analysis. However, the

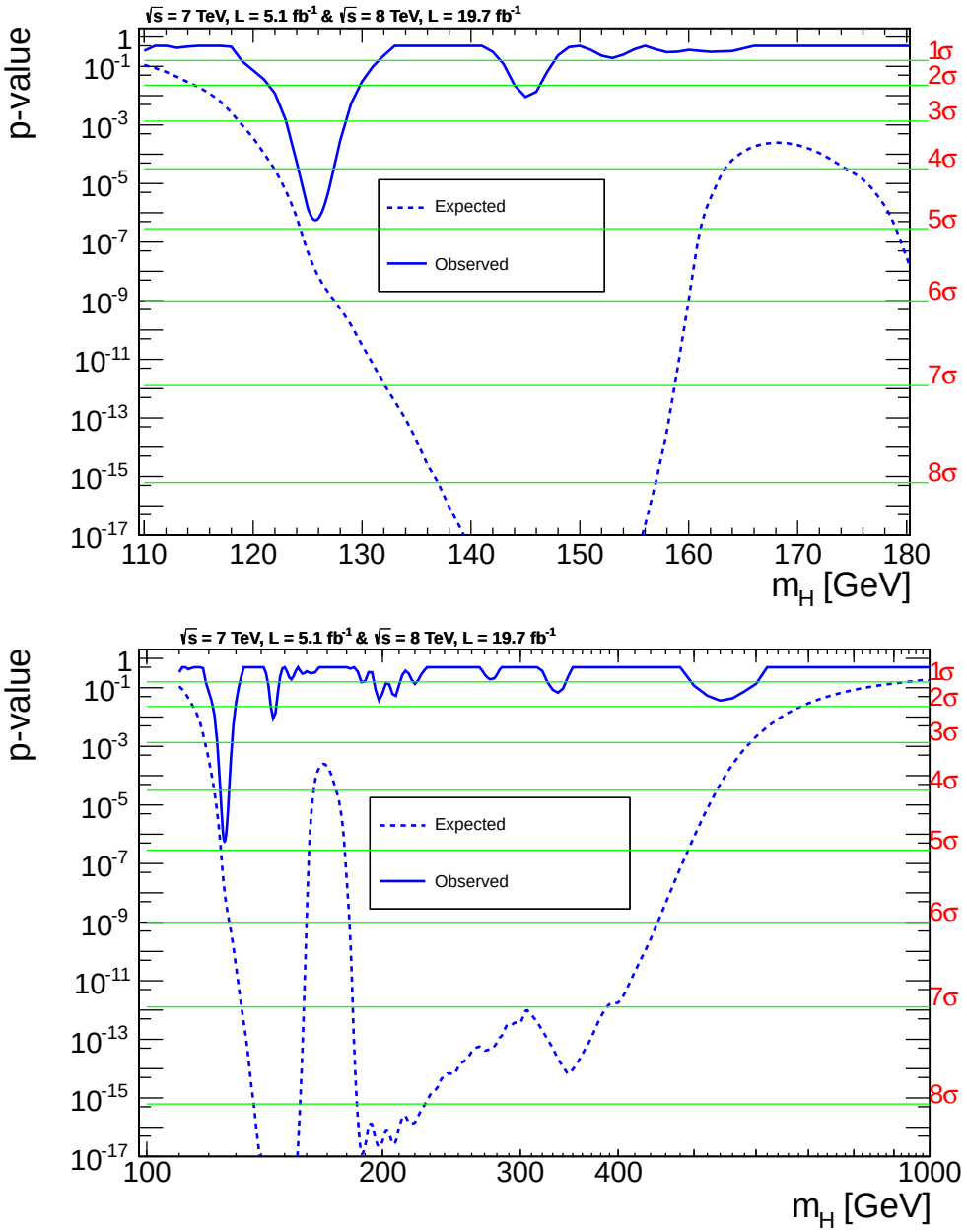

Figure 5.19 The p-value distribution obtained in the $m_{4\ell}$ shape analysis for the low mass region of 110–180 GeV (left) and for the full mass range of 110–1000 GeV (right). We can see a 4.9σ dip in the p-value distribution at $m_{\mathrm{H}} = 125.7$ GeV. The expected significance for the SM Higgs boson of the same mass is 5.5σ. No other significant excess is seen in the entire mass range. A small $\sim 2.5\sigma$ excess is observed around $m_{\mathrm{H}} = 145$ GeV but this is consistent with a statistical fluctuation.

four-lepton system provides access to additional kinematic information that can help to improve upon the separation between signal and background events thereby enhancing the search sensitivity [167, 168]. Each of the four leptons in our analysis has three momentum coordinates associated with it. This adds up to a total of twelve degrees

of freedom that are required to define the four-lepton system. Three of these twelve degrees of freedom can be used to define the momentum vector of the ZZ system. If we move boost into the rest frame of the ZZ system we are left with nine degrees of freedom. One of these nine degrees of freedom is the azimuthal (ϕ) orientation of the ZZ system around the z-axis. Our experiment is completely symmetric in this variable and hence we can choose to ignore it or in other words integrate it out from all kinematic considerations. Of the remaining eight degrees of freedom, three can be ascribed to the Z_1 mass (m_{Z_1}), Z_2 mass (m_{Z_2}) and the mass of the ZZ system (m_{ZZ} or $m_{4\ell}$). The five degrees of freedom that are left can be described in terms of the production and decay angles of the ZZ system as shown in Fig. 5.20. The five angles can be described as follows

- θ^* is the polar angle of the Z_1 candidate in the ZZ rest frame
- Φ_1 is the angle between the $Z_1 \to \ell^+\ell^-$ plane and the $pp \to \mathrm{H} \to ZZ$ plane in the ZZ rest frame
- θ_1 and θ_2 are helicity angles of the leptons in the Z_1 and Z_2 rest frames respectively
- Φ is the angle between the $Z_1 \to \ell^+\ell^-$ and $Z_2 \to \ell^+\ell^-$ planes.

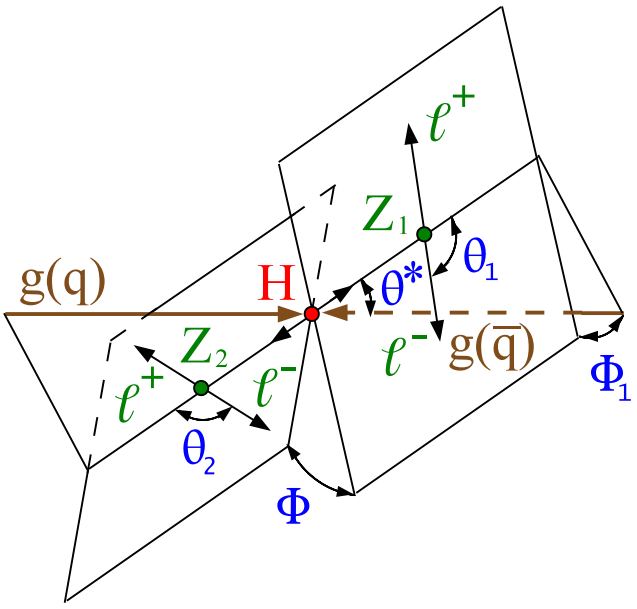

Figure 5.20 A schematic of the Higgs boson decaying into four leptons.

5.5.1 Search Strategy

In the $m_{4\ell}$ bump hunt we ignore the information from seven out of the eight variables available at our disposal. In order to incorporate this missing information, a kinematic discriminant is built using the five angles represented as $\vec{\Omega}$ and the two Z masses m_{Z_1} and m_{Z_2}. For a given value of $m_{4\ell}$ the probability of a signal or a background event to have a given set of $(\vec{\Omega}, m_{Z_1}, m_{Z_2})$ values is proportional to the square of its matrix element. In the case of signal we can treat $m_{4\ell}$ to be the same as $m_{\rm H}$. The kinematic discriminant can then be written in the following way

$$K_D = \frac{f_{sig}\left(\vec{\Omega}, m_{Z_1}, m_{Z_2}|m_{4\ell}\right)}{f_{sig}\left(\vec{\Omega}, m_{Z_1}, m_{Z_2}|m_{4\ell}\right) + f_{bkg}\left(\vec{\Omega}, m_{Z_1}, m_{Z_2}|m_{4\ell}\right)} = \left[1 + \frac{f_{bkg}\left(\vec{\Omega}, m_{Z_1}, m_{Z_2}|m_{4\ell}\right)}{f_{sig}\left(\vec{\Omega}, m_{Z_1}, m_{Z_2}|m_{4\ell}\right)}\right]^{-1} \tag{5.10}$$

where f_{sig} and f_{bkg} are given by the square of the matrix elements for the signal and the dominant $qq \to ZZ$ background. Some additional $m_{4\ell}$-dependent factors are used to normalize f_{sig} and f_{bkg} in order to ensure that the signal events are concentrated in the region $K_D > 0.5$ while the background events are concentrated in the region $K_D < 0.5$. The matrix element amplitudes used for evaluating the signal likelihood function f_{sig} are obtained from the JHUGEN Monte Carlo generator while the matrix elements for the ZZ background are computed using the MCFM generator.

Fig. 5.21 and 5.22 show the distribution of the conditional p.d.f.s $P_{sig}\left(K_D|m_{4\ell}\right)$ and $P_{qq\to ZZ}\left(K_D|m_{4\ell}\right)$ constructed using the signal and $qq \to ZZ$ background simulations respectively. In the case of the signal, the conditional p.d.f. is constructed from a mixture of several Higgs boson simulations generated using different values of $m_{\rm H}$. Similar conditional p.d.f.s are also constructed for the $gg \to ZZ$ and $Z + X$ backgrounds. We then obtain the two-dimensional $(K_D, m_{4\ell})$ p.d.f.s for the signal and background processes using the following relations

$$\begin{aligned} P_{sig}\left(K_D, m_{4\ell}|m_{\rm H}\right) &= P_{sig}\left(K_D|m_{4\ell}\right) \times P_{sig}\left(m_{4\ell}|m_{\rm H}\right) \\ P_{bkg}\left(K_D, m_{4\ell}\right) &= P_{bkg}\left(K_D|m_{4\ell}\right) \times P_{bkg}\left(m_{4\ell}\right) \end{aligned} \tag{5.11}$$

where $P_{sig}\left(m_{4\ell}|m_{\rm H}\right)$ and $P_{bkg}\left(K_D, m_{4\ell}\right)$ are the four-lepton mass shapes of the signal and background processes that we used in the $m_{4\ell}$ based analysis described in the pre-

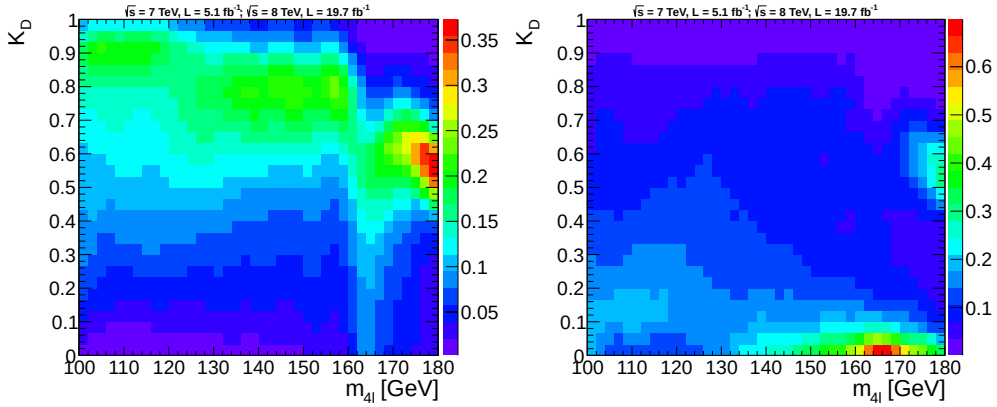

Figure 5.21 Conditional p.d.f.s $P_{sig}\left(K_D|m_{4\ell}\right)$ (left) and $P_{qq\to ZZ}\left(K_D|m_{4\ell}\right)$ (right) in the the low mass region of $m_{4\ell} \in [100, 180]$ GeV.

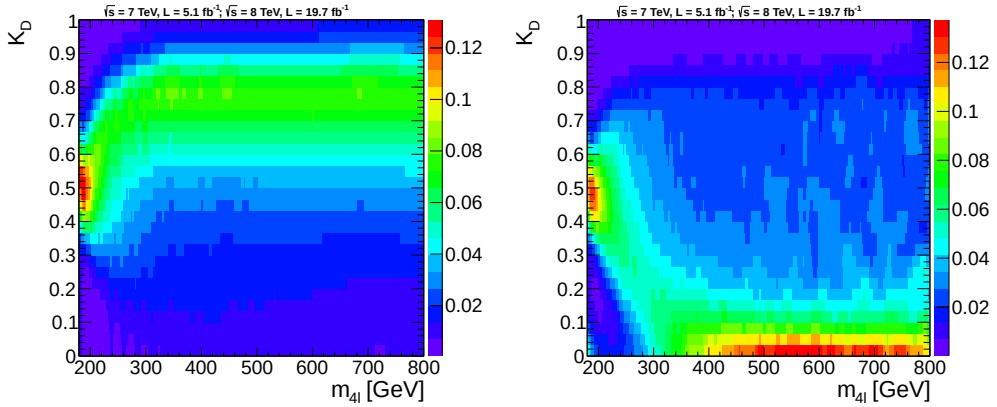

Figure 5.22 Conditional p.d.f.s $P_{sig}\left(K_D|m_{4\ell}\right)$ (left) and $P_{qq\to ZZ}\left(K_D|m_{4\ell}\right)$ (right) in the the high mass region of $m_{4\ell} \in [180, 800]$ GeV.

vious section. These p.d.f.s are used to construct a two-dimensional unbinned likelihood with which we fit the observed data.

5.6 Results

The event yields in the 2D($K_D, m_{4\ell}$) analysis remain the same as in the case of the 1D($m_{4\ell}$) analysis since the event selection is kept unchanged. The normalization uncertainties on the signal and background processes and the shape uncertainties associated with the scale and resolution of the signal shape are propagated to the 2D analysis. A shape certainty is assigned to the $Z + X$ conditional p.d.f. $P_{Z+X}\left(K_D|m_{4\ell}\right)$ by taking the p.d.f. of the $qq \to ZZ$ background as the alternate bounding shape.

Fig. 5.23 shows the two-dimensional (2D) K_D v/s $m_{4\ell}$ distribution of four-lepton

events observed in data. We can see a clustering of events in the narrow island region corresponding to the 126 GeV Higgs boson signal. The p-value distribution obtained in the 2D analysis is shown in Fig. 5.24. The most significant deviation from the background only prediction is observed again at $m_{\mathrm{H}} = 125.7$ GeV. The expected signficance at this mass point is 6.5σ whereas the observed significance is 6.7σ. Furthermore, no other significant excess is observed in any other region of m_{H}. This can also be seen from Fig. 5.25 which shows the distribution of the expected and observed upper limits at 95% CL on the signal strength of the SM Higgs boson production and decay into four leptons as a function of m_{H}. Apart from the excess around 126 GeV, the observed upper limits are consistent with the expectation. A SM-like Higgs boson is excluded in the mass range of 115–118 GeV and 129–830 GeV. The expected exclusion range is 115–720 GeV.

Chapter 5, in full, is the reprint of the material as it appears in "Measurement of the properties of a Higgs boson in the four-lepton final state", by CMS Collaboration, Phys. Rev. D 89 (2014) 092007, and "Observation of a new boson at a mass of 125 GeV with the CMS experiment at the LHC" by CMS Collaboration, Phys. Lett. B 716 (2012) 30. The dissertation author was the primary investigator and author of this paper.

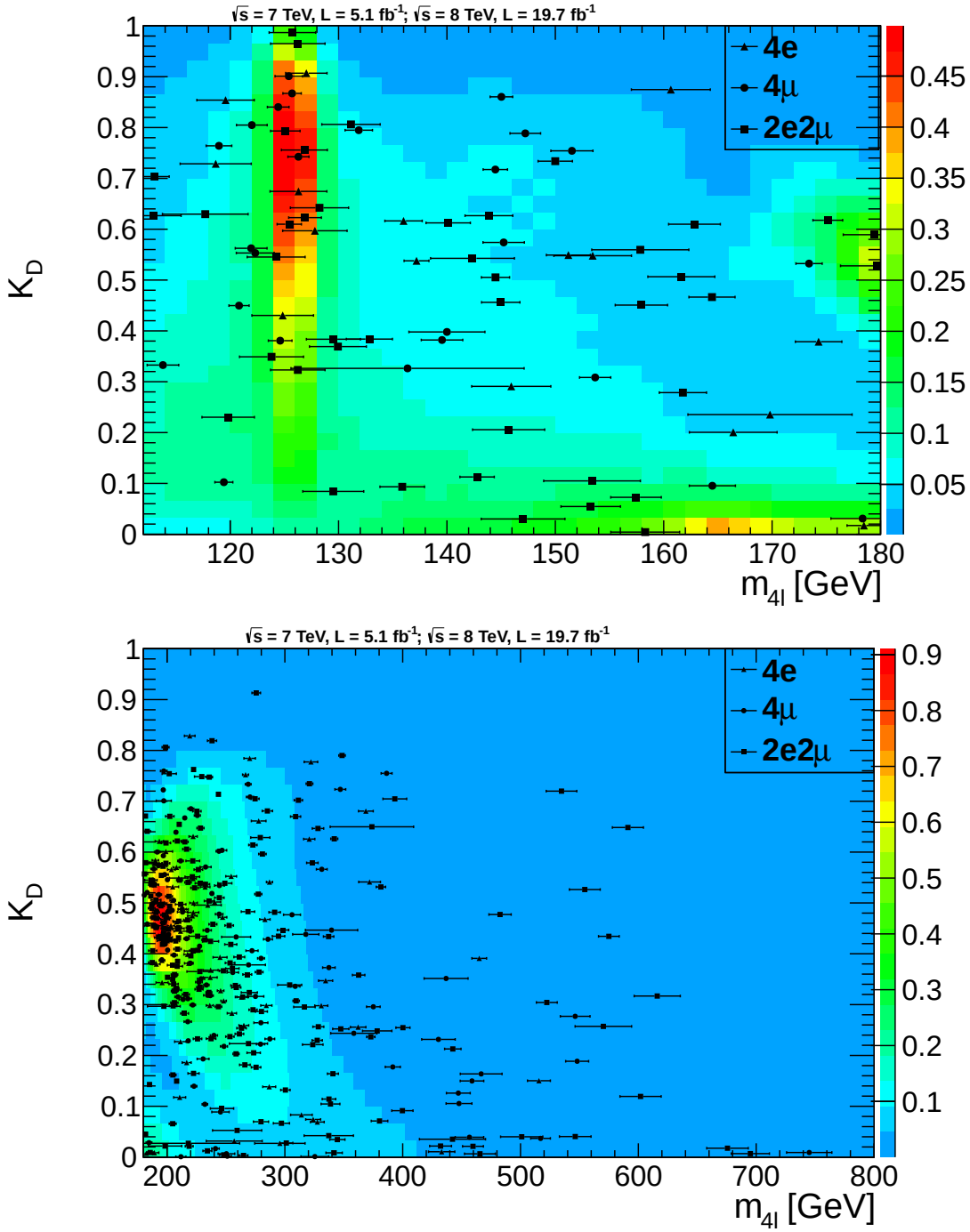

Figure 5.23 Two dimensional K_D v/s $m_{4\ell}$ distribution of four-lepton events in data in the low mass region of $m_{4\ell} \in [100, 180]$ GeV (top) and the high mass region of $m_{4\ell} \in [180, 1000]$ GeV (bottom). The top plot shows data points overlaid on top of the signal (126 GeV) plus background prediction. We can see that the Higgs boson signal is largely concentrated in the red colored island around $m_{4\ell} \sim 126$ GeV and $K_D > 0.5$ while the background is mostly spread out in the region of $K_D < 0.5$. The bottom plot shows the data points overlaid on the background prediction in the high mass range. The error bars on the data points in both the plots correspond to the event-by-event uncertainties on the measured value of $m_{4\ell}$.

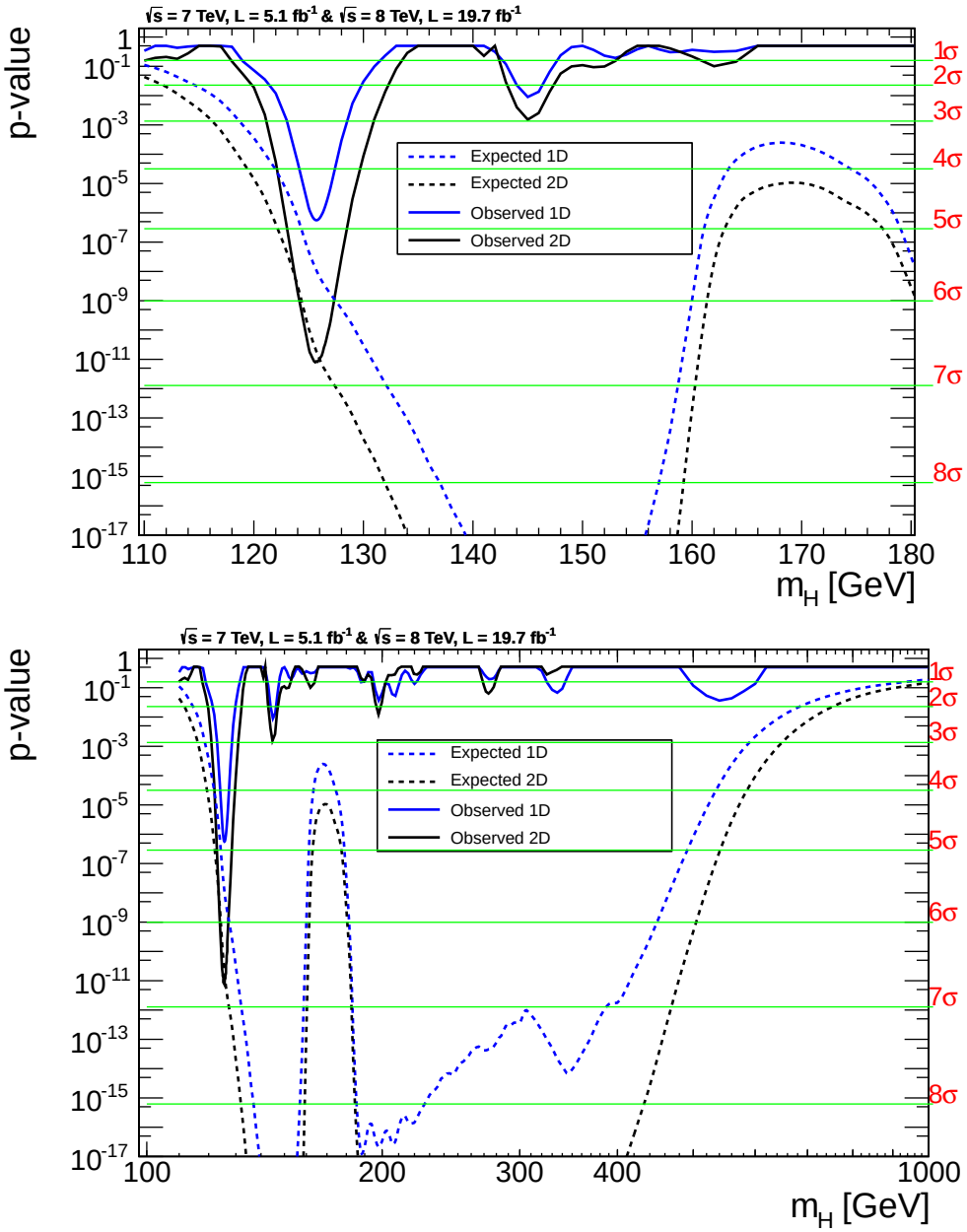

Figure 5.24 Figure on the top shows the p-value scan in the low mass region of 110–180 GeV while the figure at the bottom shows the p-value distribution for the full mass range of 110–1000 GeV. The expected and observed p-values for the 1D $m_{4\ell}$ search described in the previous section are shown by the blue lines while the expected and observed p-values for the K_D v/s $m_{4\ell}$ 2D analysis are depicted by the black lines. We can clearly see the improvement in sensitivity in the 2D analysis as compared to the $m_{4\ell}$ bump hunt. In particular we observe a 6.7σ excess at $m_{\mathrm{H}} = 125.7$ GeV. The expected significance at this mass point for the SM Higgs boson is 6.5σ. In the 1D case we have already seen that the observed significance at the same mass point is 4.9σ while the expected significance is 5.5σ. We do not see any other significant excess in the entire mass range but there several small dips in the p-value distribution that are consistent with statistical fluctuations. The most prominent of these dips is a 3σ excess around $m_{\mathrm{H}} = 145$ GeV.

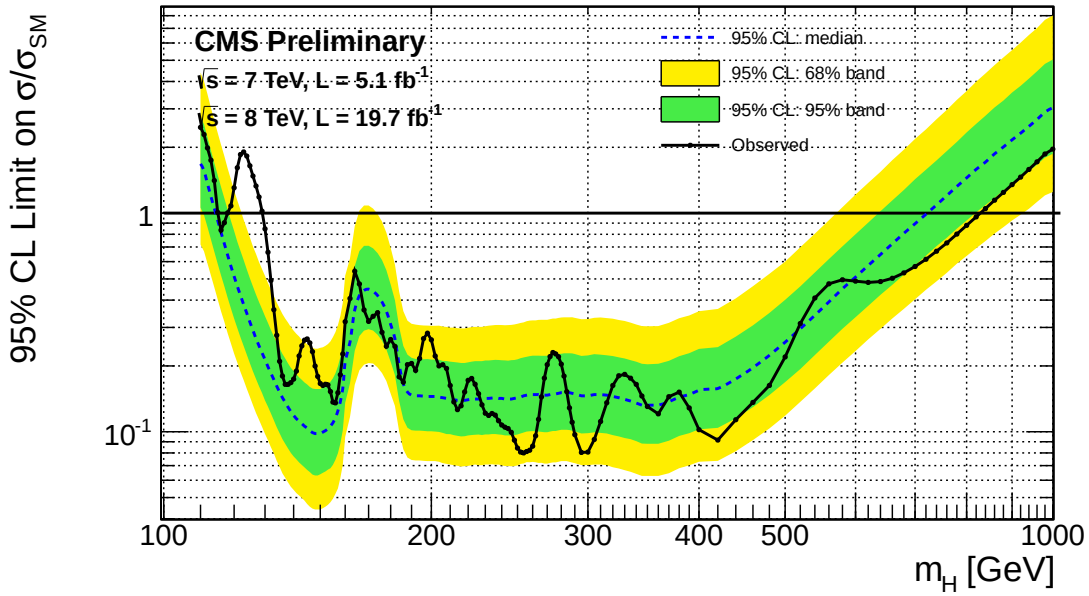

Figure 5.25 Expected and observed upper limits at 95% CL on the signal strength of the SM Higgs boson production and decay into four leptons as a function of m_{H}.

Chapter 6

Properties of the New Boson

In this chapter we examine and measure the properties of the Higgs boson candidate whose existence we established in the previous chapter. We start by performing a measurement of the mass and width of this particle. We then measure its signal strength with respect to the predicted cross-section of the production and decay of the SM Higgs boson at the measured mass value. Finally, we end the chapter by probing its spin and parity quantum numbers.

6.1 Mass Measurement

In order to measure the mass of the Higgs boson candidate, we construct the likelihood function with two parameters of interest - namely the signal strength (μ) and the mass (m_{H}). The best estimate of m_{H} can then be obtained by scanning the likelihood to find the point where the χ^2 function is at a minimum. The procedure is discussed in greater detail in Sec. 3.3. To construct the likelihood function we improve upon the 2D $(m_{4\ell}, K_D)$ model by adding a third dimension corresponding to the event-by-event uncertainty on the measured value of $m_{4\ell}$. The motivation for adopting this 3D approach is as follows. When we construct the p.d.f. for the mass shape of the signal, we essentially model the average detector response to signal events. If we have a large ensemble of signal events, its $m_{4\ell}$ distribution will indeed be described by this averaged p.d.f. However, in the $\mathrm{H} \to ZZ \to 4\ell$ analysis we only have ~ 20 signal events at hand. If we are lucky some of these events could have a smaller uncertainty

on the measured mass compared to the average resolution. In order to make optimal use of available data, we should give a larger weight to events that are measured more precisely than the average expectation. This is achieved by substituting the σ-parameter of the dCB function used to model the detector resolution with the event-by-event mass uncertainty. The inclusion of the event-by-event mass uncertainties leads to an eight percent reduction in the expected uncertainty on the mass measurement with respect to the 2D analysis. Similarly, it improves the expected results for the width measurement which is discussed in the next section by ten percent.

6.1.1 Evaluation of Event-by-event Mass Uncertainty

The event-by-event mass uncertainty is measured by propagating the uncertainty on the momentum of each of the four leptons to measured mass value. In the case of muons, the momentum uncertainty is estimated from the track fit. In the case of electrons, the momentum uncertainty is estimated by using a multivariate regression that combines the uncertainties on the ECAL energy and the track momentum. This regression algorithm takes the same set of inputs as those used in the regression employed for assigning the electron momentum.

The total four-lepton mass uncertainty ($\tilde{\sigma}_{m_{4\ell}}$) is evaluated as the quadrature sum of the mass uncertainties obtained by propagating the momentum errors of each of the four leptons. This uncertainty is then calibrated in data and in simulation by using J/Ψ and Z resonances for muons and just the Z resonance for electrons. These resonances are modeled by using a convolution of the BW function with a dCB function. The σ-parameter of the dCB function is set equal to $\sigma_{m_{4\ell}} = \lambda \times \tilde{\sigma}_{m_{4\ell}}$, and a fit is performed to obtain the value of λ which is computed for different ranges of p_T and η of the leptons. The λ calibration factor is found to be ~ 1.2 for electrons and ~ 1.1 for muons. Fig. 6.1 shows the distribution of event-by-event mass uncertainties estimated for four-lepton events in the mass range of 80–100 GeV. These events almost entirely belong to the s-channel $qq \to ZZ \to 4\ell$ process which peaks at the Z-boson mass of 91 GeV as seen in Fig. 5.17.

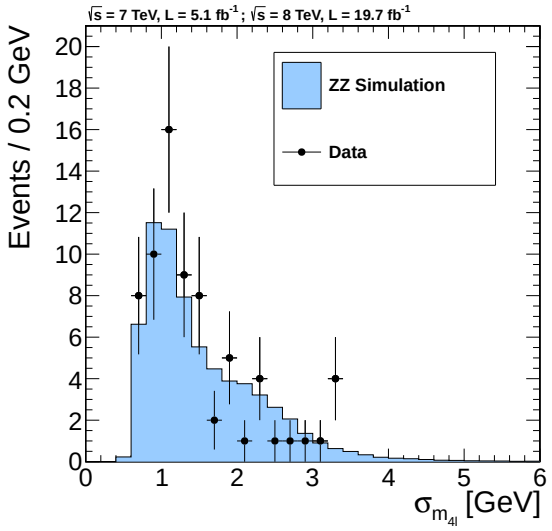

Figure 6.1 Distribution of the mass uncertainty of four-lepton candidates in the mass range of 80–100 GeV.

6.1.2 Construction of the 3D Model Using Event-by-event Mass Uncertainties

The three-dimensional p.d.f.s that include the event-by-event mass uncertainties are constructed using the following relations for the signal and background processes.

$$\begin{aligned} P_{sig}\left(K_D, m_{4\ell}, \delta_{m_{4\ell}}|m_{\rm H}\right) &= P_{sig}\left(K_D|m_{4\ell}\right) \times P_{sig}\left(m_{4\ell}|m_{\rm H}\right) \times P_{sig}\left(\delta_{m_{4\ell}}|m_{\rm H}\right) \\ P_{bkg}\left(K_D, m_{4\ell}, \delta_{m_{4\ell}}\right) &= P_{bkg}\left(K_D|m_{4\ell}\right) \times P_{bkg}\left(m_{4\ell}\right) \times P_{bkg}\left(\delta_{m_{4\ell}}\right) \end{aligned} \quad (6.1)$$

where $\delta_{m_{4\ell}} = \sigma_{m_{4\ell}}/m_{4\ell}$ is the relative mass uncertainty. The reason to use the relative mass uncertainty in the construction of the 3D model is that it has very little dependence on $m_{4\ell}$. This is an important consideration since eq. 6.1 is valid only when the variable used to represent the mass uncertainty is uncorrelated with $m_{4\ell}$ and K_D. The correlation between K_D and $\delta_{m_{4\ell}}$ is confirmed to be negligible in simulation.

The shape of $\delta_{m_{4\ell}}$ is modeled by using a sum of the Landau and Gaussian functions. In the case of the signal and the ZZ background, the $\delta_{m_{4\ell}}$ is derived from simulation while in the case of the $Z+X$ background, it is obtained from the $Z+2$ loose leptons control sample. Fig. 6.2 and 6.3 show the distributions of $\delta_{m_{4\ell}}$ in the 4μ, $2e2\mu$ and $4e$ channels for a 126 GeV Higgs boson signal and the dominant ZZ background.

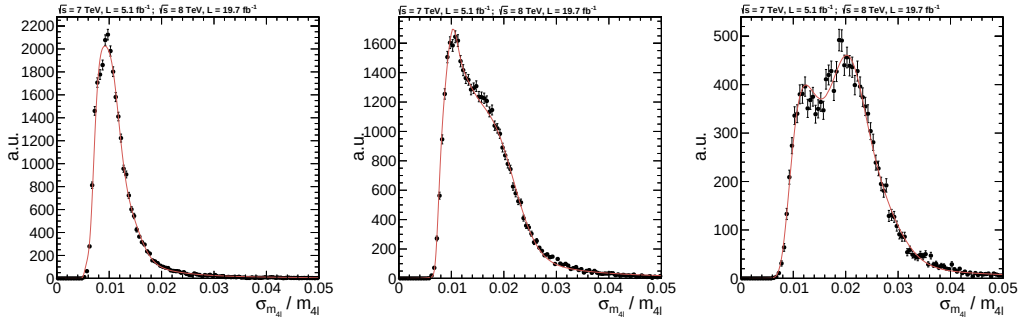

Figure 6.2 Distributions of the relative mass uncertainty $\delta_{m_{4\ell}}$ in 4μ (left), $2e2\mu$ (middle), and $4e$ (right) events from the decay of a 126 GeV Higgs boson.

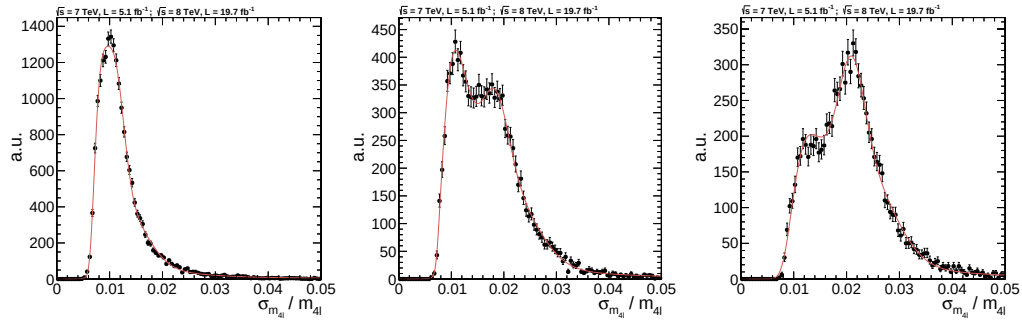

Figure 6.3 Distributions of the relative mass uncertainty $\delta_{m_{4\ell}}$ in 4μ (left), $2e2\mu$ (middle), and $4e$ (right) events corresponding to the ZZ background.

6.1.3 Results

Fig. 6.4(a) shows the scan of the profile likelihood as a function of m_{H} while Fig. 6.4(b) shows the scan of the likelihood as a function of both the signal strength and m_{H} . We find that the best estimate of the mass of the Higgs boson candidate is $125.6 \pm 0.4(\mathrm{stat}) \pm 0.2(\mathrm{syst})$ GeV. The measurement is dominated by the statistical uncertainty of 0.4 GeV. The systematic uncertainty of 0.2 GeV can almost entirely be attributed to the scale uncertainty. Table 6.1 lists the measured values of m_{H} in the three individual channels.

6.2 Width Measurement

In order to measure the width of the Higgs boson candidate we use the same three-dimensional model that was defined in the previous section. While performing the mass measurement we use a dCB function to model the signal shape. As was discussed in Sec. 5.4.1 this is a valid approximation for a SM Higgs boson with mass less than

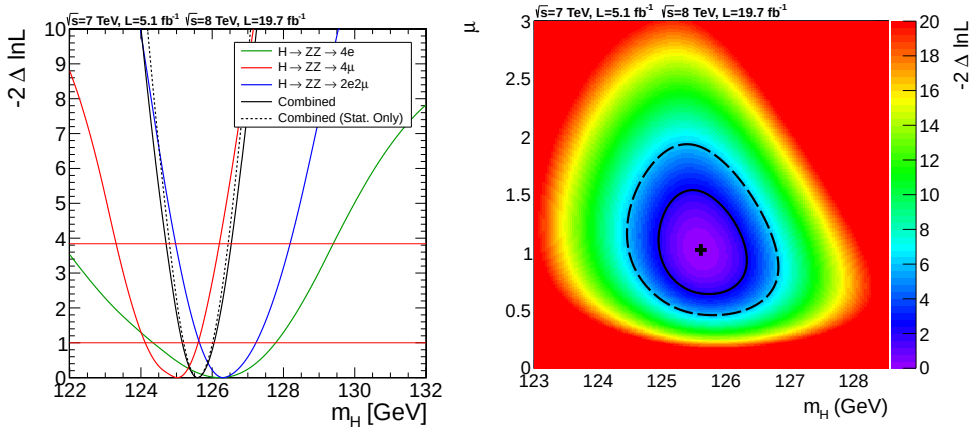

(a) (b)

Figure 6.4 Fig.(a) shows profile likelihood distribution as a function of m_{H}. The signal strength is profiled in this distribution. Fig.(b) shows the scan of the likelihood as a function of both signal strength and m_{H}.

Table 6.1 Best fit mass of the Higgs boson candidate measured in the 4μ, $4e$ and $2e2\mu$ channels individually and in the combination of the these channels.

Channel	Measured Mass (GeV)
4μ	$125.1^{+0.6}_{-0.9}$
$2e2\mu$	$126.3^{+0.9}_{-0.7}$
$4e$	$126.2^{+1.5}_{-1.8}$
4ℓ	$125.6 \pm 0.4(\mathrm{stat}) \pm 0.2(\mathrm{syst})$

180 GeV since its width is expected to be much smaller than the detector resolution. But when performing the width measurement itself, we need to revert back to the signal model in which we take a convolution of the dCB function with the BW function. The Γ parameter of the BW function (see eq. 5.2) now becomes our parameter of interest. In order to measure Γ we perform a likelihood scan wherein the signal strength and the mass are profiled along with the nuisance parameters. Since we are dealing with a three-dimensional model the likelihood scan becomes computationally quite intensive. The bottle-neck lies in the evaluation of the convolution of the dCB and BW functions. One possibility is to perform the convolution numerically using Fast Fourier Transform (FFT) technique. However, this approach is found to be too slow. An alternate approach

is adopted in which the convolution is performed analytically using an approximate functional form for the dCB function. The method is described below

6.2.1 Analytical Evaluation of the Convolution Function

In order to explain how the convolution is performed we start with a single-sided Crystal Ball (CB) function. The CB function is defined as follows

$$f_{\rm CB}(x;\alpha,n,x_0,\sigma) = \begin{cases} e^{-(x-x_0)^2/2\sigma^2} & \text{if } -\alpha < (x-x_0)/\sigma \\ A(B-\frac{x-x_0}{\sigma})^{-n} & \text{if } (x-x_0)/\sigma < \alpha \end{cases} \tag{6.2}$$

where $A = \left(\frac{n}{\alpha}\right)^n \times e^{-\alpha^2/2}$, $B = \left(\frac{n}{\alpha} - \alpha\right)$. Essentially, a CB function has a polynomial tail only on one side as opposed to the dCB function which has polynomial tails on both sides. The CB function can be recast as a Gaussian function (G) extending over all values of x and an additional tail function (T). In this form, the CB function becomes

$$\begin{aligned} f_{\rm CB}(x;\alpha,n,x_0,\sigma) &= G(x;x_0,\sigma) + T(x;\alpha,n,x_0,\sigma) \\ G(x;x_0,\sigma) &= e^{-\frac{(x-x_0)^2}{2\sigma^2}} \text{ for } -\infty < x < \infty \\ T(x;\alpha,n,x_0,\sigma) &= \left\{ \begin{array}{ll} A(B-\frac{x-x_0}{\sigma})^{-n} - e^{-\frac{(x-x_0)^2}{2\sigma^2}} & \text{if } \frac{x-x_0}{\sigma} \le -\alpha \\ 0 & \text{otherwise} \end{array} \right\} \end{aligned} \tag{6.3}$$

The CB function decomposed into the Gaussian and tail functions is shown in Fig. 6.5. The convolution of the CB and BW functions can be written in terms of the Gaussian and tail functions as :

$$f_{\rm CB\otimes BW}(x) = \int_{-\infty}^{\infty} G(x-y) f_{\rm BW}(y) dy + \int_{-\infty}^{\infty} T(x-y) f_{\rm BW}(y) dy \tag{6.4}$$

The convolution of the Gaussian and BW functions is called the Voigtian function. There exist fast lookup tables for the Voigtian function which can be used for quick computation of the Gaussian core of CB $\otimes$ BW. However, the convolution integral of the tail function [Eq. 6.3] and BW cannot be evaluated analytically. Therefore, we recast the tail function using an approximation of its actual shape and then use this

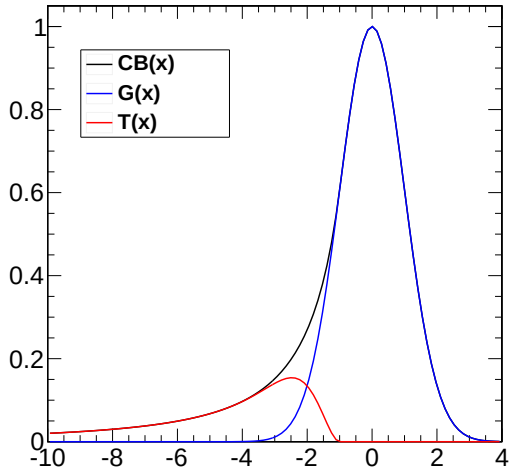

Figure 6.5 Crystal Ball function (black curve) can be written as a sum of the Gaussian core (blue curve) and the tail (red curve).

approximation to evaluate the convolution integral analytically. This approximate form of the tail function is as follows

$$T(x;\alpha,n,x_0,\sigma) = \left\{ \begin{array}{ll} A(B-\frac{x-x_0}{\sigma})^{-n} & \text{if } \frac{x-x_0}{\sigma} \leq -\alpha-\beta \\ c_1(\frac{x-x_0}{\sigma}+\alpha)^2 + c_2(\frac{x-x_0}{\sigma}+\alpha) & \text{if } -\alpha-\beta < \frac{x-x_0}{\sigma} \leq -\alpha \\ 0 & \text{otherwise} \end{array} \right\} \tag{6.5}$$

The motivation for this form is the following. When x is far away from the peak of the CB function, the value of $T(x)$ is essentially driven by the power law since the Gaussian exponential dies off quickly. In this region the value of $T(x)$ can be approximated from the power law alone. The range of x in which the power law is a good approximation for $T(x)$ is determined by the parameter β in eq. 6.5. In the range $-\alpha-\beta < \frac{x-x_0}{\sigma} \leq -\alpha$, the tail function is approximated by a quadratic function. The quadratic is constrained so that it goes to zero at $\frac{x-x_0}{\sigma} = -\alpha$. The parameters c_1 and c_2 are determined from boundary conditions at $\frac{x-x_0}{\sigma} = -\alpha-\beta$ requiring the approximate tail function and its derivative to be continuous. This approximation of the CB function is shown in Fig. 6.6. Typically, setting the value of β between 2.3 to 2.7 yields good agreement between the approximate and exact CB shapes. In Fig. 6.6 the value of β is set to 2.3. The advantage of expressing $T(x)$ in the above form is that we can perform

the integral $\int_{-\infty}^{\infty} T(x-y) f_{\mathrm{BW}}(y) dy$ analytically. This means that we can hard-code the form of the convolution function $f_{\mathrm{CB}\otimes\mathrm{BW}}(x)$ into the likelihood which avoids the need to perform a numerical integration. This helps to substantially reduce the computation time required to perform the width measurement.

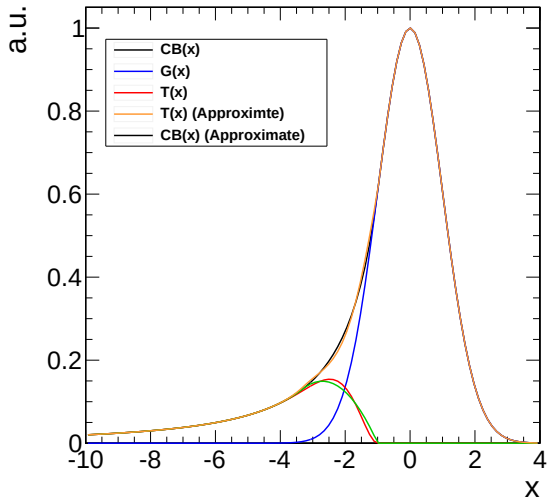

Figure 6.6 The tail function (red curve) of the CB function (black curve) is approximated as the green curve and the corresponding CB shape obtained on adding the green curve with the core Gaussian (blue curve) is shown by the orange curve. $\beta = 2.3$ is used for obtaining the green and orange curves.

In the case of the dCB function, the convolution integral can be written as

$$f_{\mathrm{dCB}\otimes\mathrm{BW}}(x) = \int_{-\infty}^{\infty} G(x-y) f_{\mathrm{BW}}(y) dy + \int_{-\infty}^{\infty} T_L(x-y) f_{\mathrm{BW}}(y) dy + \int_{-\infty}^{\infty} T_R(x-y) f_{\mathrm{BW}}(y) dy \tag{6.6}$$

where $T_L(x)$ and $T_R(x)$ are the tails on the left and right side of the peak respectively. While $T_L(x)$ is identical to the tail $T(x)$ of the single-sided CB function, the convolution integral of $T_R(x)$ can be computed in an analogous manner to the convolution of $T(x)$. Fig. 6.7 shows the comparison between $f_{\mathrm{dCB}\otimes\mathrm{BW}}$ shapes obtained using numerical integration and the analytical approximation.

6.2.2 Results

Fig. 6.8 shows the profile likelihood distribution as a function of the total width of the Higgs boson candidate (Γ_{H}). From this plot we can infer an upper limit of 3.6 GeV at 95% CL on Γ_{H}.

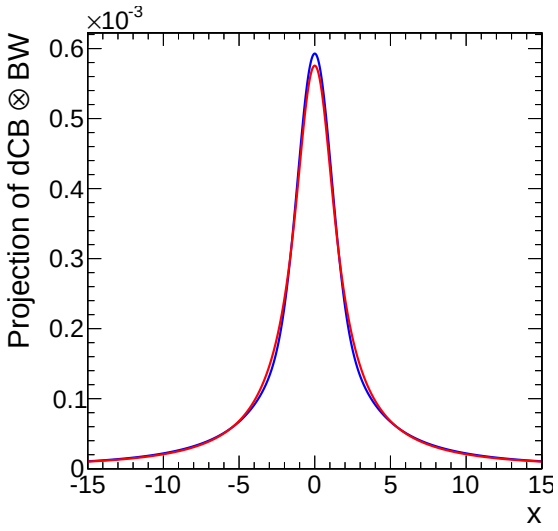

Figure 6.7 Comparison is shown between the shapes obtained by performing the convolution of a dCB function with the BW function using numerical integration (red curve) and using the analytical approximation described above (blue curve). In this figure, the dCB function has $x_0 = 0, \sigma = 1, \alpha_L = \alpha_R = 1, n_L = n_R = 2$ and the BW function has $\Gamma = 1$.

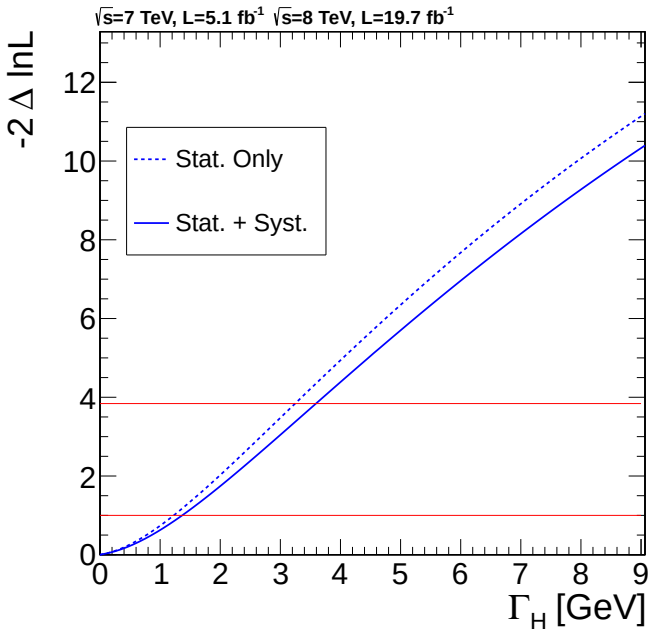

Figure 6.8 Profile likelihood distribution as a function of the total width (Γ_H) of the Higgs boson candidate.

6.3 Signal Strength

One important test of compatibility between the Higgs boson candidate and the theoretical prediction of the SM is the estimate of the signal strength parameter.

Table 6.2 lists the best fit values of signal strength obtained from the three-dimensional likelihood in each of the three individual channels and their combination. The fit is performed by fixing the value of m_{H} to 125.6 GeV. The signal strength is estimated to be $1.04^{+0.29}_{-0.25}(\mathrm{stat})\ ^{+0.14}_{-0.08}(\mathrm{syst})$, which implies that the event yield of the Higgs boson candidate is consistent with the SM prediction.

Table 6.2 Best fit mass of the Higgs boson candidate measured in the 4μ, $4e$ and $2e2\mu$ channels individually and in the combination of the these channels.

Channel	Signal Strength
4μ	$0.93^{+0.49}_{-0.37}$
$2e2\mu$	$1.09^{+0.47}_{-0.37}$
$4e$	$1.18^{+0.75}_{-0.55}$
4ℓ	$1.04^{+0.29}_{-0.25}(\mathrm{stat})\ ^{+0.14}_{-0.08}(\mathrm{syst})$

6.4 Spin and Parity

The standard model Higgs boson is a scalar particle. The Higgs field remains invariant under boosts or rotations, and unlike a pseudoscalar it does not change sign under a parity transformation. In order to establish the standard model credentials of the Higgs boson candidate found in data, it is important to ensure that it has zero spin, and a parity quantum number of +1. To study these properties let us consider the interaction amplitude between a generic spin-zero particle and a massive vector field Z^{μ}. This amplitude can be written as follows [167, 168, 171]

$$\begin{aligned} A &= \upsilon^{-1}\epsilon_1^{*\mu}\epsilon_2^{*\nu}\left(a_1 g_{\mu\nu} m_{\mathrm{H}}^2 + a_2 q_\mu q_\mu + a_3 \epsilon_{\alpha\beta\mu\nu} q^\mu q^\nu\right) \\ &= A_1 + A_2 + A_3 \end{aligned} \tag{6.7}$$

where ϵ_i and q_i are the polarization vectors and momenta of the two Z bosons coupling to the Higgs field, a_1, a_2 and a_3 are coupling constants, and $\epsilon_{\alpha\beta\mu\nu}$ is the Levi-Civita anti-symmetric tensor. The term A_1 in eq. 6.7 represents the SM interaction between the Higgs and the Z fields at tree level. The amplitude term A_3 represents the coupling

between a pseudoscalar particle and the Z fields, while the A_2 term models the interaction of a scalar particle that does not participate in electroweak symmetry breaking. From these amplitudes we can construct three models of spin-zero particle interactions: model $0^+_{\rm SM}$ corresponding to amplitude A_1, model 0^- corresponding to amplitude A_3, and model 0^+_h corresponding to amplitude A_2. The kinematic differences between these models get reflected in the distributions of the decay variables as shown in Fig. 6.9. For example, in the case of a scalar particle the decay planes of the two Zs are more likely to be parallel (the decay angle Φ peaks at 0 or $\pm\pi$) while in the case of a pseudoscalar particle they are more likely to be perpendicular (Φ peaks $\pm\pi/2$)[1]. We can therefore use the decay variables to construct discriminators that can help to distinguish between the models. Let us now consider a hypothesis test through which we can examine the compatibility of the particle observed in data with the SM Higgs boson ($0^+_{\rm SM}$) and a pseudoscalar (0^-).

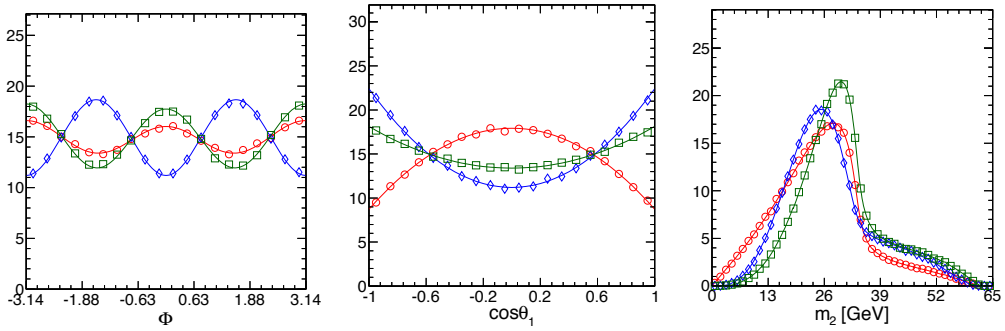

Figure 6.9 Distributions of the decay angles Φ (left) and $\cos(\theta_1)$ (center), and the mass of the Z_2 candidate (right). The $0^+_{\rm SM}$ model is shown in red, the 0^- mode is shown in blue, while the 0^+_h model is shown in green. The plots are taken from ref. [168].

6.4.1 Test of Pseudoscalar v/s Scalar Hypothesis

In order to test the signal model, we need to construct an analysis that can firstly isolate the signal events from the background, and then discriminate these signal events based on their parity. This is achieved with the help of two discriminators. The variable D_{bkg} helps to isolate signal events from the background and is constructed using the following formulation

[1]This can be intuitively understood through C. N. Yang's paper [172] in which he showed that when a scalar particle decays to two photons, the linear polarization planes of the photons are aligned, while in the case of a pseudoscalar the polarization planes are orthogonal to each other.

$$D_{bkg} = \left[1 + \frac{f_{bkg}\left(\vec{\Omega}, m_{Z_1}, m_{Z_2}|m_{4\ell}\right) \times P_{bkg}\left(m_{4\ell}\right)}{f_{sig}\left(\vec{\Omega}, m_{Z_1}, m_{Z_2}|m_{4\ell}\right) \times P_{sig}\left(m_{4\ell}|m_{\mathrm{H}}\right)}\right]^{-1} \tag{6.8}$$

where $f_{sig}\left(\vec{\Omega}, m_{Z_1}, m_{Z_2}|m_{4\ell}\right)$ and $f_{bkg}\left(\vec{\Omega}, m_{Z_1}, m_{Z_2}|m_{4\ell}\right)$ are the likelihood functions as defined in eq. 5.10 that were used in constructing the kinematic discriminant for the 2D search analysis in the last chapter, while $P_{sig}\left(m_{4\ell}|m_{\mathrm{H}}\right)$ and $P_{bkg}\left(m_{4\ell}\right)$ are the shapes of the signal and background mass distributions respectively. The variable D_{bkg} effectively combines the information of the production and decay angles, the Z masses, and the four-lepton mass into a single discriminant. Fig. 6.10(a) shows the D_{bkg} distribution of four-lepton events in data compared to the signal and background expectation. The 4ℓ events in the spin-parity studies are required to be in the mass window of +15/-20 GeV around the best fit value of m_{H}. We can see in Fig. 6.10(a) that the signal events are mostly concentrated in the region $D_{bkg} > 0.5$ while the background is concentrated in the region $D_{bkg} < 0.5$.

We now define a second variable that helps to discriminate between the 0^+_{SM} model which we treat as the null hypothesis, and the 0^- model which is treated as the alternate hypotheses. This variable D_{0^-} is defined as follows

$$D_{0^-} = \left[1 + \frac{f_{0^-}\left(\vec{\Omega}, m_{Z_1}, m_{Z_2}|m_{4\ell}\right)}{f_{0^+_{\mathrm{SM}}}\left(\vec{\Omega}, m_{Z_1}, m_{Z_2}|m_{4\ell}\right)}\right]^{-1} \tag{6.9}$$

where f_{0^-} and $f_{0^+_{\mathrm{SM}}}$ are the likelihood functions derived from the matrix element amplitudes of the 0^- model and 0^+_{SM} models respectively. Fig. 6.10(b) shows the distributions of this discriminant in the signal-enriched region of $D_{bkg} > 0.5$.

In order to perform the hypothesis test a binned two-dimensional likelihood is constructed using the D_{bkg} and D_{0^-} variables. As described in Sec. 3.5 we define a test statistic $q = -2 \times \log(L_{0^-}/L_{0^+_{SM}})$ and obtain the distributions of this test statistic for the 0^- and 0^+_{SM} models from a large set of pseudoexperiments. These distributions are shown in Fig. 6.11 along with the observed value of q. The pseudoexperiments are generated assuming signal yields obtained from the best fit values of signal strength for each of the two models. The expected separation between the two hypotheses is 2.4σ. The consistency of the observed test-statistic (q_{obs}) with the 0^+_{SM} hypothesis is quantified

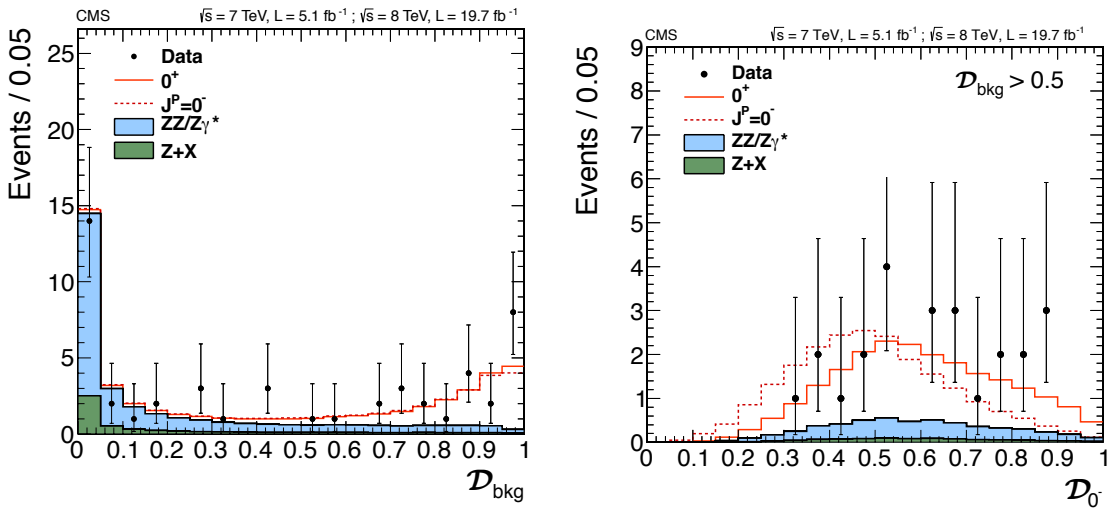

(a) (b)

Figure 6.10 Fig.(a) shows the distribution of D_{bkg} in data compared to the signal and background expectation for four-lepton events in the mass range of 105.6–140.6 GeV. Fig.(b) shows the distribution of D_{0^-} in events with $D_{bkg} > 0.5$.

by the p-value $P(q < q_{obs}|\hat{\mu}S_{0^+_{\rm SM}} + B)$, which is found to be -1.0σ. The negative sign is used to simply indicate that q_{obs} falls on the right of the median expected value of the $0^+_{\rm SM}$ hypothesis distribution. Similarly the consistency of of q_{obs} with the 0^- hypothesis can be quantified by the p-value $P(q > q_{obs}|\hat{\mu}S_{0^-} + B)$, which is found to be 3.8σ. We can also define a $\rm CL_s$ criterion (see Sec. 3.6.3) given by the relation $P(q > q_{obs}|\hat{\mu}S_{0^-} + B)/P(q > q_{obs}|\hat{\mu}S_{0^+_{\rm SM}} + B)$, whose value is found to be 0.05%. We can therefore infer that the pseudoscalar hypothesis is disfavored in comparison to the SM hypothesis at 99.95% CL.

6.4.2 Measurement of f_{a3}

The hypothesis test performed in the last section assumes that the signal is a CP eigenstate. However, the Higgs boson candidate could possibly be a mixture of CP-odd and CP-even eigenstates. This would happen if both a_1 and a_3 are non-zero in eq. 6.7. To see if this is the case, a parameter called f_{a3} is defined as follows

$$f_{a3} = \frac{|a_3|^2\sigma_3}{|a_1|^2\sigma_1 + |a_3|^2\sigma_3} \tag{6.10}$$

where σ_i are the effective cross-sections for the scenarios $a_i = 1, a_{j\neq i} = 0$. The values of σ_i can be slightly different from each other due do interference effects in the $4e$ and

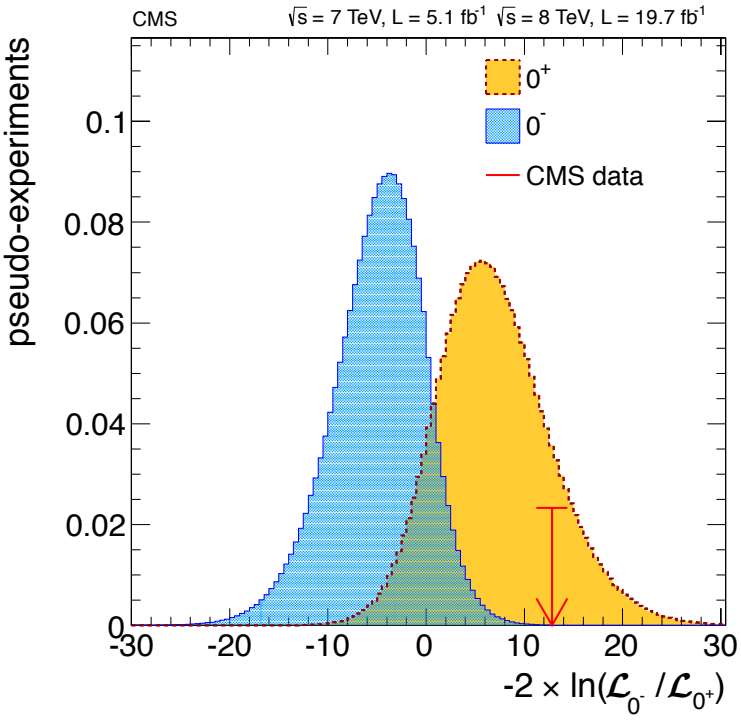

Figure 6.11 Distribution of the test statistic $q = -2 \times log(L_{0^-}/L_{0^+_{SM}})$ assuming the 0^- model (blue) and the $0^+_{\rm SM}$ (yellow). The red arrow points to the observed value of the test statistic (q_{obs}).

4μ final states. In this formulation we have assumed $a_2 = 0$. We should keep in mind that f_{a3} is not a measure of the mixture of the CP-odd and CP-even eigenstates. The parameters a_1 and a_3 depend not only on the fraction of the CP-odd and CP-even states but also on the strength with which these states interact with the Z bosons which may not necessarily be equal. In order to perform a fit of the f_{a3} parameter we define a likelihood function as follows

$$L_{f_{a3}} \equiv (1 - f_{a3})L_{0^+_{\rm SM}} + f_{a3}L_{0^-} \tag{6.11}$$

where $L_{0^+_{\rm SM}}$ and L_{0^-} are the 2D binned likelihood functions for the pure $0^+_{\rm SM}$ and 0^- models that we used to perform the hypothesis test in the last section. Fig. 6.12 shows the scan of of the likelihood function $L_{f_{a3}}$. The best-fit value of f_{a3} is found to be $0.00^{+0.15}_{-0.00}$, and $f_{a3} < 0.47$ at 95% CL.

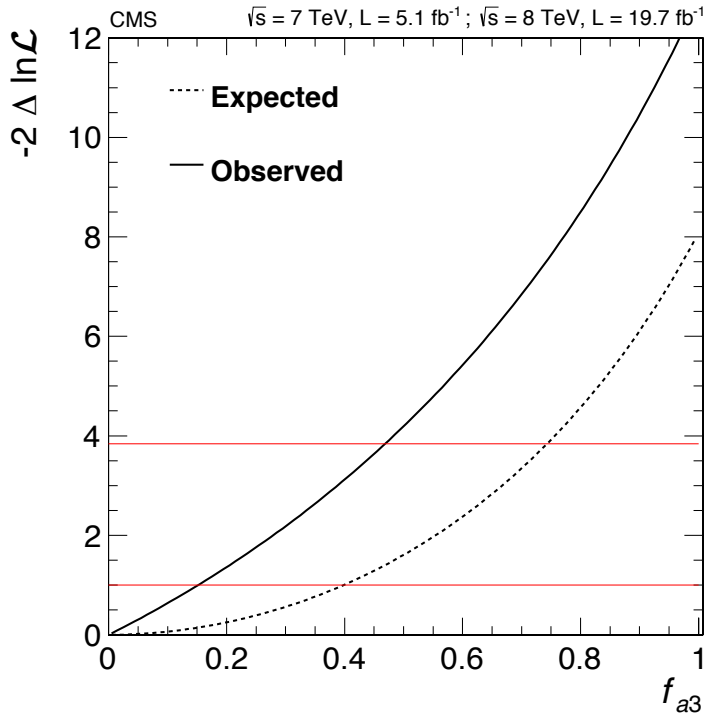

Figure 6.12 Expected and observed χ^2 distributions shown as a function of f_{a3}. The best fit value of f_{a3} is $0.00^{+0.15}_{-0.00}$, and $f_{a3} < 0.47$ at 95% CL.

6.4.3 Tests for Other Spin-parity Models

It is possible to extend our investigation to include several other spin-parity hypotheses [167,168,171]. We can construct the amplitude functions for a generic spin-one and a spin-two particle similar to the spin-zero amplitude of eq. 6.7 and then use these functions to build discriminants (D_{JP}) for several spin-one and spin-two hypotheses. However, we need to be mindful of the fact that the D_{JP} discriminant of a spin-one or a spin-two particle is sensitive to the signal production mode. This dependence enters through the two production angles θ^* and Φ_1. Therefore while performing hypothesis tests two scenarios are considered - exclusive gluon fusion production and exclusive vector boson fusion production. For spin-one hypotheses only the quark induced VBF production is considered since gluon fusion is expected to be strongly suppressed. We can remove the dependence on the production angles by integrating them out while constructing the kinematic discriminants. These discriminants are represented as D^{dec}_{bkg}, and D^{dec}_{JP} where the superscript '*dec*' indicates that only the decay information is used. Table 6.3 lists the various spin-parity models that have been considered. Table 6.4 gives the results of the hypothesis tests performed on each of these models. The spin-one

models are excluded at a confidence level of 99.9% or higher, while the spin-two models are excluded at 95% CL or higher. A hypothesis test of the 0_h^+ model corresponding to the A_2 amplitude in eq. 6.7 is also performed and the model is disfavored at 95.5% CL. Fig. 6.13 shows a graphical representation of the expected and observed separation between the various spin-parity models and the SM hypothesis. Overall we see that the data is consistent with the SM Higgs boson.

Table 6.3 Spin-parity models used for performing hypothesis tests in addition to the pseudoscalar model.

Discriminant	Model
$D_{0_h^+}$	Non-SM scalar with higher dimension operators (0_h^+)
D_{1^-}	Exotic vector, VBF
D_{1^+}	Exotic pseudovector, VBF
$D^{gg}_{2_m^+}$	Graviton-like with minimal couplings, gluon fusion
$D^{qq}_{2_m^+}$	Graviton-like with minimal couplings, VBF
$D^{gg}_{2_b^+}$	Graviton-like with SM in the bulk, gluon fusion
$D^{gg}_{2_h^+}$	Tensor with higher dimension operators, gluon fusion
$D^{gg}_{2_h^-}$	Pseudotensor with higher dimension operators, gluon fusion
$D^{dec}_{1^-}$	Exotic vector, decay only information
$D^{dec}_{1^+}$	Exotic pseudovector, decay only information
$D^{dec}_{2_m^+}$	Graviton-like with minimal couplings, decay only information

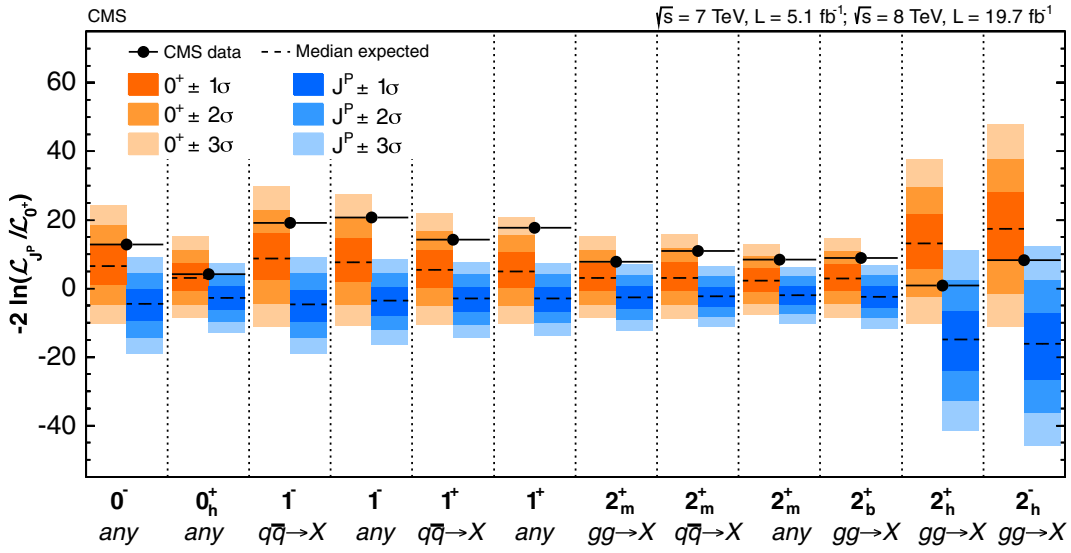

Figure 6.13 Expected and observed separation between the different spin-parity models and the SM hypothesis. The orange bands represent the 1σ, 2σ and 3σ spread around the median expectation for the SM hypothesis. Similarly, the blue bands represent the alternate J^P scenarios.

Table 6.4 Results of the hypothesis tests performed on spin-parity models listed in Tab. 6.3. The expected separation between a given J^P hypothesis and the SM is computed by using the signal strength μ obtained from a fit to the data. The observed separation shows the consistency of data with the SM hypothesis and a given J^P hypothesis. The confidence level for the exclusion of a given hypothesis is computed using the $\mathrm{CL_s}$ criterion. We see that all the alternate spin-parity hypotheses are excluded at a confidence level greater than 95% in relation to the SM. In particular, the spin-one hypotheses are excluded at greater than 99.9% CL. The 0^+_h hypothesis is excluded at 95.5% CL. In the case of the spin-two models, we find that except for the 2^+_h hypothesis which is excluded at 97.7% CL, all the spin-two models are excluded at 99% CL or higher. All the spin-parity models under consideration except for the 2^+_h and 2^-_h models have an observed p-value that is smaller than (or in other words they have a larger observed separation) than the expectation. This can be attributed to the correlations between the various models, particularly in the Z_2 mass shapes.

J^P model	J^P Production	Expected	Obs. 0^+	Obs. J^P	CL_s
0^+_h	any	1.7σ	-0.3σ	$+2.1\sigma$	4.5%
1^-	$qq \to X$	2.7σ	-1.4σ	$+4.7\sigma$	0.002%
1^-	any	2.5σ	-1.8σ	$+4.9\sigma$	0.001%
1^+	$qq \to X$	2.1σ	-1.5σ	$+4.1\sigma$	0.02%
1^+	any	2.0σ	-2.1σ	$+4.8\sigma$	0.004%
2^+_m	$gg \to X$	1.9σ	-1.1σ	$+3.0\sigma$	0.9%
2^+_m	$qq \to X$	1.7σ	-1.7σ	$+3.8\sigma$	0.2%
2^+_m	any	1.5σ	-1.6σ	$+3.4\sigma$	0.7%
2^+_b	$gg \to X$	1.6σ	-1.4σ	$+3.4\sigma$	0.5%
2^+_h	$gg \to X$	3.8σ	$+1.8\sigma$	$+2.0\sigma$	2.3%
2^-_h	$gg \to X$	4.2σ	$+1.0\sigma$	$+3.2\sigma$	0.09%

Chapter 5, in full, is the reprint of the material as it appears in "Measurement of the properties of a Higgs boson in the four-lepton final state", by CMS Collaboration, Phys. Rev. D 89 (2014) 092007. The dissertation author was the primary investigator and author of this paper.

Chapter 7

Summary and Outlook

In the previous chapters we have discussed the search for the SM Higgs boson in the CMS experiment through the lens of the H $\rightarrow ZZ$ channel. We have seen conclusive evidence of a Higgs boson candidate with a mass of $125.6 \pm 0.4(\text{stat}) \pm 0.2(\text{syst})$ GeV. The signal yield is found to agree with the SM prediction. Moreover, the spin-parity character of this particle is found to be consistent with a scalar boson as expected in the SM. But in order to fully explore and appreciate the role of this particle in the framework of the SM we need to go beyond the H $\rightarrow ZZ$ channel and look at the interaction of the Higgs boson candidate with other particles. As we saw in Sec. 1.3.4 the Higgs boson is expected to decay into a pair a photons, a pair of W bosons and also to a pair of fermions apart from decaying into a pair of Z bosons. We will look at the results of these searches performed in both the CMS and ATLAS experiments in the next section. Having seen evidence of the Higgs boson across different channels we collate the information from these channels to test the consistency of the SM. In particular, it is of interest to address the following questions. Does the observed yield of the Higgs boson signal agree with the SM prediction across the different decay modes? Do we have a consistent measurement of the mass of the Higgs boson candidate across channels (at least the two most sensitive ones, namely H $\rightarrow ZZ \rightarrow 4\ell$ and H $\rightarrow \gamma\gamma$) and across experiments? A crucial feature of the Higgs sector is the custodial symmetry which helps to constrain the relation between the masses of the W and Z to all orders of radiative corrections. Do we see evidence of this feature of the SM in data? Lastly does the Higgs boson give us a glimpse into the physics beyond the SM? In a way, the

interactions of the Higgs boson are encoded in its natural width. And so, any deviation of the width of the Higgs boson candidate from the SM expectation would be a clear indication of new physics. In the following sections, we will discuss all these questions one by one.

7.1 Higgs Boson Searches in ATLAS and CMS

In the previous chapters we have discussed the search for the SM Higgs boson in the CMS experiment through the lens of the $\mathrm{H} \to ZZ$ channel. We have seen conclusive evidence of a Higgs boson candidate with a mass of $125.6 \pm 0.4(\mathrm{stat}) \pm 0.2(\mathrm{syst})$ GeV. The signal yield is found to agree with the SM prediction. Moreover, the spin-parity character of this particle is found to be consistent with a scalar boson as expected in the SM. Similar results have also been reported by the ATLAS experiment which observes a 6.6σ excess in the four-lepton final state at a mass of 124.3 GeV [173], as shown in Fig. 7.1. Moreover, this resonance is found to be consistent with a scalar particle and several alternate spin-parity hypotheses have been excluded at a confidence level greater than 97% [174].

Going beyond the $\mathrm{H} \to ZZ$ channel, there is also corroborative evidence of a Higgs boson candidate decaying to two photons in the $\mathrm{H} \to \gamma\gamma$ searches in both the CMS and ATLAS experiments [175–177]. As shown in Fig. 7.2 the CMS experiment observes a 5.7σ excess at the mass of 124.7 GeV, while the ATLAS experiment observes a maximum of 7.4σ local significance at $m_{\mathrm{H}} = 126.5$ GeV. In the third diboson channel, namely $\mathrm{H} \to W^+W^-$, both experiments report a broad $\sim 4\sigma$ excess which is consistent with the prediction of the SM Higgs boson with a mass of 125 GeV [178–180].

The coupling of the Higgs boson to the fermionic particles is another crucial piece of the SM. As we have seen in Sec. 1.3.3 the Higgs boson is mainly produced at the LHC through gluon fusion involving a top-quark loop. Therefore, the observed signal strength of the Higgs boson candidate helps to constrain the interaction between the Higgs boson and the top quark which is an up-type quark. In order to probe the coupling between the Higgs boson and down-type quarks, we need to directly measure the rates of the Higgs boson decay to fermions such as the bottom quark and the tau lepton. The ATLAS

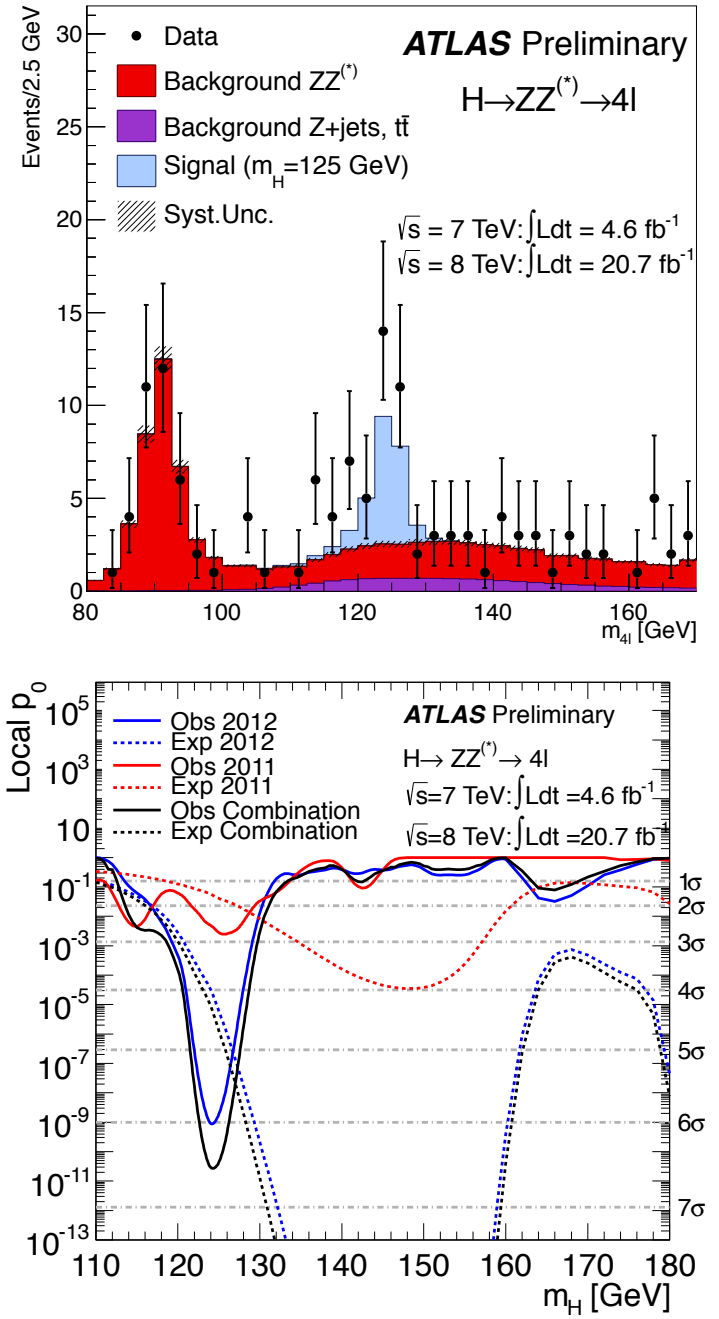

Figure 7.1 The four-lepton mass distribution observed in the H $\to ZZ \to 4\ell$ search performed by the ATLAS experiment is shown on the left. Plot on the right shows the corresponding p-value scan as a function of m_{H}.

experiment has reported a 4.1σ excess in the H $\to \tau^+\tau^-$ channel that is consistent with a 125 GeV Higgs boson [181], but it does not observe any significant excess in the H $\to b\bar{b}$ channel [182]. Fig. 7.3(a) shows the ditau mass distribution observed in the ATLAS H $\to \tau^+\tau^-$ analysis. The CMS experiment observes a 3.2σ excess in H $\to \tau^+\tau^-$ channel [183] and a 2.1σ in the H $\to b\bar{b}$ channel [184] for $m_{\mathrm{H}} = 125$ GeV. The combined

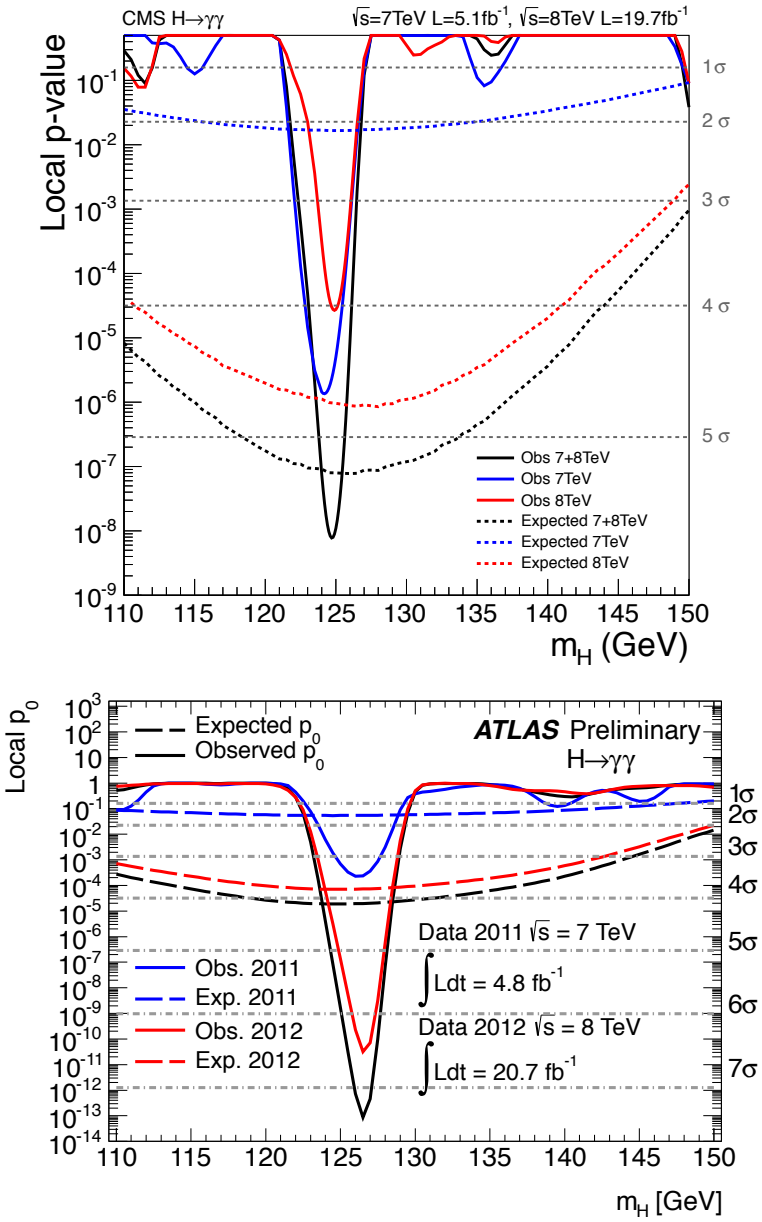

Figure 7.2 The p-value distribution in the H $\rightarrow \gamma\gamma$ search performed by CMS (left) and ATLAS (right).

significance of these two down-type fermionic channels is found to be 3.8σ [185] as shown in Fig. 7.3(b). A clearer understanding of the fermionic interactions of the Higgs boson candidate will only emerge with more data.

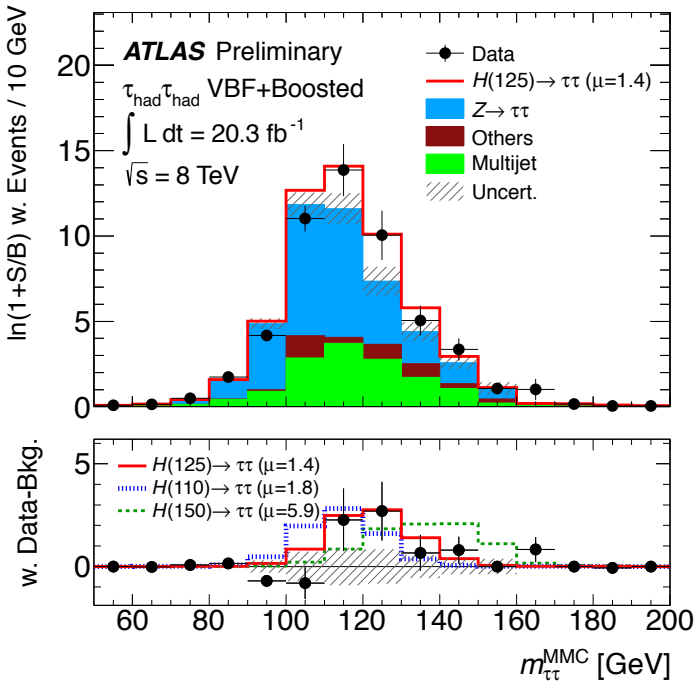

(a)

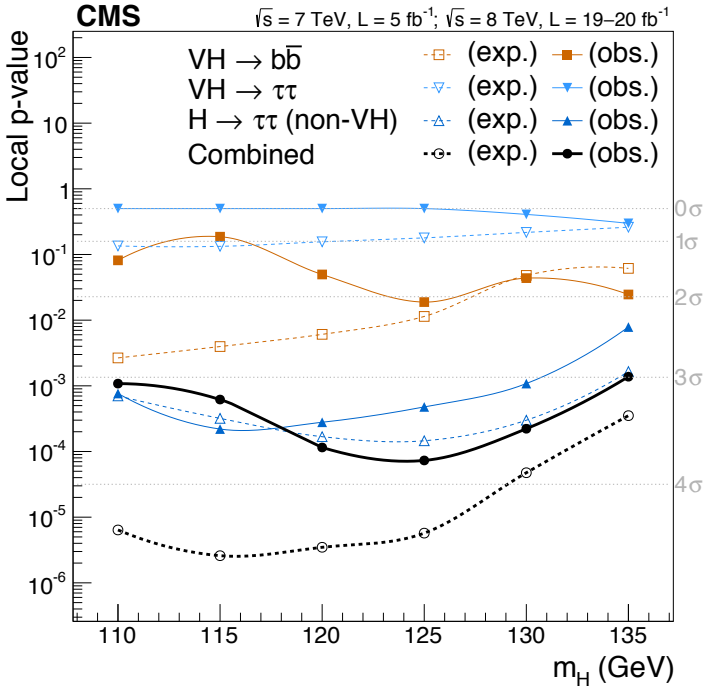

(b)

Figure 7.3 Fig.(a) shows the ditau mass distribution in the H $\rightarrow \tau^+\tau^-$ search performed by the ATLAS experiment. Fig.(b) shows the p-value distributions for the H $\rightarrow \tau^+\tau^-$ and H $\rightarrow b\bar{b}$ searches in the CMS experiment and their combination.

7.2 Mass of the Higgs boson

The evidence from all the Higgs boson searches suggests that we have indeed discovered the SM Higgs boson. The mass of the Higgs boson is the last input necessary

to complete the description of the SM. From an experimental point of view, the $H \to \gamma\gamma$ and $H \to ZZ \to 4\ell$ channels provide the most sensitive measurements of m_H. Both of these channels can measure the mass of the Higgs boson at sub-percent level precision. Table 7.1 lists the best fit values of m_H measured in these two channels by the ATLAS and CMS experiments. The results are consistent with a 125.6 GeV Higgs boson.

Table 7.1 Best fit mass of the Higgs boson candidate measured in $H \to \gamma\gamma$, $H \to ZZ \to 4\ell$ channels by the CMS and ATLAS experiments.

Channel	Measured Mass (GeV)
CMS $H \to \gamma\gamma$	$124.72 \pm 0.31(\text{stat}) \pm 0.16(\text{syst})$
CMS $H \to ZZ \to 4\ell$	$125.6 \pm 0.4(\text{stat}) \pm 0.2(\text{syst})$
ATLAS $H \to \gamma\gamma$	$126.8 \pm 0.2(\text{stat}) \pm 0.7(\text{syst})$
ATLAS $H \to ZZ \to 4\ell$	$124.3^{+0.6}_{-0.5}(\text{stat})\ ^{+0.5}_{-0.3}(\text{syst})$

7.3 Signal Strength of the Higgs Boson

The standard model gives a very precise prediction for the production and decay of the Higgs boson at the LHC. As a result, the signal strength parameter μ provides a crucial input in establishing the consistency of the observed rate of signal events in a given final state with the SM expectation. A significant deviation of μ from unity would be indicative of some new physics beyond the SM. Fig. 7.4 shows the measured values of μ in different channels across the CMS and ATLAS experiments. We find the data to be consistent with the SM.

7.4 Width of the Higgs Boson

The width of the Higgs boson provides a crucial probe of physics beyond the SM. All the particles that interact with the Higgs boson contribute directly to the natural width of the Higgs resonance. Therefore a significant deviation of the Higgs boson width from the SM expectation implies the existence of physics beyond the SM. The

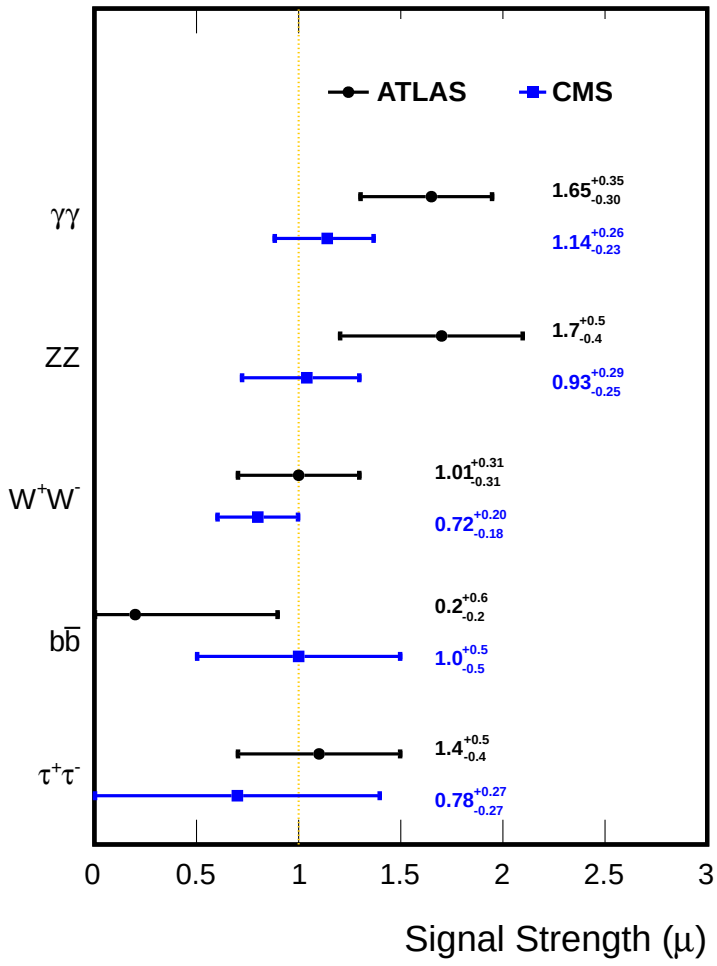

Figure 7.4 Measurements of the signal strength μ in the different Higgs decay channels. The measurements performed by ATLAS are shown in black while the measurements performed by CMS are shown in blue. The results are consistent with unity within two standard deviations. The signal strength reported for the ZZ channel from CMS is taken from [125] and is different from the result quoted in the thesis. The measurement of μ in [125] is performed by separating the four-lepton events in VBF-tagged and untagged categories and then employing a different 3D fit that takes into account the kinematics of the VBF and gluon fusion events but does not use the event-by-event mass uncertainties.

total width of a 125 GeV Higgs boson is about 4 MeV. A direct measurement of the Higgs boson width from the signal resonance is not sensitive to such small values. As discussed in the last chapter such a measurement in the $\mathrm{H} \to ZZ \to 4\ell$ channel yields an upper limit of 3.6 GeV at 95% CL. Here, we are essentially dominated by the momentum resolution of the detector which is several orders of magnitude worse than the expected Higgs boson width. However, it has been recently shown that the off-shell contribution of the Higgs boson signal can help to dramatically improve the sensitivity of the width

measurement [186, 187]. In the off-shell region with high ($m_{ZZ} > 200$ GeV or so), the overall process $gg \to 4\ell$ process can be modeled as follows

$$P_{gg\to 4\ell} = \mu r P_{gg\to \mathrm{H}\to ZZ\to 4\ell} + \sqrt{\mu r} P_{\mathrm{interference}} + P_{gg\to 4\ell} \tag{7.1}$$

where $P_{gg\to \mathrm{H}\to ZZ\to 4\ell}$ is the probability distribution of signal events in the off-shell region, $P_{gg\to 4\ell}$ is the probability of the $gg \to ZZ$ background, and $P_{\mathrm{interference}}$ is the interference term between the signal and the background [188]. The parameter μ represents the signal strength measured from the on-shell region and $r = \Gamma/\Gamma_{\mathrm{H}}$ is the ratio of the observed width to the expectation for a 125.6 GeV SM Higgs boson.

During the writing of this thesis, the CMS experiment experiment has reported a measurement of the Higgs boson width using off-shell events [189]. The measurement combines the results from the $\mathrm{H} \to ZZ \to 4\ell$ and $\mathrm{H} \to ZZ \to 2\ell 2\nu$ channels using the 8 TeV dataset. Fig. 7.5 shows the χ^2 distribution as a function of the parameter r. The observed value of r is found to be $0.3^{+1.5}_{-0.3}$ with an upper limit of $r < 4.2$ at 95% CL. The Higgs boson width has therefore been constrained to within four times the SM expectation.

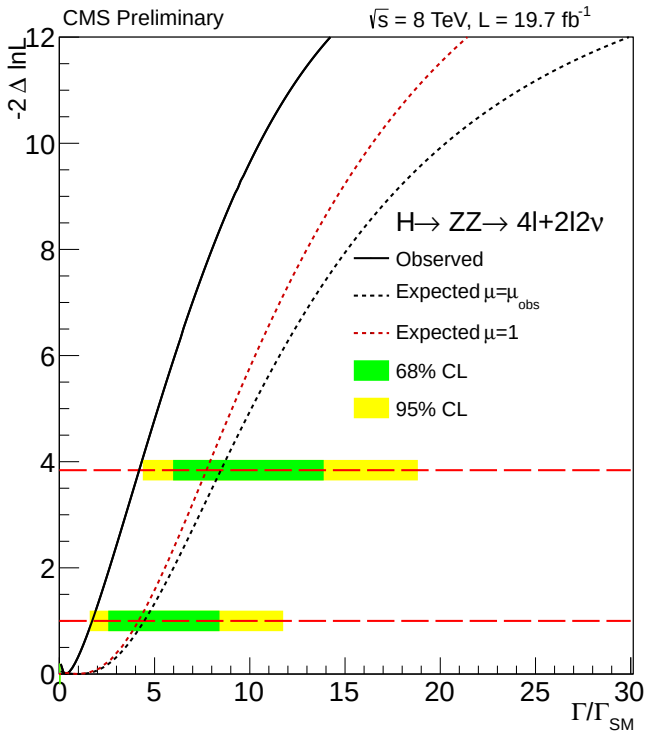

Figure 7.5 χ^2 distribution as a function of the parameter $r = \Gamma/\Gamma_{\rm H}$. The best fit value of r is $0.3^{+1.4}_{-0.3}$ and $r < 4.1$ at 95% CL.

7.5 Test of Custodial Symmetry

In the SM, the Higgs potential (Eq. 1.9) has a global $\mathrm{SU(2)_L \times SU(2)_R}$ symmetry which gets broken due to the BEH mechanism down to the diagonal SU(2) subgroup. The symmetry associated with this subgroup is known as the 'custodial symmetry'. This is not an exact symmetry of the SM and it is explicitly broken by the Yukawa and the $\mathrm{U(1)_Y}$ gauge interactions (If this were to be an exact symmetry, the up-type and down-type quarks would have the same mass). Nevertheless, the custodial symmetry helps to protect the tree level relation between the W and Z boson masses ($M_W = M_Z \cos\theta_W$) from large radiative corrections, and so it forms a crucial feature of Higgs sector [190, 191]. The custodial symmetry can be tested in data by measuring the consistency of the ratio of the couplings between the W and Z bosons and the Higgs boson with unity. In other words, if we assume κ_W and κ_Z to be the scale factors that modify the strength of the SM Higgs boson couplings to the W and Z bosons respectively, then we expect the measurement of $\lambda_{WZ} = \kappa_W/\kappa_Z$ to be consistent with unity if the custodial symmetry is valid. The results for this measurement are shown in

Fig. 7.6 [192]. Two scenarios are considered. In one case, the fermionic couplings of the SM Higgs boson are fixed to the SM expectation, while in the other case the fermionic couplings are themselves profiled from data. We can see that λ_{WZ} in consistent with unity in either case.

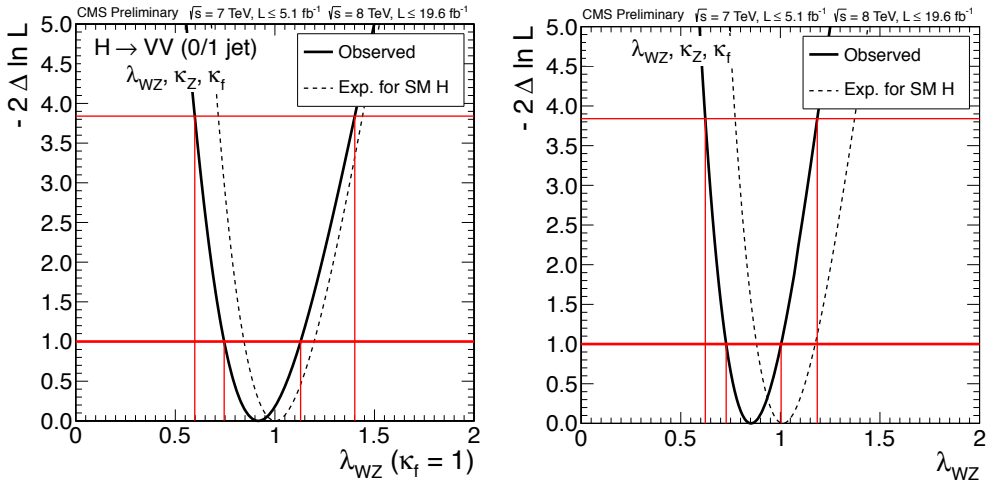

Figure 7.6 Plot on the left shows the measurement of λ_{WZ} performed using untagged (gluon fusion enriched) $H \to W^+W^- \to 2\ell 2\nu$ and all-inclusive $H \to ZZ \to 4\ell$ events. In this measurement the fermionic couplings of the Higgs boson are fixed to the SM expectation. Plot on the right shows the measurement of λ_{WZ} performed by introducing an additional fermionic coupling modifier κ_f which is then profiled from data.

7.6 Theoretical Implications of a 125 GeV Higgs Boson

The value of the Higgs boson mass is critical in establishing the consistency and calculability of the SM at high energies. A Higgs boson mass of 125 GeV is consistent with the unitarity constraints imposed by the weak diboson scattering process. Moreover, $m_{\mathrm{H}} \sim 125$ GeV implies that the parameters of the SM including the Higgs quartic coupling λ remain perturbatively calculable right up to the Planck scale (M_{planck}). Fig. 7.7 shows the evolution of λ as a function of the renormalization scale for $m_{\mathrm{H}} = 125.7$ GeV [193–196]. The quartic coupling needs to be positive for the vacuum state to have a lower bound and hence be stable. We find that λ becomes negative at an energy scale of about 10^{10} TeV. This raises the possibility of new physics emerging at an intermediate scale below M_{planck}. However, the probability to tunnel out of the SM vacuum

remains larger than the age of the universe thus making the electroweak vacuum state metastable.

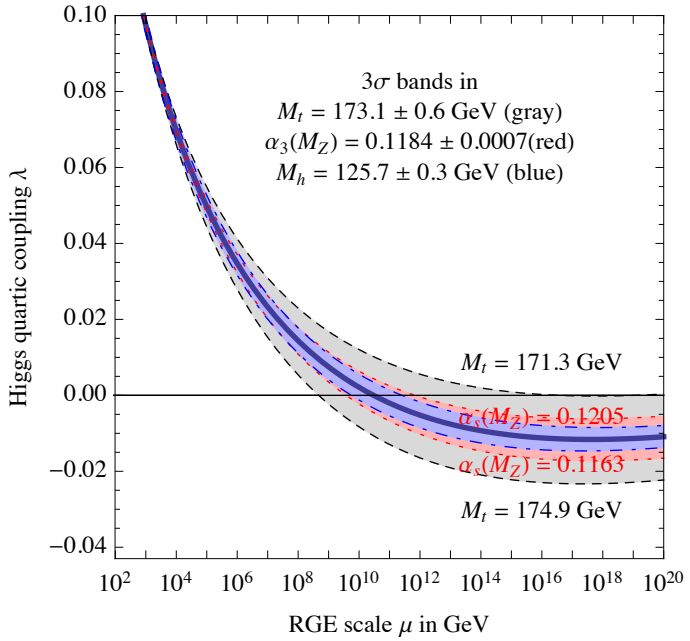

Figure 7.7 The evolution of the quartic coupling of the Higgs potential as a function of the renormalization scale assuming the Higgs boson mass to be 125.7 GeV.

7.7 Concluding Remarks

This thesis has presented conclusive evidence of the existence of a Higgs boson decaying to four leptons. Moreover, compelling evidence has been presented to support the claim that this particle is indeed the Higgs boson of the SM. The Higgs boson searches at the ATLAS and CMS experiments vindicate the SM which still stands the test of time. However, some nagging questions concerning the Higgs sector still remain unanswered. For example, we don't know what protects the mass of the Higgs boson from large quantum corrections (the hierarchy problem). We also have no explanation for the apparently arbitrary structure of the masses of quarks and leptons. These and several more questions can only be answered through physics which goes beyond the standard model. The second run of the LHC which is due to start in 2015 may possibly shed some light on these issues. On the Higgs front, the couplings to fermions still await a more sensitive investigation. With new data streaming in, it would be possible

to perform precision measurements of the Higgs boson properties which in turn would help to probe new physics beyond the standard model. It can only be hoped that more surprises come along our way in the near future.

Chapter 8

Contributions to the CMS Experiment

8.1 Electron Isolation

As I end the thesis document I would like to talk about the contributions that I have to the CMS experimental effort in general and to the CMS Higgs search in particular. I began my journey into experimental high energy physics in the latter half of 2009 when LHC was gearing up towards the launch of its first run at $\sqrt{s} = 7$ TeV. My first project was to study the isolation properties of electrons. As we have seen in this thesis, lepton isolation is a crucial discriminant that helps separate the electroweak processes such as the $Z \to \ell^+\ell^-$ decays from the large QCD background. When I started my work in 2009 the isolation energy surrounding a lepton was computed by summing up transverse energy measured around the lepton in the tracker, the ECAL and the HCAL. The isolation of electrons in particular was complicated by the fact that electrons radiated photons while traversing through the tracker and these photons, if not properly accounted for, would 'spoil' the isolation measurement by contributing to an increase in the isolation energy, thereby reducing the efficiency of the isolation selection. Fig. 8.1 shows the simulated geometrical distribution of ECAL crystals that register a hit due to an electron of $p_T \in [35, 45]$ GeV. We can see a circular bulge in the $\eta - \phi$ space surrounding the electron's position on the ECAL surface. This corresponds to crystals in which the electron dumps its energy. But we also see a strip in $\Delta\phi$ for $\Delta\eta \sim 0$. These

ECAL crystal hits can be attributed to the photons that the electron radiates. This feauture had been studied before and a 'Jurassic veto' had been designed in which all ECAL crystals that fall in a certain circle+strip geometry around an electron would be ignored when computing the isolation sum.

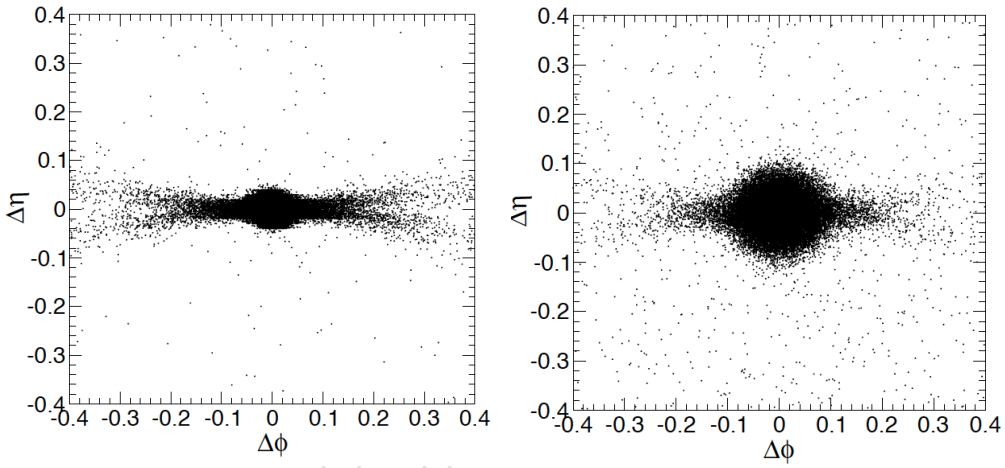

Figure 8.1 Figure on the left shows the geometrical distribution of the reconstructed ECAL crystal hits surrounding an electron with $p_T \in [35, 45]$ GeV when the electron falls inside the ECAL barrel region. Figure on the right shows the corresponding distribution for electrons that fall in the ECAL endcaps.

The study that I performed [197] showed that such a strip feature was present not only in the ECAL but also in the tracker as shown in Fig. 8.2 which shows the geometrical distribution of reconstructed tracks around the same set of electrons. These tracks come from the conversions of photons that are radiated by the electron. By adding a strip veto, a considerable improvement was observed in the discrimination between isolated and non-isolated electrons particularly in the endcaps as shown in Fig. 8.3. This became the default selection for tracker-based electron isolation in CMS and was used in many analysis starting from the early measurements of W and Z cross-sections to several Higgs searches.

8.2 The Higgs Hunt

In 2010, preparations for the Higgs boson search started in full swing as the experiment transitioned from the commissioning phase to the physics era. This year being the first year of LHC operarions, a meager 36 pb^{-1} of integrated luminosity was

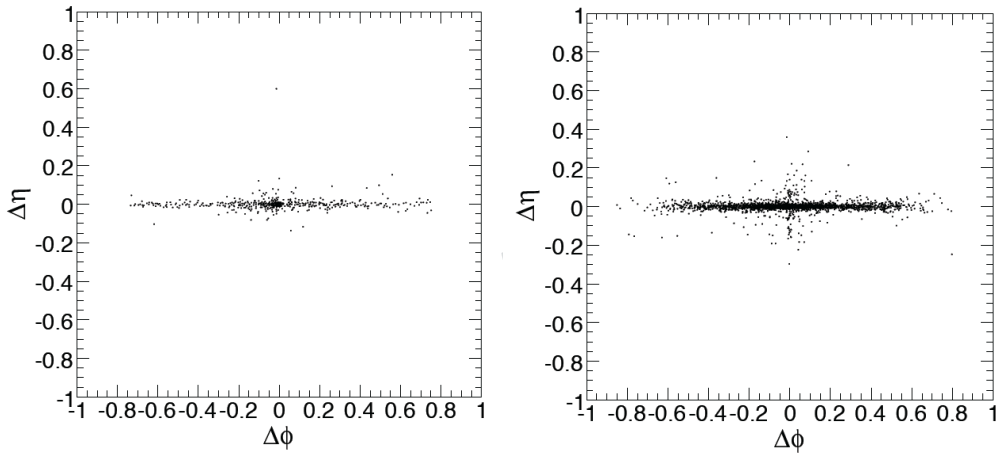

Figure 8.2 Figure on the left shows the geometrical distribution of the reconstructed tracks surrounding an electron with $p_T \in [35, 45]$ GeV when the electron falls inside the ECAL barrel region. Figure on the right shows the corresponding distribution for electrons that fall in the ECAL endcaps.

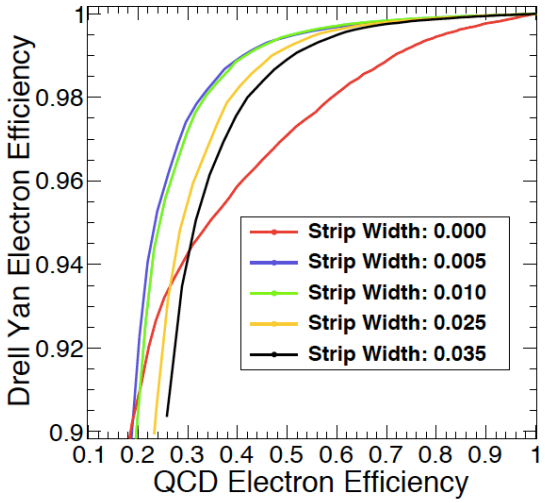

Figure 8.3 Signal v/s background efficiency curves for different choices of the width of the strip veto used in tracker-based isolation of electrons in the endcaps.

delivered. Hence the year was spent in planning for the luminosity ramp up that was poised to happen in 2011, which would bring the Higgs boson searches into focus. At the time, the Higgs boson searches were confined to the canonical channels, namely $\mathrm{H} \to ZZ \to 4\ell$, $\mathrm{H} \to WW \to 2\ell 2\nu$, $\mathrm{H} \to \gamma\gamma$ and $\mathrm{H} \to \tau^+\tau^-$. While these channels were highly sensitive to a low mass Higgs boson, their reach was not expected to extend much beyond $m_{\mathrm{H}} \sim 300$ GeV with the first couple of fb^{-1} of data that would to be collected in 2011.

In the summer of 2010, I started exploring the $\mathrm{H} \to ZZ \to 2\ell 2\nu$ channel to see

if it could help in improving the Higgs boson search reach in the high mass region. At the time this channel was not considered to be very useful in the initial phase of data-taking [198]. However, I was able to show that the $H \to ZZ \to 2\ell 2\nu$ mode was not just useful but it had the potential to be the most sensitive channel in the high mass region. I followed this up by performing a feasibility study of the $H \to ZZ \to 2\ell 2b$ channel, showing that it too had the potential to help improve the high mass search reach. These encouraging results prompted me to focus on the $H \to ZZ \to 2\ell 2\nu$ channel in 2011.

The task was to transform the feasibility study into a full-blown analysis. A critical feature of any search analysis is the estimation of the background processes. I devised strategies for a data-driven estimation for several key backgrounds that are involved in the analysis. As we have seen in chapter 4, the Z+jets process forms a crucial background to the $H \to ZZ \to 2\ell 2\nu$ signal. We have also seen that this background cannot be reliably estimated from simulation. This meant that a data-driven technique was essential to estimate the Z+jets contribution. In the beginning of 2011, I developed a novel procedure to use γ+jets events in data for estimating this background. Then I put into place the strategy of using $e\mu$ events to get a data-driven estimate of the non-resonant background. By the summer of 2011 I was able to perform a complete analysis of this mode which was then presented in that year's EPS and Lepton-Photon conferences. By the end of 2011, I extended the analysis to the full 5 fb^{-1} 7 TeV dataset and wrote a paper describing the results that was published in the Journal of High Energy Physics [166].

With the 2011 data, the CMS and ATLAS experiments were able to exclude on their own a large swathe of the SM Higgs boson landscape and the focus shifted to a tiny mass strip between 120–130 GeV. It was clear that if the SM Higgs boson was sitting in this mass range, the two channels that would show clear signs of its existence were $H \to \gamma\gamma$ and $H \to ZZ \to 4\ell$. This is when I decided to shift my focus on to the four leptons analysis. Here I contributed to the studies of the reducible background which needs to be estimated from data. Furthermore, I contributed to the measurement of the mass and width (width from the on-shell events) of the newly discovered Higgs boson candidate. This includes the development of the analytical approximation for the CB$\otimes$BW convolution which enabled the computation of the width results in a reasonable

amount of time. All of this work has contributed directly towards the publication of the $H \to ZZ \to 4\ell$ results starting from the discovery paper in 2012 [48] to the Run I legacy paper in 2013 [199]. I have put together a completely independent analysis framework with which I have performed the 4ℓ analysis that has been presented in this thesis. All the physics results discussed in chapters 4,5 and 6 with the exception of the spin-parity studies have been obtained using this analysis framework.

8.3 Detector Work

Over the years I have been an active participant in several activities related to the CMS tracker and also the track reconstruction effort. For the past four years, I have served as the contact person for the tracking group tasked with performing validation of the tracking software in simulation. The CMS software has a release cycle such that improvements and changes to the software are announced on a regular (weekly or biweekly). It is my responsibility to validate these changes in the context of track reconstruction by making detailed comparisons with an earlier software release. Apart from performing checks on the current state of the tracking software, I also validate the on-going tracking work in the context of the future upgrades to the CMS detector.

In the last two years I have also been involved in the operations and commissioning activities of the CMS strip tracker. In 2012, while the LHC was delivering data, I was one of the on-call experts for the tracker data acquisition system. In addition I have performed several studies concerning the performance of the strip tracker. Using data collected from a dedicated 2012 commissioning run I studied the time profile of the signal in different parts of the tracker. Certain delays get introduced in the propagation of the signal on account of several factors such as hardware response, time of flight of particles, etc. The readout of the tracker has to be synchronized to account for these delays. The results of the analysis that I performed are shown in Fig. 8.4. The plot shows the deviation of the signal peak from the nominal sampling or readout point for different regions of the strip tracker. As we can see, the tracker readout is synchronized with the signal within a couple of nano-seconds.

Another study I have performed involves the identification of noisy strips in the

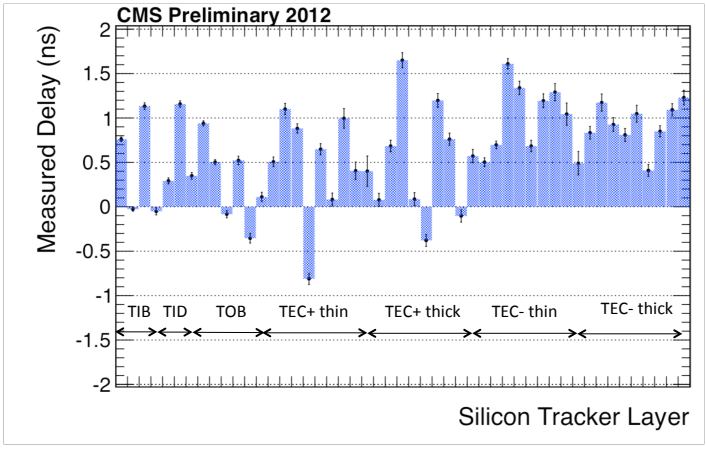

Figure 8.4 Plot shows the shift in time of the position of the signal peak for the different parts of the strip tracker.

tracker. We typically expect the strip noise to have a Gaussian shape. However, there are certain strips that exhibit some abnormalities as shown in fig: 8.5. Such strips need to be identified so that, if need be, they may be masked from the tracker readout. The study that I performed was aimed at identifying such strips by performing statistical tests to check the compatibility of their noise profile with the normal distribution.

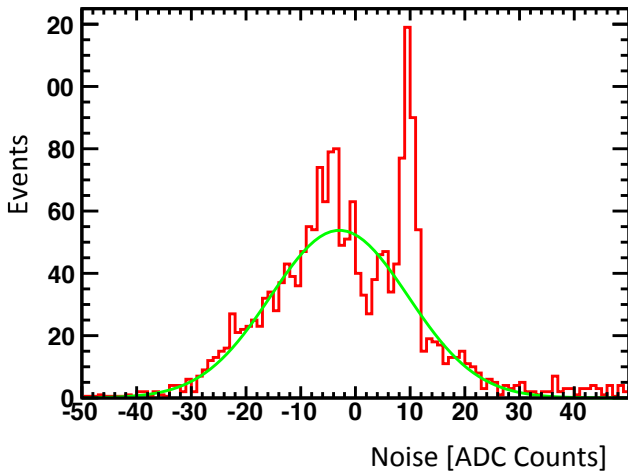

Figure 8.5 Noise distribution of a strip that shows some abnormal, non-Gaussian features. The green curve is the attempted Gaussian fit to this distribution.

I have also helped to set up the analysis to estimate the bias voltage to be applied to the tracker modules based on their noise v/s bias profile. More recently,

I have been working on upgrading the software interface that is used for performing various commissioning tasks. As of now I am involved in the commissioning of the tracker as CMS gears up towards the second run of the LHC.

Bibliography

[1] S. L. Glashow. Partial symmetries of weak interactions. *Nucl. Phys.*, 22:579, 1961.

[2] S. Weinberg. A model of leptons. *Phys. Rev. Lett.*, 19:1264, 1967.

[3] A. Salam. Weak and electromagnetic interactions in elementary particle physics: relativistic groups and analyticity. *Proceedings of eighth Nobel Symposium*, page 367, 1968.

[4] G. 't Hooft and M. J. G. Veltman. Renormalization of massless Yang-Mills. *Nucl. Phys. B*, 33:173, 1971.

[5] G. 't Hooft and M. J. G. Veltman. Renormalizable lagrangians for massive Yang-Mills fields. *Nucl. Phys. B*, 35:167, 1971.

[6] M. Gell-Mann. A schematic model of baryons and mesons. *Phys. Lett.*, 8:214, 1964.

[7] G. Zweig. An SU(3) model for strong interaction symmetry and its breaking I. *CERN REPORT*, 8182/TH401, 1964.

[8] G. Zweig. An SU(3) model for strong interaction symmetry and its breaking II. *CERN REPORT*, 8418/TH412, 1964.

[9] O. W. Greenberg. Spin and unitary independence in a paraquark model of baryons and mesons. *Phys. Rev. Lett.*, 13:598, 1964.

[10] M. Y. Han and Y. Nambu. Three-triplet model with double SU(3) symmetry. *Phys. Rev. B*, 139:1006, 1965.

[11] D. Gross and F. Wilczek. Ultraviolet behavior of non-abelian gauge theories. *Phys. Rev. Lett.*, 30:1343, 1973.

[12] H. D. Politzer. Reliable perturbative results for strong interactions? *Phys. Rev. Lett.*, 30:1346, 1973.

[13] F. Englert and R. Brout. Broken symmetry and the mass of gauge vector mesons. *Phys. Rev. Lett.*, 13:321, 1964.

[14] P. W. Higgs. Broken symmetries, massless particles and gauge fields. *Phys. Lett.*, 12:132, 1964.

[15] P. W. Higgs. Broken symmetries and the masses of gauge bosons. *Phys. Rev. Lett.*, 13:508, 1964.

[16] G. S. Guralnik, C. R. Hagen, and T. Kibble. Global conservation laws and massless particles. *Phys. Rev. Lett.*, 13:585, 1964.

[17] P. W. Higgs. Broken symmetry breakdown without massless bosons. *Phys. Rev.*, 145:1156, 1966.

[18] T. W. B. Kibble. Symmetry breaking in non-abelian gauge theories. *Phys. Rev.*, 155:1554, 1967.

[19] CDF Collaboration. Observation of top quark production in $\bar{p} - p$ collisions with the Collider Detector at Fermilab. *Phys. Rev. Lett.*, 74:2626, 1995.

[20] D0 Collaboration. Observation of the top quark. *Phys. Rev. Lett.*, 74:2632, 1995.

[21] C. N. Yang and R. Mills. Conservation of isotopic spin and isotopic gauge invariance. *Phys. Rev.*, 96:191, 1954.

[22] A. Djouadi. The anatomy of electroweak symmetry breaking: Tome I. *Phys. Rept.*, 457:1, 2008.

[23] J. Bardeen, L. N. Cooper, and J. R. Schrieffer. Microscopic theory of superconductivity. *Phys. Rev.*, 106:162, 1967.

[24] J. Bardeen, L. N. Cooper, and J. R. Schrieffer. Theory of superconductivity. *Phys. Rev.*, 108:1175, 1967.

[25] Y. Nambu. Quasiparticles and gauge invariance in the theory of superconductivity. *Phys. Rev.*, 117:648, 1960.

[26] Y. Nambu and G. Jona-Lasinio. Dynamical model of elementary particles based on an analogy with superconductivity I. *Phys. Rev.*, 122:345, 1961.

[27] Y. Nambu and G. Jona-Lasinio. Dynamical model of elementary particles based on an analogy with superconductivity II. *Phys. Rev.*, 124:246, 1961.

[28] J. Goldstone. Field theories with superconductor solutions. *Il Nuovo Cimento*, 19:154, 1961.

[29] J. Goldstone, A. Salam, and S. Weinberg. Broken symmetries. *Phys. Rev.*, 127:965, 1962.

[30] J. Schwinger. Gauge invariance and mass. *Phys. Rev.*, 125:397, 1962.

[31] J. Schwinger. Gauge invariance and mass II. *Phys. Rev.*, 128:2425, 1962.

[32] P. W. Anderson. Plasmons, gauge invariance, and mass. *Phys. Rev.*, 130:439, 1963.

[33] A. Migdal and A. Polyakov. Spontaneous breakdown of strong interaction symmetry and the absence of massless particles. *Sov. Phys.JETP*, 24:91, 1965.

[34] N. Cabibbo. Unitary symmetry and leptonic decays. *Phys. Rev. Lett.*, 10:531, 1963.

[35] M. Kobayashi and T. Maskawa. CP-Violation in the renormalizable theory of weak interaction. *Progress of Theoretical Physics*, 49:652, 1973.

[36] T. van Ritbergen and R. G. Stuart. Complete 2-loop quantum electrodynamic contributions to the muon lifetime in the Fermi Model. *Phys. Rev. Lett.*, 82:488, 1999.

[37] M. J. G. Veltman. Second threshold in weak interactions. *Acta Phys. Polon. B*, 8:475, 1977.

[38] B. W. Lee, C. Quigg, and H. B. Thacker. Weak interactions at very high energies: The role of the Higgs boson mass. *Phys. Rev. D*, 16:1519, 1977.

[39] B. W. Lee, C. Quigg, and H. B. Thacker. The strength of weak interactions at very high energies and the Higgs boson mass. *Phys. Rev. Lett.*, 38:883, 1977.

[40] M. S. Chanowitz and M. K. Gaillard. The TeV physics of strongly interacting W's and Z's. *Nucl. Phys. B*, 261:379, 1985.

[41] S. P. Martin. A supersymmetry primer. arXiv:hep-ph/9709356, 1997.

[42] M. M. Kado and C. G. Tully. The searches for the Higgs bosons at lep. *Annu. Rev. Nucl. Part. Sci.*, 52:65, 2002.

[43] ALEPH, DELPHI, L3, OPAL collaborations, and LEP Working Group For Higgs Boson Searches. Search for the standard model Higgs boson at LEP. *Phys. Lett. B*, 565:61, 2003.

[44] CDF and D0 collaborations. Combination of tevatron searches for the standard model higgs boson in the W^+W^- decay mode. *Phys. Rev. Lett.*, 104:061802, 2010.

[45] ALEPH, CDF, DO, DELPHI, OPAL, SLD collaborations, LEP Electroweak Working Group, Tevatron Electroweak Working Group, and SLD Electroweak Heavy Flavour Groups. Precision electroweak measurements and constraints on the standard model. *CERN-PH-EP/2010-095*, 2010.

[46] CMS Collaboration. Combined results of searches for the standard model higgs boson in pp collisions at sqrt(s) = 7 TeV. *Phys. Lett. B*, 710:26, 2012.

[47] ATLAS Collaboration. Observation of a new particle in the search for the standard model Higgs boson with the ATLAS detector at the LHC. *Phys. Lett. B*, 716:1, 2012.

[48] CMS Collaboration. Observation of a new boson at a mass of 125 gev with the CMS experiment at the LHC. *Phys. Lett. B*, 716:30, 2012.

[49] CDF and D0 collaborations. Evidence for a particle produced in association with weak bosons and decaying to a bottom-antibottom quark pair in Higgs boson searches at the Tevatron. *Phys. Rev. Lett.*, 109:071804, 2012.

[50] CDF and D0 collaborations. Higgs boson studies at the Tevatron. *Phys. Rev. D*, 88:052014, 2013.

[51] E. Eichten, I. Hinchliffe, K. Lane, and C. Quigg. Supercollider physics. *Rev. Mod. Phys.*, 56:579, 1984.

[52] C. Quigg. LHC physics potential vs. energy. FERMILAB-FN-0839-T, 2009.

[53] H. M. Georgi, S. L. Glashow, M. E. Machacek, and D. V. Nanopoulos. Higgs bosons from two-gluon annihilation in proton-proton collisions. *Phys. Rev. Lett.*, 40:692, 1978.

[54] D. Graudenz, M. Spira, and P.M. Zerwas. QCD corrections to Higgs-boson production at proton-proton colliders. *Phys. Rev. Lett.*, 70:1372, 1993.

[55] M. Spira, A. Djouadi, D. Graudenz, and P.M. Zerwas. Higgs boson production at the LHC. *Nucl. Phys. B*, 453:17, 1995.

[56] S. Dawson. Radiative corrections to Higgs boson production. *Nucl. Phys. B*, 359:283, 1991.

[57] A. Djouadi, M. Spira, and P. M. Zerwas. Production of Higgs bosons in proton colliders: QCD corrections. *Phys. Lett. B*, 264:440, 1991.

[58] R.V. Harlander. Virtual corrections to $gg \to H$ to two loops in the heavy top limit. *Phys. Lett. B*, 492:74, 2000.

[59] S. Catani, D. de Florian, and M. Grazzini. Higgs production in hadron collisions: Soft and virtual QCD corrections at NNLO. *JHEP*, 05:025, 2001.

[60] R.V. Harlander and W.B. Kilgore. Soft and virtual corrections to $gg \to H + X$ at NNLO. *Phys. Rev. D*, 64:013015, 2001.

[61] R.V. Harlander and W.B. Kilgore. Next-to-Next-to-Leading Order Higgs production at hadron colliders. *Phys. Rev. Lett.*, 88:201801, 2002.

[62] C. Anastasiou and K. Melnikov. Higgs boson production at hadron colliders in NNLO QCD. *Nucl. Phys. B*, 646:220, 2002.

[63] V. Ravindran, J. Smith, and W.L. van Neerven. NNLO corrections to the total cross-section for Higgs boson production in hadron hadron collisions. *Nucl. Phys. B*, 665:325, 2003.

[64] J. Blumlein and V. Ravindran. Mellin moments of the next-to-next-to leading order coefficient functions for the Drell-Yan process and hadronic Higgs-boson production. *Nucl. Phys. B*, 716:128, 2005.

[65] S. Catani, D. de Florian, M. Grazzini, and P. Nason. Soft-gluon resummation for Higgs boson production at hadron colliders. *JHEP*, 0307:028, 2003.

[66] A. Djouadi and P. Gambino. Leading electroweak correction to Higgs boson production at proton colliders. *Phys. Rev. Lett.*, 73:2528, 1994.

[67] S. Actis, G. Passarino, C. Sturm, and S. Uccirati. NLO electroweak corrections to Higgs boson production at hadron colliders. *Phys. Lett. B*, 670:12, 2008.

[68] U. Aglietti, R. Bonciani, G. Degrassi, and A. Vicini. Two-loop light fermion contribution to Higgs production and decays. *Phys. Lett. B*, 595:432, 2004.

[69] G. Degrassi and F. Maltoni. Two-loop electroweak corrections to Higgs production at hadron colliders. *Phys. Lett. B*, 600:255, 2004.

[70] C. Anastasiou, R. Boughezal, and F. Petriello. Mixed QCD-electroweak corrections to Higgs boson production in gluon fusion. *JHEP*, 0904:003, 2009.

[71] T. Han, G. Valencia, and S. Willenbrock. Structure-function approach to vector-boson scattering in pp collisions. *Phys. Rev. Lett.*, 69:3274, 1992.

[72] T. Figy, C. Oleari, and D. Zeppenfeld. Next-to-leading order jet distributions for Higgs boson production via weak-boson fusion. *Phys. Rev. D*, 68:073005, 2003.

[73] T. Figy and D. Zeppenfeld. QCD corrections to jet correlations in weak boson fusion. *Phys. Lett. B*, 591:297, 2004.

[74] E. L. Berger and J. Campbell. Higgs boson production in weak boson fusion at next-to-leading order. *Phys. Rev. D*, 70:073011, 2004.

[75] M. Ciccolini, A. Denner, and S. Dittmaier. Strong and electroweak corrections to the production of a Higgs boson + 2jets via weak interactions at the Large Hadron Collider. *Phys. Rev. Lett.*, 99:161803, 2007.

[76] M. Ciccolini, A. Denner, and S. Dittmaier. Electroweak and QCD corrections to Higgs production via vector-boson fusion at the CERN LHC. *Phys. Rev. D*, 77:013002, 2008.

[77] A. Denner, S. Dittmaier, and A. Muck. HAWK. http://omnibus.uni-freiburg.de/sd565/programs/hawk/hawk.html.

[78] K. Arnold, M. Bahr, G. Bozzi, F. Campanario, C. Englert, T. Figy, N. Greiner, C. Hackstein, V. Hankele, B. Jager, G. Klamke, M. Kubocz, C. Oleari, S. Platzer, S. Prestel, M. Worek, and D. Zeppenfeld. VBFNLO: A parton level monte carlo for processes with electroweak bosons. *Comput. Phys. Commun.*, 180:1661, 2009.

[79] M. Spira. VV2H. http://people.web.psi.ch/spira/vv2h.

[80] N. E. Adam, T. Aziz, J.R. Andersen, A. Belyaev, T. Binoth, S. Catani, M. Ciccolini, J.E. Cole, S. Dawson, A.Denner, S. Dittmaier, A. Djouadi, M. Drees, U. Ellwanger, C. Englert, T. Figy, E. Gabrielli, D. Giordano, S. Gleyzer, R. Godbole, M. Grazzini, S. Greder, V. Halyo, M. Hashemi, S. Heinemeyer, G. Heinrich, M. Herquet, S. Hesselbach, C. Hugonie, C.B. Jackson, N. Kauer, R. Kinnunen, S.F. King, S. Lehti, F. Maltoni, B. Mele, P. Mertsch, M. Moretti, S. Moretti, M. Muhlleitner, A.K. Nayak, A. Nikitenko, C. Oleari, F. Piccinini, R. Pittau, J. Rathsman, I. Rottlaender, C.H. Shepherd-Themistocleous, M. Schumacher, J.M. Smillie, A. Sopczak, M. Spira, M. Takahashi, A. M. Teixeira, I.R. Tomalin, M. Vazquez Acosta, G. Weiglein, C.D. White, and D. Zeppenfeld. Higgs working group summary report. arXiv:0803.1154[hep-ph], 2008.

[81] T. Figy, S. Palmer, and G. Weiglein. Higgs production via weak boson fusion in the standard model and the MSSM. *JHEP*, 1202:105, 2012.

[82] P. Bolzoni, F. Maltoni, S. O. Moch, and M. Zaro. Higgs boson production via vector-boson fusion at next-to-next-to-leading order in QCD. *Phys. Rev. Lett.*, 105:011801, 2010.

[83] S. L. Glashow, D. V. Nanopoulos, and A. Yildiz. Associated production of higgs bosons and Z particles. *Phys. Rev. D*, 18:1724, 1978.

[84] T. Han and S. Willenbrock. QCD correction to the pp $\rightarrow$ WH and ZH total cross sections. *Phys. Lett.*, 273:167, 1991.

[85] H. Baer, B. Bailey, and J. F. Owens. O (alpha-s) Monte Carlo approach to W + Higgs associated production at hadron supercolliders. *Phys. Rev. D*, 47:2730, 1993.

[86] J. Ohnemus and W. J. Stirling. Order alpha-s corrections to the differential cross-section for the W H intermediate mass Higgs signal. *Phys. Rev. D*, 47:2722, 1993.

[87] A. Stange, W. J. Marciano, and S. Willenbrock. Higgs bosons at the Fermilab Tevatron. *Phys. Rev. D*, 49:1354, 1994.

[88] A. Stange, W. J. Marciano, and S. Willenbrock. Associated production of Higgs and weak bosons, with H $\rightarrow$ b anti-b, at hadron colliders. *Phys. Rev. D*, 50:4491, 1994.

[89] R. Hamberg, W. L. van Neerven, and T. Matsuura. A complete calculation of the order αs2 correction to the Drell-Yan K factor. *Nucl.Phys. B*, 359:343, 1991.

[90] O. Brein, A. Djouadi, and R. Harlander. NNLO QCD corrections to the Higgs-strahlung processes at hadron colliders. *Phys. Lett. B*, 579:149, 2004.

[91] L. Altenkamp, S. Dittmaier, R. V. Harlander, H. Rzehak, and T. J. E. Zirke. Gluon-induced Higgs-strahlung at next-to-leading order QCD. *JHEP*, 1302:078, 2013.

[92] M. L. Ciccolini, S. Dittmaier, and M. Kramer. Electroweak radiative corrections to associated WH and ZH production at hadron colliders. *Phys. Rev. D*, 68:073003, 2003.

[93] A. Denner, S. Dittmaier, S. Kallweit, and A. Muck. Electroweak corrections to higgs-strahlung off W/Z bosons at the Tevatron and the LHC with HAWK. *JHEP*, 1203:75, 2012.

[94] R. Raitio and W. W. Wada. Higgs-boson production at large transverse momentum in quantum chromodynamics. *Phys. Rev. D*, 19:941, 1979.

[95] J. N. Ng and P. Zakarauskas. QCD-parton calculation of conjoined production of Higgs bosons and heavy flavors in pp collisions. *Phys. Rev. D*, 29:876, 1984.

[96] J. F. G. Gunion. Associated top anti-top Higgs production as a large source of W H events: Implications for Higgs detection in the lepton neutrino gamma gamma final state. *Phys. Lett. B*, 261:510, 1991.

[97] W. J. Marciano and F. E. Paige. Associated production of Higgs bosons with $t\bar{t}$pairs. *Phys. Rev. Lett.*, 66:2433, 1991.

[98] W. Beenakker, S. Dittmaier, M. Kramer, B. Plumper, M. Spira, and P. M. Zerwas. Higgs radiation off top quarks at the Tevatron and the LHC. *Phys. Rev. Lett.*, 87:201805, 2001.

[99] L. Reina and S. Dawson. Next-to-leading order results for tth production at the Tevatron. *Phys. Rev. Lett.*, 87:201804, 2001.

[100] S. Dawson, L. H. Orr, L. Reina, and D. Wackeroth. Next-to-leading order QCD corrections to pp tth at the CERN Large Hadron Collider. *Phys. Rev. D*, 67:071503, 2003.

[101] W. Beenakker, S. Dittmaier, M. Kramer, B. Plumper, M. Spira, and P. M. Zerwas. NLO qcd corrections to t anti-t H production in hadron collisions. *Nucl. Phys. B*, 653:151, 2003.

[102] R. N. Cahn and S. Dawson. Production of very massive Higgs bosons. *Phys. Lett. B*, 136:196, 1984.

[103] https://twiki.cern.ch/twiki/bin/view/LHCPhysics/CrossSections.

[104] LHC Higgs Cross section Working Group. Handbook of LHC Higgs cross sections: 1. Inclusive observables. arXiv:1101.0593 [hep-ph], 2011.

[105] P. M. Nadolsky et al. Implications of CTEQ global analysis for collider observables. *Phys. Rev. D*, 78:013004, 2008.

[106] A. D. Martin, W. J. Stirling, R. S. Thorne, and G. Watt. Parton distributions for the LHC. *Eur. Phys. J. C*, 63:189, 2009.

[107] R. D. Ball, L. Del Debbio, S. Forte, A. Guffanti, J. I. Latorre, J. Rojo, and M. Ubiali. A first unbiased global NLO determination of parton distributions and their uncertainties. *Nucl. Phys. B*, 838:136, 2010.

[108] M. LeBourgeois. Search for the standard model Higgs boson in the fully leptonic WW decay channel at CMS. CMS Thesis, 2012.

[109] G. Passarino, C. Sturm, and S. Uccirati. Higgs pseudo-observables, second riemann sheet and all that. *Nucl. Phys. B*, 834:77, 2010.

[110] S. Goria, G. Passarino, and D. Rosco. The Higgs boson lineshape. arXiv:1112.5517 [hep-ph], 2012.

[111] LHC Higgs Cross section Working Group. Handbook of LHC Higgs cross sections: 2. Differential distributions. arXiv:1201.3084 [hep-ph], 2012.

[112] ECFA-CERN. *Large Hadron Collider in the LEP Tunnel*, 1984.

[113] L. Evans and P. Bryant. LHC machine. *JINST*, 3:S08001, 2008.

[114] M. Lamont. The LHC's first long run. *CERN Courier*, 53(7):25, 2013.

[115] CMS Collaboration. CMS physics TDR: Volume I (PTDR1), detector performace and software, 2006. CERN-LHCC-2006-001.

[116] D. Froidevaux and P. Sphicas. General-purpose detectors for the Large Hadron Collider. *Annu. Rev. Nucl. Part. Sci.*, 56:375, 2006.

[117] CMS Collaboration. The CMS experiment at the CERN LHC. *JINST*, 3:S08004, 2008.

[118] CMS Collaboration. Description and performance of track and primary vertex reconstruction with the CMS tracker, 2014. To be published.

[119] CMS Collaboration. Performance of electron reconstruction and selection with the CMS detector at sqrt(s)=8TeV, 2013. Similar older plots can be found here: Eur. Phys. J. C, 49, 1099 (2007).

[120] J. Brooke. Performance of the CMS Level-1 Trigger. ICHEP 2012 Conference Report: CR-2012-322, 2012.

[121] S. Beauceron. The CMS High Level Trigger. ICHEP 2012 Conference Report: CR-2012-355, 2012.

[122] CMS Collaboration. Electron reconstruction and identification at sqrt(s) = 7 TeV, 2008. CMS-PAS-EGM-10-004.

[123] CMS Collaboration. Photon reconstruction and identification at sqrt(s) = 7 TeV, 2010. CMS-PAS-EGM-10-004.

[124] CMS Collaboration. Energy calibration and resolution of the CMS electromagnetic calorimeter in pp collisions at sqrt(s) = 7 TeV. *JINST*, 8:P09009, 2013.

[125] CMS Collaboration. Measurement of the properties of a Higgs boson in the four-lepton final state. *Phys. Rev. D*, 89:092007, 2014.

[126] S. Catani, Y. L. Dokshitzer, M. H. Seymour, and B. R. Webber. Longitudinally invariant Kt clustering algorithms for hadron hadron collisions. *Nucl. Phys. B*, 406:187, 1993.

[127] D. E. Soper S. D. Ellis. Successive combination jet algorithm for hadron collisions. *Phys. Rev. D*, 48:3160, 1993.

[128] Y. L. Dokshitzer, G. D. Leder, S. Moretti, and B. R. Webber. Better jet clustering algorithms. *JHEP*, 9708:001, 1997.

[129] Gerald C. Blazey, Jay R. Dittmann, Stephen D. Ellis, V. Daniel Elvira, K. Frame, S. Grinstein, Robert Hirosky, R. Piegaia, H. Schellman, R. Snihur, V.Sorin, and Dieter Zeppenfeld. Run II jet physics: Proceedings of the Run II QCD and weak boson physics workshop. arXiv:hep-ex/0005012, 2000.

[130] M. Cacciari, G. P. Salam, and G. Soyez. Energy calibration and resolution of the CMS electromagnetic calorimeter in pp collisions at sqrt(s) = 7 TeV. *JHEP*, 0804:063, 2008.

[131] CMS Collaboration. Particle-flow event reconstruction in CMS and performance for jets, taus, and MET. *CMS Physics Analysis Summary*, CMS-PAS-PFT-09-001, 2010.

[132] CMS Collaboration. Commissioning of the particle-flow event reconstruction with the first LHC collisions recorded in the CMS detector. *CMS Physics Analysis Summary*, CMS-PAS-PFT-10-001, 2010.

[133] CMS Collaboration. Commissioning of the particle-flow reconstruction in minimum-bias and jet events from pp collisions at 7 TeV. *CMS Physics Analysis Summary*, CMS-PAS-PFT-10-002, 2010.

[134] CMS Collaboration. Commissioning of the particle-flow event reconstruction with leptons from J/ψ and W decays at 7 TeV. *CMS Physics Analysis Summary*, CMS-PAS-PFT-10-003, 2010.

[135] CMS Collaboration. Determination of jet energy calibration and transverse momentum resolution in CMS, 2011.

[136] M. Cacciari and G. P. Salam. Pileup subtraction using jet areas. *Phys. Lett. B*, 659:119, 2008.

[137] M. Cacciari, G. P. Salam, and G. Soyez. The catchment area of jets. *JHEP*, 04:005, 2008.

[138] M. Cacciari, G. P. Salam, and G. Soyez. FastJet user manual (for version 3.0.2). *Eur. Phys. Jour. C*, 72:1896, 2012.

[139] CMS Collaboration. Jet energy resolution in CMS at sqrt(s)=7 TeV, 2011. CMS-PAS-JME-10-014.

[140] CMS Collaboration. Performance of tau-lepton reconstruction and identification in CMS. *JINST*, 7:P01001, 2012.

[141] CMS Collaboration. Identification of b-quark jets with the CMS experiment. *JINST*, 8:P04013, 2013.

[142] CMS Collaboration. Performance of missing transverse momentum reconstruction algorithms in proton-proton collisions at sqrt(s) = 8 TeV with the CMS detector. *CMS Physics Analysis Summary*, CMS-PAS-JME-12-002, 2013.

[143] CMS Collaboration. Pileup jet identification, 2013. CMS-PAS-JME-13-005.

[144] F. Maltoni and T. Stelzer. MadEvent: Automatic event generation with MadGraph. *JHEP*, 02:027, 2003.

[145] S. Frixione, P. Nason, and C. Oleari. Matching NLO QCD computations with parton shower simulations: the POWHEG method. *JHEP*, 11:070, 2007.

[146] S. Weinzierl. Introduction to monte carlo methods. arXiv:hep-ph/0006269, 2000.

[147] T. Sjostrand, S. Mrenna, and P. Skands. PYTHIA 6.4 Physics and Manual. *JHEP*, 0605:026, 2006.

[148] T. Gleisberg, S. Hoeche, F. Krauss, M. Schoenherr, S. Schumann, F. Siegert, and J. Winter. Event generation with sherpa 1.1. *JHEP*, 0902:007, 2009.

[149] G. Corcella, I. G. Knowles, G. Marchesini, S. Moretti, K. Odagiri, P. Richardson, M. H. Seymour, and B. R. Webber. HERWIG 6.5. *JHEP*, 0101:010, 2001.

[150] R. Field. Early lhc underlying event data findings and surprises. arXiv:hep-ph/9709356 (The Z2 tune differs from the Z1 tune presented here in using CTEQ6 PDF set instead of CTEQ5.), 2010.

[151] S. Agostinelli, J. Allison, K. Amako, J. Apostolakis, H. Araujo, P. Arce, M. Asai, D. Axen, S. Banerjee, G. Barrand, F. Behner, L. Bellagamba, J. Boudreau, L. Broglia, A. Brunengo, H. Burkhardt, S. Chauvie, J. Chuma, R. Chytracek, G. Cooperman, G. Cosmo, P. Degtyarenko, A. Dell'Acqua, G. Depaola, D. Dietrich, R. Enami, A. Feliciello, C. Ferguson, H. Fesefeldt, G. Folger, F. Foppiano, A. Forti, S. Garelli, S. Giani, R. Giannitrapani, D. Gibin, J.J. Gomez Cadenas, I. Gonzalez, G. Gracia Abril, G. Greeniaus, W. Greiner, V. Grichine, A. Grossheim, S. Guatelli, P. Gumplinger, R. Hamatsu, K. Hashimoto, H. Hasui, A. Heikkinen, and A. Howard. Geant4 - a simulation toolkit. *Nucl. Instrum. Meth. A*, 506:250, 2003.

[152] R. J. Barlow. *Statistics: A Guide to the Use of Statistical Methods in the Physical Sciences*. John Wiley and Sons, 1989.

[153] J. Conway. *Statistical Data Analysis*. Oxford Science Publications, 1998.

[154] W. T. Eadie, D. Drijard, F. E. James, M. Roos, and B. Sadoulet, editors. *Statistical Methods in Experimental Physics*. North-Holland Publishing Company, 1971.

[155] A. G. Frodesen, O. Skjeggestad, and H. Tofte, editors. *Probability and Statistics in Experimental Physics*. Universitetsforlaget, 1979.

[156] J. Neyman and E. S. Pearson. On the problem of the most efficient tests of statistical hypotheses. *Phil. Trans. R. Soc. Lond. A*, 231:289, 1933.

[157] CMS Collaboration. Combined results of searches for the standard model Higgs boson in pp collisions at sqrt(s) = 7 tev. *Phys. Lett. B*, 710:26, 2012.

[158] G. Cowan, K. Cranmer, E. Gross, and O. Vitells. Asymptotic formulae for likelihood-based tests of new physics. *Eur. Phys. J. C*, 71:1554, 2011.

[159] T. Junk. Confidence level computation for combining searches with small statistics. *Nucl. Instrum. Meth. A*, 434:435, 1999.

[160] A. Read. Modified frequentist analysis of search results (The CLs method), 2000. CERN-OPEN-2000-005.

[161] ATLAS Collaboration. Explanatory figures for the higgs boson exclusion plots. http://atlas.ch/news/2011/simplified-plots.html, 2011.

[162] J. M. Campbell and R. Ellis. MCFM for the Tevatron and the LHC. *Nucl. Phys. Proc. Suppl.*, 205:10, 2010.

[163] T. Binoth, N. Kauer, and P. Mertsch. Gluon-induced qcd corrections to pp $\rightarrow$ ZZ $\rightarrow$ l anti-l l' anti-l'. arXiv:hep-ph/0807.0024, 2008.

[164] K. S. Cranmer. Kernel estimation in high-energy physics. *Comput. Phys. Commun.*, 136:198, 2001.

[165] CMS Collaboration. CMS luminosity based on pixel cluster counting - Summer 2012 update. *CMS Physics Analysis Summary*, CMS-PAS-LUM-12-001, 2012.

[166] CMS Collaboration. Search for the standard model Higgs boson in the H to ZZ to 2l 2nu channel in pp collisions at sqrt(s) = 7 tev. *JHEP*, 03:040, 2011.

[167] Y. Gao, A. V. Gritsan, Z. Guo, K. Melnikov, M. Schulze, and N. V. Tran. Spin determination of single-produced resonances at hadron colliders. *Phys. Rev. D*, 81:075022, 2010.

[168] S. Bolognesi, Y. Gao, A. V. Gritsan, K. Melnikov, M. Schulze, N. V. Tran, and Andrew Whitbeck. On the spin and parity of a single-produced resonance at the lhc. *Phys. Rev. D*, 86:095031, 2012.

[169] CMS Collaboration. Performance of CMS muon reconstruction in pp collision events at $\sqrt{s} = 7$ TeV. *JINST*, 7:P10002, 2012.

[170] CMS Collaboration. Search for the standard model Higgs boson decaying to a W pair in the fully leptonic final state in pp collisions at $\sqrt{s} = 7$ TeV. *Phys. Lett. B*, 710:91, 2012.

[171] A. De Rujula, J. Lykken, M. Pierini, C. Rogan, and M. Spiropulu. Higgs look-alikes at the lhc. *Phys. Rev. D*, 82:013003, 2010.

[172] C. N. Yang. Selection rules for the dematerialization of a particle into two photons. *Phys. Rev.*, 77:242, 1950.

[173] ATLAS Collaboration. Measurements of the properties of the Higgs-like boson in the four lepton decay channel with the ATLAS detector using 25 fb^{-1} of proton-proton collision data. *ATLAS Conference Report*, ATLAS-CONF-2013-013, 2013.

[174] ATLAS Collaboration. Evidence for the spin-0 nature of the Higgs boson using ATLAS data. *Phys. Lett. B*, 726:120, 2013.

[175] CMS Collaboration. Observation and measurement of the two photon decay of the 125 GeV Higgs boson. *Eur. Phys. J. C*, To be published, 2013.

[176] C. Palmer. Observation of and measurements with a Higgs boson decaying to two photons. CMS Thesis, 2014.

[177] ATLAS Collaboration. Measurements of the properties of the Higgs-like boson in the two photon decay channel with the ATLAS detector using 25 fb^1 of proton-proton collision data. *ATLAS Conference Report*, ATLAS-CONF-2013-012, 2013.

[178] CMS Collaboration. Measurement of Higgs boson production and properties in the WW decay channel with leptonic final states. *JHEP*, 01:096, 2013.

[179] J. H. Yoo. Evidence of Higgs to WW to two leptons and two neutrinos at CMS. CMS Thesis, 2014.

[180] ATLAS Collaboration. Measurements of the properties of the higgs-like boson in the $WW^* \to \ell\nu\ell\nu$ decay channel with the ATLAS detector using 25 fb^1 of proton-proton collision data. *ATLAS Conference Report*, ATLAS-CONF-2013-030, 2013.

[181] ATLAS Collaboration. Evidence for Higgs boson decays to the tau+tau- final state with the ATLAS detector. *ATLAS Conference Report*, ATLAS-CONF-2013-108, 2013.

[182] ATLAS Collaboration. Search for the bb decay of the standard model Higgs boson in associated (W/Z)H production with the ATLAS detector. *ATLAS Conference Report*, ATLAS-CONF-2013-079, 2013.

[183] CMS Collaboration. Evidence for the 125 GeV Higgs boson decaying to a pair of tau leptons. *JHEP*, To be published, 2013.

[184] CMS Collaboration. Search for the standard model Higgs boson produced in association with a W or a Z boson and decaying to bottom quarks. *Phys. Rev. D*, 89:012003, 2014.

[185] CMS Collaboration. Evidence for the direct decay of the 125 GeV Higgs boson to fermions. *Nature Phys.*, 00:00, 2014.

[186] F. Caola and K. Melnikov. Constraining the higgs boson width with ZZ production at the LHC. *Phys.Rev. D*, 88:054024, 2013.

[187] Ciaran Williams John M. Campbell, R. Keith Ellis. Bounding the Higgs width at the LHC using full analytic results for $gg \to 2e2\mu$. arXiv:hep-ph/1311.3589, 2013.

[188] N. Kauer and G. Passarino. Inadequacy of zero-width approximation for a light higgs boson signal. arXiv:hep-ph/1206.4803, 2012.

[189] CMS Collaboration. A measurement of the Higgs boson width from off-shell production and decay to $ZZ \to \ell\ell\ell'\ell'$ and $\ell\ell\nu\nu$. *CMS Physics Analysis Summary*, CMS-PAS-HIG-14-002, 2014.

[190] M. Veltman. Limit on mass differences in the Weinberg model. *Nucl. Phys. B*, 123:89, 1997.

[191] P. Sikivie. Isospin breaking in technicolor models. *Nucl. Phys. B*, 173:189, 1980.

[192] CMS Collaboration. Measurements of the properties of the new boson with a mass near 125 GeV. *CMS Physics Analysis Summary*, CMS-PAS-HIG-13-005, 2013.

[193] J. Elias-Miro, J. R. Espinosa, G. F. Giudice, G. Isidori, A. Riotto, and A. Strumia. Higgs mass implications on the stability of the electroweak vacuum. *Phys. Lett. B*, 709:222, 2012.

[194] G. Degrassi, S. D. Vita, J. Elias-Miro, J. R. Espinosa, G. F. Giudice, G. Isidori, and A. Strumia. Higgs mass and vacuum stability in the standard model at NNLO. *JHEP*, 1208:098, 2012.

[195] D. Buttazzo, G. Degrassi, P. P. Giardino, G. F. Giudice, F. Sala, A. Salvio, and A. Strumia. Investigating the near-criticality of the Higgs boson. arXiv:hep-ph/1307.3536, 2013.

[196] J. Beringer and others (Particle Data Group). The Review of Particle Physics. *Phys. Rev. D*, 86:010001, 2012. 2013 update: http://pdg.lbl.gov/2013/reviews/rpp2013-rev-higgs-boson.pdf.

[197] A. Vartak, M. LeBourgeois, and V. Sharma. Lepton isolation in the CMS Tracker, ECAL and HCAL. CMS Analysis Note: AN-10-106, 2010.

[198] S. Bolognesi. Muon detection in CMS: from the detector commissioning to the standard model higgs search. CMS Thesis: http://personalpages.to.infn.it/ bolognes/docu/tesi.pdf, 2009.

[199] CMS Collaboration. Measurement of the production and decay of a higgs boson in the four-lepton final state. Expected: Phys. Rev. D. [arXiv:1312.5353 [hep-ex]].